”Search for Supersymmetry in Final States with Jets, Missing Transverse Energy and one charged Lepton with the ATLAS-Experiment”

Dissertation
zur Erlangung des Grades

“Doktor
der Naturwissenschaften”

am Fachbereich Physik, Mathematik und Informatik
der Johannes Gutenberg-Universität
in Mainz

Carsten Meyer
geb. in Koblenz

Mainz, den 23.04.2014

1. Berichterstatter:
2. Berichterstatter:
Datum der mündlichen Prüfung: 08.04.2014

Abstract

In the year 2011, the ATLAS experiment at the Large Hadron Collider collected 4.7 fb^{-1} of data at a center of mass energy of 7 TeV. Part of the extensive physics programm of the ATLAS experiment is the search for physics beyond the standard model. Supersymmetry - a new symmetry which transforms bosons into fermions and vice versa - is considered to be the most promising candidate for new physics, and numerous direct and indirect searches for supersymmetry have been performed over the last decades.

In the following thesis, a direct search for supersymmetry in final states with jets, missing transverse energy and *exactly* one electron or muon is performed. The analyzed dataset of $\int Ldt = 4.7$ fb^{-1} contains all data that was collected with the ATLAS experiment at a center of mass energy of 7 TeV. The results of the analysis are combined with several other leptonic search channels in order to maximize the sensitivity on various supersymmetric production and decay mechanisms. No deviation between measured data and standard model expectation is observed, and limits are set in several different supersymmetric models.

Kurzfassung

Im Jahr 2011 wurde am Large Hadron Collider mit dem ATLAS Experiment ein Datensatz von 4.7 fb^{-1} bei einer Schwerpunktsenergie von 7 TeV aufgezeichnet. Teil des umfangreichen Physikprogrammes des ATLAS Experiments ist die Suche nach Physik jenseits des Standardmodells. Supersymmetrie - eine neue Symmetrie zwischen Bosonen und Fermionen - wird als aussichtsreichester Kandidat für neue Physik angesehen, und zahlreiche direkte und indirekte Suchen nach Supersymmetrie wurden in den letzten Jahrzehnten bereits durchgeführt.
In der folgenden Arbeit wird eine direkte Suche nach Supersymmetrie in Endzuständen mit Jets, fehlender Transversalenergie und *genau* einem Elektron oder Myon durchgeführt. Der analysierte Datensatz von $\int Ldt = 4.7$ fb^{-1} umfasst die gesamte Datenmenge, welche am ATLAS Experiment bei einer Schwerpunktsenergie von 7 TeV aufgezeichnet wurde. Die Ergebnisse der Analyse werden mit verschiedenen anderen leptonischen Suchkanälen kombiniert, um die Sensitivität auf diversen supersymmetrischen Produktions- und Zerfallsmodi zu maximieren. Die gemessenen Daten sind kompatibel mit der Standardmodellerwartung, und neue Ausschlussgrenzen in verschiedenen supersymmetrischen Modellen werden berechnet.

Contents

1 Introduction

In the reductionistic approach, understanding nature as a whole enforces the understanding of its most fundamental constituents and interactions among them. Since the discovery of the electron in 1897 - which can be considered as the birth of high energy physics - advancing technologies allowed to discover more and more fundamental particles over the last century. In our current understanding, each microscopic phenomenon can be described by interactions among 12 fundamental particles[1]. So far, four fundamental interactions are known. 'Electromagnetism' - the force between electrically charged particles - allows to describe the properties of atoms and molecules. The 'strong force' is responsible for binding protons and neutrons within the nucleus, while the 'weak force' describes radioactive decays[2] . 'Gravity' - despite beeing the most important force for large scale structure formation in the universe and cosmological evolution as a whole - plays a negligible role at very small length scales.

Except gravity, these interactions and the fundamental particles are described in the so called 'standard model of particle physics', which will be introduced in detail in the following sections. In summer 2012, the last missing piece of the standard model - the Higgs boson - was discovered at the LHC, completing the standard model from an experimental point of view. Despite this discovery and several high precision tests of the standard model, it cannot provide the final theory of microscopic nature for several reasons discussed later on. Given this fact, physicists tried to extend the standard model over the last decades, in order to account for its weak points. Arguably the most promising extension is the so called 'supersymmetry', which transforms fermionic degrees of freedom into bosonic ones and vice versa. As a consequence of this new symmetry, new particles are predicted, which can in principle be searched for at collider experiments.

This thesis presents a search for supersymmetry in final states with one charged lepton[3], jets and missing transverse momentum, using data recorded with the ATLAS[4] experiment at the Large Hadron Collider (LHC) based at CERN[5] in Geneva. The analyzed dataset contains roughly 5 fb^{-1} recorded at a center of mass energy of 7 TeV. After introducing the necessary theoretical and experimental concepts in chapter 2 and 3, chapter 4 will relate the previous chapters by describing how supersymmetric particles are produced at the LHC. In chapter 5 the most important theoretical sources of systematic uncertainties and their impact on the final measurement will be discussed. In addition, a method, which allows to constrain some major theoretical uncertainties using ATLAS data will be presented. Finally, in chapters 6, 7 and 8 the results of the search and interpretations in several supersymmetric models will be shown. The results obtained in this thesis have been

[1] 12 = 6 quarks + 6 leptons, neglecting their antiparticles and gauge bosons for simplicity.

[2] More precisely, the force binding protons and neutrons in the nucleus is an effect of a fundamental force called 'quantum chromodynamics', which binds the quarks within hadrons.

[3] In the following, 'charged lepton' always denotes an electron or muon.

[4] **A** **T**oroidal **L**HC **A**pparatu**S**

[5] **C**onseil **E**uropéen pour la **R**echerche **N**ucléaire

published by the ATLAS Collaboration [73].

2 Theoretical principles

The following section gives an overview about the current understanding of high energy physics phenomena. After briefly establishing the standard model of particle physics, the concept of supersymmetry is introduced.

2.1 The standard model of high energy physics

The standard model of particle physics provides the best description of fundamental particles and their interactions currently known. A particle is called 'fundamental' if no evidence for further substructure exists. After introducing all known fundamental particles and their properties, the known interactions among them will be discussed. Currently three of the four fundamental forces of nature can be described within the framework of the standard model, while no quantum description of gravity exists so far. Experimental proof of the standard model comes from various fields of modern physics, testing the theory with very high precision.

The standard model is formulated as a Lagrangian quantum field theory with following schematic Lagrangian density

$$\mathcal{L}_{SM} = \mathcal{L}_{EW} + \mathcal{L}_{QCD} + \mathcal{L}_{Higgs} \tag{1}$$

The individual terms will be discussed in the following chapters. The standard model is a gauge theory, where the properties of each interaction are given by the requirement of local gauge invariance of the Lagrangian density. The gauge group of the standard model can be written as the following direct product

$$SU(3)_c \times SU(2)_L \times U(1)_Y \tag{2}$$

where $\mathrm{SU}(3)_c$ denotes the gauge group of the strong force and 'c' stands for 'color', which is the naming convention for the strong charge. The gauge group of electroweak interactions before spontaneous symmetry breaking can be written as the direct product $\mathrm{SU}(2)_L \times \mathrm{U}(1)_Y$, where '$Y$' denotes the so called weak hypercharge, which is the charge of U(1), and 'L' emphasizes that the behaviour of the weak force depends on the helicity of a particle. Formal details about the corresponding Lagrangian densities will be given in the following sections. After spontaneous symmetry breaking, the gauge group breaks down to

$$SU(3)_c \times U(1)_{EM}, \tag{3}$$

where 'EM' denotes the electromagnetic force. The mechanism of spontaneous symmetry breaking is a necessary part of the standard model and will be discussed in chapter 2.1.4.

2.1.1 Particle content

The particle spectrum of the standard model can be divided into fermions, which carry half integer spin and bosons with integer spin. Fermions are subdivided into quarks and leptons, dependent on the interactions they participate in. Quarks -

particle	symbol	mass
Up quark	u	$2.3\ ^{+0.7}_{-0.5}$ MeV
Down quark	d	$4.8\ ^{+0.7}_{-0.3}$ MeV
Strange quark	s	95 ± 5 MeV
Charm quark	c	1.275 ± 0.025 GeV
Bottom quark	b	4.18 ± 0.03 GeV
Top quark	t	$173.5 \pm 0.6 \pm 0.8$ GeV

Table 1: Quarks of the standard model [1].

as they carry electrical, strong and weak charge - take part in the electromagnetic, strong and weak force. Leptons do not carry strong charge and therefore only participate in the weak force and - if they carry electric charge - in the electromagnetic force. Table 1 summarizes the quarks, while table 2 shows the leptons[6]. In quantum field theories, the fundamental interactions are described by an exchange of a boson, called the 'carrier' of the force under consideration. Table 3 shows the fundamental bosons and some of their important characteristics.

In addition to the gauge bosons responsible for mediating forces, one boson called the 'Higgs boson' is part of the standard model, which is the only fundamental boson with spin zero. In chapter 2.1.4 it will be described why this boson is necessary for the standard model and how it is linked to the so called 'Higgs mechanism', which is responsible for the creation of mass of all fundamental particles. In august 2012, ATLAS and CMS published papers discovering a new particle in various final states, which is compatible with the standard model Higgs boson [2] [3][7]. The discovery of the Higgs boson can be considered to be the most important result for high energy physics over the last decades.

A more detailed presentation of how the interactions can be described in the framework of the standard model is given in the following sections. It is important to note that each particle, except the Higgs boson, gluon, Z^0 boson and photon, is accompanied by its antiparticle, which shares the same quantum number except the electric charge, which is flipped between particle and antiparticle.

2.1.2 Electroweak interactions

Despite being historically discovered as two distinct phenomena, Sheldon Glashow, Abdus Salam and Steven Weinberg managed to unify electromagnetism and the weak force in a theoretical framework called 'GSW theory' in 1967 [4]. Interactions

[6]The errors on the electron and muon mass are discarded as they are sub permille level [1]. All masses are given in natural units, fulfilling $c = \hbar = 1$.

[7]It should be stressed that not all properties of this new particle have been measured so far. Therefore its not yet proven whether this new resonance really is the standard model Higgs boson. So far the measured cross section and branching ratios are compatible with a standard model Higgs boson, but the spin for example could still be two instead of zero. Because of this, the properties of the Higgs boson listed in table 3 are put in brackets.

particle	symbol	mass
Electron	e	0.511 MeV
Muon	μ	105.658 MeV
Tau	τ	1776.82 $\pm$ 0.16 MeV
Electron Neutrino	ν_e	$<$ 2 eV
Muon Neutrino	ν_μ	$<$ 0.19 MeV
Tau Neutrino	ν_τ	$<$ 18.2 MeV

Table 2: Leptons of the standard model [1]

particle	symbol	mass	spin
Photon	γ	0	1
Gluon	g	0	1
Z^0 boson	Z^0	91.188 $\pm$0.098 GeV	1
$W^\pm$ boson	$W^\pm$	80.385 $\pm$0.015 GeV	1
Higgs boson	h	(126.0 $\pm$ 0.4(stat) $\pm$ 0.4(syst)) GeV	(0)

Table 3: Gauge bosons and the Higgs boson of the standard model [1]. The mass of the Higgs boson and corresponding uncertainties are taken from [2].

which contain either a photon, a Z^0 boson or a $W^\pm$ boson are called 'electroweak'. It turned out that interactions via electrically neutral photons or Z^0 bosons (neutral currents) behave differently compared to interactions containing the charged $W^\pm$ bosons (charged currents). To state this more precisely, the following quantity called ''helicity' of a particle, which describes the projection of the spin on the direction of the momentum, is introduced:

$$H := \frac{\mathbf{s} \cdot \mathbf{p}}{|\mathbf{s}| \cdot |\mathbf{p}|} = \begin{cases} +1 & (\angle(\mathbf{s}, \mathbf{p}) = 0) \\ -1 & (\angle(\mathbf{s}, \mathbf{p}) = \pi) \end{cases} \tag{4}$$

The helicity itself - as a scalar product of an axial vector (spin) and a vector (momentum) - is a pseudoscalar quantity, which changes sign under parity transformations. Helicity states with $H = 1$ are called 'right handed', while states with $H = -1$ are called 'left handed'. In general, interactions described by exchanges of a spin 1 particle can be vector or axial vector like. If parity is supposed to be conserved by the interaction under consideration, only pure vector or pure axial vector character is allowed. For charged currents, the matrix element of the interaction contains a vector and axial vector component of same strength and opposite sign. Therefore $W^\pm$ bosons couple only to left handed fermions and right handed antifermions, which means that parity is violated in the maximal way. Given this complication, table 1 and 2 are extended as shown in tables 4 and 5.
The newly introduced quantum number (I) is called 'weak isospin' and accounts for the parity violation in charged current interactions. Left handed particles have I = 1/2, while right handed particles have I = 0. Within each generation, the left handed quarks and leptons build a weak isospin doublet. In this doublet, the

Fermions	Generation	Electr. charge [e]	I	I_3
Leptons	$\nu_e \quad \nu_\mu \quad \nu_\tau$ $e \quad \mu \quad \tau$	0 -1	$1/2$	$+1/2$ $-1/2$
Quarks	$u \quad c \quad t$ $d \quad s \quad b$	$+2/3$ $-1/3$	$1/2$	$+1/2$ $-1/2$

Table 4: Left handed fermions of the standard model

Fermions	Generation	Electr. charge [e]	I	I_3
Leptons	$e \quad \mu \quad \tau$	-1	0	0
Quarks	$u \quad c \quad t$ $d \quad s \quad b$	$+2/3$ $-1/3$	0 0	0 0

Table 5: Right handed fermions of the standard model

two components transform into each other by emission or absorption of a $W^{\pm}$ boson, changing the third component of the weak isospin from +1/2 to -1/2 and vice versa[8]. Right handed fermions are described by a weak isospin singlet, as they do not couple to charged currents. In particular, no right handed neutrinos have been observed so far[9].

The Lagrangian density of electroweak interactions has the following form

$$\mathcal{L}_{EW} = \mathcal{L}_{Gauge} + \mathcal{L}_{fermion} \tag{5}$$

where the first term reads as

$$\mathcal{L}_{Gauge} = -\frac{1}{4} B_{\mu\nu} B^{\mu\nu} - \frac{1}{4} W^a_{\mu\nu} W^{\mu\nu}_a \tag{6}$$

with the two field strength tensors

$$B_{\mu\nu} = \partial_\mu B_\nu - \partial_\nu B_\mu \tag{7}$$

$$W^a_{\mu\nu} = \partial_\mu W^a_\nu - \partial_\nu W^a_\mu - g\epsilon^a_{bc} W^b_\mu W^c_\nu \tag{8}$$

$$\mu, \nu = 0, 1, 2, 3 \tag{9}$$

$$a, b, c = 0, 1, 2 \tag{10}$$

$B_{\mu\nu}$ denotes the field strength tensor of the commutative $U(1)_Y$, while $W^a_{\mu\nu}$ denotes the field strength tensor of the non commutative $SU(2)_L$. g denotes the accordant

[8]The concept is analogous to the 'strong isospin formalism' in nuclear physics, where the proton and neutron are considered as two components of a strong isospin doublet.

[9]It should be mentioned that neutrinos are assumed to be massless in the standard model, although proof from neutrino flavour oscillation experiments exists that they have a non vanishing mass. Several extensions of the standard model try to give explanations for the very small mass of the left handed standard model neutrinos by introducing heavy right handed neutrinos. This approach is known as the 'see saw mechanism' [5].

coupling constant and ϵ_{abc} the epsilon tensor. Therefore $\mathcal{L}_{Gauge}$ contains the propagators of the gauge bosons B_μ of $U(1)_Y$ and W_μ^a of $SU(2)_L$. While $B_{\mu\nu}$ only contains free terms (like in the classical description of electromagnetism), $W_{\mu\nu}^a$ also contains self interaction terms.

The gauge eigenstates B_μ and W_μ^a differ from the mass eigenstates ($W^\pm$ boson, Z^0 boson and photon). These are obtained by mixing the gauge eigenstates like

$$W_\mu^\pm = \frac{1}{\sqrt{2}}(W_\mu^1 \mp iW_\mu^2) \tag{11}$$

$$Z_\mu^0 = -B_\mu sin\Theta_\omega + W_\mu^0 cos\Theta_\omega \tag{12}$$

$$A_\mu^0 = B_\mu cos\Theta_\omega + W_\mu^0 sin\Theta_\omega \tag{13}$$

where A_μ^0 denotes the photon field and Θ_ω the amount of mixing called 'Weinberg angle' or 'weak mixing angle'.
The second term of equation 5, which describes how fermions couple to the weak gauge bosons reads as

$$\mathcal{L}_{fermion} = \bar{R}(iD_\mu^R\gamma^\mu)R + \bar{L}(iD_\mu^L\gamma^\mu)L \tag{14}$$

with the covariant derivatives, which ensure local gauge invariance

$$D_\mu^R = \partial_\mu + ig'B_\mu Y \tag{15}$$

$$D_\mu^L = \partial_\mu + ig'B_\mu Y + igW_\mu^a T^a \tag{16}$$

Here, Y denotes the generator of the U(1) group, while T^a denote the generators of the SU(2) group. R (L) denotes the right handed (left handed) component of the fermion field. As already discussed, the weak interaction behaves differently for left handed and right handed particles, which is taken into account by the form of the Lagrangian density. The first term of equation 14 - which describes the coupling of right handed fermions to the gauge field B_μ - contains one coupling constant (g') in the covariant derivative, while the second term contains the same coupling to the gauge field B_μ and in addition a coupling to W_μ^a with strength g.

2.1.3 Strong interactions

The strong interaction or 'quantum chromodynamics' (QCD) is responsible for binding quarks within hadrons. The corresponding gauge group of QCD is $SU(3)_c$. Quarks come in three different colors, which are named as red, green and blue (r,g,b) and their anticolors ($\bar{r}$,$\bar{g}$,$\bar{b}$). The carrier of the strong force is a massless particle called 'gluon', which itself carries a color and an anticolor of different type[10].

As for the weak interaction, the Lagrangian density of QCD is separated into a gauge term - which contains the gluon propagators and gluon-gluon interactions - and a term describing the coupling of gluons to quarks

[10]More precisely, the SU(3) symmetry allows for 9 color combinations yielding a color octet and a color singlet, where the color octet contains the 8 gluons of QCD.

$$\mathcal{L}_{QCD} = \mathcal{L}_{Gauge} + \mathcal{L}_{fermion} \tag{17}$$

The Gauge term reads as

$$\mathcal{L}_{Gauge} = -\frac{1}{4} G^a_{\mu\nu} G^{\mu\nu}_a \tag{18}$$

with the field strength tensor of QCD

$$G^a_{\mu\nu} = \partial_\mu G^a_\nu - \partial_\nu G^a_\mu - g f^a_{bc} G^b_\mu G^c_\nu \tag{19}$$

The first two terms are analogous to the field strength tensor of electromagnestism, while the last term describes the self interaction of the gluon. This self interaction is caused by the non abelian structure of SU(3), which is similar to what was already presented for the W^a_μ fields in $\mathrm{SU}(2)_L$. g denotes the coupling constant of QCD. The generators of SU(3) obey the following commutator relation

$$[T_a, T_b] = i f_{abc} T_c \tag{20}$$

where f_{abc} denotes the structure constants of QCD. Inserting the field strength tensor into the Lagrangian density yields cubic and quartic terms in G^a_μ, representing pure gluon vertices with 3 and 4 legs. The coupling strength of QCD increases with distance (decreases with momentum transfer) between colored objects, only allowing for colorless bound states. This mechanism is called 'confinement' and explains why the strong interaction has a very short range, despite the gluon being massless.
The second term in equation 17 has the following form

$$\mathcal{L}_{fermion} = -g(\bar{q}\gamma^\mu T_a q) G^a_\mu \tag{21}$$

and describes the coupling of quarks to gluons, where q denotes the quark fields.

2.1.4 Spontaneous symmetry breaking and the Higgs mechanism

Introducing explicit dirac mass terms like $m\bar{\Psi}\Psi$ in the standard model Lagrangian density violates local gauge invariance of weak interactions. To avoid this, a new field called the Higgs field is introduced and masses are generated indirectly via 'spontaneous symmetry breaking'. The Lagrangian of the Higgs sector has the following form

$$\mathcal{L}_{Higgs} = (D^L_\mu H)^\dagger (D^{L\mu} H) + \mu^2 H^\dagger H - \lambda (H^\dagger H)^2 \tag{22}$$

where H denotes the complex Higgs field doublet:

$$H = \begin{pmatrix} H^+ \\ H^0 \end{pmatrix} \tag{23}$$

The first term in equation 22 describes the coupling of the Higgs field to the gauge bosons of weak interaction via the covariant derivatives already introduced with equations 15 and 16. The second and third term describe the Higgs potential, where μ^2 and λ are positiv real numbers. The most important characteristic of this

potential is that the minimum is circular degenerate for $H \neq 0$. The amount of the Higgs field at the minimum is called 'vacuum expectation value' (VEV) of the Higgs field and has the following form:

$$\nu := | < H > | = \sqrt{\frac{\mu^2}{2\lambda}} \tag{24}$$

Expanding the Higgs potential around a certain vacuum state breaks the symmetry of equation 22 and gives mass terms for the weak gauge bosons, while it preserves the $U(1)_{EM}$ symmetry yielding a massless photon. In addition, a kinetic term and a mass term for a new scalar particle appears, which is identified with the Higgs boson.

The mass generation of the standard model fermions is obtained in an analogous way by adding couplings of the fermion fields to the Higgs field,

$$\mathcal{L}_{Yukawa} = -G(\bar{L}HR + \bar{R}H^{\dagger}L) \tag{25}$$

where G denotes free parameters called 'Yukawa' couplings of the Higgs field to left and right handed fermion fields. After spontaneous symmetry breaking, all fermions obtain gauge invariant mass terms. It is important to note that neither the masses of the weak gauge bosons nor the fermion masses are predicted by the Higgs mechanism and therefore need to be measured[11].

2.1.5 Summary and open questions

The standard model was tested by various experiments to very high precision, and its predictions are used in almost every field of modern physics, like nuclear physics, atomic physics or even cosmology. The LEP collider at CERN allowed for a very precise measurement of some of the standard model parameters at the electroweak scale by colliding electrons and positrons and creating on shell Z^0 bosons. Figure 1 shows a comparison between the predicted SM parameters using a global fit with five input parameters ($\alpha(m_Z^2)$, $\alpha_s(m_Z^2)$, m_Z , m_t , m_{Higgs}) and the direct measurements of them [6]. Also shown is the 'pull' for each variable, defined as the deviation between the fit prediction and the measurement devided by the error on the measurement. Only one variable shows a deviation larger than 2 standard deviations.

Despite the enormous experimental proof of the standard model, it cannot be the final description of microscopic nature due to some severe drawbacks. First of all, not all known fundamental forces of nature are included in the model. While electromagnetism, weak and strong interactions are described with astounding accuracy, gravity is not contained at all. From a pragmatic point of view, this might not be a real problem, as gravity can be neglected at these length scales due to the much smaller coupling strength. Nevertheless, all fundamental particles also carry energy and therefore interact gravitationally, and a 'complete' theory of nature should be able to describe these interactions as well.

[11] Only relations between the masses of the weak gauge bosons, the size of the weak coupling constants and the Higgs VEV are predicted by the theory.

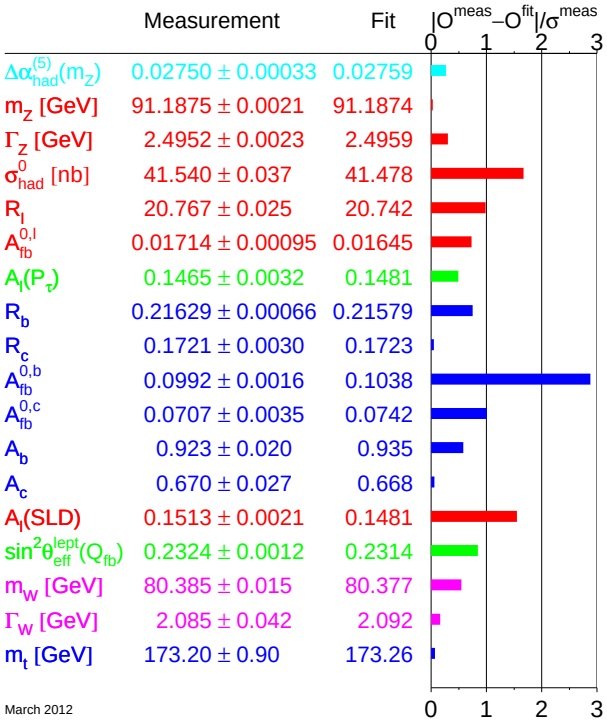

Figure 1: Comparison between the predicted SM parameters using a global fit with five input parameters and direct measurements [6].

Furthermore, the large amount of free parameters is not satisfying in an esthetic sense. As discussed in the section about the Higgs mechanism for example, it was noted that each Yukawa coupling between the Higgs boson and fermions of the standard model is a free parameter. Regarding esthetics, this kind of problem is also present for the structure of the standard model particles and forces. No mechanism is known, which explains the number of generations or the observed mass hierarchies for example.

One of the severe problems of the standard model, where supersymmetry helps in a very convenient way is the so called 'Hierarchy problem'. In quantum field theories, masses of particles are schematically described the following way

$$m_{phys.} = m_{bare} + \Delta m_{rad.} \tag{26}$$

where $m_{phys.}$ denotes the physical mass (i.e. what is measured with experiments). This mass is the sum of m_{bare}, which is the mass parameter of the corresponding particle in the Lagrangian density at leading order, and $\Delta m_{rad.}$, which describes

all quantum corrections to the bare mass for arbitrary high orders in pertubation theory. For the Higgs boson, these radiative corrections are several orders of magnitude larger than what is expected for the mass of the Higgs boson, which leads to an enormeous finetuning in order to obtain a physical mass at the order of ≈ 100 GeV. Another severe problem with the standard model is that it cannot explain cosmological observations, which suggest the existence of a new heavy and solely weak interacting particle. In addition, the matter-antimatter asymmetry in today's universe cannot be explained by the small CP violation of the standard model.
In the following section - where supersymmetry will be motivated - some of these drawbacks are discussed in more detail and potential solutions, obtained by introducing supersymmetry, are presented.

2.2 Supersymmetry

Given the discussed weak points of the standard model, theorists tried to either extend the model, or to embed it in a more general theory over the last decades. Especially supersymmetry [7] [8] attracts the interest of many physicists working on model building for several good reasons that will be discussed in chapter 2.2.1. The concept of supersymmetry is rather simple. A new operator is introduced that relates fermionic to bosonic states and vice versa. Given this, fermions and bosons are described by a new multiplet, and the supersymmetry operator transforms the states contained in this multiplett into each other.
Historically the concept of introducing a new multiplett has been very useful to describe nucleons as a strong isospin doublet and also left handed quarks and leptons as doublets under $SU(2)_L$. The following presentation of supersymmetry follows the presentation of [9] in most aspects.

2.2.1 Motivation

As discussed in the section about the standard model, supersymmetry provides a couple of improvements[12]. It was already mentioned that an enormous finetuning is necessary, in order to compensate for the huge loop effects contributing to the physical Higgs mass. In supersymmetry, this is solved in a very elegant way and directly arises from the new symmetry itself. The one loop contribution of every fermion to the Higgs mass can be written as

$$\Delta m_H^2 = -\frac{|\lambda_f|^2}{8\pi^2}\Lambda_{UV}^2 + ... \tag{27}$$

while scalar particles yield contributions like [9]

$$\Delta m_H^2 = \frac{\lambda_s}{16\pi^2}[\Lambda_{UV}^2 - 2\mathrm{m}_s^2 \ln(\frac{\Lambda_{UV}}{\mathrm{m}_s}) + ...] \tag{28}$$

λ_f (λ_s) denotes the coupling strength of a fermion (boson) with mass m_f (m_s) to the Higgs boson. Λ_{UV} is a cutoff energy used to regulate the loop integral, which can be interpreted as the energy scale where physics beyond the standard model will appear. The size of Λ_{UV} is usually chosen to be of the order of the Planck scale ($\approx 10^{19}$ GeV), which leads to corrections that are roughly 30 orders of magnitude larger than the squared physical Higgs mass of order $(100\ \mathrm{GeV})^2$.

In the standard model, no fundamental scalar particles except the Higgs boson itself are present, and the huge contributions only arise from the couplings of quarks and leptons to the Higgs boson like described by equation 27[13]. In supersymmetry, each standard model fermion is accompanied by two scalar fields, which all contribute as shown in equation 28. Both types of contributions differ by sign. Fermions increase

[12] It should be stressed that historically supersymmetry was *not* developed to solve the problems of the standard model, but for pure mathematical esthetic reasons. The fact that it solves some of the main drawbacks of the standard model was discovered later.

[13] These contributions are by far dominated by the top quark contributions due to its large Yukawa coupling.

the Higgs mass, while scalar particles decrease it. For the special case of $\lambda_s = |\lambda_f|^2$, the contributions quadratically in Λ_{UV} cancel exactly, stabilizing the Higgs mass at the expected value of $m_H^2 \approx (100\ \text{GeV})^2$ [14].

Apart from the solution of the hierarchy problem, supersymmetry even predicts an upper bound on the mass of the lightest Higgs boson at tree level

$$m_{h^0} < |\cos(2\beta)| m_Z \tag{29}$$

which cannot exceed the mass of the Z^0 boson. Taking into account corrections at higher order in pertubation theory, this bound is softened to roughly 135 GeV [11]. However, in contrast to the standard model, where the Higgs boson mass is completely unconstrained, this is a significant improvement[15].

In quantum field theories, the coupling strengths of all forces included in the model are not constant, but depend on the energies of the particles involved. Quantitatively, this is described by the so called 'Renormalization Group Equations' (RGEs). At higher orders, diagrams including loops will appear, and the specific form of the RGEs at given order depends on the particle content of the model, which can contribute to loop diagrams. Figure 2 compares how the couplings run depending on the energy scale in the standard model and in the minimal supersymmetric extension of the standard model (MSSM) [9].
Within the standard model, the couplings approach each other for energies of roughly 10^{14} GeV. For the MSSM, the values exactly overlap at roughly 10^{16} GeV. It should be stressed that a unification of couplings is not necessary from a theoretical point of view[16], and that the behaviour of couplings shown in figure 2 might just be a coincidence. However, the unification could be motivated by arguing that also electromagnetism and the weak force are unified above a certain energy scale. Furthermore, it might also be seen as a hint for a grand unified theory (GUT) or superstring theory, which both can unify the gauge couplings below the Planck scale.

Another strong motivation for supersymmetry comes from astrophysics and cosmology. Since the early 20th century a severe discrepancy between the amount of luminous matter and the total matter - obtained by gravitational observations - is known, which displays itself at different length scales. The first evidence for this discrepancy comes from measuring the tangent movement of objects within galaxies, which was first performed by Fritz Zwicky in the nineteen-thirties. It turned out that the tangent velocities at large distances from the galactic centers cannot be

[14] One should mention that another problem regarding finetuning exists in supersymmetry called the 'μ-problem' or 'little hierarchy problem', which is considered much less severe by most physicists and can be solved in supersymmetric models like the 'next to minimal supersymmetric standard model' [10].

[15] It should be noted that quantum field theoretical arguments exist, which constrain the Higgs mass in the standard model at high energy scales [12]. However, given that the allowed range of the Higgs mass is very large for energies where the standard model is still expected to work, and the model runs into several problems at very high energy scales anyway (where the constrains on the Higgs mass are stronger), the explanatory power of such arguments is questionable.

[16] Unless you develop models which explicitly include a grand unification of interactions.

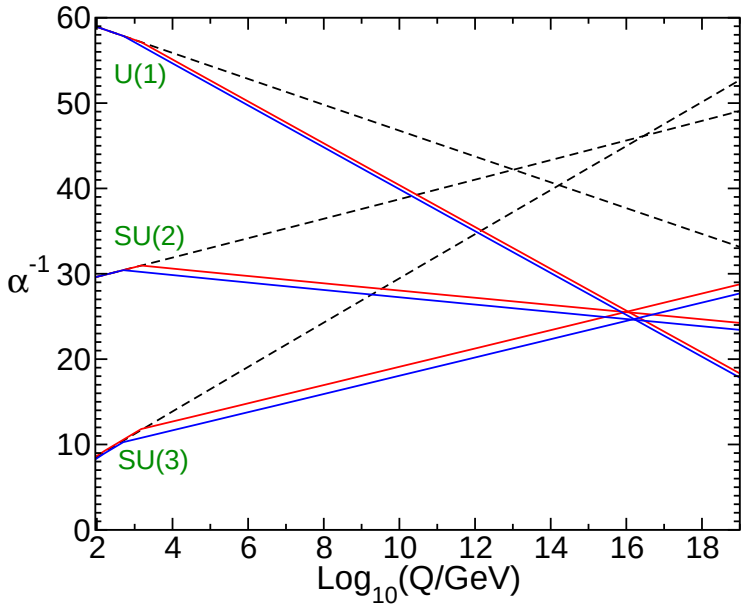

Figure 2: Running of the inverse coupling constants in dependence of the energy scale for the standard model and the MSSM at 2 loop level [9]. The dashed lines correspond to the standard model, while the solid lines show an extrapolation with error bands for the MSSM.

described by the gravitational potential arising from the observable matter within the galaxies. In order to model these 'rotational curves' properly, an additional, non luminous matter component was introduced, which is located in the galactic halos. This component was labeled 'dark matter' [13].

A further very illustrative evidence for dark matter comes from the observation of gravitational lensing. General relativity (GR) predicts that the trajectories of photons will be distracted by the curved spacetime, caused by large accumulations of matter. If a large aggregation of matter is in the line of sight between an observer and a bright light source - like a galaxy - the image of the light source will appear distorted, leading to so called 'arcs' or 'einstein rings'. Comparing the amount of matter of the lensing object estimated by the emitted radiation on the one hand, and the gravitational impact on the other hand, shows a clear mismatch, which allows to evaluate the amount of dark matter within the lensing object. This effect was observed for several galaxies [14]. Figure 3 shows two pictures of 1E0657-558, which is a cluster merger at a redshift[17] of 0.296. The left picture shows the merging clusters in the optical spectrum, while the right picture shows an x-ray image. The green contours represent the centers of mass of each cluster obtained by weak lensing observations. The gas in each cluster got heated up during the collision and radiates in the x-ray spectrum, while the centers of mass of both clusters passed each other

[17]The cosmological redshift is a consequence of the expanding spacetime and defined as $z := \frac{a(t_a)}{a(t_e)} - 1$, where $a(t_a)(a(t_e))$ denotes the cosmological expansion factor at the time the photon was absorbed (emitted).

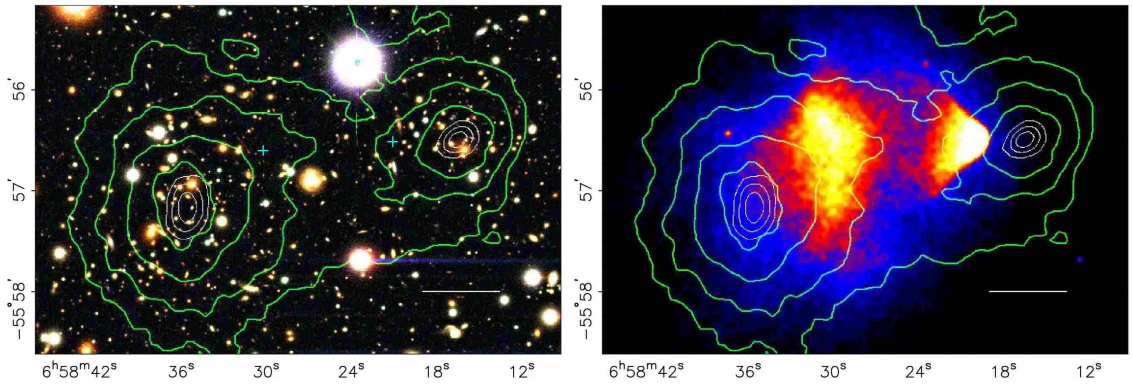

Figure 3: Pictures of the cluster merger 1E0657-558 in the optical spectrum (left) and in the x-ray spectrum (right). The white bar indicates 200 kpc at the distance of the cluster. The green contours show the centers of mass, obtained by weak lensing observations [14].

without interacting much. Given the total mass - obtained by the gravitational lensing - the fraction of mass contained in the gas can be estimated to be roughly 10% of the total cluster mass. The remaining 90% were assigned to the dark matter in each cluster.

Even on the largest scales, strong evidence for dark matter appears. In the past several simulations were performed, which try to reproduce the observed distribution of matter within the universe by evolving the gravitational structure formation of a system containing roughly 10^{10} particles from early phases of the universe up to today. It turned out that only simulations including dark matter manage to reproduce the distribution of galaxies we observe today [15]. Figure 4 shows the result of the simulation for today's epoch of the universe.
The existence of dark matter at cosmological scales cannot only be deduced from gravitational structure formation. Also precise observations of the cosmic microwave background (CMB) enforce a non relativistic and non baryonic matter component. The WMAP experiment measured the CMB, which is made of frozen out photons from the big bang nucleosynthesis, very precisely. Its power spectrum can only be described properly assuming a dark matter particle, which contributed to the CMB via annihilation processes in the early phases of the universe [16].

However, the properties of the dark matter particle - except that it must be cold (i.e. slow compared to the speed of light) - and the underlying theory are still unknown. Within the standard model, no particle exists that could come into consideration. The neutrino, being the only particle which only interacts via weak interactions is already ruled out due to its too small mass[18]. For some assumptions - which will be discussed later - supersymmetry postulates a particle that could play the role of the dark matter particle[19].

[18]Given the known standard model couplings

[19]It should be noted that the dark matter particle does not necessarily needs to be massive (order of 100 GeV), like is predicted by several supersymmetric models. The hypothetical axion, which solves the strong CP problem can have masses of only several eV and also provides a candidate for

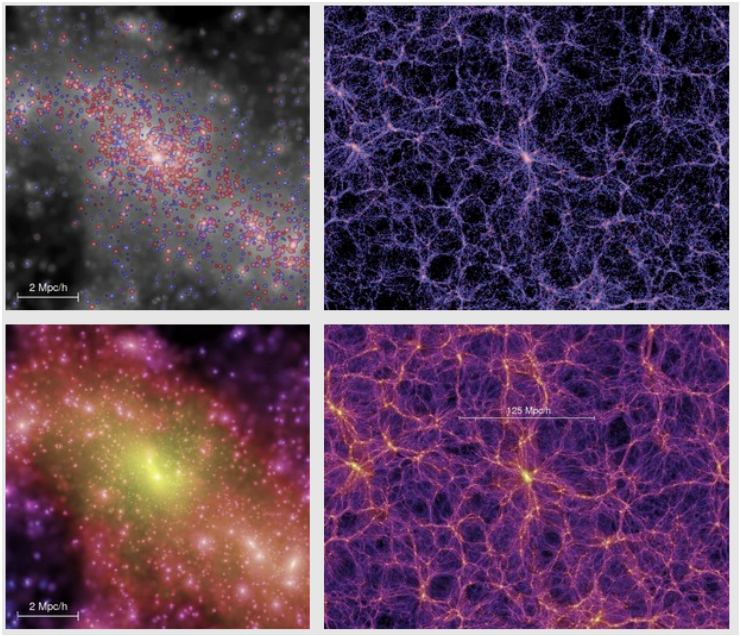

Figure 4: Result of the Millennium simulation for today's epoch of the universe. The simulation manages to reproduce the observed distribution of mass on various length scales assuming roughly 15% cold dark matter [15]. The upper row shows the distribution of luminous matter on two different length scales indicated by the white bar. The lower row shows the corresponding distribution of dark matter. Especially on large length scales, the luminous matter traces the distribution of dark matter.

For completeness, it should be mentioned that different approaches exist to explain the astrophysical observations stated above, without postulating a new matter component. For example, gravity could behave differently on very large length scales [19].

As already discussed in the introduction of the standard model, gravity is not included in this model at all. In the next section, it will be shown that the supersymmetry transformations obey commutator relations, which relate the generators of supersymmetry with the generator of the Poincaré group. As GR is based on the invariance under general coordinate transformations, these commutator relations can be considered as a very first step towards an inclusion of gravity in a high energy physics theory.

2.2.2 Theoretical concepts

As already mentioned in the introduction, supersymmetry relates the two kinds of fundamental particles we know - fermions and bosons - via a new symmetry. If S is a generator of the supersymmetry transformation, its effect on a particle state can be written schematically as

dark matter [17]. However, cosmological observations actually favour a dark matter particle with a mass around the electroweak scale, which is known as the 'WIMP miracle' [18].

$$S|\text{boson} > \sim |\text{fermion} > \tag{30}$$

and

$$S|\text{fermion} > \sim |\text{boson} > \tag{31}$$

which means that supersymmetry transformations change the spin of a particle by 1/2. If the Lagrangian density is invariant under supersymmetry transformations, a conserved current appears and the generators of the supersymmetry transformations can be expressed as conserved charges. S is a fermionic operator and satisfies the following anticommutator relations

$$\{S_\alpha, S_\beta^\dagger\} = 2\sigma_{\alpha\beta}^\mu P_\mu \tag{32}$$

$$\{S_\alpha, S_\beta\} = \{S_\alpha^\dagger, S_\beta^\dagger\} = 0 \tag{33}$$

and the commutator relation

$$[S_\alpha, P_\mu] = [S_\alpha^\dagger, P_\mu] = 0 \tag{34}$$

where σ^μ denotes the Pauli matrices, μ lorentz indices, α and β spinor indices, and P^μ the generator of the space time translations. Using equation 34 directly yields

$$[P^2, S] = [P^2, S^\dagger] = 0 \tag{35}$$

$P^2 = P^\mu P_\mu = m^2$ is the mass operator, which means that for each standard model particle the corresponding supersymmetric particle should have equal mass, given that supersymmetry is an exact symmetry of nature. However, light supersymmetric particles would have been discovered already along with their standard model counterparts, and therefore sypersymmetry must be broken. The mechanism responsible for breaking supersymmetry at a higher energy scale is not determined by the structure of the symmetry itself. In chapter 2.2.5, several different approaches will be discussed.

2.2.3 The MSSM

Supersymmetric models, which contain a minimal number of new fields in addition to the standard model fields are summarized as the MSSM (Minimal Supersymmetric Standard Model). Within the MSSM the following equation holds

$$n_F = n_B \tag{36}$$

where n_F (n_B) denotes the number of fermionic (bosonic) degrees of freedom of all fields in the model. As was shown before, the supersymmetry transformation changes the spin of each particle by 1/2, but it was not fixed whether the spin is lowered or increased. Equation 36 can only be fulfilled if each standard model boson gets a fermionic superpartner with spin 1/2, while each standard model fermion gets

two bosonic partners with a spin of zero[20]. As each standard model fermion has two degrees of freedom - because of the two possible helicity components - each helicity state gets a bosonic superpartner of spin zero. The bosonic particle spectrum arising from this condition is shown in Table 6.

In general, all particles with the same quantum numbers can mix, which means that for example the mass eigenstates of all up-type scalar quarks can be a mixture of all up-type gauge eigenstates. It turns out that the mixing angles are very small for most of them, leading to an almost diagonal mass matrix. However, for the top squark this does not hold and large mixings between $\tilde{t}_L$ and $\tilde{t}_R$ can occur, yielding mass eigenstates denoted as $\tilde{t}_1$ and $\tilde{t}_2$ satisfying $m_{\tilde{t}_1} < m_{\tilde{t}_2}$. The same argument holds for the bottom squark and the tau slepton slepton in the leptonic sector.

In section 2.1.4, one complex Higgs doublet was introduced, which generates the masses of the weak gauge bosons and the Higgs boson after spontaneous symmetry breaking. Equation 25 shows that the masses of the down-type quarks are generated via the couplings to the Higgs doublet, while the masses of the up-type quarks are generated via the couplings to the hermitian conjugate of the Higgs doublet.
In supersymmetry another approach must be used and *two* complex Higgs doublets are introduced, yielding eight degrees of freedom. The Higgsinos listed in table 7 are the corresponding fermionic supersymmetric gauge eigenstates. After spontaneous symmetry breaking, three degrees of freedom are absorbed to generate the masses of the weak gauge bosons, while five degrees of freedom are left, which correspond to five Higgs bosons. Table 7 also shows the gauge eigenstates of the partners of the weak and strong gauge bosons.

The supersymmetric partners of the Higgs bosons and weak gauge bosons can mix to give the accordant mass eigenstates called 'gauginos'. The neutral Higgs bosons and gauge bosons mix to give neutral mass eigenstates called 'neutralinos', while the charged ones give charged mass eigenstates called 'charginos'. In contrast to the fermion mixing - where only the 3rd generation shows a significant mixing - the mixing angles in the gaugino sector can be rather large, yielding potentially large contributions from several gauge eigenstates for each mass eigenstate. Table 7 shows the observable mass eigenstates arising from this mixing. As the gluino is the only fermionic state which carriers color, the gauge eigenstates and mass eigenstates are identical. For the neutralinos and charginos, the indexing is chosen to satisfy

$$m_{\tilde{\chi}_1^0} < m_{\tilde{\chi}_2^0} < m_{\tilde{\chi}_3^0} < m_{\tilde{\chi}_4^0} \tag{37}$$

$$m_{\tilde{\chi}_1^\pm} < m_{\tilde{\chi}_2^\pm} \tag{38}$$

The nomenclature for the bosonic supersymmetric particles reflects their spin. The scalar supersymmetric partners have the same name as the corresponding fermionic standard model particles with an additional 'S' in front of the name, which stands

[20]The term 'standard model bosons' denote the gluon and *massless* electroweak gauge bosons before spontaneous symmetry breaking, which have spin 1 and therefore two degrees of freedom.

particle	symbol	spin
scalar quarks		
up squarks	$\tilde{u}_L$,$\tilde{u}_R$	0
down squarks	$\tilde{d}_L$,$\tilde{d}_R$	0
strange squarks	$\tilde{s}_L$,$\tilde{s}_R$	0
charm squarks	$\tilde{c}_L$,$\tilde{c}_R$	0
bottom squarks	$\tilde{b}_1$,$\tilde{b}_2$	0
top squarks	$\tilde{t}_1$,$\tilde{t}_2$	0
scalar leptons		
selectrons	$\tilde{e}_L$,$\tilde{e}_R$	0
selectron sneutrino	$\tilde{\nu}_e$	0
smuons	$\tilde{\mu}_L$,$\tilde{\mu}_R$	0
smuon sneutrino	$\tilde{\nu}_\mu$	0
staus	$\tilde{\tau}_1$,$\tilde{\tau}_2$	0
stau sneutrino	$\tilde{\nu}_\tau$	0

Table 6: Bosonic mass eigenstates in the MSSM. For the scalar top quarks, scalar bottom quarks and scalar tau leptons, the superpartners are mixtures of the helicity eigenstates as described in the text.

for 'scalar'. The fermionic supersymmetric partners obtain the suffix 'ino'.

2.2.4 R-parity

In its general form, the supersymmetric Lagrangian density contains lepton and baryon number violating terms. Historically, a new quantum number called R-parity was introduced to avoid rapid proton decay. For example, the decay $p \rightarrow e^+ \pi^0$ via a virtual strange squark violates lepton and baryon number and can lead to decay rates, which severly contradict the lower bound on the proton lifetime of $\Gamma_{p\rightarrow e^+\pi^0} \gtrapprox 10^{32}$ years [1]. If R-parity is not conserved, at least one of the involved couplings (lepton or baryon number violating) must be very small. Several experiments - and ATLAS in particular - search for supersymmetric models including explicit R-parity violation, allowing to constrain the strength of R-parity violating couplings [20] [21]. From a theoretical point of view, the conservation of R-parity is not necessary and several other discrete symmetries are known, which yield agreement with the bounds on lepton or baryon violating decays [22].

R-parity is multiplicative and defined like

$$P_R = (-1)^{3B-L+2S} = \begin{cases} +1 & \text{(standard model particles)} \\ -1 & \text{(supersymmetric particles)} \end{cases} \tag{39}$$

where L denotes the lepton number, B the baryon number and S the spin of the corresponding particles. If R-parity is an exact symmetry of nature - i.e. conserved at each vertex - some remarkable phenomenological consequences appear:

particle	symbol	spin	particle	symbol	spin
gauge eigenstates			**mass eigenstates**		
gluino	$\tilde{g}$	1/2	gluino	$\tilde{g}$	1/2
winos	$\tilde{W}^0$,$\tilde{W}^1$,$\tilde{W}^2$	1/2	neutralino 1	$\tilde{\chi}_1^0$	1/2
bino	$\tilde{B}$	1/2	neutralino 2	$\tilde{\chi}_2^0$	1/2
H_1^0 higgsino	$\tilde{H}_1^0$	1/2	neutralino 3	$\tilde{\chi}_3^0$	1/2
H_2^0 higgsino	$\tilde{H}_2^0$	1/2	neutralino 4	$\tilde{\chi}_4^0$	1/2
H_1^- higgsino	$\tilde{H}_1^-$	1/2	chargino 1	$\tilde{\chi}_1^\pm$	1/2
H_2^+ higgsino	$\tilde{H}_2^+$	1/2	chargino 2	$\tilde{\chi}_2^\pm$	1/2

Table 7: Gauge eigenstates (left) and mass eigenstates (right) of the fermionic supersymmetric partners. The electrically neutral (charged) gauge eigenstates mix, yielding the mass eigenstates, called neutralinos (charginos). As the gluon is the only elemental boson in the standard model which carries color, its superpartner cannot mix with the other supersymmetric fermions.

1. **Supersymmetric particles can only be produced in pairs**
   At a collider, standard model particles are collided and the initial state has a positive R-parity, fixing the final state to positive R-parity as well. Given the multiplicative nature of R-parity, positive R-parity directly enforces two supersymmetric particles in the final state.

2. **Each supersymmetric particle decays into a state with an odd number of supersymmetric particles**
   A single supersymmetric particle has a negative R-parity, fixing the final state after decay also to negative R-parity. Again, the multiplicative nature of R-parity leads to an odd number of supersymmetric decay products.

3. **The lightest supersymmetric particle (LSP) is stable**
   The decay of the lightest supersymmetric particle into other supersymmetric particles is kinematically forbidden. As a decay into standard model particles would violate R-parity, the LSP must be a stable particle. As supersymmetric particles were produced during the big bang together with their standard model counterparts, a stable LSP can neither be electrically nor strongly charged, given the universe we observe today. Therefore it provides a candidate for cold dark matter[21].

2.2.5 Supersymmetry breaking mechanisms

In the section about the supersymmetry transformations, it was noticed that supersymmetry must be broken, as an exact symmetry leads to equal masses for the standard model particles and the corresponding superpartners, which is already

[21]Precisely, only interacting weakly is not a sufficient characteristic to be a potential cold dark matter candidate. There are several cosmological constraints on the mass and annihilation rate of the dark matter particle, ensuring the proper big bang nucleosynthesis and expansion behaviour.

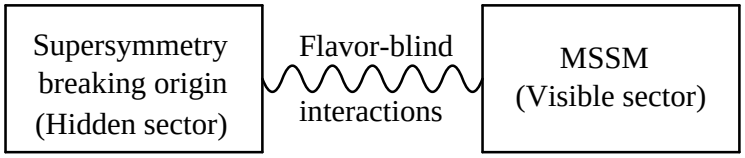

Figure 5: Sketch of the supersymmetry breaking mechanism [9].

ruled out experimentally. The breaking is achieved by adding soft breaking terms to the MSSM Lagrangian:

$$\mathcal{L} = \mathcal{L}_{MSSM} + \mathcal{L}_{Soft} \tag{40}$$

The subscript 'Soft' means that the supersymmetry breaking part of the Lagrangian density only contains terms, which do not reintroduce corrections to the Higgs mass quadratic in Λ_{UV}. The exact form of the soft breaking terms depends on the unknown underlying theory, which means that $\mathcal{L}_{Soft}$ is an effective Lagrangian parametrizing the unknown mechanism of supersymmetry breaking. The breaking itself cannot be obtained by the MSSM fields, but takes place in a so called 'hidden sector', which hardly interacts with the particles of the MSSM. Figure 5 sketches the general picture [9].
Several mechanisms how supersymmetry breaking could be performed and mediated into the MSSM exist.

1. **Supergravity (SUGRA)**
   In this scenario, the mediation of supersymmetry breaking takes place by interactions arising from new physics at the Planck scale, including gravity. Invariance of the Lagrangian density under local supersymmetry transformations enforces the inclusion of a spin 2 particle (the graviton) and its spin 3/2 supersymmetric partner (the gravitino). The gravitino obtains its mass by absorbing a goldstino during the breaking of local supersymmetry[22]. The mass of the gravitino is of the order of the other supersymmetric particles, but it interacts exclusively gravitationally and therefore does barely influence high energy phenomenology.
   A special model based on supergravity is the so called 'minimal supergravity' (mSUGRA), which embeds supergravity in a GUT theory. The model implies the following GUT conditions:

   (a) All fermionic supersymmetric particles unify at a certain energy scale, called the 'GUT scale' (M_{GUT}) and their masses unify at $m_{1/2}$.

   (b) All scalar supersymmetric particles unify at the GUT scale with mass m_0.

   (c) All trilinear couplings unify at the GUT scale with a value A_0.

[22]The meachnism is called 'Super Higgs mechanism' and is similar to the Higgs mechanism in the standard model, where the gauge bosons receive their masses by absorbing a goldstone boson.

In addition, the size of the Higgsino mass parameter μ is fixed by requiring the correct form of the Higgs potential at the electroweak scale and only its sign is a free parameter. The whole model can be described by 5 parameters ($m_{1/2}$, m_0, A_0, sign(μ), tan(β)), where $\tan(\beta) = \frac{\nu_1}{\nu_2}$ denotes the ratio of the Higgs VEVs in a two Higgs doublet model as introduced in the section about the MSSM.

2. **Gauge mediated supersymmetry breaking (GMSB)**
In GMSB models, the supersymmetry breaking is mediated via the regular gauge interactions of the standard model. New fields called 'messengers' are introduced that couple to the underlying origin of supersymmetry breaking in the hidden sector and also to the fields of the MSSM. Gravitational interactions between the source of supersymmetry breaking and the MSSM are still present but negligible compared to the gauge interactions. The minimal GMSB model can be described by six parameters (Λ, M_{mes}, N_5, tan(β), sign(μ), C_{Grav}), where tan(β) and sign(μ) are the same parameters as for mSUGRA. Λ is the supersymmetry breaking scale. M_{mes} is the mass scale and N_5 is the number of messenger fields. C_{Grav} is the scale of the gravitino coupling.

3. **Extra dimensional and anomaly mediated supersymmetry breaking**
In extra dimensional and anomaly mediated supersymmetry breaking models, additional spacial dimensions are postulated and assigned to the hidden sector. The higher dimensional space is separated into a 'brane', which contains the MSSM and at least one additional brane (the 'hidden brane(s)'), where supersymmetry breaking takes place. There is a large variety of different models of this kind, proposing different numbers of additional dimensions and underlying theories like string theories, warped extra dimensions or Kaluza Klein models.

2.2.6 Current exclusion limits

The exclusion limits shown in this chapter reflect the status of searches for supersymmetry at the time this thesis was started. Already before the LHC era, direct searches for supersymmetric particles were performed. The most stringent bounds were obtained at the TeVatron and LEP collider and the associated experiments. The TeVatron was a proton antiproton collider operating at a center of mass energy of 1.96 TeV at Fermilab, while LEP was an electron positron collider based at CERN operating at center of mass energies up to 208 GeV. Given the enormeous amount of new parameters introduced with the MSSM, limits on the supersymmetric particle masses were set assuming specific breaking models. The left part of figure 6 summarizes the results of direct searches performed in the squark gluino mass plane for a mSUGRA scenario with $\tan(\beta) = 3$, $A_0 = 0$ and $\mu < 0$ obtained by several experiments [23].

Besides searches for squarks and gluinos, searches for the direct production of charginos and neutralinos were performed. Already at LEP lower limits on the masses of the $\tilde{\chi}_1^0$ and $\tilde{\chi}_1^\pm$ were set at $m_{\tilde{\chi}_1^0} > 59$ GeV and $m_{\tilde{\chi}_1^\pm} > 103.5$ GeV [24]. Fig-

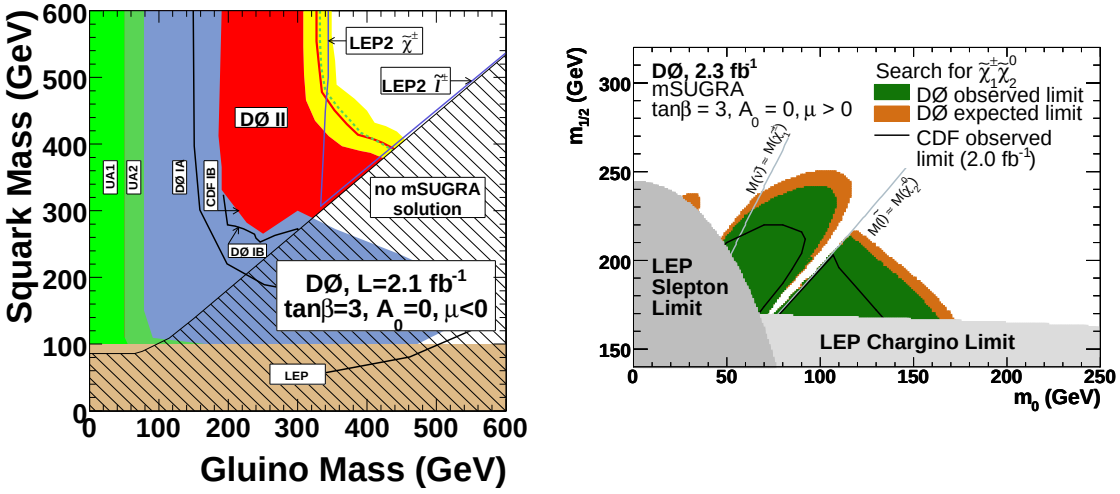

Figure 6: Left: Summary of direct searches for squarks and gluinos in a mSUGRA scenario with $\tan(\beta) = 3$, $A_0 = 0$ and $\mu < 0$ obtained by various experiments. The most stringend bounds were obtained by the DØ experiment at the TeVatron using data with an integrated luminosity of 2.1 fb^{-1} [23]. The solid (dashed) line corresponds to the observed (expected) limits at 95% C.L. The surrounding dotted line indicates the systematic effect of PDF and scale variations for the signal processes. Right: Observed and expected exclusion at 95% C.L. in the m_0 - $m_{1/2}$ plane obtained by searches for associated $\tilde{\chi}_2^0\tilde{\chi}_1^{\pm}$ production in final states with 3 charged leptons, at the DØ experiment using 2.3 fb^{-1}. The assumed mSUGRA parameters are $\tan(\beta) = 3$, $A_0 = 0$ and $\mu > 0$ [25].

ure 7 shows the limit on the mass of the lightest chargino (neutralino) as a function of the sneutrino mass ($\tan(\beta)$), obtained by combining results from the **A**LEPH, **D**ELPHI, **L**3 and **O**PAL experiments (**ADLO**).

These limits were significantly improved in certain areas of the mSUGRA parameter space by the search for associated $\tilde{\chi}_2^0\tilde{\chi}_1^{\pm}$ production in final states with 3 charged leptons at the DØ experiment [25]. The right part of Figure 6 shows the obtained exclusion in the mSUGRA m_0 - $m_{1/2}$ plane.

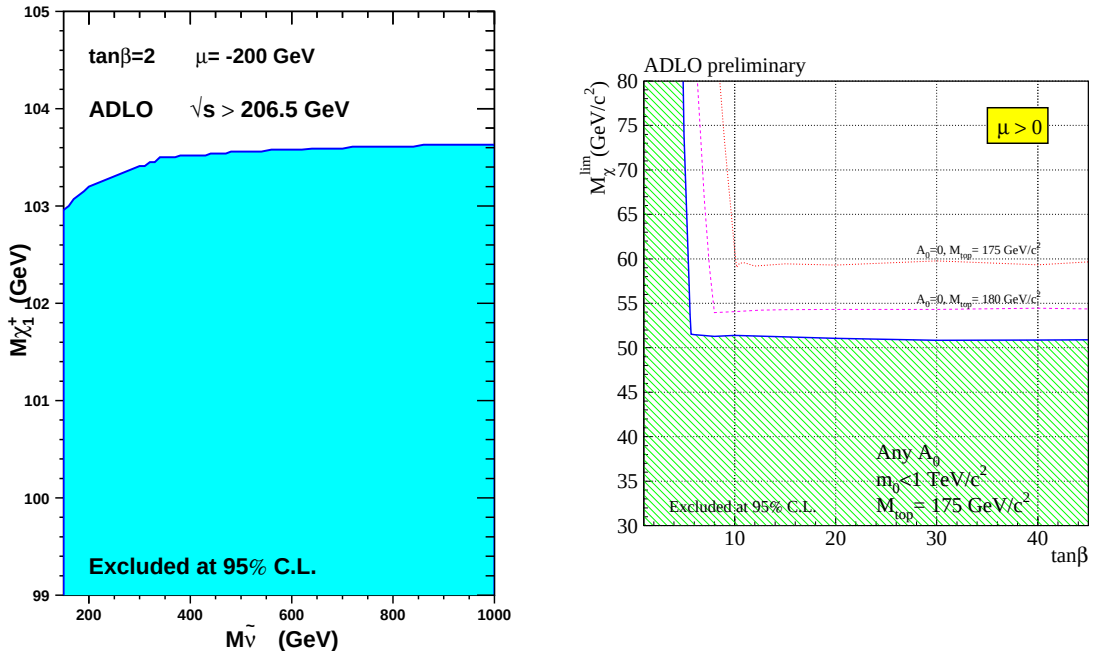

Figure 7: Exclusion limits at 95% CL on the masses of the lightest chargino and neutralino obtained by ADLO [24]. Left: Limit on the mass of the lightest chargino as a function of the sneutrino mass. The value quoted in the text of $m_{\tilde{\chi}_1^\pm} \geq 103.5$ GeV corresponds to the most stringend bound, obtained for large values of $m_{\tilde{\nu}}$. Right: Limit on the mass of the lightest neutralino as a function of $\tan(\beta)$. The limit of $m_{\tilde{\chi}_1^0} \geq 59$ GeV quoted in the text corresponds to the most stringent limit, obtained for $A_0 = 0$ and $M_t = 175$ GeV.

3 Experimental methods

The following chapter will introduce the large hadron collider and the ATLAS experiment. After briefly establishing the main characteristics of the LHC, the subdetectors of ATLAS will be discussed in more detail, focussing on the functionality relevant for this analysis.

3.1 The large hadron collider

The large hadron collider is a proton proton collider based in Switzerland near Geneve at CERN[23]. Figure 8 shows the whole injection chain. In the first step, the protons are accelerated with linear accelerators (LINACS) and passed to the Proton Synchrotron (PS), where the energy gets ramped up to 25 GeV. In the next step, these protons are injected to the Super Proton Synchrotron (SPS), where they gain momentum up to 450 GeV and finally are passed to the LHC, where the acceleration up to 7 TeV per beam occurs. The counter rotating proton beams are collided at 4 different interaction points, each of them surrounded by a different experiment. ATLAS is located at the so called 'interaction point 1' (IP1). The protons do not appear as single particles in the beam, but are clumped together within so called 'bunches' of roughly 10^{11} protons. In the years 2010 and 2011, the final proton energy per beam was limited to 3.5 TeV and the following analysis will be performed on datasets matching this energy. In the year 2012, the energy per beam was increased to 4 TeV.

Besides the center of mass energy, the instantaneous luminosity is another important characteristic of a collider. It is a measure for how many proton proton interactions take place per area and time. Equation 41 defines this quantity [26]

$$L = \frac{N_p^2 n_b f_{rev} \gamma}{4\pi \epsilon_n \beta^*} F \tag{41}$$

N_p denotes the number of protons per bunch, n_b the number of bunches per beam, f_{rev} the revolution frequency in the LHC, γ the Lorentz gamma factor, ϵ_n the normalized transverse beam emittance, β^* the beta function at the interaction point and F a geometrical factor, which takes the luminosity losses due to the crossing angle at the interaction point into account. Integrating the instantaneous luminosity over a specific time period yields the integrated luminosity, which is a measure for the amount of data provided by the LHC. Figure 9 shows how the instantaneous luminosity changed for the 7 TeV data taking period in 2011 and in addition the growth in the total integrated luminosity[24] [27]. On average, increasing the number of protons per bunch leads to more proton proton interactions per bunch crossing.

The additional amount of interactions makes high demands on the detector side, as the analyzed objects should be reconstructed in a way that only takes the hard

[23] In addition, the LHC also accelerates and collides lead ions for a short period of time. This is of particular interest for the ALICE (**A** **L**arge **I**on **C**ollider **E**xperiment) experiment [29].

[24] The instantaneous luminosity per fill is not constant due to proton losses within the bunches arising from th e coulomb repulsion.

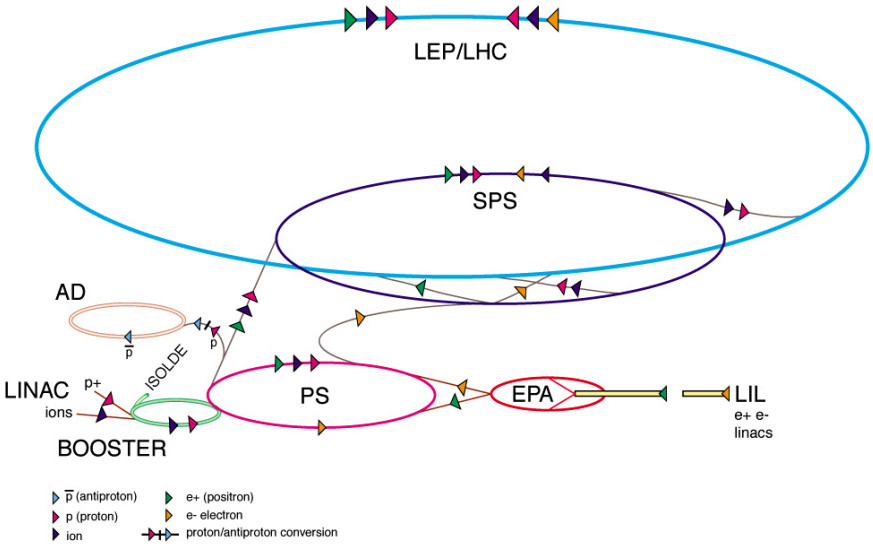

Figure 8: Schematic injection chain of the LHC [30]. For illustrative purposes, the injection chain of the previous collider LEP is shown as well.

interaction into account and is robust against energy deposits from additional interactions. Figure 10 shows the average number of interactions per bunch crossing for data taken in 2011 (2012) at 7 TeV (8 TeV). In later chapters - especially in 3.2.6 - some complications arising from additional interactions per bunch crossing will be discussed. In the following, the effect of multiple interactions on the ATLAS detector will be called 'pileup'. In addition to the 'in time pileup', which denotes the effect of additional energy depositions arising from multiple interactions *within* the current bunch crossing, also bunch crossings before or after the current one can contribute to the total measured energy due to the slowness of the calorimeters. This additional component is called 'out of time pileup'.

Given a specific integrated luminosity, the expected number of events for a given process can be written as

$$N_{process} = \sigma_{process} \times \int Ldt \tag{42}$$

where $\sigma_{process}$ denotes the cross section for proton proton collisions of the process under consideration. The proton level cross section can be obtained using the parton level cross section and the proton parton density functions (PDFs) via the factorization theorem [28].

$$\sigma = \sum_{a,b} \int dx_a dx_b f_a(x_a, \mu_F^2) f_b(x_b, \mu_F^2) \hat{\sigma}_{ab}(x_a, x_b, s) \tag{43}$$

where the sum runs over all parton pairs, which contribute to the given process. The PDFs are written as f_a and f_b and $\hat{\sigma}_{ab}$ denotes the parton level cross section as a function of the parton momenta x_a and x_b and the square of the center of mass energy s. μ_F is the so called 'Factorization scale' which qualitatively describes the

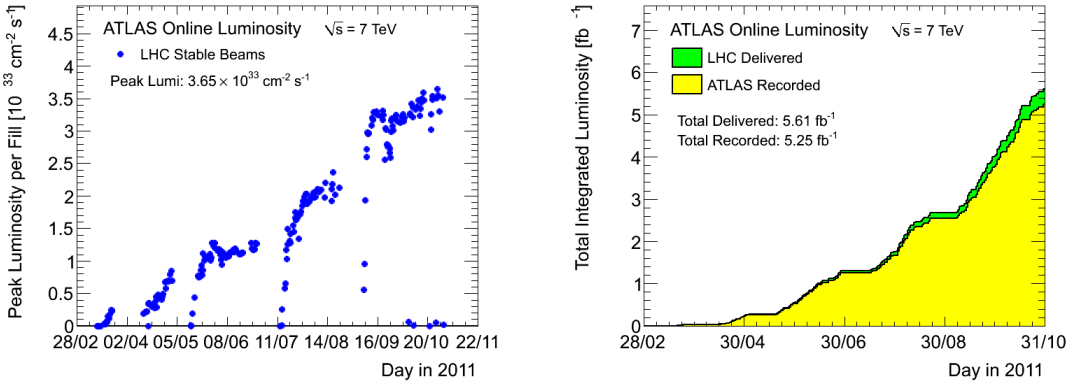

Figure 9: Left: Maximal instantaneous luminosity per fill for the data taking period at $\sqrt{s} = 7$ TeV in 2011. Right: Integrated luminosity for the same data taking period [27].

resolution with which the proton is being probed in the collision. Given that the parton momenta within the colliding protons for a specific collision are unknown and large imbalances can occur - leading to boosts of the final state system in the direction of the beam - slight complications in describing the phenomenology need to be taken into account. Instead of using the whole four vector information for a given event (like done at lepton colliders), momentum conservation is only imposed with respect to the transverse plane, as the parton momenta in this direction are tiny compared to the momentum in the beam direction. Defining the beam direction to align with the z-axis, the transverse momentum for a given object in the final state can be written as

$$p_T = \sqrt{p_x^2 + p_y^2} \tag{44}$$

Instead of using the polar angle θ, which is the angle of an object relative to the beam pipe, often the so called 'pseudorapidity' is used

$$\eta = -\ln\left[\tan\left(\frac{\theta}{2}\right)\right] \tag{45}$$

At hadron colliders, the flux of particles per equidistant η-interval is roughly constant, which is the main advantage of η compared to the normal polar angle. In addition, diffences between two pseudorapidities are approximately Lorentz invariant. It is common to either describe the whole event topology in four dimensional 'cartesian' coordinates (p_x, p_y, p_z, E) or transforming them into the basis (p_T, η, ϕ, E), where ϕ denotes the angle within the transverse plane and E the total energy of the object.

3.2 The ATLAS experiment

The ATLAS experiment is one of the two multi purpose detectors at the LHC, CMS (**C**ompact **M**uon **S**olenoid) being the other one [31]. The detector is suited for a complex physics program covering QCD, electroweak, Higgs, top quark physics

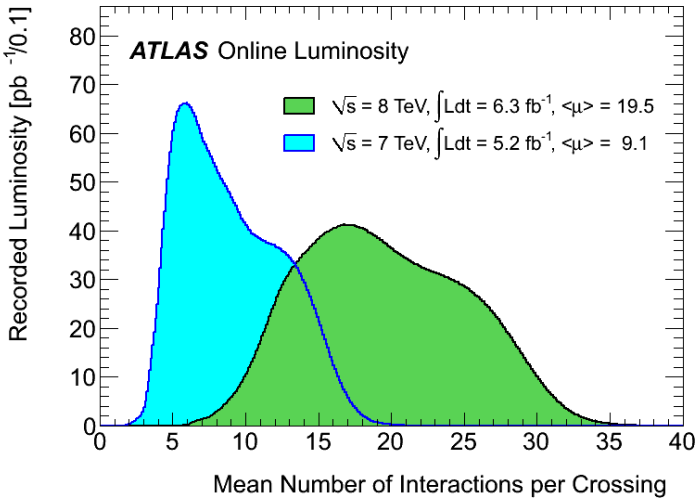

Figure 10: Average number of proton proton interactions per bunch crossing for data taken in 2011 and 2012 [27].

and searches for physics beyond the standard model in several different final states. The layout of ATLAS consists of a tracking system, which is capable of measuring trajectories of charged particles with high spatial and momentum resolution, an electromagnetic and hadronic calorimeter, and a dedicated muon detector as the outer most layer. Figure 11 schematically shows the whole detector.

In the following, each subdetector will be discussed in more detail. The focus of the presentation lies on the basic operation mode and performance criteria relevant for the analysis performed in this thesis.

3.2.1 The luminosity detectors

As already discussed in section 3.1, a precise knowledge of the instantaneous luminosity and integrated luminosity is crucial, in order to calculate the expected number of events for any physics process at the LHC according to equations 41 and 42. Within the ATLAS detector, several subdetectors measure the luminosity delivered by the LHC at the interaction point 1 [33]. The Cerenkov detector LUCID surrounds the beampipe at both longitudinal ends of the ATLAS detector, covering a pseudorapidity range of $5.6 < \eta < 6.0$. The LUCID detector electronics is synchronized with the LHC clock, allowing for a measurement of the event rate for any specific bunch crossing. The Beam Conditions Monitor (BCM) consists of four diamond sensors, located around the beampipe on each side of IP1. The four sensors are arranged in a cross pattern. The vertical pairs and horizontal pairs are read out seperately, allowing for two independent luminosity measurements. In addition, the BCM monitors the background arising from beam gas and beam halo events, possibly issuing an emergency beam dump, if beam losses start to potentially damage the ATLAS detector.

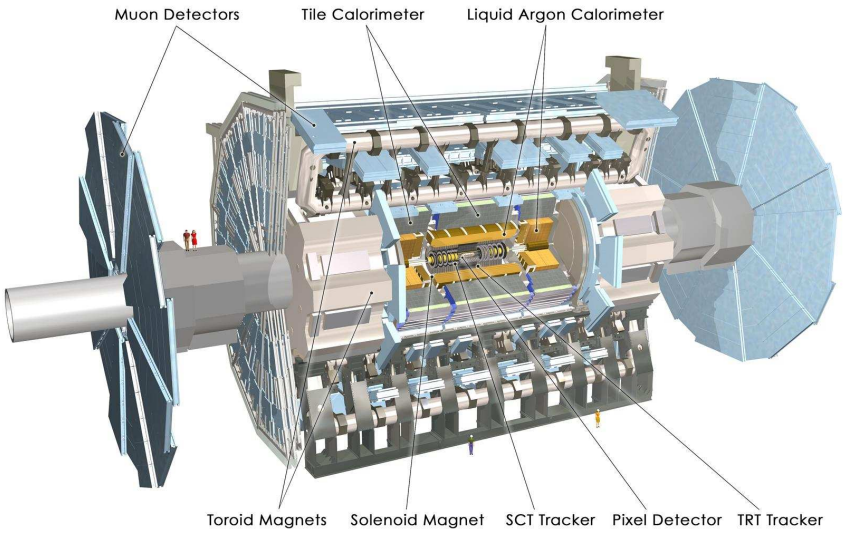

Figure 11: Schematic figure of the ATLAS detector [32].

The instantaneous luminosity is measured in dedicated LHC runs via so called 'van der Meer' scans (vdM), where in a first step the beams are dislocated in the transverse plane and afterwards brought to collision in a second step. During this procedure, the total event rate is recorded as a function of the beam separation. The left side of figure 12 shows the result of such a vdM scan in x direction, obtained for a specific LHC fill with the BCM detector. In addition to the measured rates, a gaussian fit including a constant background is shown. The right side of figure 12 shows the visible cross section, defined as $\sigma_{\text{vis}} = \epsilon \times \sigma_{\text{inel}}$, where ϵ denotes the efficiency for a particular detector and measurement algorithm, while σ_{inel} is the total inelastic proton proton cross section. The results were obtained with the LUCID detector. Similar measurements were also performed with the BCM detectors.

Given these measurements, the uncertainty on the total integrated luminosity for the dataset recorded in 2011 is computed to be 3.8%. The uncertainty arising from the vdM scan yields the dominant source of uncertainty, contributing with 3.4% to the total uncertainty.

3.2.2 The inner detector

The ATLAS inner detector is built up of three different subdetectors as shown in Figure 13, and each component is designed for specific requirements. The whole inner detector is surrounded by a solenoidal magentic field of 2 T, which allows for a precise momentum measurement of various electrically charged particles. The inner detector covers pseudorapidities up to $|\eta| < 2.5$[25] with an almost full 2π coverage in ϕ and consists of a cylindric part in the central region and end caps at higher pseudorapidities, which are arranged orthogonal with respect to the beam pipe.

[25]The TRT only covers pseudorapidities up to $|\eta| < 2.0$.

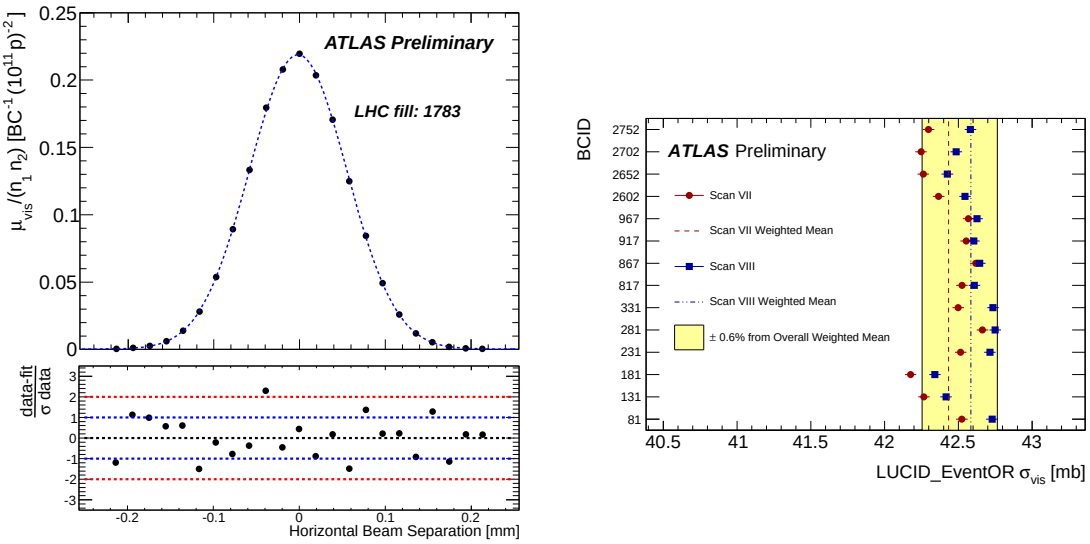

Figure 12: Left: Specific interaction rate vs. beam separation in x direction [33]. The residual deviation between measured rates and a gaussian including a constant background is shown in the bottom panel, assuming purely statistical errors on the data. Right: Visible cross sections in mb obtained in 14 independent measurements with the LUCID detector. The vertical lines indicate the weighted average over all measurements, while the yellow band indicates a 0.6% variation from the average, which reflects the total systematic uncertainty of each measurement.

1. **The Pixel detector**
   The pixel detector consists of three layers and represents the inner most component of the ATLAS inner detector. The whole pixel detector is composed of 1744 silicon pixel sensors, covering 19×63 mm^2 each. Each pixel sensor is made up of 46080 pixels with a size of 50×400 μm^2 (R-ϕ × z)[26]. The intrinsic accuracy is 10 μm in R-ϕ and 115 μm in z (R) in the barrel (end caps). The pixel detector is especially important for measuring the location of primary and secondary vertices precisely, which allows for 'tagging' heavy flavour jets on the one hand, and separating the hard collision vertex from additional vertices arising from softer collisions on the other hand. Both requirements are crucial for the analysis discussed in this thesis, and some figures, illustrating the performance of the inner detector under a high luminosity environment, will be discussed at the end of this section.

2. **The SCT (Silicon Microstrip Detector)**
   The SCT is made of 15912 sensors within 4 layers and surrounds the pixel detector. Each sensor is made of 768 active strips of 12 cm length. The intrinsic accuracy of the SCT is 17 μm in R-ϕ and 580 μm in z (R) in the barrel (end caps).

[26]More precisely, the pixels close to the front-end chips cover 50×600 μm^2 (R-ϕ × z) and constitute roughly 10% of the total amount.

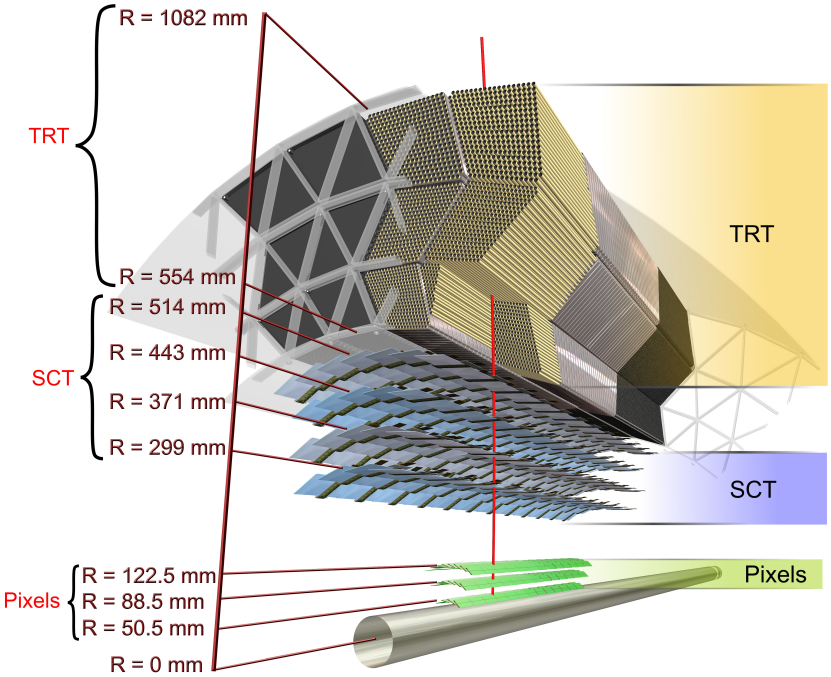

Figure 13: Schematic figure of the ATLAS inner detector [32].

3. **The TRT (Transition Ratiation Tracker)**
   The TRT is a gas drift chamber detector and represents the outer most component of the ATLAS inner detector system. It consists of Polyimide drift straw tubes of 4 mm diameter interleaved with transition radiation material. The gas chambers are filled with a mixture of 70% Xe, 27% of CO_2 and 3% O_2. The TRT only provides spatial information in the R-ϕ direction with an intrinsic resolution of 130 μm per straw. In the barrel region, the straws are parallel to the beam axis, while they are arranged radially in the end cap region.

As already mentioned, the interplay of all three subdetectors allows for a precise spatial measurement of tracks and their transverse momenta. Especially if the LHC runs at high instantaneous luminosities - leading to a large amounts of hits in the inner detector - the correct assignment of hits to a reconstructed track can be very challenging, potentially lowering the efficiencies and resolutions of track and vertex reconstruction. The top panel of figure 14 shows the transverse and longitudinal impact parameters measured at different LHC running conditions. The different curves correspond to different instantaneous luminosities leading to different numbers of average interactions per bunch crossing. No drastic deviations in the shape of these distributions is observed and the current track reconstruction is suited to deal with high pileup environments. Only the longitudinal impact parameter shows

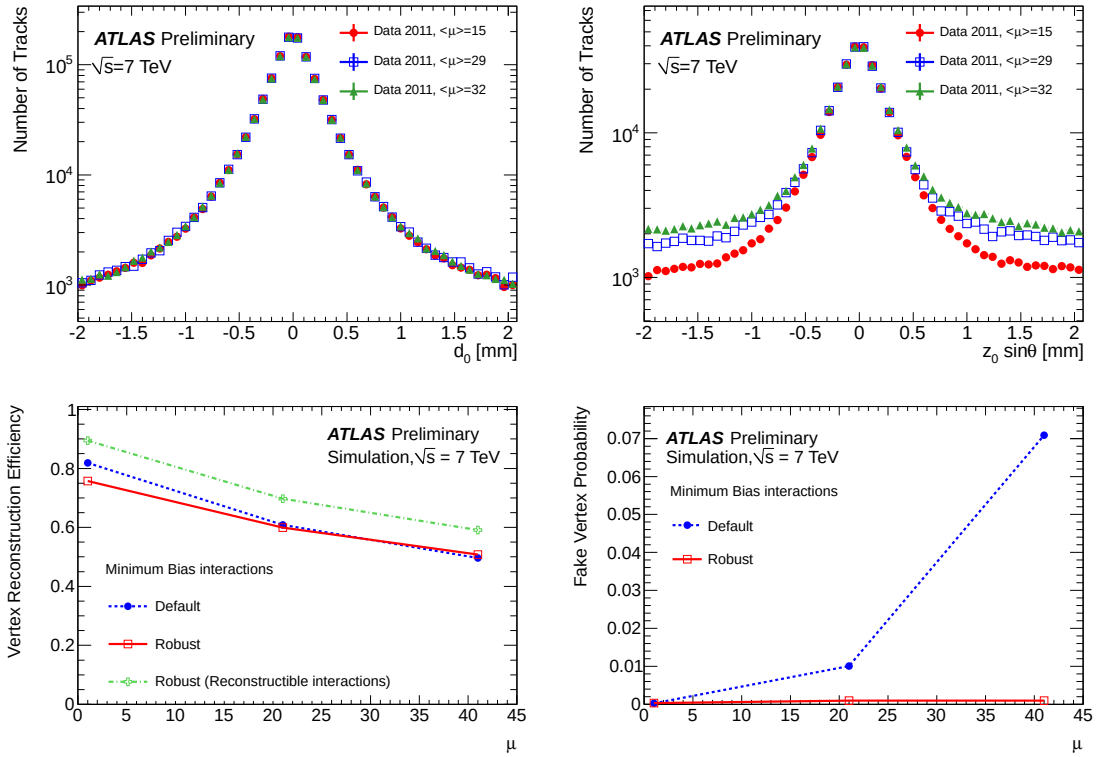

Figure 14: Top: Distribution of the transversal impact parameter (left) and the longitudinal impact parameter (right) for different LHC running conditions. $<\mu>$ denotes the average number of interactions per bunch crossing. Bottom: Vertex reconstruction efficiency (left) and fake vertex reconstruction probability (right) as a function of the average number of interactions per bunch crossing for different vertex reconstruction algorithms [34].

a slight increase in the tails due to additional interactions along the beam direction. The bottom panel of figure 14 shows the vertex reconstruction efficiency (left) and the fake vertex reconstruction probability (right) as a function of the average interactions per bunch crossing for different vertex reconstruction algorithms. For the 'robust' reconstruction algorithm, which was designed to handle a high pileup environment, the reconstruction efficiency drops by roughly 20% for $\mu = 40$, while the fake vertex reconstruction probability is almost zero.

3.2.3 Calorimetry

The ATLAS calorimeter is a sampling calorimeter[27], designed to measure the energies of all particles except neutrinos and muons. Neutrinos will most likely not interact in ATLAS at all - given that they exclusively interact weakly - and therefore cannot be measured directly, while for muons a dedicated detector exists, which will be discussed in the following section. In many supersymmetric models, the LSP is

[27]Sampling calorimeters consist of two parts. An absorber medium, where the incoming particles shower, and an active medium, where the deposited energy is measured. Both media are arranged alternately.

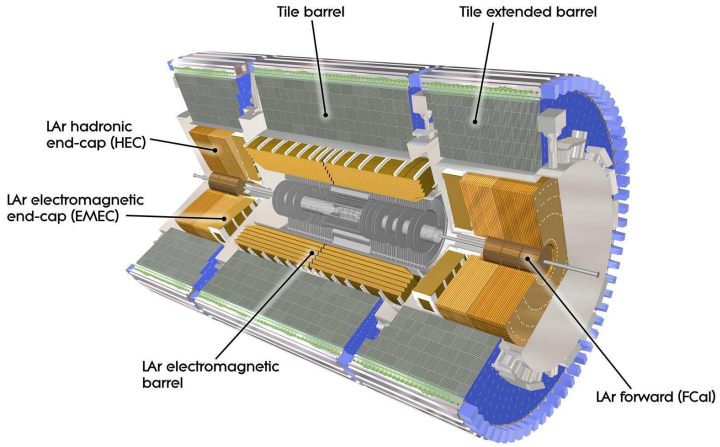

Figure 15: Sketch of the ATLAS calorimeter [32].

only interacting weakly, and therefore can be considered as a heavy neutrino from the detector perspective. As such LSPs will also pass ATLAS undetected, a full 4π coverage of the calorimeter is crucial in order to reconstruct the missing energy in the event. The ATLAS calorimeter as shown in figure 15 is made of an electromagnetic calorimeter and a hadronic one:

1. **The electromagnetic calorimeter**
   The electromagnetic (EM) calorimeter is the inner part of the ATLAS calorimetry. It uses liquid argon (LAr) as the active medium and lead plates as absorbers, arranged in an 'accordeon' like structure. LAr was chosen due to its stability in response over time and intrinsic radiation hardness. The EM calorimeter is composed of three parts, covering different regions in pseudorapidity. The electromagnetic barrel in the central region covers η values up to 1.475, while the electromagtic end caps (EMEC) cover $1.375 < \eta < 3.2$. In addition, a forward calorimeter exists for very large η values above 3.2. The LAr calorimeter is segmented in three sections in depth called 'layers'. In addition a presampler is attached to the inner most layer, in order to correct for potential energy losses before hitting the calorimeter.

2. **The hadronic calorimeter**
   The hadronic calorimeter is the outer part of the ATLAS calorimetry. It consists of two subsystems. In the barrel, the sampling medium is made of scintillator tiles and the absorber is made of steel, covering pseudorapidities up to 1.7. In addition, LAr hadronic end caps exist, covering $1.5 < \eta < 3.2$.

The energy resolution for objects reconstructed based on energy deposits in calorimeter cells can be parametrized by an energy resolution function

$$\frac{\sigma(E)}{E} = \frac{N}{E} \oplus \frac{S}{\sqrt{E}} \oplus C \tag{46}$$

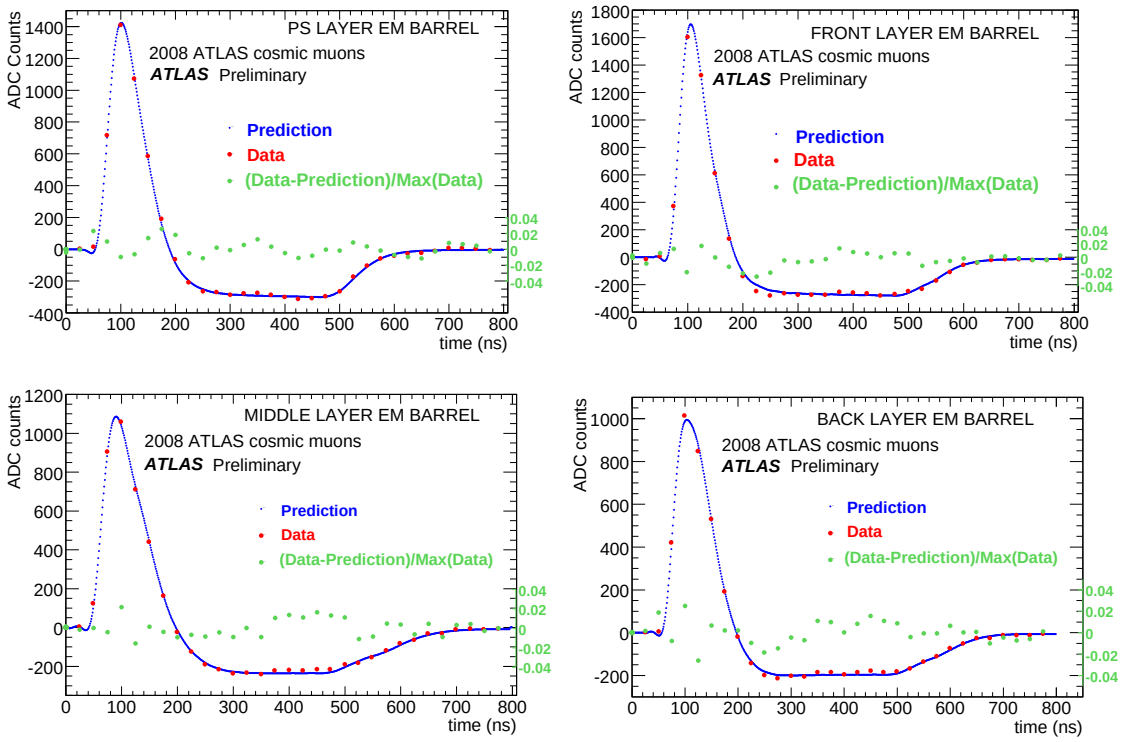

Figure 16: Ionization pulse shapes in all layers of the EM barrel obtained in cosmic data in 2008 [32]. In addition, the prediction obtained by Monte Carlo simulations is shown.

which tries to separate the different sources that influence the total resolution by their energy dependence. The noise term (N) includes electronic and detector noise as well as contributions from pileup. It is expected to dominate at low energies. The stochastic term (S) describes statistical fluctuations in the energy measurements and dominates intermediate energy ranges. At high energies, the constant term (C), which summarizes fluctuations that are a constant fraction of the objects energy - like signal losses in passive materials - dominates the total resolution. As the parameters are highly correlated for most recent measurements, they cannot be uniquely disentangled [35].

The ionization pulse shapes occurring within each cell as a consequence of an energy deposit, as shown for all layers in the central barrel in figure 16, extend much further than the LHC design bunch spacing of 25 ns. Therefore energy depositions from various bunch crossings can contribute to the pulse shape in a single cell. This effect will be important for the studies in chapter 3.2.6, where the impact of high instantaneous luminosities on the ATLAS level 1 calorimeter trigger will be discussed.

3.2.4 The muon system

The muon system, as shown in figure 17, is the outer most part of ATLAS and designed to measure momenta and trajectories of muons. As muons are minimal

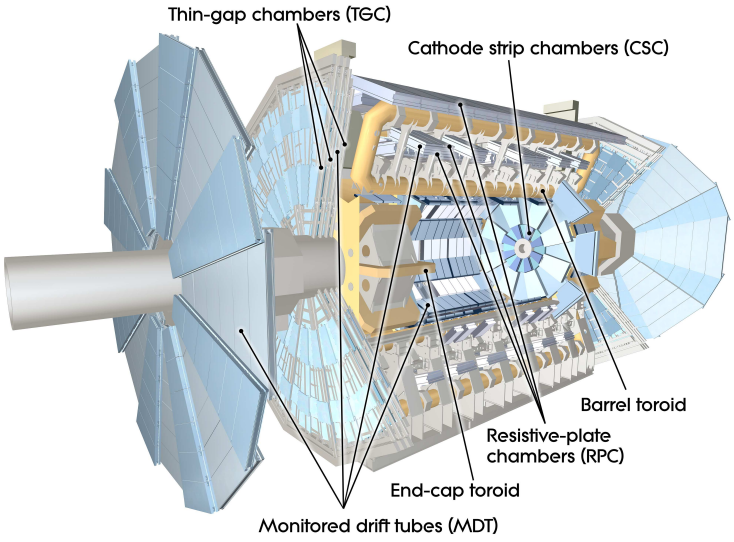

Figure 17: Schematic view of the ATLAS muon system [32].

ionizing particles (MIPs), they pass the calorimeters barely depositing any energy. The whole muon system is enclosed in a toroidal magnetic field, which gives ATLAS its name and is needed to bend the muon tracks and allow for their momentum measurement. The muon spectrometer covers a pseudorapidity range up to 2.7.

In total, four different subdetectors contribute to the muon detector. The Monitored Drift Tube Chambers (MDTs) and the Cathode Strip Chambers (CSCs) are designed for a precision measurement of muon tracks and are arranged in a central barrel and two endcaps. For triggering, the Resistive Plate Chambers (RPCs) are used in the barrel, while the Thin Gap Chambers (TGCs) are used in the end caps. Each chamber is arranged in three so called 'stations'.

3.2.5 The trigger system and data acquisition

The ATLAS trigger system is composed of three parts as sketched in figure 18. The first level (L1) is purely hardware based and combines information from the calorimeters and the muon system and reduces the rate of events from roughly 1 GHz[28] to the L1 output rate of roughly 75 kHz. The L1 algorithms localize energy depositions within the calorimeter and hits in the muon system using reduced granularity information and pass these so called 'Regions of Interest' (RoIs) to the second part of the trigger system (L2). At level 2, the seed RoIs are analyzed by software algorithms and the total rate is further limited to roughly 3.5 kHz. As a last step, the third level (Event Filter) uses calorimeter and muon system information with full granularity to reduce the rate down to roughly 200 Hz. In addition, information from the inner detector is used for the trigger decision. The second and

[28] Assuming a bunchcrossing rate of 40 MHz and approximately 25 interactions per bunch crossing.

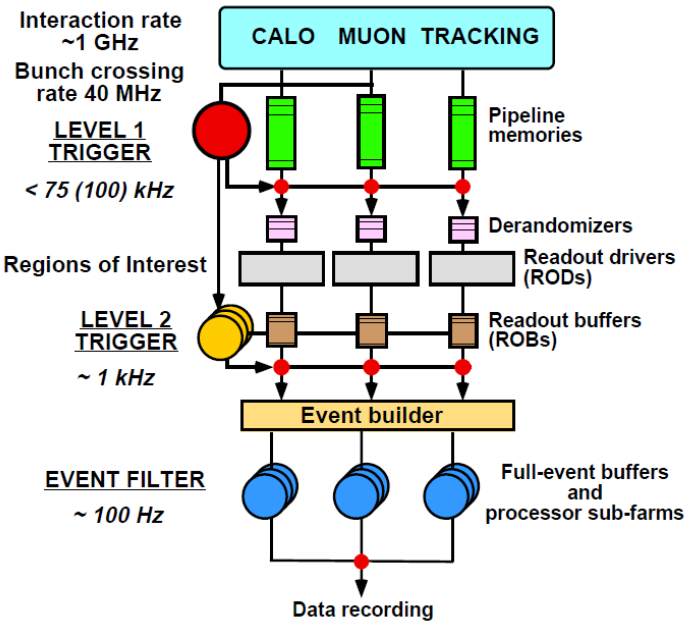

Figure 18: Sketch of the ATLAS trigger system [36].

third level are often considered as the 'High Level Trigger' (HLT), as - in contrast to L1 - they are software based and the algorithms operates on events, reconstructed with information from all subdetectors.

As already mentioned, L1 is composed of two trigger subsystems. The L1 calorimeter trigger (L1calo) and the L1 muon trigger (L1muon). In this chapter, the L1calo system will be discussed in more detail, which is necessary to understand which changes in hardware and software are mandatory to cope with the design instantaneous luminosity of 10^{34} cm^{-2} s^{-1}. Figure 19 schematically shows how the L1 trigger operates.

The L1calo trigger is composed of two different subprocessors, both designed to quickly trigger on different types of particles:

1. **The Cluster Processor (CP)**
   The goal of the cluster processor is to identify RoIs arising from electrons, photons and hadronically decaying tau leptons above a certain, adjustable, E_T threshold. Information about energy deposits in the EM and hadronic calorimeters using a granularity of 0.1 $\times$ 0.1 in $\Delta\eta \times \Delta\phi$, which corresponds to one so called 'trigger tower', are used. The identification criteria that can be applied for electrons and photons, in order to suppress the dominant QCD background, are a transverse isolation on the one hand, and a veto on showers, which significantly leak into the hadronic calorimeter on the other hand. The algorithm first identifies the location of the RoI by searching for a local maximum in the EM calorimeter in a region of 2 $\times$ 2 trigger towers, which is called the 'core' of the RoI. In addition, the energy deposits in the 12 sur-

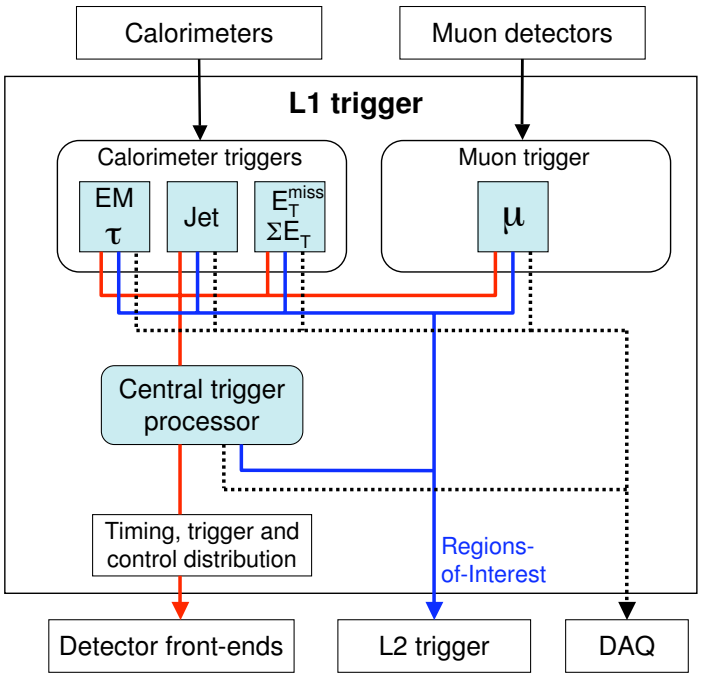

Figure 19: The ATLAS L1 trigger system [36].

rounding trigger towers are summed up, vetoing the RoI, if the sum exceeds a certain adjustable threshold. Furthermore, the corresponding 4×4 trigger towers in the hadronic calorimeter are examined for a significant energy deposit. For the electron and photon algorithms, the energy deposited in the core of hadronic part of the RoI is not allowed to exceeds a certain, programmable value. For the tau identification, the surrounding 12 trigger towers in the hadronic calorimeter, are again summed up to apply an isolation. In contrast to the electron and photon algorithm, no veto on the hadronic activity in the core is applied for obvious reasons.

2. **The Jet / Energy Sum Processor (JEP)**
The jet / energy sum processor identifies RoIs arising from jets in the calorimeter and also sums up the total transverse energy in the event. In contrast to the CP, the algorithms operate on a lower granularity of 0.2×0.2 in $\Delta\eta \times \Delta\phi$. Furthermore, no distinction between the EM calorimeter and the hadronic calorimeter is made. The algorithms of the JEP consider the sum of 2×2 trigger towers in the EM calorimeter and 2×2 trigger towers in the hadronic calorimeter as a new basic unit, called the 'jet element'. As for the CP, a RoI building algorithm uses the energy deposits in all of these basic units to localize the RoI. The number of jet elements summed up to define the RoI can have three different values as shown in Figure 20. The ambiguity in localizing the center of the RoI for the intermediate size, is solved by considering the 2×2 subblock with the highest E_T as the core. Like for the CP, the sum of E_T for each window size is compared to adjustable thresholds, in or-

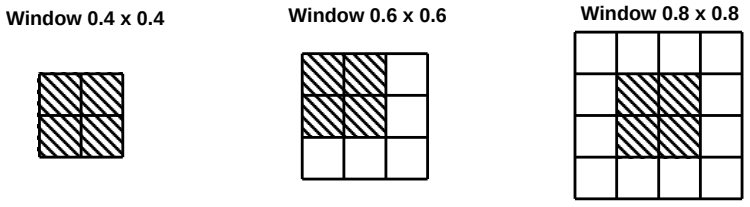

Figure 20: The three possible jet trigger algorithm windows used by the JEP. For each window size, the energy deposits in a certain number of jet elements are summed to define the total energy within the jet RoI. For the case of using 3×3 jet elements, the 2×2 subwindow with the highest energy sum is considered the core of the RoI[36].

der to decide, whether or not an energy deposit should be counted as a jet RoI.

For determing the total transverse energy and missing transverse energy in the event, the energy deposit in each jet element is multiplied by a geometrical constant which projects the total energy onto its transverse components i.e. E_x and E_y. The scalar (vectorial) sum of all jet elements is then used to calculate a rough estimate of the total (missing) transverse energy in the event, and compared to adjustable thresholds for the trigger decision.

As a final step, information from the CP and JEP are transmitted to the 'Central Trigger Processor' (CTP), which is responsible for combining these information and making the trigger decision at level 1. For the following discussion, it is very important to stress, which kind of information is used by the CTP. Only the *number* of RoIs above certain thresholds - sent by the CP and JEP - and the *exceeded thresholds* for the total transverse energy and missing transverse energy are used for the trigger decision. As indicated by the blue lines in figure 19, the full information of each RoI is only used to seed the higher trigger levels, where more sophisticated algorithms are used to refine the trigger decision. This deficit in the level 1 trigger functionality will limit the potential of ATLAS significantly even at design luminosities of 10^{34} $\mathrm{cm}^{-2}\mathrm{s}^{-1}$ as will be shown in the following section.

3.2.6 Prospects for LHC upgrades and implications for the L1 calorimeter trigger

Up to now, the LHC was not operating at its full potential. For example, the center of mass energy was limited to 7 TeV (8 TeV) for the data taking in the years 2010/2011 (2012). During the scheduled long shutdown in 2013/2014 (LS1), the goal is to change ATLAS in a way that it can in principle deal with the LHC running at design parameters. Furthermore the LHC itself will be prepared for running at its current technical limits[29]. Further upgrades of the LHC and ATLAS are also

[29]Currently, the exact LHC running conditions after LS1 are still not completely settled. As a best guess, the LHC will most likely run at $\sqrt{s} = 13$ TeV and roughly at its design luminosity with a bunch spacing of 25 ns.

scheduled for 2018 and beyond, which require major hardware changes, but those will not be the subject of this study [37] [38].
Increasing the center of mass energy and instantaneous luminosity will directly translate into higher event rates for each physics process as described by equation 42. Increasing the center of mass energy is especially important for searches for new, heavy particles, as these particles can only be produced, if the partonic center of mass energy exceeds the mass of the particle. In contrast, increasing the instantaneous luminosity will increase the event yield equally for all type of processes. The following studies are motivated by supersymmetry with conserved R-parity leading to events with jet activity and missing transverse energy. For these kind of events, a trigger requiring a certain number of jet RoIs and missing transverse energy above certain thresholds will be utilized.

The goal of this study is to quantify what event rates at level 1 for several jet/E_T^{miss} related triggers will occur, given that the LHC runs at its design run parameters. In addition, topological algorithms, which reduce the corresponding trigger rates, are studied and the benefit is quantified.

The total rate for a jet based trigger is dominated by the strong production of quarks and gluons, given their high cross sections. The current L1calo trigger system can only decrease the total rate by raising the E_T thresholds on the RoIs effectively, as discussed in the previous chapter. The huge drawback of this solution is that signatures of new physics processes potentially contain low energetic objects, which would also be rejected by the trigger already at level 1. Depending on the new model under consideration, a separation from the dominant QCD background could be obtained using information about the event topology. Several simple algorithms, which manage to lower the rate at level 1 below the hardware limitation of 75 kHz, will be presented. The layout of a topological level 1 calorimeter trigger processor (L1Topo), which will be implemented in ATLAS during LS1, was partially motivated by these studies [39].

The studies are based on Monte Carlo simulations of inclusive minimum bias collisions. The generator used is `Pythia` [40]. The simulation of particles crossing the ATLAS detector and interacting with its material are done using `GEANT4` [41]. The reconstruction of physical objects at level 1, using the input events generated with `GEANT4`, is done with the ATLAS simulation software [42]. The simulated LHC running conditions are $\sqrt{s}$ = 14 TeV and L = 10^{34} cm^{-2}s^{-1} with a bunch spacing of 25 ns. The average number of proton proton interactions per bunch crossing, given these LHC running conditions, is 23.

Figure 21 shows the E_T and η distributions of jet RoIs for all three different window sizes. In addition, for the E_T plots, the missing transverse energy is overlayed for comparison. As expected, the amount of energy within each RoI grows with increasing window size. Furthermore, a sizable amount of missing energy is observed.

The rates of several dijet + E_T^{miss} L1 triggers are roughly evaluated using trigger

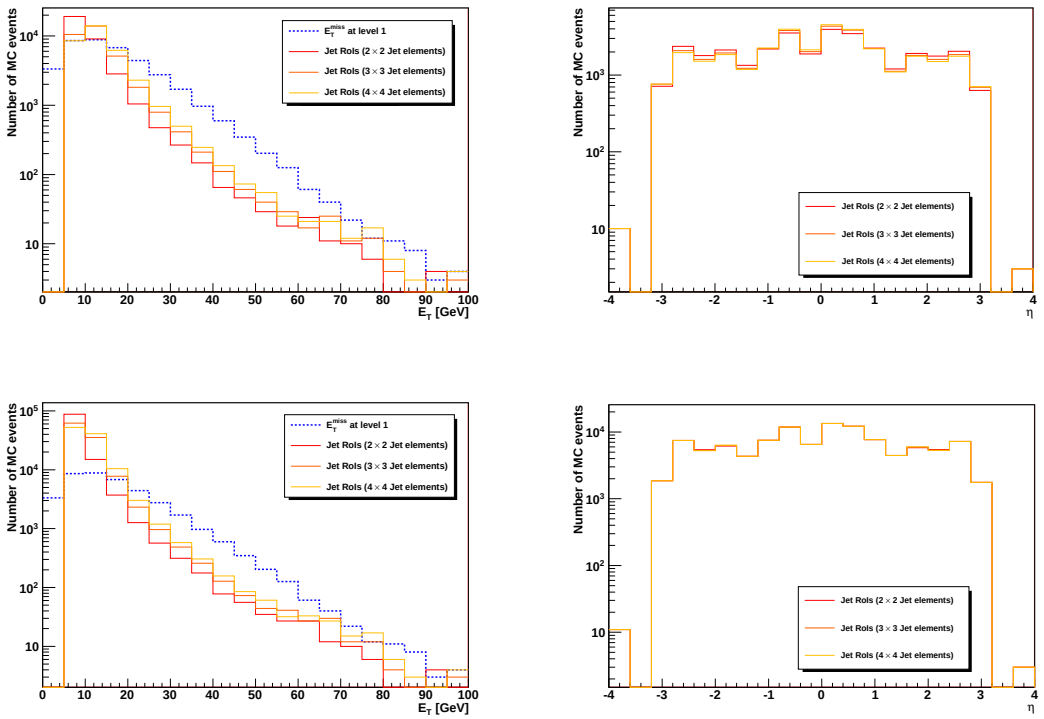

Figure 21: E_T and η distributions of jet RoIs for an inclusive minimum bias Monte Carlo sample at $\sqrt{s}$ = 14 TeV, L = 10^{34}cm^{-2}s^{-1} and a bunch spacing of 25 ns. For the E_T distributions, the missing transverse energy is overlayed for comparison. Top: E_T (left) and η (right) of the RoI with the highest transverse energy. Bottom: Inclusive distributions.

efficiencies estimated on the inclusive minimum bias sample. The total rate for a given trigger is evaluated as the bunch crossing rate of 40 MHz times the efficiency for the trigger under consideration[30]. Table 8 shows a couple of L1 jet/E_T^{miss} triggers relevant for searches for supersymmetry in the pure hadronic final state. The nomenclature is 'AJB_XEC', where A denotes the number of jet RoIs above E_T threshold B/GeV, and C the exceeded E_T^{miss} threshold in GeV. The rates correspond to jet RoIs with the largest window size of 4 × 4 jet elements. The reason why dijet + E_T^{miss} are studied is motivated in chapter 4. It will be shown, that each pair production of supersymmetric particles via the strong interaction yields at least 2 jets and a certain amount of missing transverse energy.

All triggers yield rates which occupy a significant amount of the total L1 output rate, or even exceed it for the case of the 2J30_XE30 trigger. Clearly non of these triggers can be used when the LHC runs at its design run parameters. As already mentioned, the current L1 hardware only counts the number of jet RoIs above certain thresholds and compares the missing transverse energy with adjustable thresholds.

[30]This estimate is justified by the fact that the minimum bias sample is inclusive, without any truth level filters applied. However, this estimate should only be considered as a rough guess. The correct rate will be determined by the exact LHC running conditions after LS1 which could differ from the simulated conditions.

Trigger	Rate [kHz]
2J30_XE30	124.7 ± 11.3
2J40_XE30	39.2 ± 6.4
2J50_XE30	13.4 ± 3.7
2J30_XE50	36.1 ± 6.1
2J40_XE50	11.3 ± 3.4
2J50_XE50	6.2 ± 2.5

Table 8: Total rates at L1 for several dijet + E_T^{miss} triggers estimated on minimum bias Monte Carlo for $\sqrt{s} = 14$ TeV, L = 10^{34} cm^{-2}s^{-1} and a bunch spacing of 25 ns. The errors are purely arising from the limited statistics of the Monte Carlo sample.

Therefore, decreasing these rates will enforce to raise these thresholds significantly. After LS1, the L1Topo processor will be implemented in the L1 trigger system, which can use *spatial* information of the RoIs for its trigger decision. The following study will only focus on applications relevant for 'AJB_XEC' triggers[31]. For these triggers, the most natural way to reduce the dominant QCD background is exploiting transverse momentum conservation. A dijet trigger with a soft cut on E_T^{miss} - as shown in table 8 - will mainly accumulate QCD events with two jets. The missing transverse energy can either arise from energy mismeasurements of the jet RoIs, or from neutrinos within the jets, which carry a significant amount of the total jet energy. The two jets must be balanced in their direction within the transverse plane, and therefore in the polar angle ϕ, leading to a 'back to back topology'.

This behaviour is demonstrated in figure 22, where the $\Delta\phi$ between the leading and second leading jet RoI, for events with at least 30 GeV of missing transverse energy at level 1, is shown. For the left plot, no cut on the transverse energy of the subleading jet RoI was applied. For the right plot, only events, where the subleading jet RoI exceeds 20 GeV of E_T are shown. While the $\Delta\phi$ is flat up to roughly a factor of 2 for the inclusive distribution, it starts to peak significantly around $\Delta\phi \approx \pi$ after requiring 20 GeV of E_T for the subleading RoI. This behaviour can be understood given figure 16 and figure 10. At instantaneous luminosities of 10^{34} cm^{-2}s^{-1}, on average, 23 proton proton interactions take place per bunch crossing. In addition due to the slowness of the calorimetry, energy depositions from several bunch crossings contribute to the energy measured at a given crossing. These additional interactions are usually low energetic minimum bias events, and the energy in a jet RoI can be the sum of several energy depositions from all contributing uncorrelated low energetic events. By selecting a certain amount of transverse energy in one object - as done for the right plot of figure 22 - chances increase that the leading RoIs are actually arising from *one* hard minimum bias event. For these 'hard' dijet events, momentum conservation is reflected in the back to back topology of the leading jet RoIs.

[31] In addition, L1Topo also uses more information from the CP and even from the level 1 muon system. Therefore more sophisticated algorithms - like jet/electron and jet/muon overlap removal - can already be considered at level 1 as discussed in [39].

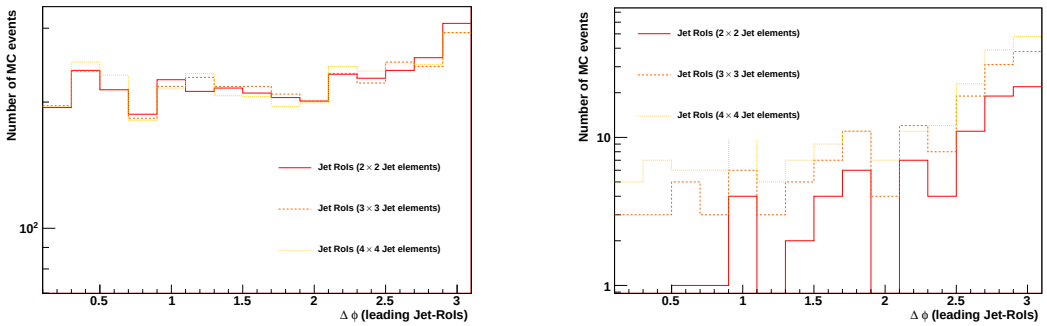

Figure 22: $\Delta\phi$ distributions between the leading and 2nd leading jet RoI for all window sizes after cutting on $E_T^{miss} > 30$ GeV on trigger level. No explicit cut on the leading jet RoI is imposed. Left: No cut on the E_T of the 2nd leading jet RoI applied. Right: A cut of $E_T > 20$ GeV on the 2nd leading jet RoI applied.

Figure 23 quantifies the gain in rate reduction exploiting this topology using jet RoIs with the smallest (left) and largest (right) window size. The red curve shows the level 1 rate for a dijet + E_T^{miss} trigger as a function of the subleading jet RoI with a cut on the missing transverse momentum of 30 GeV. No explicit requirement on the leading jet RoI is applied. For the blue curve an additional cut on the $|\Delta\phi$(Leading jet RoIs)$| < 2.5$ is deployed. At low transverse energies of the subleading jet RoI up to roughly 20 GeV, the gain in rate reduction is about 20-30%. For higher transverse energies - where the dijet topology starts to be more pronounced - the curves diverge, leading to a rate reduction of a factor of ≈7 (≈5) for the smallest (largest) window size at 40 GeV. A precise estimate of rates at even higher transverse energies cannot be done on this sample, due to the limited Monte Carlo statistics[32]. However, extrapolating the curves from a region with sufficient statistics into higher E_T regimes suggests that the benefit of a $\Delta\phi$ requirement at level 1 inceases with increasing trigger thresholds.

Using topological information already at the lowest trigger level helps to reduce the total L1 output rate by large factors, while keeping the E_T thresholds comparably low. Of course, potential efficiency losses for supersymmetric signal events will occur as well, which unfortunately cannot be quantified due to the lack of corresponding Monte Carlo simulations at the desired instantaneous luminosity at the time the study was performed. However, given that the presented triggers target supersymmetric decays of heavy squarks and gluinos via comparably long cascade decays - like it will be discussed in chapter 4 - the correlation in $|\Delta\phi$(Leading jet RoIs)$|$ is much less pronounced compared to QCD dijet production. Assuming a flat $|\Delta\phi$(Leading jet RoIs)$|$ distribution for these signal processes, an efficiency loss of roughly 20% due to the requirement of $|\Delta\phi$(Leading jet RoIs)$| < 2.5$ is expected.

[32] At the time this study was done, generating 40k events of minimum bias at L = 10^{34} cm^{-2}s^{-1} was still a huge challenge, only possible on special computers with enough memory.

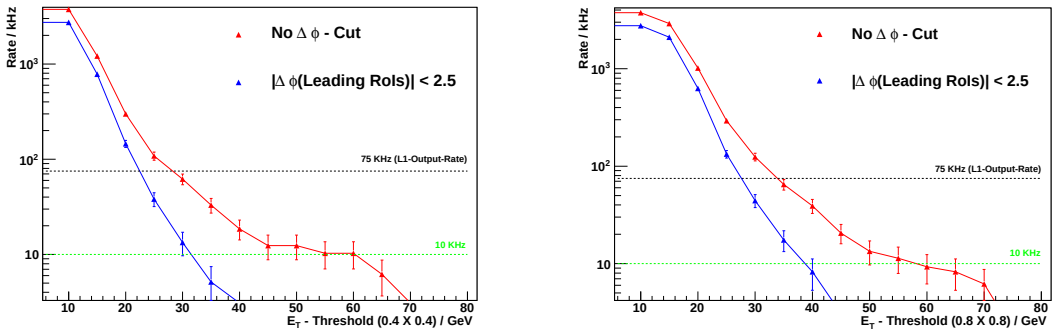

Figure 23: Total level 1 rate for a dijet + E_T^{miss} trigger as a function of the E_T of the subleading jet RoI, using the smallest window size (left) and the largest window size (right). The E_T^{miss} threshold is fixed at 30 GeV. The red curve shows the rate without any constraint on the dijet topology. The blue curve shows the rate for a cut on $|\Delta\phi(\text{Leading jet RoIs})| < 2.5$. The errors arise purely from the limited statistics of the Monte Carlo sample.

3.2.7 Data storage and grid computing

Given the large number of collected data and Monte Carlo simulations for various physics processes, an efficient data storage and distribution system is used within the ATLAS collaboration, in order to share the load between several computing clusters and enable a fast access. In a first step, the raw data is processed with the reconstruction software on the tier 0 CERN computing cluster. After that, the reconstructed data and simulations are distributed to lower tier computing centers, based all over the planet, which form a high performance computing grid. Instead of downloading the required data sets and running the analysis on the local cluster, the user usually sends the analysis jobs to one of the lower tier sites, which contain the necessary data and sufficient computing power. After the analyis job is finished, only the output information is copied back to the user. This approach avoids dispensable copying of large amounts of data and is necessary given the limited bandwidth, memory and large amount of physicists working at the ATLAS experiment.

4 Phenomenology at hadron colliders

In chapter 3.1 the theoretical description of how particles are produced in general at hadron colliders was given with equations 42 and 43. In this chapter, it will be discussed how supersymmetric particles in various models are produced at the LHC and how they decay further into standard model particles that can be detected with the ATLAS detector. For all supersymmetric decays, R-parity is always assumed to be exactly conserved, and the lightest neutralino is the LSP. Furthermore, the phenomenology of the relevant standard model background processes will be described.

4.1 Production of supersymmetric particles

In general, supersymmetric particles can be produced either via the electroweak force or via the strong force. For each production mechanism, the cross section depends on the masses of the produced particles. As supersymmetry inherits its coupling strengths from the standard model, strong production is likely by far the dominant mechanism at hadron colliders[33]. The diagrams contributing to electroweak production of supersymmetric particles are not listed, as the following analysis was designed to target final states arising from squark and gluino decays. Searches for gauginos arising from electroweak production channels are also performed at the ATLAS experiment in different analyses [43].

The different production channels via the strong force can be classified as follows. All diagrams were generated using the `MadGraph` software [44]. Scalar supersymmetric particles (squarks and sleptons) are represented by straight dashed lines. The gluino is an overlay of a gluon line and a solid straight line. The weak gauginos (charginos and neutralinos) are an overlay of a photon line and a solid straight line. All standard model particles are displayed following the common convention for Feynman graphs.

1. **Gluino Pair Production**
   In this process, a pair of gluon partners is produced. Figure 24 shows all Feynman graphs that contribute to this process at tree level. The initial state can either contain two gluons or two quarks, as shown in the first two and last two diagrams.

2. **Squark Pair Production**
   In this production mode, a pair of quark partners is produced. Figure 25 shows all Feynman graphs that contribute to this process at tree level. The initial state can either contain two gluons or two quarks, as shown in the first two and last two diagrams. For simplicity, no distinction between quarks and antiquarks is made.

[33] In general, this satement is not necessarily true. If the production of gluinos and squarks is kinematically forbidden because their masses are beyond the accessible partonic centre of mass energy, the weak production of lighter gauginos can dominate the total cross section.

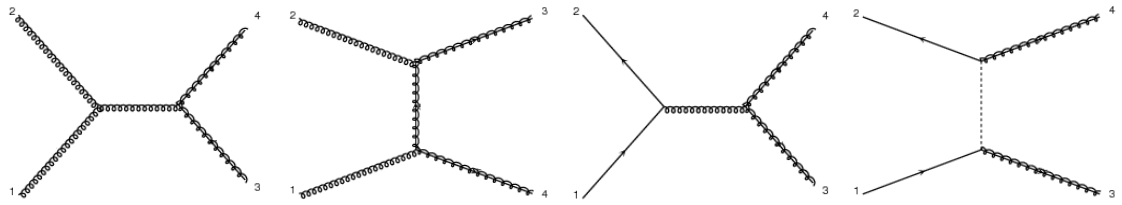

Figure 24: Feynman diagrams contributing to gluino pair production at hadron colliders. The initial state can either contain two gluons (first two graphs) or two quarks (last two graphs). The u-channel diagrams, resulting from the t-channel diagrams with interchanged final state legs, are ommited for simplicity.

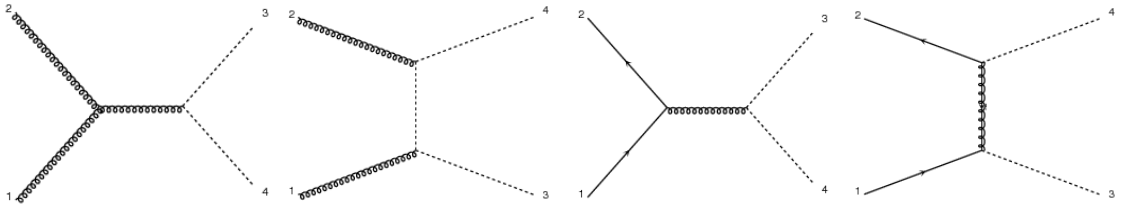

Figure 25: Feynman diagrams contributing to squark pair production at hadron colliders. The initial state can either contain two gluons (first two graphs) or two quarks (last two graphs). The u-channel diagrams, resulting from the t-channel diagrams with interchanged final state legs, are ommited for simplicity.

3. **Associated Production of a Squark and a Gluino**
   For this process, a gluino is produced together with a squark. Figure 26 shows all Feynman graphs that contribute to this process at tree level. All diagrams have a quark and a gluon in the initial state. For simplicity, again no distinction between quarks and antiquarks is made.

The relative contribution of these three different processes to the total cross section for strong production depends on the mass spectrum of the model under consideration. In addition - as each process probes different PDFs within the protons - the relative contribution also depends on the center of mass energy.

4.2 Supersymmetric decays

In this section, the possible decay modes of supersymmetric particles are discussed, assuming initial squarks and gluinos were produced as discussed in the previous section. Figure 27 shows the possible decay modes for squarks and gluinos. All decays, which do not violate R-parity or a symmetry of the standard model are illustrated. If the squark decays via the electroweak force as in the right graph of figure 27, the produced gaugino can either be a neutralino or a chargino. The possible weak gaugino decays are listed in figure 28[34]. Each cascade decay eventually ends with

[34]In principle also decays of weak gauginos into higgs bosons are possible, and the branching ratio depends on the mass differences and the size of the higgsino field content within the weak gauginos. However, as the light weak gauginos are dominantly wino or bino in mSUGRA, and no phenomenological model with higgsino decays is studied in this thesis, this decay mode is excluded

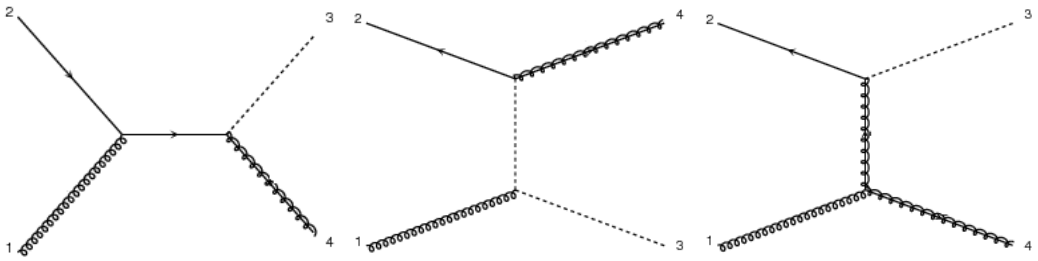

Figure 26: Feynman diagrams contributing to an associated production of a squark and a gluino. Only diagrams with a quark and a gluon in the initial state are possible.

the LSP. As the gaugino can also decay into a slepton, as shown in the middle graph of figure 28, the following slepton decay graph is also shown.

The analysis presented in this thesis searches for supersymmetric signatures involving jets, missing transverse energy and exactly one isolated charged lepton. These final state objects arise from the decays discussed above. Hadronic jets evolve from quarks produced in squark and gluino decays as shown in figure 27, radiated gluons or from hadronically decaying standard model gauge bosons. The missing transverse energy arises from the LSPs. In addition, potential neutrinos arising from W boson, Z boson, sneutrino or tau decays can also contribute to E_T^{miss}. Charged leptons can either be produced in decays of W and Z bosons like in the left diagram of figure 28, or in gaugino decays into a slepton and a standard model lepton, like in the middle graph of figure 28. In addition, also sleptons can decay into charged leptons as shown in the right graph of figure 28. As the analysis targets signatures with *exactly* one charged lepton, final states containing *one* leptonically decaying W boson arising from a chargino decay are the dominant decay mode. Depending on the mass difference between the chargino and the LSP, the W boson can either be virtual or real, yielding a three body decay of the chargino in the former case and two consecutive two body decays in the latter case, if the decay of the W boson is also taken into account. For signal models with a small mass difference between the weak gauginos, the decay products from the gaugino decays can be rather soft. In contrast, for large mass splittings, the decay of the real W boson usually yields a charged lepton with a high transverse momentum, given the W boson mass of approximately 80 GeV.

4.3 mSUGRA phenomenology

In chapter 2.2.5 the mSUGRA model was already briefly discussed, focussing on the aspect of supersymmetry breaking. The 5 parameters describing the model were introced as $m_{1/2}$, m_0, A_0, sign(μ) and tan(β). These parameters are defined at the GUT scale of roughly 10^{16} GeV, which represents the energy scale, at which the electroweak and strong force unify. The choice of these parameters directly translates into masses and couplings of the supersymmetric particles at lower energy scales,

from the discussion.

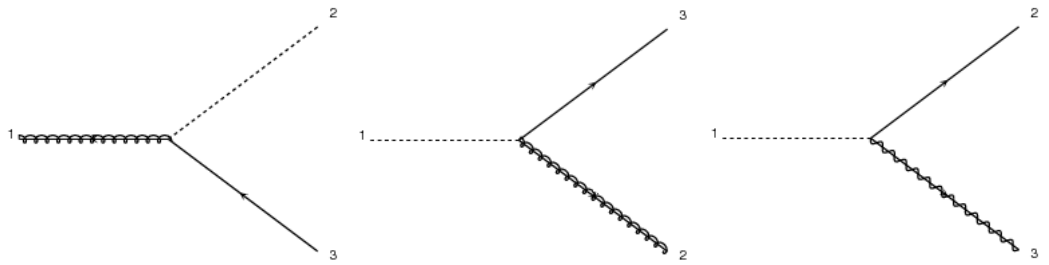

Figure 27: Possible decay modes for gluinos and squarks in the MSSM. Gluinos are only strongly charged and therefore decay via strong interactions exclusively into a squark and a quark (left). Squarks can either decay via QCD into a gluino and a quark (middle) or via weak interactions into a weak gaugino and a quark (right). If kinematically allowed, decays via strong interactions are heavily favoured due to the much larger coupling strength.

which can be calculated using renormalization group equations. Figure 29 shows how the running of the renormalization group equations looks like for the special case of $m_{1/2}$ = -A_0 = 320 GeV, m_0 = 3.2 TeV, tan(β) = 10, sign(μ) = positive and $M_{GUT} = 2 \times 10^{16}$ GeV [9].

The masses of the supersymmetric particles are derived via the renormalization group equations as a function of the mSUGRA parameters. Figures 30 and 31 show how the particle masses depend on the unified mass parameters m_0 and $m_{1/2}$. The distributions were derived with the `SPheno` software [54]. While the masses of all scalar particles increase significantly with growing m_0, the gaugino masses - and the gluino mass in particular - are nearly unaffected by a change of the unified scalar mass parameter. Variations in the gaugino mass parameter however have a drastic impact on all supersymmetric particle masses, and the masses of all scalar quarks and gauginos grow approximately linearly as a function of $m_{1/2}$.

As mentioned in the previous section, the production cross section for different initial states depends on the masses involved and the parton density functions of the proton. As the masses of the supersymmetric particles within mSUGRA mostly depend on the unified masses m_0 and $m_{1/2}$, the cross sections for different production channels strongly depend on these two parameters as well. Figure 32 shows the cross sections for all possible initial states within mSUGRA in the plane spanned by m_0 and $m_{1/2}$. The cross sections were calculated using the program `NLL fast` [46] [47] [48] [49] [50]. The other parameters are fixed at A_0 = 0 GeV , tan(β) = 10 and sign(μ) positive, which can be partially motivated by indirect fits [51]. The dominant contributions involve gluinos due to the large size of the gluon PDFs within the colliding protons at a center of mass energy of $\sqrt{s}$ = 7 TeV [53]. For gluino pair production, the cross sections drops rapidly with $m_{1/2}$, while being approximately independent of m_0, indicating that the gluino mass barely depends on m_0 and strongly increases with $m_{1/2}$, as already mentioned in the discussion of figures 30 and 31.

Besides different cross sections, each production mode also leads to different final states. In parameter regions where the gluino is heavier than the lightest squark,

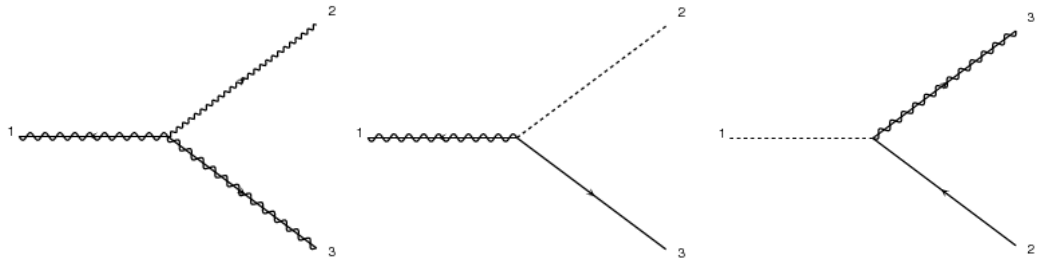

Figure 28: Possible decay modes for weak gauginos and sleptons in the MSSM. Left: Decay of a weak gaugino into a lighter weak gaugino and a standard model weak gauge boson. Depending on the masses of the weak gauginos, the standard model gauge boson can either be real - yielding two consecutive two body decays, if the decay of the weak gauge boson is also considered - or virtual, leading to a three body decay with softer decay products. Middle: Decay of a weak gaugino into a slepton and a standard model lepton. Decays can involve charged and electrically neutral leptons, respecting conservation of charge at each vertex. Right: Decay of a scalar lepton into a weak gaugino and a standard model lepton. If the slepton is charged it can decay into a charged standard model lepton of same flavour and a neutralino or into the corresponding neutrino and a chargino. If the slepton is a sneutrino it can either decay into into the corresponding standard model neutrino and a neutralino or into a chargino and a charged lepton of opposite sign.

squark (anti)squark production contributes significantly to the total cross section. The squarks will dominantly directly decay via 2 body decays into a quark and a weak gaugino, leading to relatively hard decay products. In parameter regions where the gluino is much lighter than the lightest squarks, gluino pair production dominates. As already shown in figure 27, the gluino can only decay via strong interactions. If the lightest squarks are heavier than the gluino, this decay is a 3 body decay including a virtual squark, yielding an additional jet from the $\tilde{g} \rightarrow \tilde{q}^* q$ decay. The virtual squark decays further as also shown in figure 27, leading to softer decay products compared to a 2 body decay.

Figure 33 compares some of the main event characteristics for two mSUGRA points with cross sections and relevant masses as given in table 9. The total cross section for both model-points is approximately 0.34 pb. The point with $m_0 = 1460$ GeV and $m_{1/2} = 240$ GeV is by far dominated by gluino pair production, while the point with $m_0 = 100$ GeV and $m_{1/2} = 390$ GeV has dominant contributions from squark pair and associated squark gluino production. The points are chosen in a way such that differences in the shown event characteristics are hardly caused by differences in the total mass scale of the produced particles. The point dominated by gluino pair production has more high energetic jets arising from the discussed 3 body decays. The point dominated by squark pair production has higher E_T^{miss} arising from larger Lorentz boosts of the LSPs produced in 2 body decays. These kinematic differences will later be used in the definition of signal regions, allowing for an optimal coverage of the whole m_0 - $m_{1/2}$ plane.

One very important characteristic of mSUGRA is that the gaugino mass param-

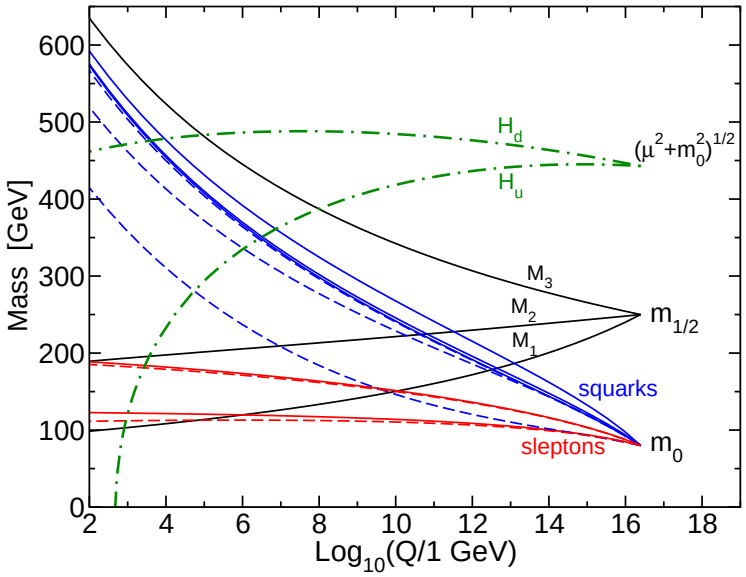

Figure 29: Renormalization group equation evolution of the scalar and fermionic SUSY masses in the mSUGRA Model with GUT conditions imposed at 2×10^{16} GeV.

eters in the MSSM Lagrangian density obey the following relation [9]

$$M_1 : M_2 : M_3 \approx 1 : 2 : 6 \tag{47}$$

where M_1 corresponds to the bino mass parameter. M_2 corresponds to the wino mass parameter and M_3 denotes the gluino mass parameter. In mSUGRA the lightest neutralino is almost purely a bino, while the lightest chargino has a dominating wino like field content. Therefore equation 47 directly translates into a relation between the different gaugino masses:

$$m_{\tilde{\chi}_1^0} : m_{\tilde{\chi}_1^\pm} : m_{\tilde{g}} \approx 1 : 2 : 6 \tag{48}$$

In general, it can be shown that a lot of different supersymmetric models make predictions on the mass relations between the gaugino mass parameters, which differ with respect to each other and also with respect to the mSUGRA pattern shown in equation 48 [56]. Obviously, interpreting results from supersymmetry searches in all available models is not feasible. Therefore, a different approach is chosen within the ATLAS collaboration, which is the subject of the following section.

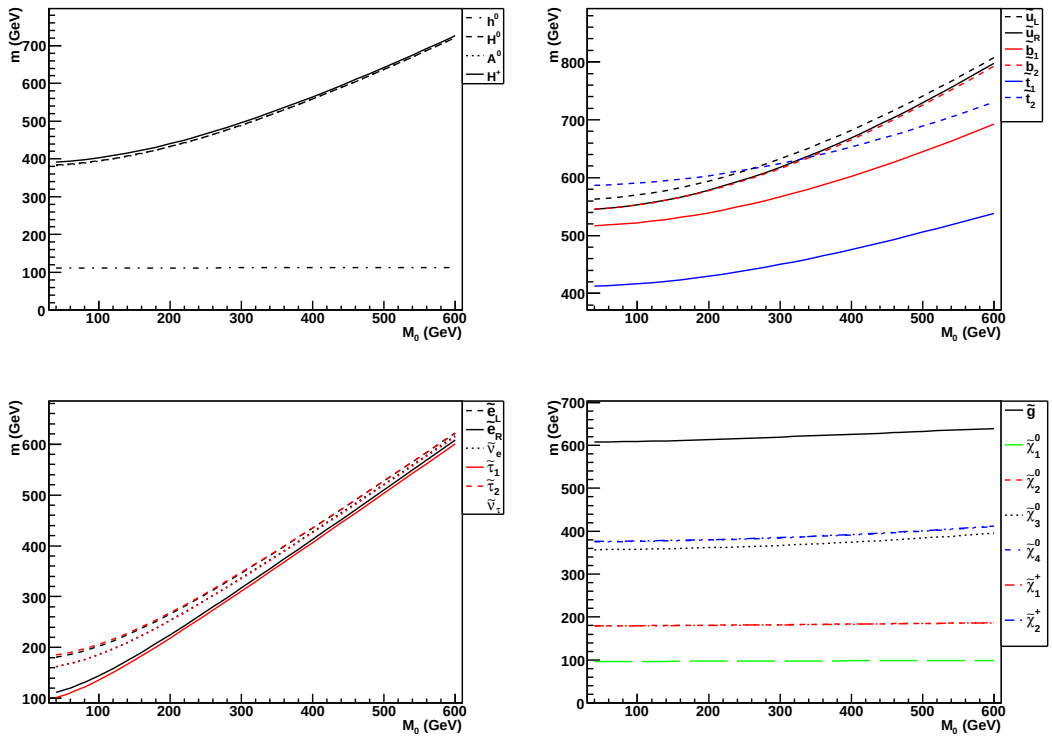

Figure 30: Masses of supersymmetric particles as a function of the scalar unified mass parameter m_0 calculated with SPheno [54]. All other mSUGRA parameters are kept constant at $m_{1/2} = 250$ GeV, $A_0 = 0$ GeV, $\tan(\beta) = 10$ and a positive μ [55].

m_0 , $m_{1/2}$ [GeV]	$m_{\tilde{q}}$ [GeV]	$m_{\tilde{g}}$ [GeV]	σ_{qq}/σ_{tot} [%]	σ_{qg}/σ_{tot} [%]	σ_{gg}/σ_{tot} [%]
100 , 390	631	916	49	33	3
1460 , 240	923	659	0.2	8	78

Table 9: Production cross sections for strong production for for two different mSUGRA points within the m_0 - $m_{1/2}$ plane for $A_0 = 0$ GeV , $\tan(\beta) = 10$ and sign(μ) positive. In addition, the masses of the produced particles are shown. The squark mass corresponds to the lightest squark. The total mass scale of the produced particles is comparable for both points. σ_{qq} denotes the sum of squark squark and squark Antisquark production. The fractions for each point do not add up to 100% due to the contributions from electroweak production modes.

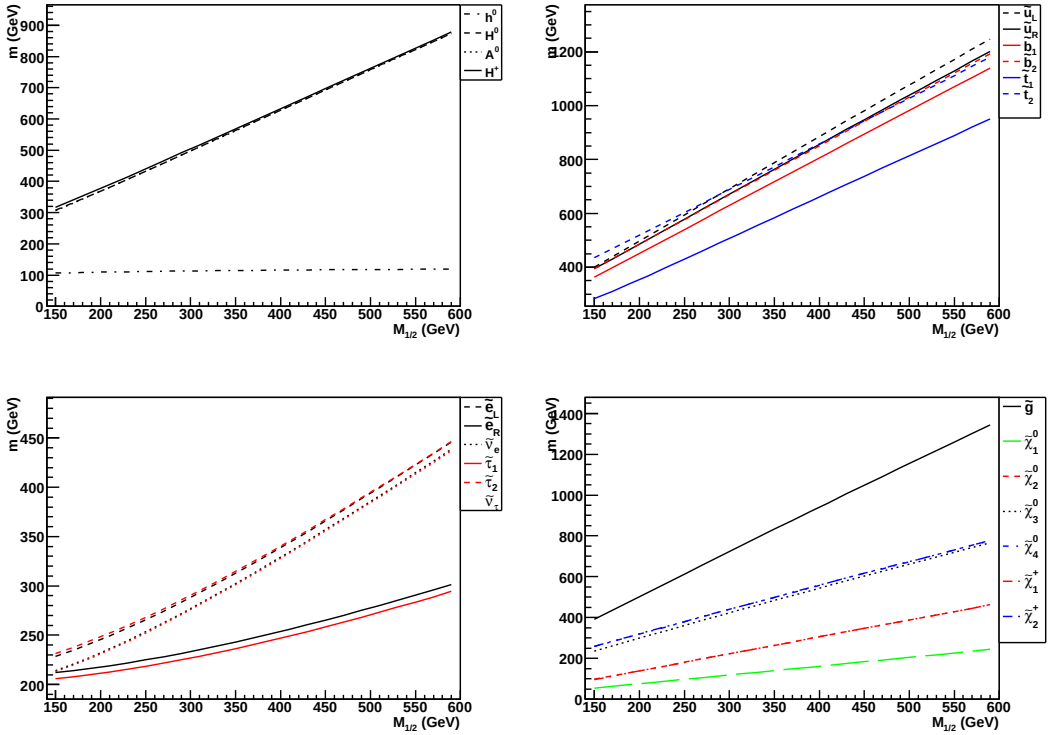

Figure 31: Masses of supersymmetric particles as a function of the gaugino unified mass $m_{1/2}$ calculated with SPheno [54]. All other mSUGRA parameters are kept constant at $m_0 = 200$ GeV, $A_0 = 0$ GeV, $\tan(\beta) = 10$ and a positive μ [55].

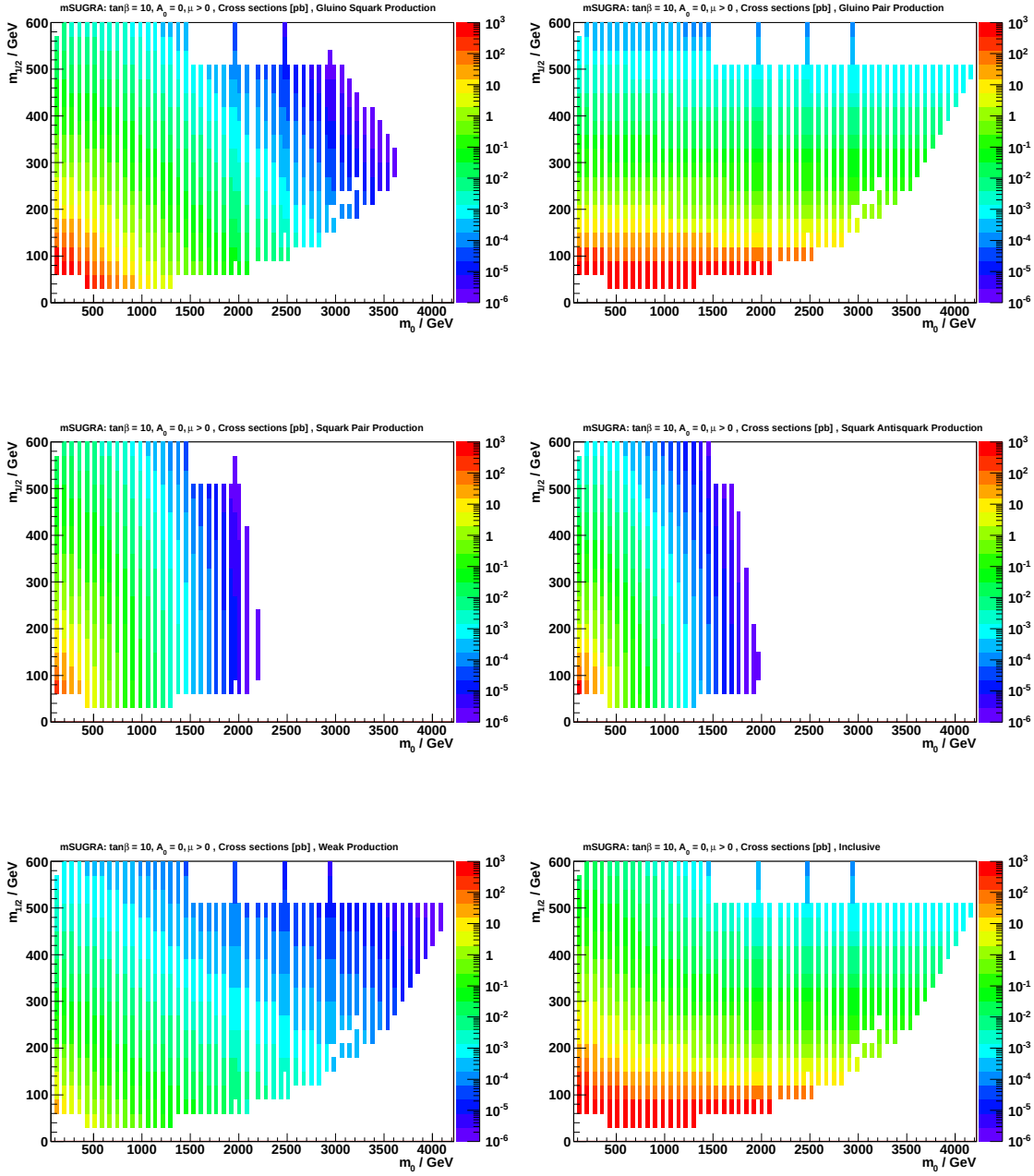

Figure 32: Cross sections in pb for different production modes in the m_0 - $m_{1/2}$ plane with $A_0 = 0$ GeV , $\tan(\beta) = 10$ and $\text{sign}(\mu)$ positive. Top left: gluino squark production. Top right: gluino pair production. Middle left: squark pair production. Middle right: squark Antisquark production. Bottom left: Production modes with contributions from weak interactions. Bottom right: Inclusive cross section. The lower right corner is excluded by theory as no electroweak symmetry breaking is possible in this area of the mSUGRA parameter space.

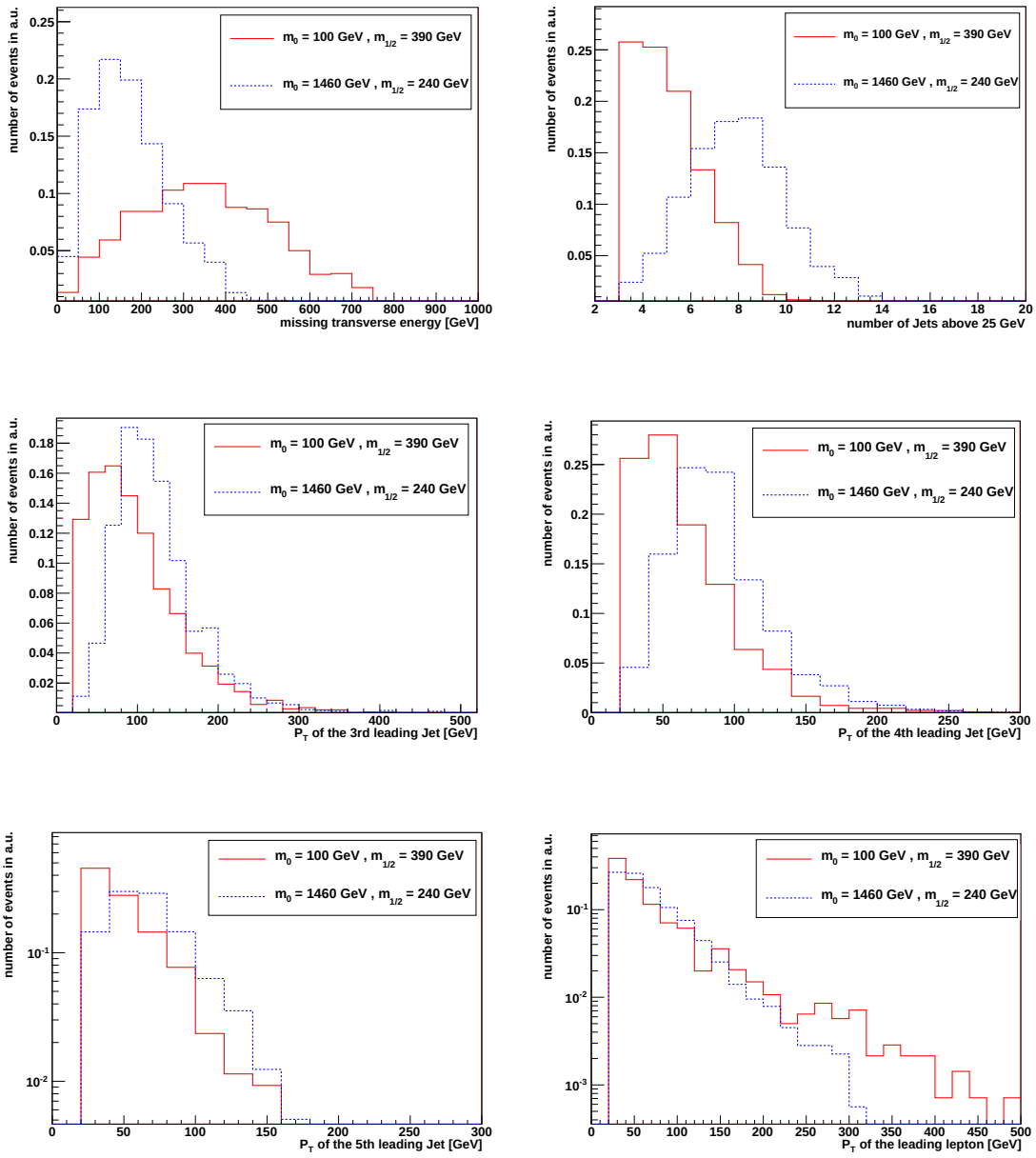

Figure 33: Comparison of important event characteristics for two different mSUGRA points within the m_0 - $m_{1/2}$ plane for $A_0 = 0$ GeV , $\tan(\beta) = 10$ and sign(μ) positive. Top left: Missing transverse energy. Top right: Amount of jets above a transverse momentum of 25 GeV. Middle left: Transverse momentum of the 3$^{\text{rd}}$ leading jet. Middle right: Transverse momentum of the 4$^{\text{th}}$ leading jet. Bottom left: Transverse momentum of the 5$^{\text{th}}$ leading jet. Bottom right: Transverse momentum of the leading lepton. All distributions are made on preselected events fulfilling $E_T^{miss} >$ 30 GeV, 3 jets above a transverse momentum of 25 GeV and at least one electron or muon above 20 GeV.

4.4 Simplified models

The term 'simplified models' denotes a purely phenomenologically motivated set of models. The label 'model' might be misleading however. In contrast to real physics models like mSUGRA or GMSB, which arise from the choice of the SUSY breaking mechanism and certain assumptions, the goal of the simplified models is to cover as many final state topologies as possible. Each simplified model consists of a fixed production and decay mode and therefore represents *one* possible way supersymmetric particles can be produced and decay within the MSSM. The only remaining parameters, determining the event topology, are the particle masses involved. Those are varied within a certain range of a certain spacing, in order to obtain a more general result.

In physics models like mSUGRA or GMSB, a lot of these different production and decay modes can occur, and the particle masses, production cross sections and branching ratios into final state particles are determined by the parameters of the underlying model. Therefore, the final goal of the simplified model approach is to allow for an interpretation of experimental results within each real physics model by combining the results interpreted in all relevant simplified models, which was already done for some regions of the mSUGRA parameter space [45]. The following set of simplified models will be interpreted in this analysis:

1. **Squark Pair Production**

   In all following simplified models, a pair of left handed squarks is produced and their masses are varied in 100 GeV steps between 200 GeV and 1.2 TeV[35]. These following decays are possible and represented by a simplified model each

   (a) **One step cascade decays**
   In the one step simplified models, the squarks decay into the lightest chargino and a quark. The chargino then decays into a W boson and the LSP. The W boson is allowed to decay in all possible ways, according to the known standard model branching ratios. In addition to the squark masses, two further parameters occur in form of the masses of the lightest chargino and the LSP. Two ways are considered to arrange these masses with respect to each other. The two possibilities are expressed using a compression parameter defined as:

   $$x_1 := (m_{\tilde{\chi}_1^\pm} - m_{\tilde{\chi}_1^0})/(m_{\tilde{q}} - m_{\tilde{\chi}_1^0}) \tag{49}$$

   In the first simplified model, the compression factor is set to 1/2, fixing the chargino mass exactly between the squark and the LSP masses, while varying the LSP mass between 15 GeV and 1092 GeV. Results are presented in a plane of squark mass versus LSP mass. In the second simplified model, the LSP mass is fixed to 60 GeV and x_1 is varied between

[35] Only left handed squarks are simulated leading to a pure decay into a chargino and a quark - given that the chargino is simulated as purely wino like - for the onestep models.

0 and 1. The results are presented in a plane of squark mass versus x_1.

(b) **Two step cascade decays**
In the two step simplified models, one additional particle occurs within the cascade. Two different particles are considered. In the first set of simplified models, the squarks decay into the lightest chargino and a quark like in the one step models. The chargino then decays into the *second* lightest neutralino and a W boson and the neutralino 2 decays into the LSP and a Z boson. Again, no constraints on the decays of the standard model gauge bosons are implied.

In the second set of two step simplified models, sleptons occur in the cascade decays. Two possibilities are considered. In the first one, both squarks are decaying into the lightest chargino and a quark as in the one step models. The charginos then decay into a slepton and the corresponding standard model lepton, conserving charge and lepton number. The sleptons decay into the corresponding standard model lepton and the LSP. In the second possibility, one squark decays like for the first possibility, but the other one decays into a neutralino 2 and a quark. The neutralino then decays also into a slepton and the corresponding standard model lepton, conserving charge and lepton number. The slepton again decays into a standard model lepton and the LSP. 'Slepton' stands for charged sleptons *and* sneutrinos. Charged sleptons and sneutrinos are set to equal mass and both decays therefore occur with same probability due to lepton universality. Furthermore, the masses of the neutralino 2 and the chargino 1 are considered to be degenerate as well[36].

For the two step models, two compression factors determine the event topology. The first one as defined in 49 and the second one being

$$x_2 := \begin{cases} (m_{\tilde{\chi}_2^0} - m_{\tilde{\chi}_1^0})/(m_{\tilde{\chi}_1^\pm} - m_{\tilde{\chi}_1^0}) & \text{Models w/o sleptons} \\ (m_{\tilde{\ell}^\pm}(m_{\tilde{\nu}}) - m_{\tilde{\chi}_1^0})/(m_{\tilde{\chi}_1^\pm}(m_{\tilde{\chi}_2^0}) - m_{\tilde{\chi}_1^0}) & \text{Models with sleptons} \end{cases} \tag{50}$$

which is the relative mass difference of the charged slepton (sneutrino) and the chargino (neutralino) to the LSP. For both types of two step models, values of $x_1 = x_2 = 1/2$ are chosen and the results are presented in the $m_{\tilde{q}}$ - $m_{\tilde{\chi}_1^0}$ plane.

[36] In all twostep models including charged sleptons, at least two charged leptons (electrons, muons *and* taus) are present in the final state. Selectrons, smuons and staus are generated with the same mass and therefore tau leptons arising from stau decays can occur. If the tau lepton decays hadronically - while an electron or muon is present in the other leg - final states with *exactly* one electron or muon can occur. In addition, single lepton final states can occur, if the $\tilde{\chi}_2^0$ decays into a sneutrino and a neutrino. As the branching ratio for both decay chains is comparably small, the contribution from the one lepton selection is rather tiny as well. However, as combined limits - where also the one lepton analysis is taken into account - are shown in chapter 8, these models are explained as well for completeness.

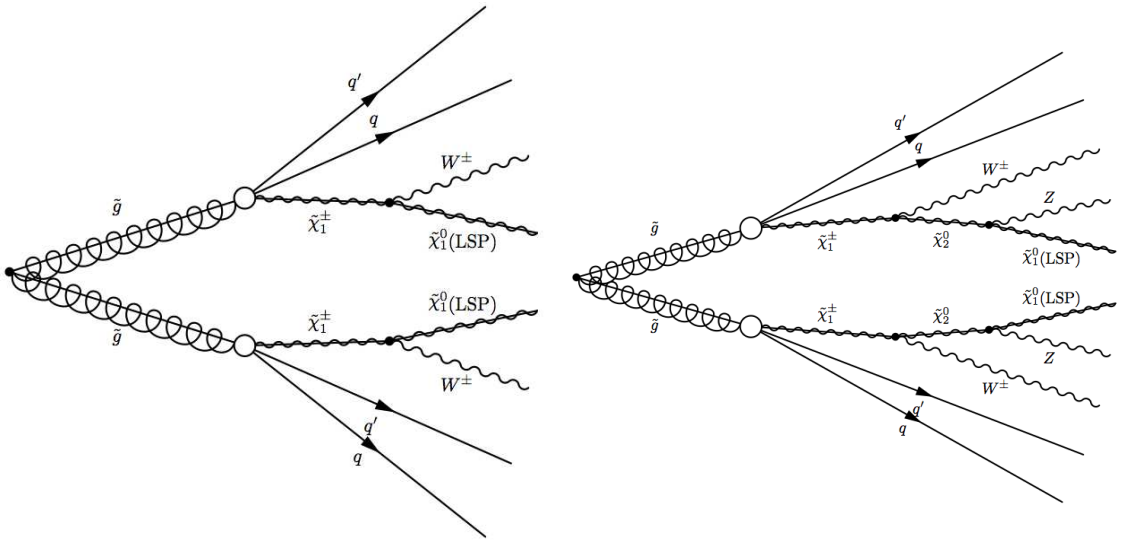

Figure 34: Left: Feynman graph of the one step simplified model with gluino pair production. Right: Feynman graph of the two step simplified model via standard model gauge bosons with gluino pair production. The white circle denotes the 3-body decay of the gluino via a virtual squark [83].

2. **Gluino Pair Production**
   For these simplified models, a pair of gluinos is produced and the masses are again varied between 200 GeV and 1.2 TeV in steps of 100 GeV. As discussed in section 4.2, the gluino can only decay via strong interactions into a squark and a quark. All subsequent decays of the squark are analogous to the simplified models with squark pair production. The only difference is the two additionally produced quarks from the $\tilde{g} \rightarrow \tilde{q^*}q$ decay. In addition, the results are presented as a function of the gluino mass and the compression factors are modified accordingly. Figure 34 shows the Feynman graphs for the one step and two step simplified models with gluino pair production.

For all simplified models, the masses of all supersymmetric particles, which do not occur within the cascade are set to 4.5 TeV. The compression factors determine how the total energy is distributed among the different final state particles, while the masses of the initially produced squarks and gluinos determine the total production cross section and energy in the event. Figure 35 shows the total cross sections for all one step simplified models calculated with the NLL fast programm [46]. For equal masses of the initial strong interacting supersymmetric particles, the cross section is much higher for the gluino pair production grid compared to squark pair production, due to the higher parton luminosity for gluons at the LHC. The cross sections drop quickly with increasing squark (gluino) masses. The sampling of the grids with varied compression factor is finer for the extreme cases of $x_1 \rightarrow 0$ and $x_1 \rightarrow 1$ for reasons becoming clear in chapter 6.

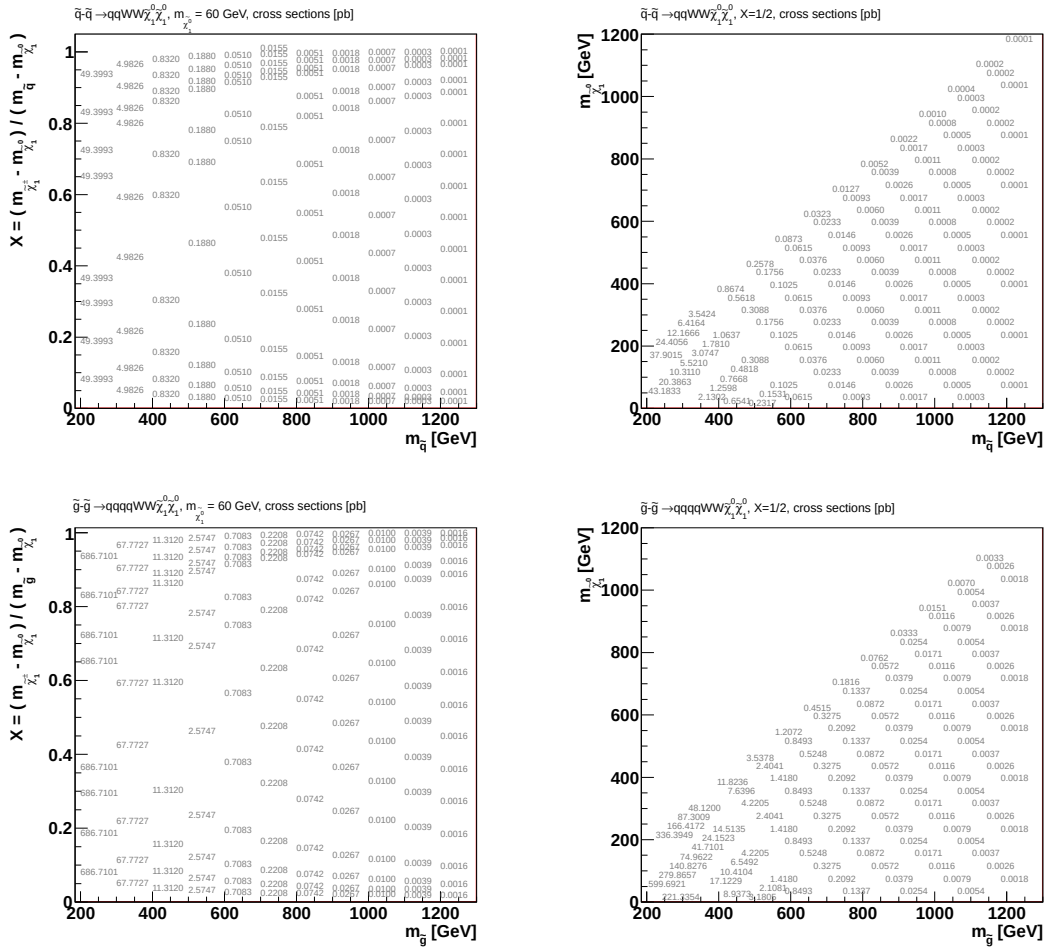

Figure 35: Cross sections in pb for the one step simplified models with squark pair production (top) and gluino pair production (bottom) calculated with the NLL fast programm [46]. Left: LSP mass fixed at 60 GeV and compression factor varied. Right: Compression factor fixed at 1/2 and LSP mass varied. At the areas with very fine grid spacing some points were taken out to improve readability.

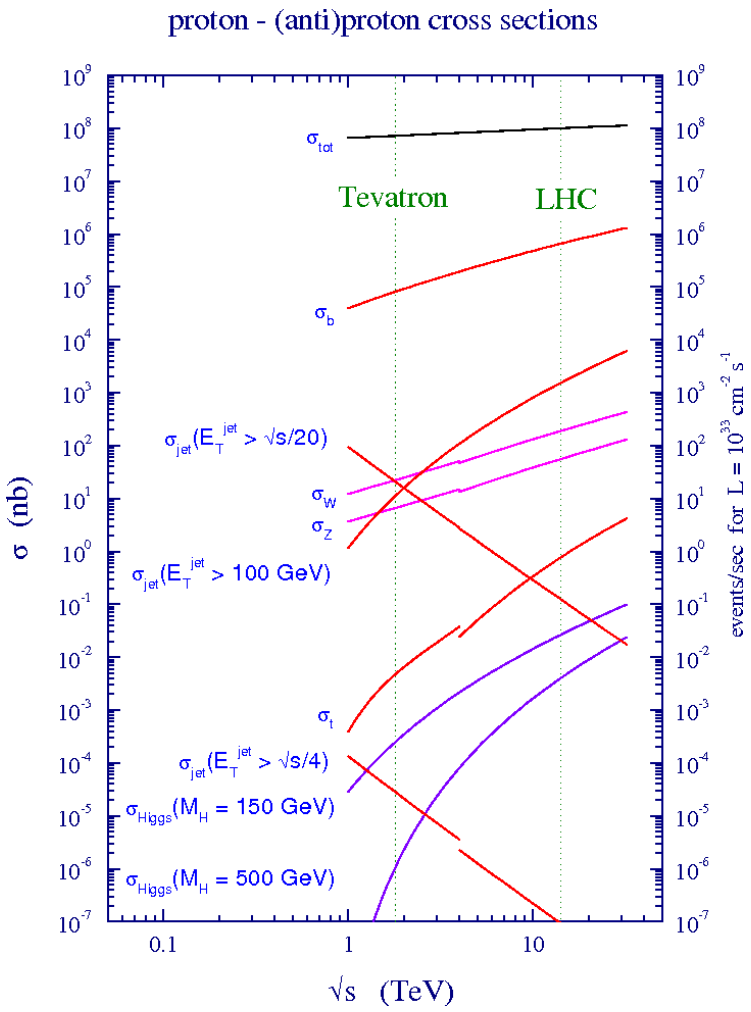

Figure 36: Cross sections in nb for various standard model processes as a function of the center of mass energy. In addition, the corresponding event rates are shown assuming the LHC operates at its design instantaneous luminosity of 10^{34} $\mathrm{cm}^{-2}\mathrm{s}^{-1}$ [32].

4.5 Standard model backgrounds

In this chapter, the standard model processes, which contribute as backgrounds for a search for supersymmetry with one charged lepton, jets and missing transverse energy, will be discussed. In general, the major backgrounds have either a high cross section or an event topology similar compared to the supersymmetric signal. Figure 36 summarizes the total cross sections and expected event rates for various standard model processes as a function of the center of mass energy, assuming an instantaneous luminosity of 10^{34} $\mathrm{cm}^{-2}\mathrm{s}^{-1}$ for the event rates [32]. The following qualitative comparisons of cross sections for different processes will refer to Figure 36. A more quantitative discussion will follow in chapter 5 and 6.

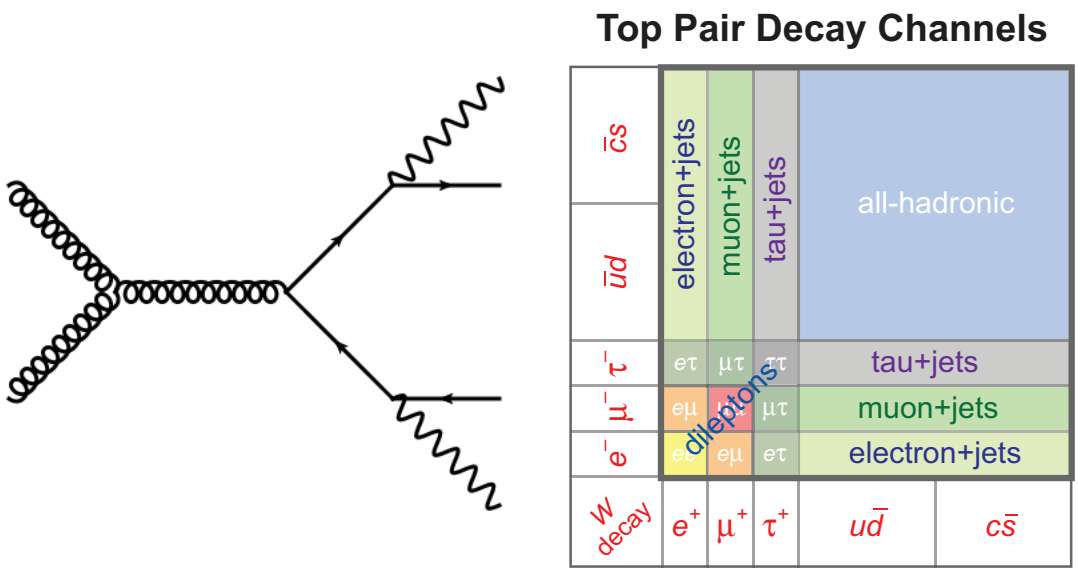

Figure 37: Left: Feynman graph of top antitop production via gluon fusion and subsequent decay of the top quark into a b quark and W boson. All additional diagrams arising from t-channel processes or initial states including two quarks are ommited for simplicity. Right: Possible final states in top antitop events dependent on the decay of the W boson. The size of the area indicates the probability of the corresponding decay mode [59].

4.5.1 Top quark pair production

The strong production of a top quark pair has an inclusive cross section of $\sigma = 166.8$ pb calculated at NLO+NLL [57] and is the main background for supersymmetry searches with isolated leptons, jets and missing energy. The left part of figure 37 shows the main production mode. The top quark decays in more than 99.9% of the time into a W boson and a bottom quark, leading to at least 2 jets in the final state [1]. The produced W boson can decay leptonically into a charged lepton and its corresponding neutrino or hadronically, yielding the possible final states in top antitop events as listed in the right part of figure 37. The dominant fraction of top antitop pairs decay fully hadronically, due to the dominant branching ratio of the W boson into hadrons of 67.6% [1]. However, this final state neither contains a prompt and charged lepton, nor missing transverse momentum and therefore differs severly from a possible R-parity conserving supersymmetric signal with leptons. Semileptonic decays, where one of the W bosons decays leptonically yield prompt charged leptons and missing transverse energy, and therefore possess a very similar topology compared to a supersymmetric signal. Fully dileptonic events are the rarest decay mode and contain an additional lepton. Nevertheless, it can be shown that dileptonic events, where one of the leptons is either a hadronically decaying tau lepton or not reconstructed in the ATLAS detector, are a substantial fraction of the total background in phase space regions examined in searches for supersymmetry [58].

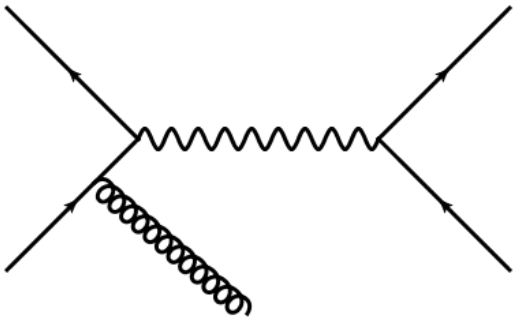

Figure 38: Feynman graph for the production of a W boson plus an additional gluon radiation in the initial state. The W boson decays according to its standard model couplings into a fermion-antifermion pair.

4.5.2 W boson production

The electroweak production of a leptonically decaying W boson is another important background. Figure 38 shows the Feynman graph for the process W$\rightarrow$l$\bar{\nu}_l$ including an additional radiated gluon in the initial state. The missing transverse momentum arises from the neutrino in the decay and additional QCD vertices lead to additional jets. However, although the inclusice cross section at NNLO for W boson production is $\sigma \times$ BR(W$\rightarrow \ell\nu$) $\approx$ 31.4 nb [60], the cross section for diagrams containing additional final state partons drops with $1/\alpha_s$ per additional order in QCD and therefore becomes small for high jet multiplicities.

4.5.3 Minor backgrounds

Minor backgrounds have either a very small cross section or differ substantially from the considered supersymmetric signals.

1. **Single Top Production**
   In contrast to the top quark pair production, discussed in section 4.5.1, a single top quark is produced electroweakly in this process[37]. If the top quark decays leptonically, the final state contains a prompt charged lepton, missing transverse momentum and one jet. Additional jets can again occur for diagrams at higher orders in QCD. As the top quark is produced via the electroweak force, the total cross section is much smaller than for strong top antitop pair production. Another process exists, where the top quark is produced with an associated W boson, which is also labeled as 'single top' in the following. In this case, single lepton final states can also occur if the top quark decays hadronically, while the associated W boson decays leptonically.

2. **Diboson Production**
   In diboson processes, a pair of electroweak gauge bosons is produced. The production of two W bosons, where one decays hadronically and the other

[37] In principle Feynman diagrams at QCD strength are possible. However, these diagrams contain a sea top quark within one of the protons, leading to a negligible probability.

leptonically has the highest relevance for a search for supersymmetry with one lepton, because it yields exactly one prompt lepton. In addition, the neutrino from the W boson decay leads to a missing energy signature, while the hadronically decaying W boson brings forth two jets.
Associated production of a W boson and a Z boson, where the Z boson decays hadronically, yields the same signature but with a much smaller cross section. Furthermore, events where the W decays hadronically and the Z boson into a pair of tau leptons - and only one of the tau leptons decays leptonically - can lead to final states with exactly one electron or muon. However, this decay channel has a very small branching ratio. Processes including two Z bosons cannot lead to exactly one prompt lepton, unless both Z bosons decay either into tau leptons - and only one of the tau leptons leptonically - or one of the Z bosons decays into a pair of neutrinos and the other one into an hadronically and leptonically decaying tau lepton. Again, both decay channels have a very small branching ratio. In addition, the cross section for ZZ production is even smaller than for the other diboson processes.

3. **Z boson Production**
   While having a much larger cross section of $\sigma \times \mathrm{BR}(\mathrm{Z}\to\ell\ell) \approx 15.1$ nb compared to single top and diboson production, a single Z boson cannot yield true missing energy *and* one prompt lepton - unless it decays via $\mathrm{Z} \to \tau\tau$ - and therefore only contributes marginally to the total standard model background.

4. **Pure QCD Processes**
   Pure QCD processes cannot lead to prompt leptons[38]. However, as these processes involve only strong couplings and no heavy particles, the cross sections are orders of magnitude larger than for any other standard model processes, as indicated in figure 36. As the identification of objects in the ATLAS detector is not perfect, even small misidentification rates of jets as leptons can yield to a significant background arising from QCD processes, while mismeasurements of jet energies can result in missing transverse energy.

[38] With the exception of top quark pair production, which is excluded from this discussion.

4.6 Monte Carlo generators

Precise simulations of physical processes are an integral component of almost every field of modern natural science. Especially within particle physics, searches for new phenomena heavily rely on an accurate description of various standard model processes, which must be taken into account as backgrounds.

All Monte Carlo generators consist of several major components, which are illustrated schematically in figure 39 for the example of a hadronically decaying W boson - produced at a hardon collider - and one additional final state leg, arising from initial state radiation. In the first step, the matrix element of the desired physics process is calculated at a certain order in pertubation theory. The product of matrix element and the available phase space in the final state represents the transition amplitude of a certain initial state into a certain final state. For the example in figure 39, the external legs and propagators, which belong to the matrix element calculation - the incoming partons, the ISR gluon, the W boson propagator and the W decay products - are shown in black. For hadron colliders like the LHC, the proton substructure is taken into account by summing over the relevant parton density functions as shown in equation 43, which is shown in red. In the last step, the fragmentation and hadronization of the final state partons into colorless particles is performed. The showering process is non-pertubative in QCD and therefore cannot be taken into account in the matrix element in the context of a quantum field theoretical calculation. Instead, empirical models are designed to describe the low energy behaviour of QCD, and the model-parameters are tuned to match soft QCD data. All lines in figure 39, which belong to the parton showering are presented in blue. The grey ellipses represent fragments, which are formed via cluster fragmentation [61] or string fragmentation models [62] from low energy partons. Finally, the black and white circles on the right side of the sketch illustrates the transition from fragments into physical baryons and mesons.

Different Monte Carlo generators are capable of performing different steps in the whole event generation process. Following classification can be done:

- **Leading order generators**
  Multipurpose leading order generators are capable of generating events for a large variety of physics processes. As the name suggests, they calculate the matrix element only at leading order, which yields a fast event generation on the one hand but limits the precision on the other hand. Especially in the context of a search for supersymmetry, the modelling of additional hard jets, which arise from diagrams at higher order in QCD are crucial. As the matrix elements are limited to leading order, all additional jets are obtained via the showering process, which is the largest drawback of these generators for searches for new physics with high jet activity. Examples for these kind of generators are `Pythia` or `Herwig` [63], which are both also capable of performing the parton showering on the partons - obtained via the matrix element calculation - themself.

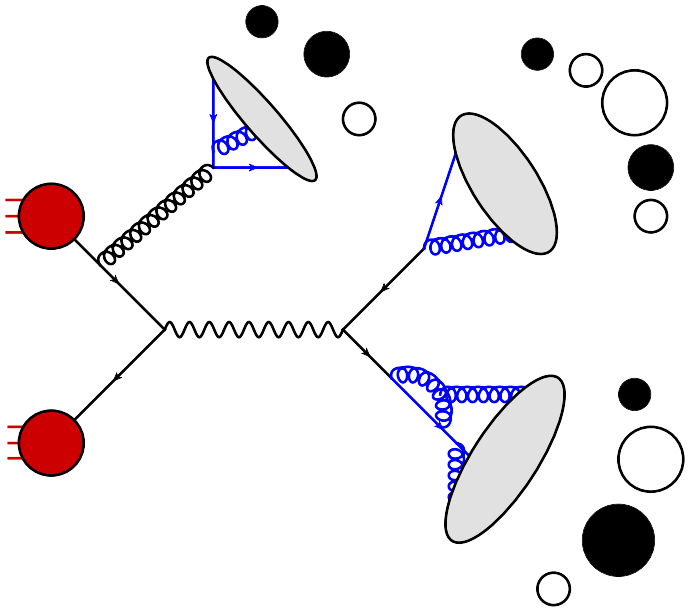

Figure 39: Schematic illustration of the different components of a Monte Carlo generator for the example of a hadronically decaying W boson plus additional initial state radiation.

- **Multileg generators**
  In contrast to the multipurpose generators, multileg generators take additional final state partons into account in the matrix element calculation. For a given number of additional final state legs, multileg generators only calculate the corresponding diagrams at the lowest possible order, which means that no diagrams containing loops are taken into account. The large advantage of this procedure is the better modelling of additional jets, because they arise from a precise quantum field theoretical calculation instead of a showering model. The disadvantage of this approach is the rather large CPU time consumption, which is inevitable if events with a large number of additional final state partons are generated. Examples for this kind of generators are `AlpGen` [64] or `MadGraph`. The fragmentation of final state partons into physical hadrons is performed by showering Monte Carlo generators like Pythia or Herwig.

- **Next to leading order generators**
  Next to leading order generators are capable of generating physics processes at next to leading order. In contrast to multileg generators, additional orders can also be realized as internal loops, while not changing the number of external legs. This means that processes including *one* additional final state partons are calculated with the same precision as done by multileg generators. Again, additional jets arise *solely* from parton showering, which is a disadvantage for physics analyses that rely on a large number of high energetic jets. Next to leading order generators are well suited for analyses that rely on a good description of differential cross sections for processes without any additional final state jets. Examples for this kind of generators are `MC@NLO` [65] or `PowHeg` [66].

Given these advantages and disadvantages, the main backgrounds are generated with the AlpGen generator, in order to obtain the most reliable modelling of additional hard jets. Table 10 lists the Monte Carlo generators for all background processes and some of their most important characteristics.

The cross sections for single electroweak gauge boson production were calculated at NNLO using `FEWZ` [60] and the `MSTW2008NNLO` [70] parton density function. For the diboson samples, the cross sections were calculated with `MCFM` [107] using the `MSTW2008NNLO` PDF set as well. For top quark pair production, `Hathor` [57] in version 1.2 was used to evaluate the cross section, again using the `MSTW2008NNLO` parton density function. The cross section for top quark pair production plus an additional W boson is taken from [108]. For top quark pair production plus an additional Z boson, the LO value is taken and multiplied by a k-factor, derived at NLO for a center of mass energy of 14 TeV [109][39]. For the production of a single top quark, the cross sections are taken from `MC@NLO`.
Parton showering and hadronization is done with `HERWIG` for the `AlpGen` and `MC@NLO` samples, while the underlying event is modelled with `JIMMY` [110]. For the `AcerMC` Monte Carlo simulations and the top quark pair plus vector boson samples, `PYTHIA` is used for the parton shower and fragmentation.
For the `AlpGen` and `MadGraph` samples, `CTEQ6L1` is used as the parton density function, while `CT10` is used for the `MC@NLO` Monte Carlo simulation and `MRSTMCal (LO**)` is used for `HERWIG`. The detector simulation is done with `GEANT` for all samples.

The signal Monte Carlo simulations for the mSUGRA model are performed with Herwig++ in version 2.5.2 [114] using the `MRST2007LO*` parton density function set [115]. The particle mass spectra of the supersymmetric particles are generated with `ISAJET 7.8` [116]. All simplified models are generated with `MadGraph5`, interfaced with `PYTHIA` for the parton showering, using the `CTEQ6L1` parton density function. All signal cross sections are computed at NLO in QCD, including resummation of soft gluon emission at NLL.

[39] This approach was necessary since no computations for a center of mass energy of 7 TeV existed.

Process	Generator	Effective σ_{tot} [pb]	σ_{tot} precision
Vector Boson related processes			
W→lν	AlpGen 2.13 [64]	10460	NNLO
W→lν + Heavy Flavour	AlpGen 2.13 [64]	1590	LO × k
Z/γ^*→ll	AlpGen 2.13 [64]	5040	NNLO
Z/γ^*→ll + Heavy Flavour	AlpGen 2.13 [64]	10.3	LO
WW	Herwig 6.5.20 [63]	44.9	NLO
WZ/γ^*	Herwig 6.5.20 [63]	18.5	NLO
Z/γ^*Z/γ^*	Herwig 6.5.20 [63]	5.96	NLO
Top Quark related processes			
$t\bar{t}$→bblν + jet/γ	AlpGen 2.13 [64]	89.854	NLO+NLL
$t\bar{t}$→bbqqqq + jet/γ	MC@NLO [65]	76.23	NLO+NLL
$t\bar{t}$ + W	MadGraph5 [44]	0.17	NLO
$t\bar{t}$ + Z	MadGraph5 [44]	0.12	LO × k
Single Top (t-channel)	AcerMC [103] 3.8	7.0	NLO
Single Top (s-channel)	MC@NLO 4.01 [65]	0.5	NLO
Single Top (Wt-channel)	MC@NLO 4.01 [65]	15.7	NLO

Table 10: Monte Carlo simulations for all relevant background processes. For the processes W→lν , Z/γ^*→ll and s- and t-channel single top production, the cross section corresponds to a single lepton flavour.

5 Theoretical uncertainties

As quantum field theories are based on a pertubation series in the coupling constants, no exact calculation of transition amplitudes is possible, as this would require evaluating these series up to arbitrary high orders. However, calculating the first orders often provides a sufficiently precise result, in order to make quantitative statements about whether data is compatible with the current knowledge of nature, or if physics beyond the standard model is necessary. In the following chapter, the major theoretical uncertainties will be discussed, focussing on top pair production, which is the most relevant background for the analysis presented in this thesis.

5.1 Background uncertainties

As inclusive supersymmetry searches rely on signatures including jets, an accurate modelling of additional jets, arising from Feynman diagrams at higher order in QCD is crucial. The studies are based on the multileg Monte Carlo generator AlpGen. As already mentioned, for each multiplicity of final state partons, AlpGen computes matrix elements at the lowest possible order, which means that no diagrams containing loops are taken into account. Monte Carlo produced with AlpGen contains a *fixed* number of addional partons in the final state, which are taken into account in the matrix element calculation. All of these subsamples must be added up and weighted by the corresponding cross sections to obtain a physical set of events. In contrast to event generators like Pythia or Herwig, AlpGen cannot simulate the parton showering, underlying event and hadronization of the final state partons. Therefore, it needs to be interfaced with one of these generators, in order to obtain physically reasonable collision events. The Herwig event generator is used for this purpose in the following studies.

Only additional partons above a certain, adjustable p_T threshold are taken into account in the matrix element, while the phase space below this threshold is filled with low energetic jets arising from parton showering. Furthermore, the partons generated in the matrix element are also showered using Herwig. If an event contains jets, which cannot be matched to one of the partons used in the matrix element calculation, the event is rejected, in order to avoid double counting. If a parton cannot be matched to a jet, the event is discarded as well. This procedure is called 'MLM matching'. For the sample including the highest number of additional partons calculated in the matrix element, any additional number of jets arising from the showering is allowed.

Theoretical systematic uncertainties arise from the lack of knowledge of higher orders, as well as from the interplay between AlpGen and the generator responsible for the parton shower and hadronization. Both sources of uncertainties will be discussed in the following sections for the main background top antitop quark production with additional partons in the final state. Similar studies have been performed for the W boson background including additional jets [67].

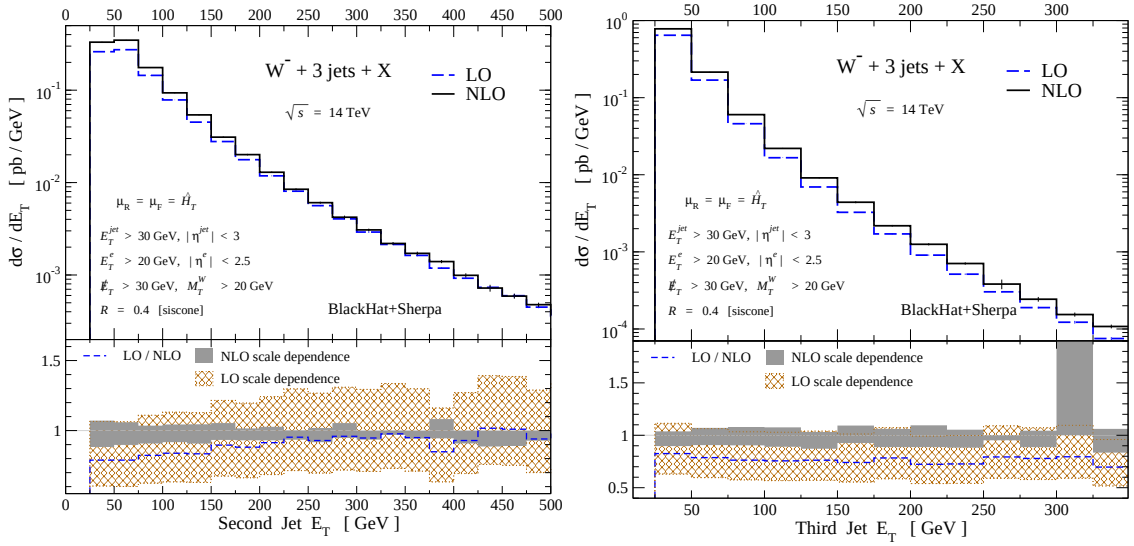

Figure 40: Scale dependence of the transverse momentum of the second (left) and third (right) leading jet in W boson events for a computation at LO (dashed blue lines) and at NLO (solid black lines) derived with the Blackhat Monte Carlo generator [68]. At next to leading order, the scale dependence - indicated in the ratio plot - is significantly lower.

5.1.1 Scale uncertainties

Scale uncertainties reflect the ignorance of higher orders, which cannot be calculated in the event generation. Therefore, the impact of scale uncertainties decreases with the amount of additional orders evaluated in the pertubation series, as shown in figure 40 for the example of W boson events with additional jets in the final state, calculated with the Blackhat Monte Carlo generator [68]. As AlpGen is a leading order event generator, scale uncertainties can be rather large and contribute as a major uncertainty to the total systematic uncertainty. The total energy scale dependence can be split into two different effects, the 'factorization scale' and the 'renormalization scale'. The factorization scale can be written as

$$Q^2 = Q^2_{fac} \times Q^2_0 \tag{51}$$

where Q_{fac} is a real number and Q_0 a function of the produced particle properties, which depends on the process under consideration. For top quark pair production, Q_0 is chosen to be:

$$Q^2_0 = m^2_t + \sum_{\text{partons}} p^2_T \tag{52}$$

where m_t denotes the top quark mass and the sum runs over all final state partons, excluding the top quark and W boson decay products. The functional form of the scale is supposed to reflect the total energy in the event, which makes equation 52 a reasonable choice for top quark pair events. However, the choice of the factorization scale is somewhat arbitrary and different choices of the scale can lead to drastically different results [68]. The common convention to estimate systematic effects arising

from factorization scale variations is to vary Q_{fac} up and down within a factor of two.

The other scale involved is the scale used to evaluate α_s at each vertex, which is called the 'renormalization scale'. The functional form of this scale is determined by the CKKW prescription using the k_T at *each* vertex defined like

$$k_T = \sqrt{t}\mathrm{z}(1-\mathrm{z}) \tag{53}$$

where t denotes the scale of the initial particle and z the fraction of the initial particles energy obtained by the *harder* outgoing particle [69]. As for the factorization scale, a global multiplicative factor, named $k_{T_{fac}}$, is introduced, enabling to change the whole scale up and downwards. As the showering Monte Carlo only obtains the four momenta of the partons generated with AlpGen and no information about the specific value of α_s, a coherent treatment of α_s between the two generators is not possible.

Monte Carlo simulations for top quark pair production and several values for Q_{fac} and $k_{T_{fac}}$ were performed, and the impact on the cross sections and jet related variables is studied. For top quark pair production, AlpGen is capable of generating Monte Carlo events with maximal 5 additional partons calculated in the matrix element[40]. Tables 11 and 12 show a comparison of cross sections obtained for the nominal AlpGen scale choice with $Q_{fac} = k_{T_{fac}} = 1$ and varied values for both scales. Fully leptonic and semileptonic events were generated as distinct sets. The cross sections are calculated at leading order by the AlpGen generator.
A variation of Q_{fac} up (down) by a factor of two, while keeping $k_{T_{fac}}$ at the nominal value, decreases (increases) the cross section for each parton multiplicity by roughly 20-40%. In contrast, varying $k_{T_{fac}}$ by a factor of two, while keeping Q_{fac} constant at the nominal value, significantly changes the relative contribution of each parton multiplicity to the total cross section. Increasing (decreasing) $k_{T_{fac}}$ by a factor of two, roughly halves (doubles) the cross section for the highest parton multiplicity compared to the nominal sample, while hardly changing the cross section for the sample without any additional parton.

In addition to changes in cross section for each parton subsample, properties of the additional partons generated *within* each subsample are tested for changes compared to the corresponding nominal sample. Figures 86 - 89 in Appendix A show the transverse momenta of the leading 5 jets and the number of jets with a $p_T >$ 25 GeV on generator level for two examplary parton multiplicities, comparing samples with nominal and varied scale. All samples are normalized arbitrarily to the same area, allowing for a pure comparison of the shape of the jet p_T spectra and multiplicities. Neither changing Q_{fac} nor $k_{T_{fac}}$ affects the transverse momenta of the additional jets within each parton multiplicity with respect to the nominal scale

[40] Actually this is no strict limitation from the generator side, but technically constrained by the necessary CPU time to generate events, because the efficiency of the Monte Carlo generator to generate a physical output event drops rapidly with the number of requested additional partons in the final state.

	0 Partons	1 Parton	2 Partons	3 Partons	4 Partons	5 Partons
Nominal						
σ_{Alpgen} (pb)	13.78	13.56	8.24	3.66	1.24	0.36
Q_{fac} **= 2.0,** $k_{T_{fac}}$ **= 1.0**						
σ_{Alpgen} (pb)	10.6	10.22	6.13	2.69	0.88	0.24
$\sigma/\sigma_{nominal}$	0.77	0.75	0.74	0.73	0.71	0.67
Q_{fac} **= 0.5,** $k_{T_{fac}}$ **= 1.0**						
σ_{Alpgen} (pb)	18.69	18.9	11.82	5.1	1.78	0.43
$\sigma/\sigma_{nominal}$	1.36	1.39	1.43	1.39	1.44	1.19
Q_{fac} **= 1.0,** $k_{T_{fac}}$ **= 2.0**						
σ_{Alpgen} (pb)	13.56	12.03	6.72	2.63	0.77	0.19
$\sigma/\sigma_{nominal}$	0.98	0.89	0.76	0.72	0.62	0.53
Q_{fac} **= 1.0,** $k_{T_{fac}}$ **= 0.5**						
σ_{Alpgen} (pb)	13.58	15.41	10.89	5.45	2.02	0.61
$\sigma/\sigma_{nominal}$	0.99	1.14	1.32	1.49	1.63	1.69

Table 11: Effective cross sections in pb for the process $t\bar{t} \rightarrow bbl\nu qq$ and different choices for Q_{fac} and $k_{T_{fac}}$ for different parton multiplicities calculated in the matrix element. The cross sections are calculated at LO by the AlpGen generator.

choice. This statement is in general true for all simulated parton multiplicities [67][41].

Given the changing cross sections as listed in tables 11 and 12 and the unaffected jet momenta and multiplicities for each parton subsample, the inclusive and physical event variables, weighting all subsamples with the corresponding cross sections and adding them up, change as shown in figures 41 - 42. All samples are normalized inclusively to the total cross section at NNLO assuming an integrated luminosity of $\int$Ldt = 4.7 fb^{-1}, which corresponds to the amount of data analyzed in this thesis. The cross sections were calculated at approximate NNLO in QCD with `Hathor` 2.1 [57] using the `MSTW2008` 90% NNLO PDF sets [70]. The effective NNLO cross section for the process $t\bar{t} \rightarrow bbl\nu qq$ is σ = 73.08 pb, and for $t\bar{t} \rightarrow bbll\nu\nu$ it is σ = 17.51 pb. The missing transverse energy is evaluated at generator level, taking into account the neutrino(s) from the $W \rightarrow l\nu$ decay. The charged lepton is as well required to arise from the $W \rightarrow l\nu$ decay on generator level.

As $\sigma_{var}/\sigma_{nom}$ hardly depends on the amount of additional partons in the final state for samples with varied factorization scale, only small variations in the chosen event variables are observed for this variation. However, variations in the renormalization scale lead to large changes in the event variables. Varying $k_{T_{fac}}$ upwards (downwards) decreases (increases) the cross sections for samples with additional partons in the matrix element, which directly translates into lower (higher) jet transverse momenta and multiplicities arising from these partons. As for the process $t\bar{t} \rightarrow bbll\nu\nu$, only 2

[41] It should be noted, that the cited note only includes sample with a maximum of 3 additional partons in the matrix element. However, the same result was also obtained for $t\bar{t}$ + 4 partons and $t\bar{t}$ + 5 partons.

	0 Partons	1 Parton	2 Partons	3 Partons	4 Partons	5 Partons
Nominal						
σ_{Alpgen} (pb)	3.39	3.41	2.09	0.92	0.3	0.08
Q_{fac} **= 2.0,** $k_{T_{fac}}$ **= 1.0**						
σ_{Alpgen} (pb)	2.62	2.54	1.56	0.68	0.23	0.06
$\sigma/\sigma_{nominal}$	0.77	0.74	0.75	0.74	0.77	0.75
Q_{fac} **= 0.5,** $k_{T_{fac}}$ **= 1.0**						
σ_{Alpgen} (pb)	4.71	4.77	2.96	1.31	0.42	0.12
$\sigma/\sigma_{nominal}$	1.39	1.40	1.42	1.42	1.4	1.5
Q_{fac} **= 1.0,** k_{Tfac} **= 2.0**						
σ_{Alpgen} (pb)	3.42	2.96	1.75	0.65	0.2	0.04
$\sigma/\sigma_{nominal}$	1.01	0.87	0.84	0.71	0.67	0.5
Q_{fac} **= 1.0,** $k_{T_{fac}}$ **= 0.5**						
σ_{Alpgen} (pb)	3.39	3.86	2.74	1.34	0.51	0.15
$\sigma/\sigma_{nominal}$	1	1.13	1.31	1.46	1.7	1.88

Table 12: Effective cross sections in pb for the process $t\bar{t} \rightarrow bbll\nu\nu$ and different choices for Q_{fac} and $k_{T_{fac}}$ for different parton multiplicities calculated in the matrix element. The cross sections are calculated at LO by the AlpGen generator.

jets arise from the $t \rightarrow bW$ decay, the probability that the 3^{rd} leading or even harder Jets originate from an additional parton is higher compared to the semileptonic final states, and therefore the effect is more pronounced.
Event variables, which are only affected at second order by a change in the final state partons - like the missing transverse energy or the transverse momentum of the lepton from the W boson decay - show almost no deviation with respect to the nominal scale within statistical uncertainties.

5.1.2 MLM matching uncertainties

As already mentioned before, AlpGen is interfaced with Herwig in order to shower the partons calculated in the matrix element, as well as to fill phase space regions not covered by the matrix element calculation. Only additional partons above a certain p_T threshold are taken into account by AlpGen in the matrix element calculation. This threshold is denoted as p_T^{min} and is chosen to be 15 GeV for the nominal AlpGen setup.

The jets are reconstructed using a cone based algorithm with parameters $\mathcal{R}_{jet}$, defining the size of the cone, and E_T^{min}, being the minimal amount of transverse energy required to form a jet. It can happen that Herwig produces additional hard jets during the showering, turning a N parton event into a N+1 jet event. As the N+1 jet event is already covered by the sample including N+1 partons in the matrix element, these events are discarded, if one of the jets cannot be matched to a parton. However, as the matrix element calculation is limited to parton multiplicities

	0 Partons	1 Parton	2 Partons	3 Partons	4 Partons	5 Partons
Nominal						
σ_{Alpgen} (pb)	13.78	13.56	8.24	3.66	1.24	0.36
p_T^{min} **= 20 GeV**						
σ_{Alpgen} (pb)	16.71	12.9	6.4	2.39	0.66	0.15
$\sigma/\sigma_{nominal}$	1.21	0.95	0.78	0.65	0.53	0.42
p_T^{min} **= 30 GeV**						
σ_{Alpgen} (pb)	21.01	11.33	4.0	1.05	0.22	0.03
$\sigma/\sigma_{nominal}$	1.52	0.84	0.49	0.29	0.18	0.08

Table 13: Effective cross sections in pb for the process $t\bar{t} \rightarrow bbl\nu qq$ and different choices for p_T^{min} for different parton multiplicities calculated in the matrix element.

	0 Partons	1 Parton	2 Partons	3 Partons	4 Partons	5 Partons
Nominal						
σ_{Alpgen} (pb)	3.39	3.41	2.09	0.92	0.3	0.08
p_T^{min} **= 20 GeV**						
σ_{Alpgen} (pb)	4.14	3.24	1.62	0.6	0.16	0.04
$\sigma/\sigma_{nominal}$	1.22	0.95	0.78	0.65	0.53	0.5
p_T^{min} **= 30 GeV**						
σ_{Alpgen} (pb)	5.26	2.79	0.98	0.26	0.06	0.01
$\sigma/\sigma_{nominal}$	1.55	0.82	0.47	0.28	0.2	0.13

Table 14: Effective cross sections in pb for the process $t\bar{t} \rightarrow bbll\nu\nu$ and different choices for p_T^{min} for different parton multiplicities calculated in the matrix element.

up to 5, there is a special case for the sample with the highest parton multiplicity in the matrix element calculation. For this sample, any additional amount of hard jets arising in the showering process is allowed. The jet-parton matching is based on the spatial distance in the η - ϕ space defined as $\Delta R = \sqrt{\Delta\eta^2 + \Delta\phi^2}$. A jet is considered as matched, if the ΔR between the jet and the parton is smaller than $\mathcal{R}_{jet}$, which is taken to be 0.7 for this study.

Samples with varied p_T^{min} were generated to extract a systematic uncertainty arising from this matching procedure. Tables 13 and 14 show the cross sections for p_T^{min} values of 20 GeV and 30 GeV[42].
Increasing the MLM matching cutoff decreases the cross sections with respect to the nominal cutoff for the samples with additional partons calculated in the matrix element, while increasing the cross section for the sample without additional final state partons. Weighting all parton subsamples with these cross sections and adding them up yields the physical distributions shown in figures 43 - 44. For jet transverse

[42]In addition, samples with a p_T^{min} of 10 GeV were generated. However, discussing with the AlpGen author M. Mangano lead to the conclusion that this value is too small and leads to unphysical holes in the phase space.

momenta in the p_T regime close to the MLM matching cutoff, deviations for different choices of p_T^{min} occur. For p_T regimes far above the MLM matching cutoff, the choice of p_T^{min} affects the jet momenta less significantly. In general, increasing the MLM matching cutoff slightly lowers the jet transverse momenta, shifting the jet multiplicity distribution to lower values compared to the nominal choice of $p_T^{min} =$ 15 GeV. For variables only indirectly influenced by changes in the MLM matching cutoff like E_T^{miss} and the transverse momentum of the lepton from the W boson decay, no significant differences for different values of p_T^{min} occur.

5.2 Constraining scale uncertainties from data

As shown in the previous section, the largest systematic uncertainties arise from variations in the renormalization scale, while variations in the factorization scale only change the total normalization of the inclusive $t\bar{t}$ + jets, and variations of the MLM matching cutoff are comparably small for jet momenta far above p_T^{min}. However, the choice of varying the scale by a factor of two is an arbitrary convention. Several searches for supersymmetry were performed in ATLAS using this convention as a quantitative estimate of the uncertainties originating from scale variations [71]. For the analysis presented in this thesis, a different approach is chosen and the impact of scale variations is quantified using data. Given the large amount of data taken with the ATLAS experiment in 2011, a variation of the scale by a factor of 2 leads to disagreements between simulation and data. Therefore, a technique is presented that constrains the change in scale, which is still allowed by the ATLAS data.

The total inclusive cross section for $t\bar{t}$ + jets is known at approximate NNLO, while the contributions arising from different parton multiplicities are only calculated in leading order within AlpGen. As variations in the renormalization scale express themself *only* in changes in the cross sections of the individual subsamples with fixed parton multiplicity, the effect of changing $k_{T_{fac}}$ can be constrained by measuring these cross sections. For variations in the factorization scale, $\sigma_{var}/\sigma_{nom}$ barely depends on the number of additional final state partons as shown in tables 11 and 12. Therefore, constraining factorization scale uncertainties on data translates into the simpler case of measuring *one* normalization for the whole $t\bar{t}$ + jets process. Two requirements need to be met in order to make this approach work:

1. Within each parton multiplicity, the jet transverse momenta do not depend on the choice of the scale. This was already examplarily shown for two parton multiplicities in Appendix A in figures 86 - 89 and validated for all other parton multiplicities as well.

2. The physical jet transverse momenta for the process $t\bar{t}$ + jets do not differ strongly between leading order and higher orders. This assumption is important, as AlpGen calculates the spectra only at LO. As no NLO Monte Carlo with a high number of final state partons exists for $t\bar{t}$, this assumption cannot be validated. However, comparisons between LO and NLO were performed for the W boson + jets process and no significant changes in the jet transverse

momenta were observed, as shown in the left panel of figure 45. This can be considered as a hint for the correctness of the assumption for $t\bar{t}$ + jets as well. In addition, figure 45 illustrates that the scale uncertainties at LO are significantly larger compared to an NLO calculation, which motivates a data driven approach to reduce the total uncertainty on the background prediction.

As the transverse momenta for jets arising from hard partons calculated in the matrix element and parton showering differ, the jet multiplicity is sensitive on the number of partons calculated in the matrix element as shown in the right panel of figure 45 for top quark pair events after a loose selection. The more final state partons are taken into account in the matrix element, the more jets with a significant momentum can arise from these partons leading to a higher jet multiplicity compared to a sample with a lower number of partons in the matrix element. In chapter 7, extracting the normalizations for each subsample with a fixed parton multiplicity - using the jet multiplicity distribution - will be discussed as one of the core ingredients of this analysis. As already mentioned in section 5.1.1, the presented results are similar for vector boson + jet events - as shown in [67] - and the same technique will be applied to this process.

5.3 Signal uncertainties

As for the major backgrounds, several theoretical systematic uncertainties, which change the event yields of the supersymmetric signals, are considered. For all signal models studied, the cross sections are calculated at NLO+NLL, if available. The computation is done using the NLL-fast interpolation package [46]. If no NLO+NLL calculation for the model exists, the cross sections are calculated with Prospino 2.1 [72].

1. **Scale uncertainties**
   The renormalization and factorization scales are varied by a factor of two up and down and the corresponding cross sections are used to estimate a systematic uncertainty on the signal event yield. The nominal scale is set to the squark (gluino) mass for squark (gluino) pair production. For mixed production the average mass is taken as $(m_{\tilde{q}} + m_{\tilde{g}})/2$.

2. **Parton density function uncertainties**
   A total of 44 (40) PDF sets is considered, which contain several experimental errors for the CTEQ (MSTW) PDF. For each variation, the difference in cross section compared to the nominal PDF is calculated and the maximal deviation is taken as a systematic uncertainty arising from PDF uncertainties.

3. **Initial state radiation uncertainies**
   In order to estimate the systematic errors that arise from the lack of knowledge of initial state radiation (ISR), several simulations with different pythia tunes related to ISR were performed. In addition, the MLM matching scale is changed within a factor of two. For both types of uncertainties, the maximal

deviations are added in quadrature, and the obtained value is taken as the total ISR uncertainty.

Figure 46 shows the total relative uncertainty on the cross section in the m_0 - $m_{1/2}$ plane for the mSUGRA scenario with $A_0 = 0$ GeV, $\tan(\beta) = 10$ and a positive sign(μ). For small values of $m_{1/2}$ - where the strong interacting supersymmetric particles are comparably light - the uncertainty is of the order of 10-20% and increases with increasing $m_{1/2}$ to a maximal value of roughly 60%.

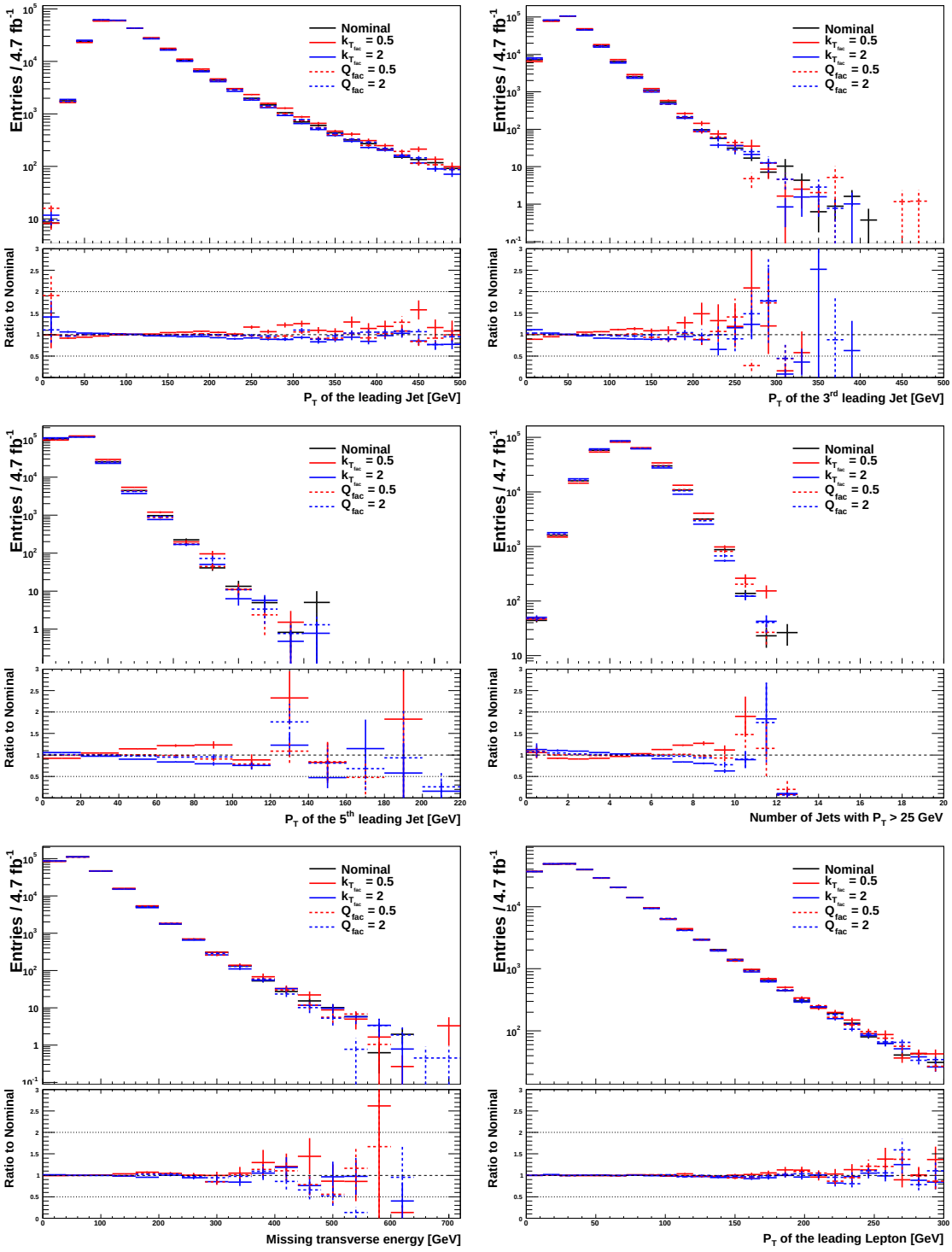

Figure 41: Jet transverse momenta, missing transverse energy and transverse momentum of the leading lepton for the inclusive process $t\bar{t} \to bbl\nu qq$ + jets, comparing factorization scale (dashed lines) and renormalization scale (solid lines) varied by a factor 2 up and down with the nominal scale choice. All samples are normalized inclusively to the total approximate NNLO cross section and $\int$Ldt = 4.7 fb^{-1}.

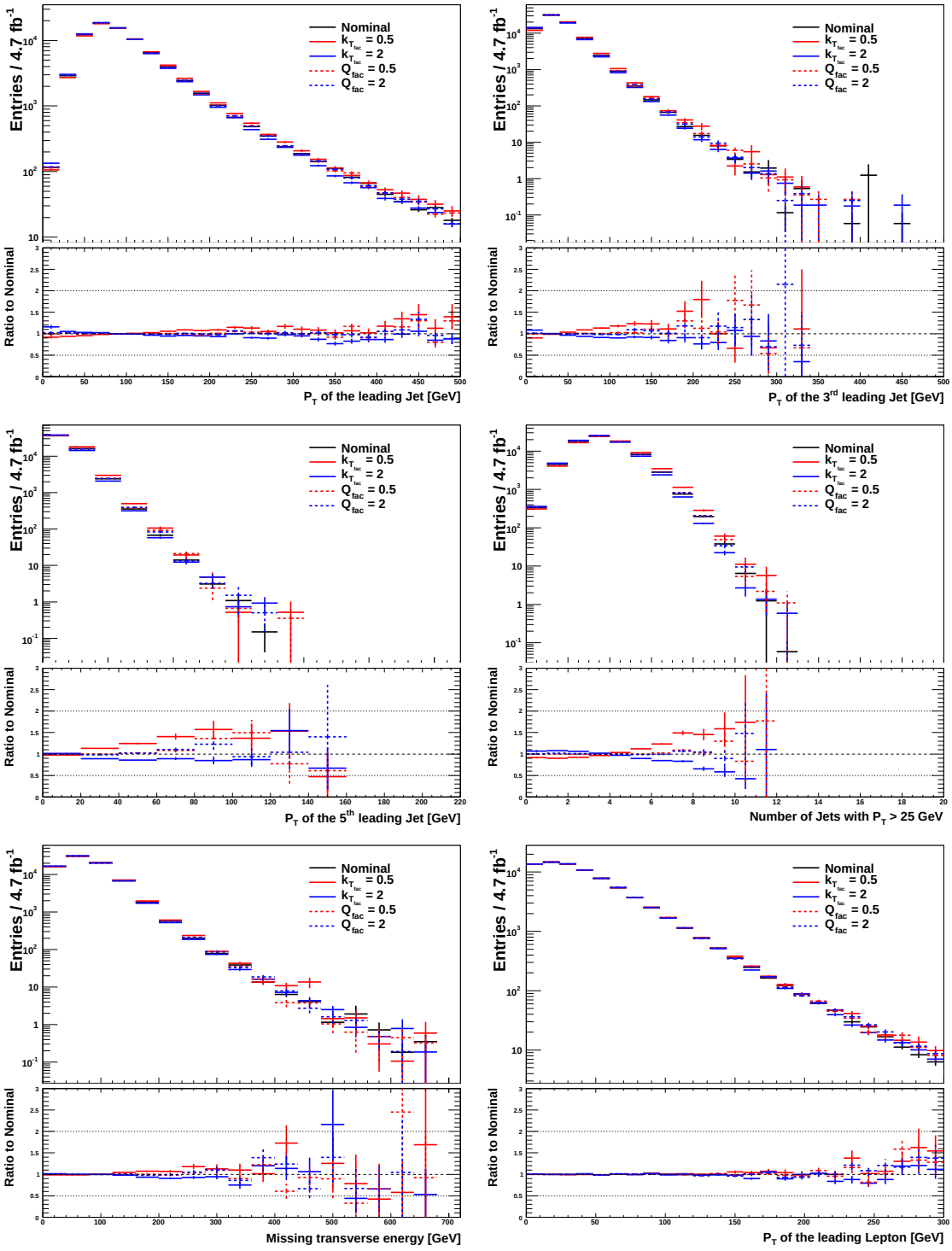

Figure 42: Jet transverse momenta, missing transverse energy and transverse momentum of the leading lepton for the inclusive process $t\bar{t} \rightarrow bbll\nu\nu$ + jets, comparing factorization scale (dashed lines) and renormalization scale (solid lines) varied by a factor 2 up and down with the nominal scale choice. All samples are normalized inclusively to the total approximate NNLO cross section and $\int$Ldt = 4.7 fb^{-1}.

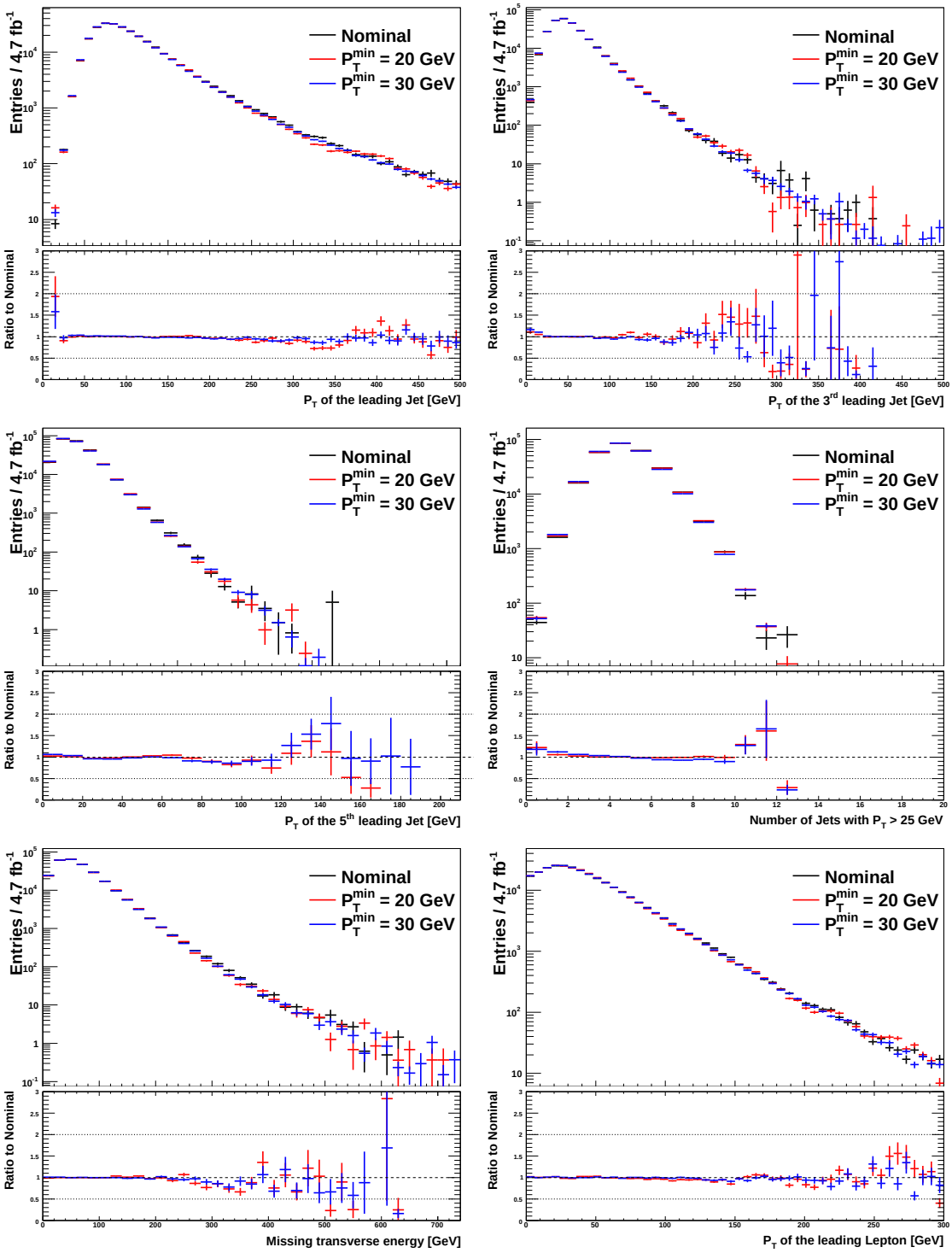

Figure 43: Jet transverse momenta, missing transverse energy and transverse momentum of the leading lepton for the inclusive process $t\bar{t} \to bbl\nu qq$ + jets, comparing nominal MLM matching cutoff with $p_T^{min} = 20$ GeV and $p_T^{min} = 30$ GeV. All samples are normalized inclusively to the total approximate NNLO cross section and $\int$Ldt = 4.7 fb^{-1}.

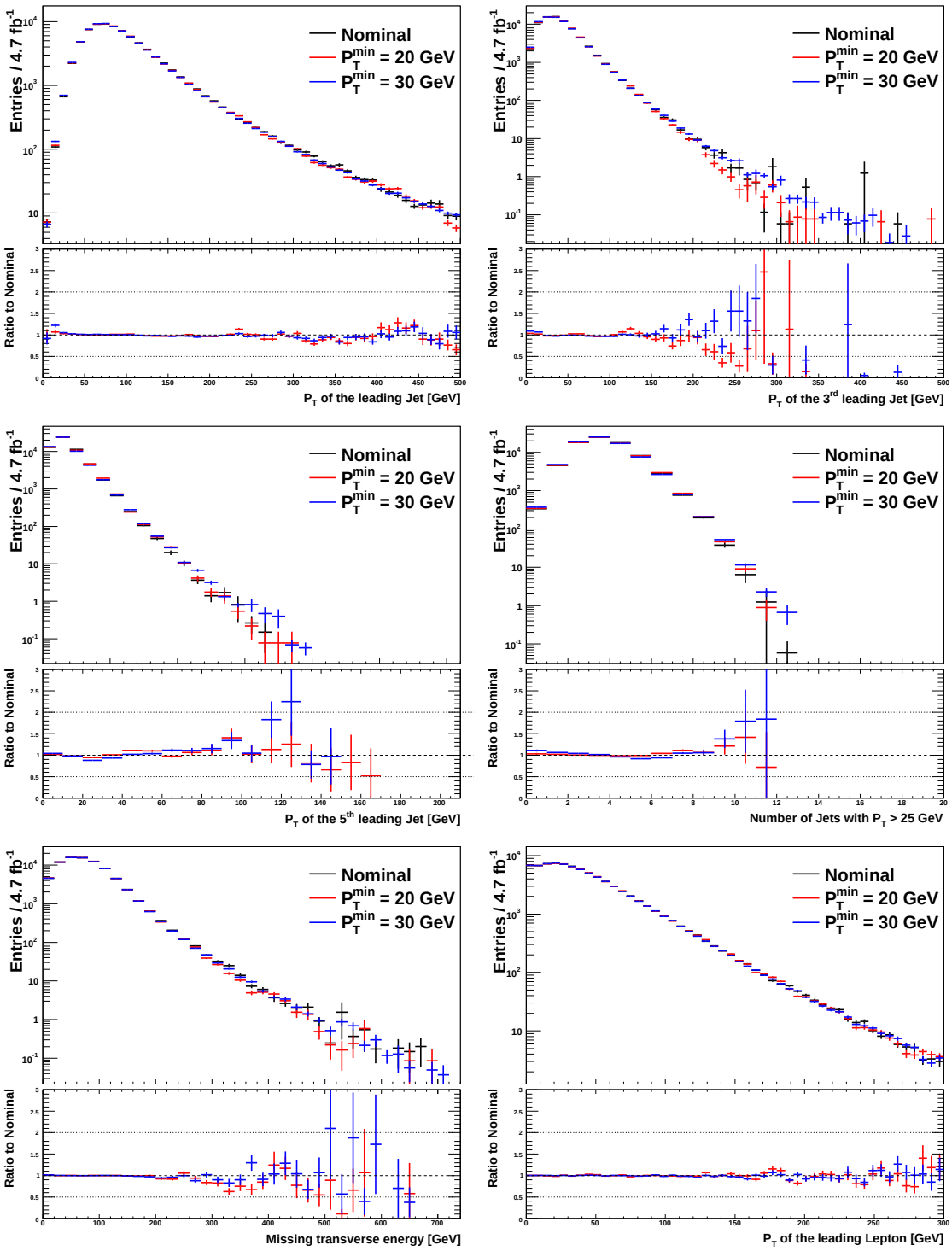

Figure 44: Jet transverse momenta, missing transverse energy and transverse momentum of the leading lepton for the inclusive process $t\bar{t} \rightarrow bbll\nu\nu$ + jets, comparing nominal MLM matching cutoff with $p_T^{min} = 20$ GeV and $p_T^{min} = 30$ GeV. All samples are normalized inclusively to the total approximate NNLO cross section and $\int$Ldt = 4.7 fb^{-1}.

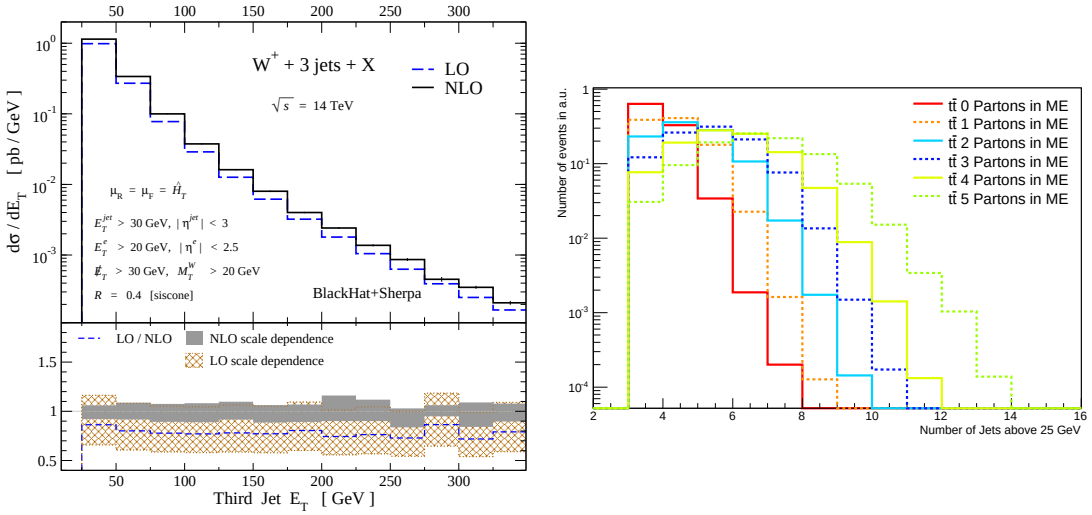

Figure 45: Left: Transverse energy of the third leading jet in $W^+ + 3$ jet events, calculated with the Blackhat Monte Carlo generator comparing a computation at leading order with a next to leading order calculation [68]. Right: Multiplicity of reconstructed jets for top quark pair events after a loose selection of at least 3 jets, and 30 GeV of missing transverse energy for AlpGen samples with a different number of additional partons calculated in the matrix element.

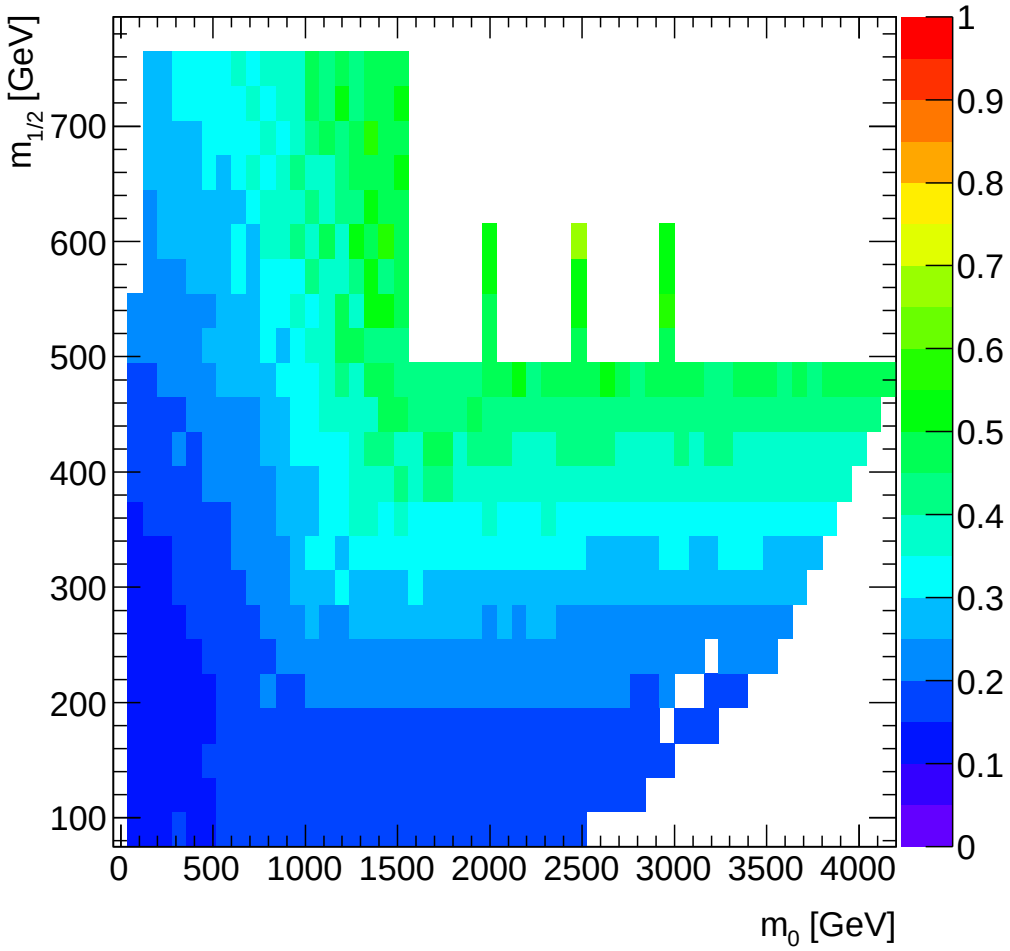

Figure 46: Total fractional uncertainty on the cross section after combining all production processes for the mSUGRA scenario with $A_0 = 0$ GeV, $\tan(\beta) = 10$ and a positive sign(μ) [83]

6 Analysis

In this chapter, several main aspects of the search for supersymmetry with one isolated charged lepton will be discussed. As the search is split into final states with exactly one electron and final states with exactly one muon, different triggers are used to select possibly interesting events. After this, the ATLAS event reconstruction software processes these recorded events to reconstruct physics objects like the leptons, jets or the missing transverse energy. Based on these objects, phase space regions are selected to model the various backgrounds and to search for potential signs for new physics beyond the standard model.

Inclusive searches for supersymmetry with one or two charged leptons in the final state are just a fraction of searches for supersymmetry at the ATLAS experiment. Similar analyses are also performed in purely hadronic final states [74] [75] or final states with more than two charged leptons [76]. Furthermore, searches targeting specific supersymmetric particles are performed - for example searching for light scalar top or bottom quarks - as exemplarily presented in [77] and [78].

Several additional final states were combined with the one lepton supersymmetry search in order to increase sensitivity over a larger phase space region [73]. The combination of search channels using a partially combined background estimation technique is described in chapter 7. All search channels are motivated and listed qualitatively in the following. The exact definition of phase space cuts is performed in a later section.

1. **Hard single lepton final state**
   The hard one lepton final state is the main channel discussed in this thesis and split into final states with exactly one electron and final states with exactly one muon. It targets supersymmetric decay chains including exactly one leptonically decaying W boson from a $\tilde{\chi}^{\pm} \rightarrow \tilde{\chi}^{0} W$ decay as discussed in chapter 4.2. In addition, models with light scalar taus can lead to exactly one isolated electron or muon. This channel has a high sensitivity in the mSUGRA model and one step simplified models.

2. **Soft single lepton final state**
   In the soft lepton analysis, final states with low energetic charged and isolated electrons and muons are selected, which occur if the supersymmetric mass spectrum is strongly compressed and therefore most of the energy is consumed to form the final state LSPs. In particular, if $m_{\tilde{\chi}_1^{\pm}} < m_{\tilde{\chi}_1^{0}} + m_W$, the decay $\tilde{\chi}_1^{\pm} \rightarrow \tilde{\chi}_1^{0} W^{*}$ turns into a 3 body decay including a virtual W boson, which significantly lowers the transverse momentum of the chargino decay products.

3. **Dilepton final states**
   This analysis includes final states with either two electrons, two muons or an eμ pair. Dileptonic final states can occur in several ways, as discussed in chapter 4.2. Especially in physics models with light sleptons like GMSB or phenomenological models explicitly including sleptons, dilepton searches pro-

vide a high sensitivity.

In the following, information regarding the soft one lepton and dilepton final states will be explicitly listed if necessary, and referenced otherwise. For all final states, signal enriched regions (**SRs**) and dedicated background control regions (**CRs**) are introduced in later sections.

6.1 Data set and trigger

This analysis is based on the ATLAS data periods B2 - M10, recorded at a center of mass energy of 7 TeV in the year 2011. The separation into different periods reflects the different LHC running conditions for different time spans of data taking. The total integrated luminosity after very basic data quality requirements[43] is (4.7 $\pm$ 0.17) fb^{-1} . The mean number of interactions per bunch crossings is $<\mu> = 9.1$ as shown in figure 10 with a maximal instantaneous luminosity of almost 3.7×10^{33} cm^{-2}s^{-1} as shown in figure 9.

Different triggers were used for final states with electrons and muons as listed in table 15. As the instantaneous luminosity increased during the data taking period 2011, the trigger thresholds were adjusted successively to avoid prescales[44].
For final states including hard electrons (muons), a single electron (muon) trigger with an E_T (p_T) threshold around 20 GeV is used[45]. Equation 48 justifies this choice for the mSUGRA scenario, as the large gaugino mass splitting between the lightest chargino and neutralino yields real W bosons in the $\tilde{\chi}_1^{\pm} \rightarrow \tilde{\chi}_1^0 W$ decay[46]. The corresponding turn on curves are shown in figure 47. Small discrepancies in the turn on curves between data and simulation are corrected via a rescaling of the Monte Carlo events. For the electron triggers, the electron at trigger level is required to be matched to a reconstructed electron. The efficiencies were estimated using a tag and probe method on $Z \rightarrow ee$ ($Z \rightarrow \mu\mu$) events for the electron (muon) based triggers. Details about this method and the related efficiency corrections can be found in [79] and [80]. For the soft lepton final state no unprescaled single lepton triggers are available with sufficiently low E_T thresholds, and E_T^{miss} based triggers with a

[43] In ATLAS, the data quality criteria are summarized in so called 'Good Run Lists' (GRL). The GRL ensures that all detector components were ready for data taking and operating within normal parameters. The GRL used is DetStatus-v36-pro10_CoolRunQuery-00-04-08 taken from the official ATLAS data preparation webpage [81].

[44] If a trigger fires more often than its rate-budget allows for, not every event is recorded. Instead, only each nth event that fires the trigger is written to tape, and n denotes the prescale factor for this specific trigger.

[45] For the muon channel, an additional muon + jet trigger (L1J10) is used to recover some inefficiencies of the pure single muon trigger

[46] For sufficiently small values of $m_{1/2}$, the W boson in the $\tilde{\chi}_1^{\pm} \rightarrow \tilde{\chi}_1^0 W$ decay turns virtual, which substantially softens the W boson decay products. However, given the exclusion limits shown in figure 6, this region is almost completely excluded by previous experiments. In addition, the chargino itself is not produced at rest, as it arises from a squark decay, which leads to an additional boost of the final state.

Periods	Data	Monte Carlo
	Electrons	
B-J	EF_e20_medium	EF_e20_medium + rescaling
K	EF_e22_medium	EF_e20_medium + rescaling
L-M	EF_e22vh_medium OR EF_e45_medium1	EF_e22vh_medium1 + rescaling
	Muons	
B-I	EF_mu18	Reweighting
J-M	EF_mu18_medium,EF_mu18_L1J10	Reweighting
	Missing Energy	
B-I	EF_xe60_noMu	EF_xe60_noMu
J-K	EF_xe60_tight_noMu	EF_xe60_tight_noMu
L-M	EF_xe60_verytight_noMu	EF_xe60_verytight_noMu

Table 15: Triggers used in data and Monte Carlo simulation for all channels included in [73]. For the electron based triggers, a rescaling is applied on the Monte Carlo events to correct for the slight Monte Carlo mismodelling of the trigger efficiency as shown in figure 47. For the muon based triggers, no trigger is required in the Monte Carlo simulation, but the samples are reweighted to the trigger efficiencies measured in data.

threshold of 60 GeV are used instead.

6.2 Particle identification at ATLAS

The particle identification for the objects used in this analysis takes place in two steps. As a first step, candidate objects are reconstructed based on hits in the inner detector and energy deposits in the calorimeters. As a second step, quality criteria on these candidates are applied in order to increase the purity. In the following sections, a detailed description of how exactly physics objects are defined is given.

6.2.1 Electrons

Electrons are reconstructed based on energy deposits in the EM calorimeter, which are called clusters[47]. Tracks measured in the inner detector are matched to clusters, in order to reduce background from non charged particles [82][48]. For finding the seed cluster, a sliding window algorithm with a window size of 3×5 in units of 0.025×0.025 in η - ϕ space in the EM calorimeter - which corresponds to the granularity of the middle layer - searches for longitudinal towers with $E_T > 2.5$ GeV. Tracks with a minimal transverse momentum of 500 MeV are assigned to the cluster via

[47]The same clusters are used to define photon objects

[48]For η regions of $|\eta| > 2.5$ not covered by the inner detector, electrons are reconstructed based on clusters exclusively.

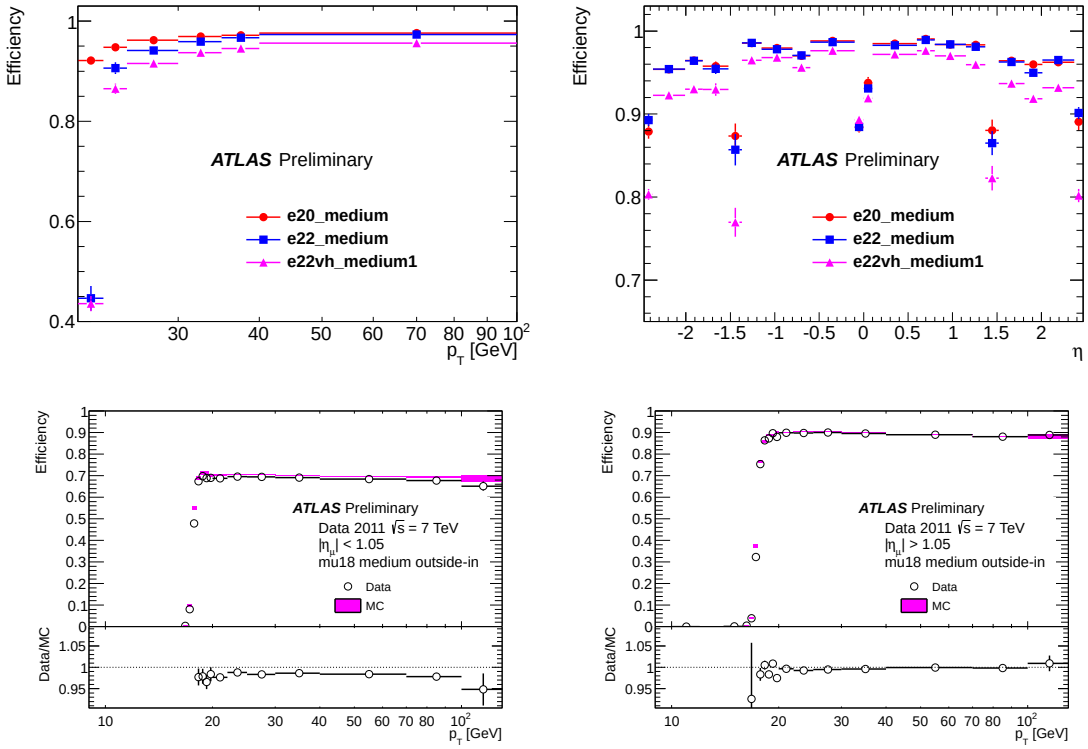

Figure 47: Trigger turn on curves with respect to the offline reconstructed leptons. Top left: Trigger efficiency for electron related triggers as a function of the offline electron transverse momentum. Top right: Trigger efficiency for electron related triggers as a function of the offline electron pseudorapidity [79]. Bottom left: Trigger efficiency for EF_mu18 in the barrel as a function of the offline muon transverse momentum. Bottom right: Trigger efficiency for EF_mu18 in the end caps as a function of the offline muon transverse momentum [80].

a loose spatial matching in $\Delta\eta$ and $\Delta\phi$. If at least one track points to an electromagnetic cluster, the combined object is reconstructed as an electron candidate. If more than one track points to a single EM cluster, the track with the smallest $\Delta R = \sqrt{\Delta\eta^2 + \Delta\phi^2}$ is assigned with the electron. After the matching, the final cluster is built based on the seed cluster, using 3×7 (5×5) longitudinal towers in the central (endcap) region. The energy for the final electron candidate is given by the cluster energy, while spatial information is taken from the matched track.

Based on these candidates, certain quality criteria on the cluster and track are imposed in order to decrease the misidentification probability. In addition, a relative calorimeter isolation is imposed to reduce the background arising from non prompt electrons. The exact criteria for the electrons used in this analysis are given in table 16. All preselected electrons are required to have a transverse momentum of at least 10 GeV with a pseudorapidity of smaller than 2.47 on cluster level. For the signal electron, the cut on the transverse momentum is raised to 25 GeV. The listed values correspond to the selection used for the *hard* lepton final states. The

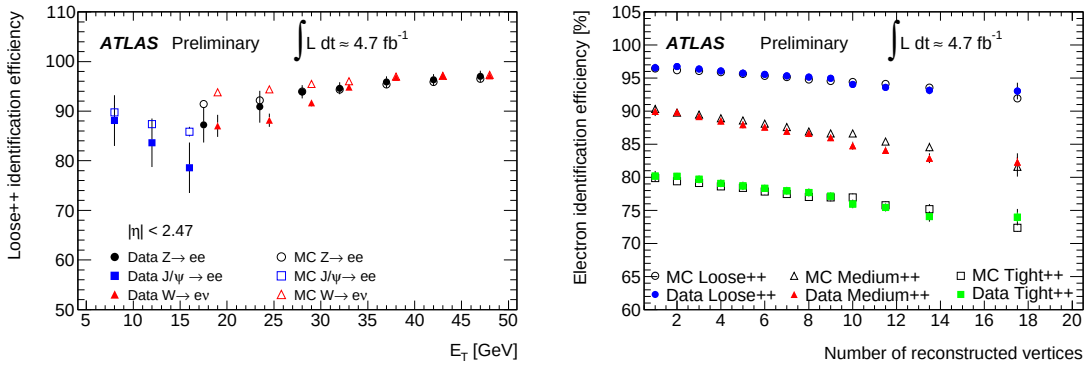

Figure 48: Left: Loose++ electron identification efficiency as a function of the electron transverse energy [84]. Right: Identification efficiency for various identification criteria as a function of the number of vertices [85].

values for the soft lepton analysis can be found in [83]. Exact definitions of electron quality criteria summarized as 'Loose++', 'Medium++' and 'Tight++' can be found in [82][49]. Preselected electrons are used to perform the overlap removal with jets, while signal electrons are used in the computation of inclusive variables like the transverse mass or effective mass.

Figure 48 exemplarily shows the Loose++ electron identification efficiency as a function of the electron transverse energy [84] (left) and the efficiency for various identification criteria as a function of the number of vertices [85] right. In the low energy regime, below transverse energies of roughly 15 GeV, the J/Ψ resonance was used to measure the Loose++ identification efficiencies of approximately 90%, while for higher E_T, vector bosons decaying into electrons were used to obtain an efficiency of roughly 95%. Given the complications for the track reconstruction due to additional vertices arising from multiple interactions, the identification efficiencies drop with the number of additional vertices. Furthermore, additional energy deposits from pileup distort the shower shapes in the calorimeter, which complicates the electron identification as well.

6.2.2 Muons

Muons are reconstructed using information from the muon systems and the inner detector using the `STACO` algorithm [86] [87][50]. In the muon system, regions of activity are identified in the RPCs and TGCs as a first step. Within each station, local segments are reconstructed in a second step. In the last step, the individual segments are combined in a global fit using hit information from the whole muon detector. Tracks reconstructed in the inner detector are combined with the tracks in the muon system using a χ^2 fit. Each combined muon with a sufficiently small

[49] More precise, the addition '++' refers to a slightly improved version of these quality criteria, which were optimized for a higher robustness against pileup. The cited note only covers the basic quality criteria without these additional improvements.

[50] There are also reconstruction algorithms available, which only use informations from the muon detectors and some algorithms, which include calorimeter information.

Criterium	Requirement
Preselected electrons	
Algorithm	AuthorElectron
Fiducial cuts	$p_T > 10$ GeV , $\lvert\eta^{cluster}\rvert < 2.47$
Electron quality	Medium++
Overlap with jets	electron removed if $0.2 < \Delta R(\text{jet}, \text{electron}) < 0.4$
Signal electrons	
Fiducial cuts	$p_T > 25$ GeV
Electron quality	Tight++
Calorimeter isolation	ptcone20/$p_T < 0.1$

Table 16: Quality criteria imposed to define the preselected and signal electrons for final states including high p_T electrons.

χ^2 is reconstructed as a muon candidate. The reconstruction efficiency for these muons were measured on data with a tag and probe method on $Z \rightarrow \mu\mu$ events [88]. Figure 49 shows the reconstruction efficiencies for muons, reconstructed with several algorithms, as a function of the transverse momentum and pseudorapidity. A flat reconstruction efficiency of roughly 95% with respect to the transverse momentum of the muon is achieved. For very central muons, the efficiency drops to approximately 60% due to the transition between the different muon detectors.

Given these candidates, further quality criteria are imposed as listed in table 17. All preselected muons are required to have a transverse momentum of at least 10 GeV with a pseudorapidity of $|\eta| < 2.4$. For the signal muon, the cut on the transverse momentum is increased to 20 GeV. Explicit cuts on the number of hits in the different components of the inner detector increase the quality of the track[51]. As for the electrons, an overlap removal is applied in order to avoid double counting of objects. In addition, an absolute track isolation - removing the muon track from the cone - is imposed to reduce backgrounds from non prompt muons.

6.2.3 Jets

Jets are reconstructed based on energy deposits in the calorimeters. Several algorithms can be used to form jet objects out of these energy depositions. The jets in this analysis are reconstructed using the `AntiKt4Topo` algorithm [89], which is based on topological clusters [90]. Topological clusters are formed from seed cells, which satisfy $|E_{cell}| > 4\sigma_{cell}$, where σ_{cell} refers to the RMS of cell energies for random events, which depends on the sampling and η position of the cell. Neighbouring cells fulfilling $|E_{cell}| > 2\sigma_{cell}$ are successively added to the topological cluster, until no fur-

[51] For the TRT, the number of outliers - hits, which can hardly be associated with the rest of the track - is required to be less than 10% of the total hits in the TRT. For the Pixel detector and SCT, the sum of numbers of holes - points, where a hit is expected due to the rest of the track, but none is found - are required to be smaller than 3.

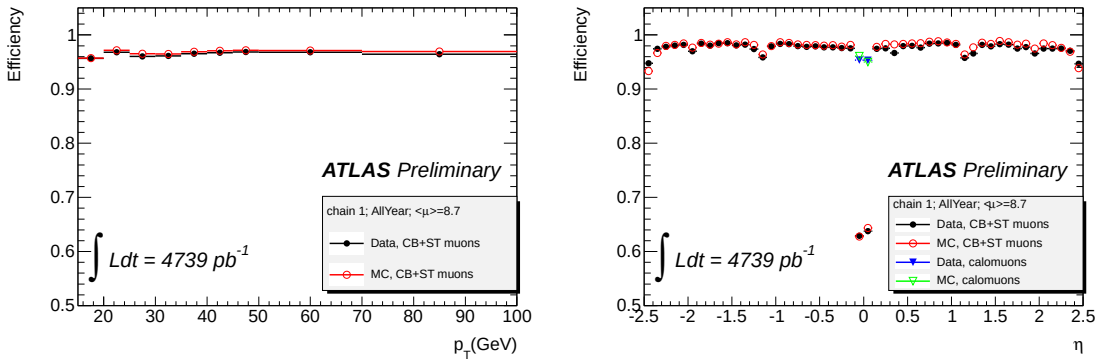

Figure 49: Reconstruction efficiency measured via tag and probe on $Z \rightarrow \mu\mu$ events for muons, reconstructed with several algorithms, as a function of the muon transverse momentum (left) and the pseudorapidity (right) [88]. 'CB' stands for combined, while 'ST' denotes the segment tagged algorithm. Results for the algorithm, adding calorimeter information, are shown as well.

ther cells satisfying this condition can be found. In a final step, all cells surrounding the topological cluster are added to the cluster as well, which improves the energy resolution of the cluster, as shown in single pion testbeam studies. All topological clusters in the event are used as input for the reconstruction algorithm as massless four vectors. The calibration scheme used to calibrate the jet energies is EM+JES, which takes the jets calibrated at the electromagnetic scale and adds a correction taking into account that the strong interaction of hadrons in the calorimeter differs from the electromagnetic interactions of electrons and photons.

Given these reconstructed jets, quality criteria are imposed to reduce certain sources of background like beam gas/halo events or electronic noise in the calorimeters. The exact definition is listed in table 18. The cut on the so called jet vertex fraction (JVF) [92] is designed to suppress jets arising from pileup. Figure 50 illustrates the idea behind this variable and how it is distributed for different types of jets. The JVF variable quantifies the probability for a jet to arise from the hard collision by associating the tracks, matched to this jet, to any reconstructed vertex. For jets with all associated tracks pointing to the primary vertex, a value of 1 for the JVF is assigned. For jets purely consisting of tracks pointing to secondary vertices, a value of zero for the JVF is assigned. If no track can be matched to the jet under consideration, a default value of -1 for the JVF is taken.
As for the electrons, preselected jets are used for the overlap removal, while signal jets are used to define the phase space regions and to compute inclusive event variables.

6.2.4 The missing transverse energy

The missing transverse energy is computed using all preselected objects in the event after overlap removal. In addition, all calorimeter clusters with $|\eta| < 4.9$ that are not associated to any of the reconstructed objects enter the calculation of E_T^{miss}. The

Criterium	Requirement
Preselected muons	
Algorithm	STACO (combined or segment tagged)
Fiducial cuts	$p_T > 10$ GeV , $\|\eta\| < 2.4$
Muon quality	Loose
Overlap with jets	muon removed if $\Delta R(\text{jet}, \text{muon}) < 0.4$
ID track quality	Number of pixel hits + number of crossed dead pixel sensors > 1 Number if SCT hits + number of crossed dead SCT sensors ≥ 6 Pixel holes + SCT holes < 3 ≥ 1 b-layer hit when it can be expected if $\|\eta\| < 1.9$: $n_{TRT} > 5$ and $n_{TRT}^{outliers} < 0.9 \times n_{TRT}$ if $\|\eta\| \geq 1.9$ and $n_{TRT} > 5$: $n_{TRT}^{outliers} < 0.9 \times n_{TRT}$
Signal muons	
Fiducial cuts	$p_T > 20$ GeV
Track isolation	$\sum p_T$ in ΔR cone of $0.2 < 1.8$ GeV

Table 17: Quality criteria imposed to define the preselected and signal muons for final states including high p_T muons.

algorithm used to reconstruct the missing transverse energy in this analysis is called `Simplified20_RefFinal`, which is a modification of the default reconstruction algorithm `RefFinal` [98]. Figure 51 shows the resolution of the missing transverse energy in both components of the transverse plane as a function of the total energy in the event, measured on $Z \rightarrow \ell\ell$ events at a center of mass energy of 7 TeV and computed on W boson Monte Carlo simulation [99].

6.2.5 Heavy flavor tagging

As described in chapter 4.5, the main backgrounds for a supersymmetry search with one lepton, jets and missing transverse energy are top quark pair production and W boson production. Later in this chapter, the Monte Carlo modelling of these processes will be studied and corrections will be extracted from data if necessary. For this purpose, it is mandatory to separate the phase space into a region enriched with top quark pair production and a region dominated by events including a W boson. This separation is based on the fact, that top quark pair production always yields two bottom quarks in the final state produced in the $t \rightarrow Wb$ decay. The bottom quark forms a B-meson in the hadronization process, which decays CKM suppressed into mesons containing an up or charm quark and therefore has a significantly longer lifetime than mesons built of light quarks.

Several algorithms exist, which exploit the kinematic differences between heavy and light flavoured meson decays. In this analysis, a neural network based tagger called `jetFitterCombNN` is used to separate jets including heavy flavour quarks from jets made of light flavour quarks. The tagging efficiencies, light flavour rejections and

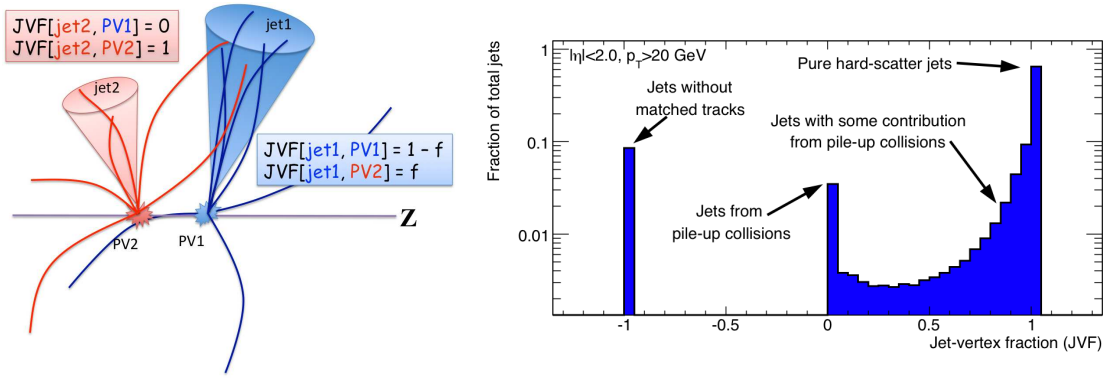

Figure 50: Left: Illustrative definition of the JVF variable. Right: Distribution of JVF for jets arising from the hard collision and pileup [93].

Criterium	Requirement
Preselected jets	
Algorithm	AntiKt4Topo
Fiducial cuts	$p_T > 20$ GeV , $\|\eta\| < 2.5$
Jet Quality	veto events with at least one loose bad jet [91]
Jet vertex fraction	JVF [92] > 0.75
Overlap with electrons	jet removed if $\Delta R(\text{jet}, \text{electron}) < 0.2$
Calibration	EM + JES
Signal jets	
Fiducial cuts	$p_T > 25$ GeV

Table 18: Quality criteria imposed to define the preselected and signal jets. The cut on the jet Vertex Fraction (JVF) suppresses the backgrounds arising from pileup [92].

their uncertainties for the relevant jet momentum regime were measured and validated on data [101] [102]. The operation point of 1.8 used in this analysis yields a b-tagging efficiency of roughly 60% with a light jet rejection of about 300. The Monte Carlo simulation is corrected to match the tagging efficiency measured in data.

6.2.6 Monte Carlo corrections and technicalities

Within the ATLAS collaboration, dedicated performance groups are responsible to optimize and update the object reconstructions, in order to cope with the current LHC run conditions. In addition, efficiencies, resolutions and - if necessary - corrections, are measured by these groups. For this analysis, the object definitions and corrections were implemented using the `SUSYTools` package [106] in version 00-00-61, which combines recommendations from various performance groups regarding the objects used in this analysis. All packages used to define the objects and apply corrections are listed in Appendix B. For all objects used, the corresponding corrections regarding efficiencies, energy scales and resolutions are applied on the Monte Carlo simulation in order to match data.

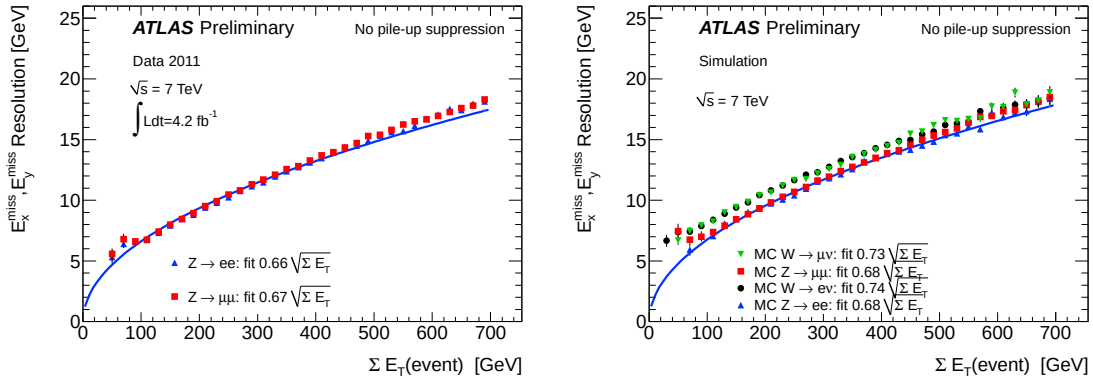

Figure 51: Resolution of the E_x^{miss} and E_y^{miss} as a function of the total energy in the event, measured on $Z \rightarrow \ell\ell$ events (left) and computed on W boson and Z boson Monte Carlo simulation (right) [99]. The total energy is evaluated by summing over all muons and the energy in the calorimeters.

6.3 Signal region selection

In this chapter, the phase space regions selected to enrich supersymmetric signals in various final states are discussed. Independent of the number and momentum of leptons in the final state, some requirements, not yet covered by the data quality criteria applied via the GRL, are common for all analyses. Furthermore, some additional corrections of the Monte Carlo simulation are introduced.

6.3.1 Preselection

The preselection is common to all signal regions and background control regions discussed in later in chapter 6.4.1

1. **Vertex Requirements**
   Each selected event is required to have at least one reconstructed primary vertex with at least five tracks associated to it. The primary vertex must be consistent with the beamspot position. If more than one vertex fulfills these criteria, the vertex with the highest scalar sum of associated squared transverse track momenta is taken as the primary vertex [95].

2. **Calorimeter Requirements**
   In April 2011, an incident lead to a loss of several front end boards (FEBs) in the LAr calorimeter. The region is located at $0.0 < \eta < 1.4$ and $-0.8 < \phi < -0.6$ and corresponds to roughly 0.4% of the total cells. In order to deal with this problem, a veto technique was developed [96]. Briefly summarized, if a jet points into this η-ϕ region, the veto first estimates the total energy in the LAr hole by using the energy deposits of the surrounding cells. If the loss of transverse energy per jet is higher than 10 GeV and contributes more than 10% to the total missing transverse energy, the event is rejected. For all signal regions an efficiency loss of below 0.5% due to the veto is observed for the supersymmetric signal processes and standard model backgrounds.

3. **Pileup Reweighting**
   As the average number of interactions per bunch crossing simulated in the Monte Carlo does not perfectly agree with the one that corresponds to the instantaneous luminosity of the recorded data, a reweighting is applied to match the run conditions given for each data period analyzed in this thesis.

4. **Cosmic Muon Veto**
   In order to suppress events arising from cosmic muons, a cut on the longitudinal impact parameter of $|z_0| < 1$ mm and transverse impact parameter of $|d_0| < 0.2$ mm with respect to the primary vertex is applied to all preselected muons. If at least one muon does not fulfill at least one of these requirements, the event is rejected.

6.3.2 Event variables

Some inclusive variables, which grant separation power between supersymmetric signals and standard model backgrounds are defined in the following. The transverse mass was already briefly introduced in chapter 5 and is defined as

$$m_T = \sqrt{2p_T^{\text{lepton}} E_T^{\text{miss}} [1 - \cos(\Delta\phi(\text{lepton}, E_T^{\text{miss}}))]} \tag{54}$$

It describes the transverse projection of the invariant mass of the missing energy and the lepton momentum. The variable is especially important for backgrounds where the missing energy arises from a single neutrino like W boson production or semileptonic top quark pair production. For these processes, the missing energy and the lepton are produced in a 2 body decay of the W boson and m_T therefore has an endpoint at m_W, due to events where the W boson decays completely in the transverse plane[52]. For signal events, always at least two exclusively weakly interacting particles are produced, and therefore m_T cannot be associated with a single particle decay into a solely weakly interacting particle and a lepton.

The second inclusive variable of interest is the effective mass (m_{eff}), which is a measure of the total mass produced in a collision event and defined as

$$m_{\text{eff}} = p_T^{\text{lepton}} + E_T^{\text{miss}} + \sum_{k=1}^{N} p_{T,k}^{\text{jet}} \tag{55}$$

The sum runs over the N leading jets in the events and N depends on the final state of interest. The amount of jets included in the effective mass is usually equal to the number of explicitly selected jets in the event. However, for some cases, the effective mass includes *all* signal jets present in the event. In this case, the variable will be denoted as m_{eff}^{incl}. In the following, the scalar sum of the jet transverse momenta and the lepton transverse momentum are summarized as H_T and m_{eff} can be written as

[52] Due to the detector resolution, the transverse mass can have values above the mass of the W boson and the endpoint is washed out.

$H_T + E_T^{\text{miss}}$[53].

A loose kinematic preselection is applied to study the Monte Carlo modelling of the backgrounds in the relevant phase space regions, as given in table 19. As the search targets final states with jets, missing transverse energy and exactly one charged isolated lepton, a cut on the jet multiplicity of at least three jets and exactly one lepton is applied, similar as for the dedicated control regions defined in 6.4.1. In addition, a loose cut on the missing transverse energy of at least 30 GeV is applied, in order to reduce the background arising from QCD.

The left panels of figure 52 and 53 show the most important distributions, which will be used to define the background control regions in chapter 6.4.1, in order to study any mismodelling affecting the agreement of data with Monte Carlo simulation in the dedicated control regions. Cleary for both lepton flavours, a mismodelling of the missing transverse energy, lepton transverse momentum and transverse momentum of the reconstructed W boson is observed. Similar observations were made for Z boson events, generated with the AlpGen generator [83], and the discrepancy was determined to be caused by a mismodelling of the vector boson transverse momentum on generator level. In order to correct for this discrepancy, a data driven reweighting technique - which will be subject of the following chapter - was applied as described in detail in [83].

6.3.3 Reweighting of the vector boson transverse momentum

In the following chapter, the reweighting of the vector boson transverse momentum and its implications are discussed briefly. The method can be sketched as follows:

1. Select a phase space region enriched with $Z \rightarrow \ell^+\ell^-$ events and kinematics comparable to the region where the discrepancy is observed by requiring two charged leptons of opposite sign and same flavour and three jets with a transverse momentum of at least 25 GeV.

2. Split the Z boson Monte Carlo sample into 5 bins of *true* Z boson transverse momentum with a binning of 50 GeV in the range [0 GeV, 200GeV] and one inclusive bin for events with a Z boson transverse momentum above 200 GeV.

3. Fit the normalizations of each subsample to data using the distribution of the *reconstructed* Z boson transverse momentum.

4. As the fit tackles a slope discrepancy, and the total normalization is extracted from data as will be explained in chapter 7, the normalizations are extracted as *relative* normalizations with respect to the subsample with the lowest Z boson transverse momentum

The relative normalization factors derived by the fit are listed in table 20. As the mismodelling of the Z boson transverse momentum is caused by mismodelling of the

[53]In many other analyses, H_T only denotes the scalar sum of all jet transverse momenta, not taking the lepton into account.

Variable	Requirement
$n_{\text{lepton}} : p_T$	$1 : 25(20)$ GeV
$n_{\text{jet}} : p_T$	$\geq 3 : 80, 25, 25$ GeV
E_T^{miss}	> 30 GeV

Table 19: Loose preselection cuts, applied to study the Monte Carlo modelling for the major backgrounds for variables used to define the control regions. If the cuts differ between the electron and muon channel, the number for the muon channel is given in brackets.

True Z boson p_T	Extracted Scalefactor
0 - 50 GeV	1.0 (fixed)
50 - 100 GeV	0.893 ± 0.043
100 - 150 GeV	0.866 ± 0.056
150 - 200 GeV	0.737 ± 0.061
> 200 GeV	0.772 ± 0.079

Table 20: Fitted scale factors for Z+jet events binned in true Z boson p_T derived on the reconstructed Z boson p_T distribution.

initial state radiation, the same scale factors can also be applied to the W boson + jets Monte Carlo simulation[54]. Extracting this correction in Z boson events and applying it to the W boson Monte Carlo simulation has the advantage that the measured Z boson p_T does not depend on the jet energy scale, because the Z boson is reconstructed solely using information from the reconstructed electrons or muons. Extracting this correction in W boson events enforces the usage of E_T^{miss} in order to reconstruct the W boson transverse momentum. As the missing transverse energy is sensitive to the energy scale of the reconstructed jets, which is one of the major uncertainties for this analysis, large correlations between the jet energy scale and generator level mismodelling of additional jets would occur.

The right panels of figures 52 and 53 again show the missing transverse energy, the transverse momentum of the leading lepton and the transverse momentum of the reconstructed W boson *after* applying the scale factors from table 20 to the AlpGen W boson Monte Carlo. A clear improvement in all variables can be observed, justifying the correction method described above. For all further Monte Carlo expectations and related figures, the reweighting factors are always applied on the vector boson + jets simulation.

[54]This is an assumption, which does not hold precisely as the masses of the Z boson and W boson differ by roughly 11 GeV.

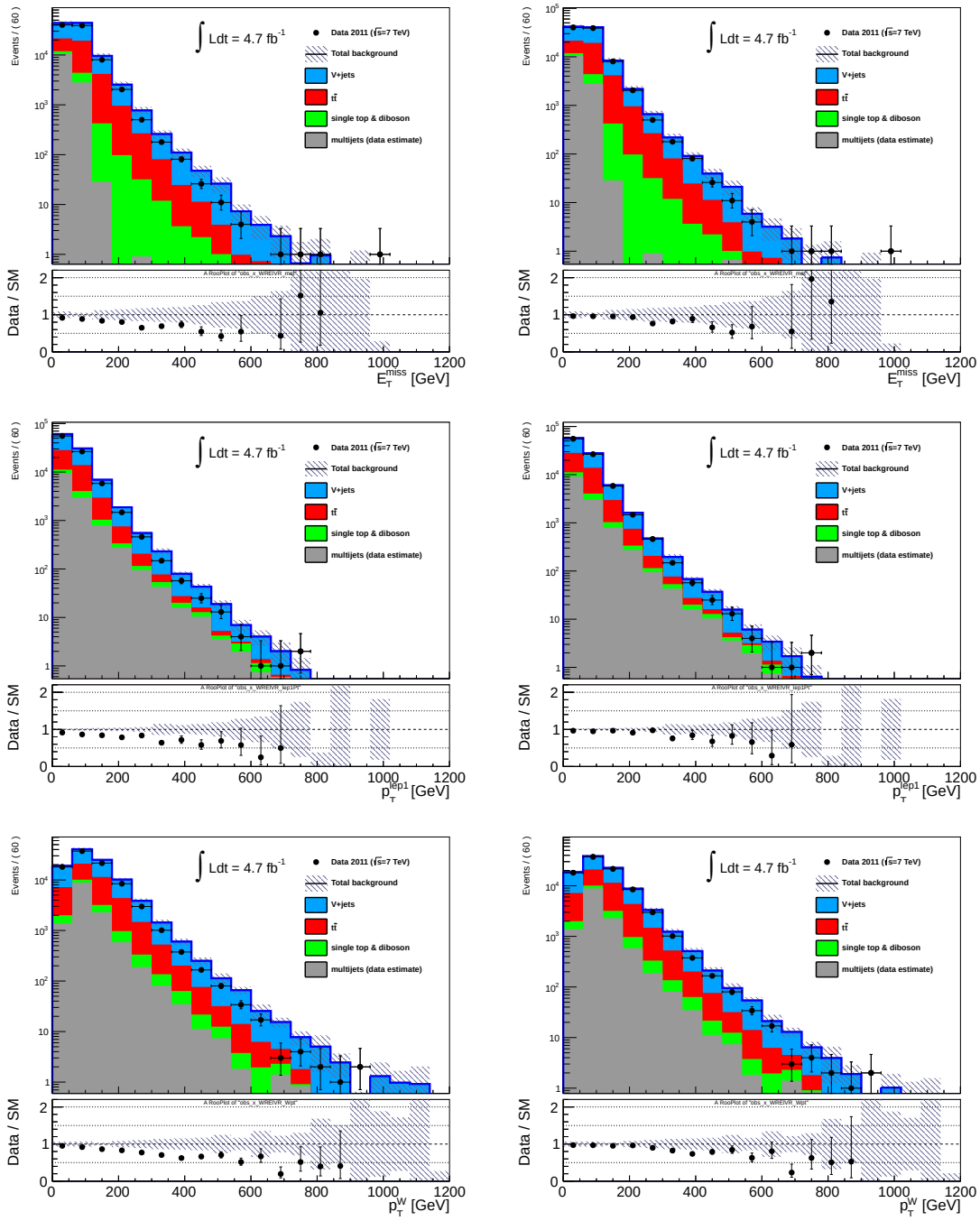

Figure 52: Basic kinematic variables after a loose signal like preselection as given in table 19 for the final state with exactly one isolated electron. The uncertainty bands cover all systematic uncertainties introduced in chapter 6.5. Left: Distributions without any correction regarding the true vector boson momentum. Right: Same distribution applying the correction factors listed in table 20 to the AlpGen vector boson + jets Monte Carlo Simulation.

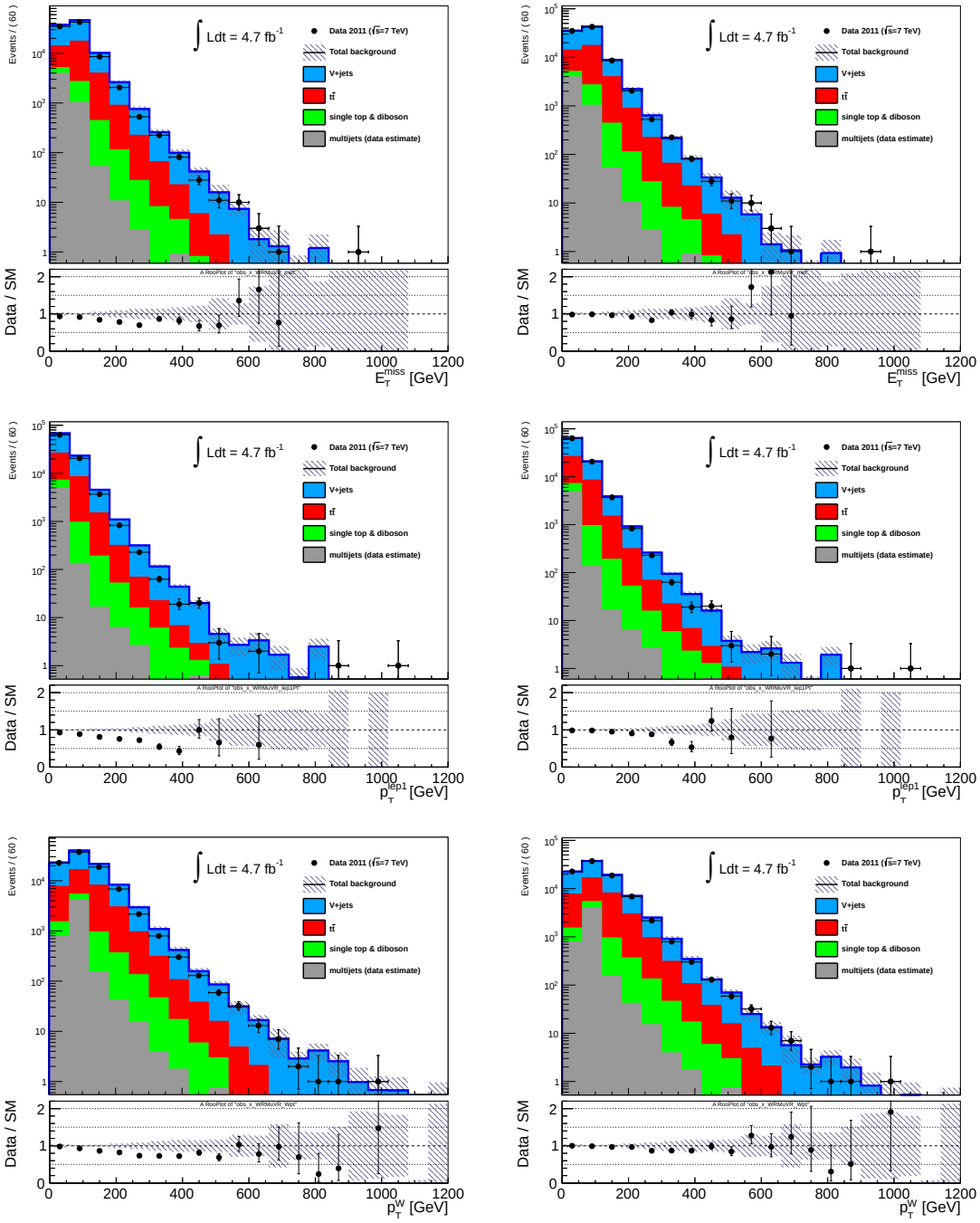

Figure 53: Basic kinematic variables after a loose signal like preselection as given in table 19 for the final state with exactly one isolated muon. The uncertainty bands cover all systematic uncertainties introduced in chapter 6.5. Left: Distributions without any correction regarding the true vector boson momentum. Right: Same distribution applying the correction factors listed in table 20 to the AlpGen vector boson + jets Monte Carlo Simulation.

Variable	3 Jet Signal Region	4 Jet Signal Region
$n_{\text{lepton}} : p_T$	1 : 25(20) GeV	1 : 25(20) GeV
$n_{\text{jet}} : p_T$	≥ 3 : 100, 25, 25 GeV , 4th jet $<$ 80 GeV	≥ 4 : 80, 80, 80, 80 GeV
E_T^{miss}	$>$ 250 GeV	$>$ 250 GeV
m_T	$>$ 100 GeV	$>$ 100 GeV
m_{eff}^{incl}	$>$ 1200 GeV	$>$ 800 GeV
E_T^{miss} / m_{eff}	$>$ 0.3	$>$ 0.2

Table 21: 3 and 4 jet signal regions for final states with exactly one hard electron or muon. If the cuts differ between the electron and muon channel, the number for the muon channel is given in brackets.

6.3.4 One hard lepton signal selection

As mentioned before, the final state with exactly one high p_T electron or muon primarily targets minimal supergravity and one step simplified models. In order to define phase space regions suited to grand a high sensitivity in a large parameter space of mSUGRA, an optimization was performed as described in [94]. As mentioned in chapter 4.2, the event topology depends quite strongly on the ratio between the gluino mass and the squark masses, which separates the mSUGRA parameter space into two different regions. In order to exploit this kinematic behaviour, two signal regions are defined. Each signal region is optimized for optimal discovery potential in *one* of these parameter regions.

For the parameter region with heavy squarks and a light gluino ($m_0 >> m_{1/2}$), a selection with at least four jets and a comparably soft cut on the missing transverse energy is imposed, taking into account the long 3 body cascade decays arising from $\tilde{g} \rightarrow \tilde{q}^* q$ decays in gluino pair production events. For the parameter region with light squarks and a heavy gluino ($m_0 << m_{1/2}$), a three jet selection with a harsh cut on $E_{\text{T}}^{\text{miss}}$ is applied, tailored to maximize sensitivity for squark-squark production events with subsequent 2 body decays into a quark and a weak gaugino. For both signal regions, a cut on the ratio of $E_{\text{T}}^{\text{miss}}$ and the effective mass proves to be useful, as - in contrast to the major standard model backgrounds - supersymmetric events are characterized by a large amount of missing energy compared to the jet activity, because the two LSPs carry a significant fraction of the total momentum in the event. In order to be orthogonal to the dilepton final state, a veto on a second lepton above 10 GeV is applied in addition to the listed cuts. The cut on the transverse momentum of the fourth leading jet in the 3 jet signal region is imposed in order to grant orthogonality to the 4 jet signal region. Table 21 summarizes the outcome of the optimization, which is also graphically shown in figure 54.

6.3.5 One soft lepton signal selection

The soft lepton analysis aims at supersymmetric models with compressed mass spectra, as realized for certain parameter regions of the simplified models introduced in

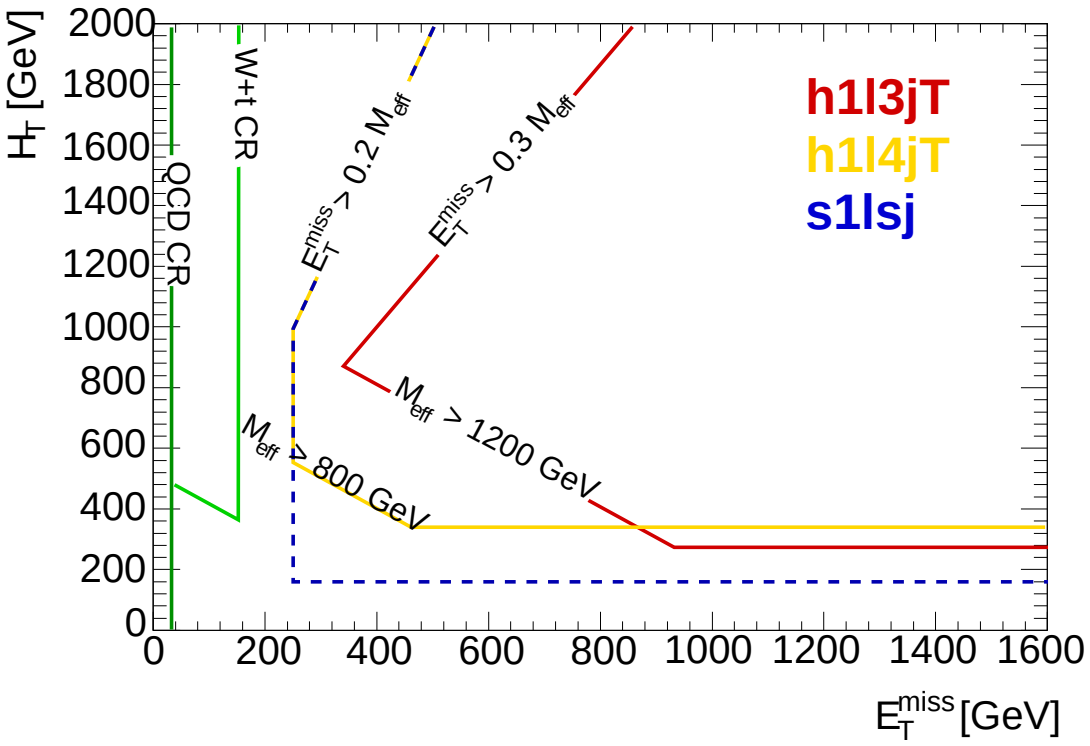

Figure 54: Cuts performed in the H_T - E_T^{miss} plane to improve the signal over background ratio in the various signal regions [83]. The red line denotes the 3 jet single lepton signal region, while the yellow line indicates the 4 jet single lepton signal region.

chapter 4.4. The exact phase space cuts, which define the signal regions are listed in table 22. More information is given in [83]. As for the hard single lepton final state, a veto on a second lepton is applied at 7 (6) GeV for electrons (muons).

6.3.6 Dilepton signal selection

The final state with two charged leptons is designed for high sensitivities in models with scalar leptons in the decay chains. As for the signal regions with one high p_T lepton, two search regions are defined in order to take the kinematic differences of squark and gluino production into account. The exact phase space cuts are given in table 23 and more information can be found in [104].

6.4 Background estimation

In order to improve the background prediction in the signal regions defined in chapter 6.3, data in several dedicated control regions is used. In this section, the phase space cuts to select relatively pure samples of a specific background will be introduced and the modelling of the Monte Carlo simulation will be studied. Detailed information on how the information gained in the control regions is used to correct for certain mismodellings will be the subject of chapter 7.

Variable	Soft Lepton Signal Region
$n_{\text{lepton}} : p_T$	1 : 7-25(6-20) GeV
$n_{\text{jet}} : p_T$	≥ 2 : 130, 25 GeV
E_T^{miss}	> 250 GeV
m_T	> 100 GeV
E_T^{miss} / m_{eff}	0.3

Table 22: Signal region for final states with exactly one soft electron or muon. If the cuts differ between the electron and muon channel, the number for the muon channel is given in brackets.

Variable	Dilepton 2 Jet Signal Region	Dilepton 4 Jet Signal Region
$n_{\text{lepton}} : p_T$	≥ 2 : 25(20), 10 GeV	≥ 2 : 25(20), 10 GeV
$n_{\text{jet}} : p_T$	≥ 2 : 200, 200 GeV	≥ 4 : 50, 50, 50, 50 GeV
E_T^{miss}	> 300 GeV	> 100 GeV
m_{eff}^{incl}	-	> 650 GeV
E_T^{miss} / m_{eff}	-	> 0.2

Table 23: 2 and 4 jet signal regions for final states with at least two high p_T charged leptons. If the cuts differ for electrons and muons, the number for muons is given in brackets.

6.4.1 Main backgrounds

As already mentioned, the main backgrounds for a supersymmetry search with jets, one lepton and missing transverse energy are leptonically decaying W bosons and top quark pair production. Backgrounds arising from leptonically decaying W bosons are characterised by an intermediate amount of missing energy and an electron or muon in the final state. For top quark pair production, additional two (four) jets emerge from the $t\bar{t} \rightarrow WWb\bar{b}$ ($t\bar{t} \rightarrow WWb\bar{b}$ + $W \rightarrow q\bar{q}$) decays if both (one) of the W bosons decay leptonically. As the search channels defined in section 6.3 imply at least three jets, the Monte Carlo simulation modelling is studied in a control region with a three jet requirement, in order to reduce uncertainties arising from extrapolating into the signal regions with respect to higher jet multiplicities.

The exact phase space cuts to investigate the Monte Carlo simulation modelling of these main backgrounds are given in table 24. The box cuts on E_T^{miss} and m_T reflect the kinematic of the W boson decay and are common for W boson production and top quark pair production. In addition, the signal contamination for the studied supersymmetry models is low due to the relatively tight upper cuts on the missing transverse energy and transverse mass, which grants orthogonality to the signal regions.

The shared phase space is separated into a top enriched (W enriched) region by

Variable	W Control Region	Top Control Region
$n_{\text{lepton}} : p_T$	$\geq 1 : 25(20)$ GeV	
$n_{\text{jet}} : p_T$	$\geq 3 : 80, 25, 25$ GeV	
n_{bTags}	0	≥ 1
E_T^{miss}	$\in$[40,150] GeV	
m_T	$\in$[40,80] GeV	
m_{eff}^{incl}	> 500 GeV	

Table 24: Control regions for W boson production and top quark pair production for final states with exactly one hard electron or muon. The number of b-tagged jets is estimated using the tagger described in [101]. Only the leading three analysis jets are taken into account for the b-tagging decision. If the cuts differ for the electron and muon channel, the cuts for the muon channel is given in brackets.

asking for one (no) b-tagged jet(s) among the leading three signal jets. A common cut on the inclusive effective mass - as also present in the signal regions - is imposed to decrease extrapolation uncertainties in this variable. All control regions are chosen to be orthogonal to the signal regions. Both types of regions being statistically independent ensures that corrections extracted in the control regions are not biased by data events, which are present in the signal regions.

Figure 55 shows the effective mass distribution - which is the most important variable to extrapolate into the signal region for all fit configurations discussed in chapter 7 - in the W control region and top control region without the explicit cut on $m_{\text{eff}}^{\text{incl}}$, separated for the single electron and single muon final states. In contrast to figures 52 and 53, the splitting into subsamples with a fixed number of additional partons calculated in the matrix element is shown for the Monte Carlo simulation for top quark pair production. While the agreement between data and Monte Carlo simulation is reasonable for W boson events, a severe discrepancy in the effective mass is observed for top quark pair production events, which is not dependent on the flavour of the leading lepton. For values of $m_{\text{eff}}^{\text{incl}}$ below approximately 400 GeV - where the samples with a low number of additional final state legs dominate - data overshoots the simulation by roughly 5-10%, while at high values of $m_{\text{eff}}^{\text{incl}}$ - where significant contributions from samples with a high number of additional final state legs occur - data is below the Monte Carlo simulation by up to 50%.

The source of this discrepancy is further disentangled by studying the the transverse momenta of the individual jets, which enter the effective mass, as shown in figures 56 and 57[55]. The same trend is observed in all jet momenta for both lepton flavours. As the effective mass - and therefore the jet momenta - is used to define the

[55]In addition, the lepton transverse momentum and the missing transverse energy enter the inclusive effective mass. However, as the box cuts on E_T^{miss} and m_T restrict the phase space quite substantially, the impact of these variables on $m_{\text{eff}}^{\text{incl}}$ is rather small. Furthermore, potential additional jets can enter the effective mass, but they also have a smaller impact compared to the leading four jets.

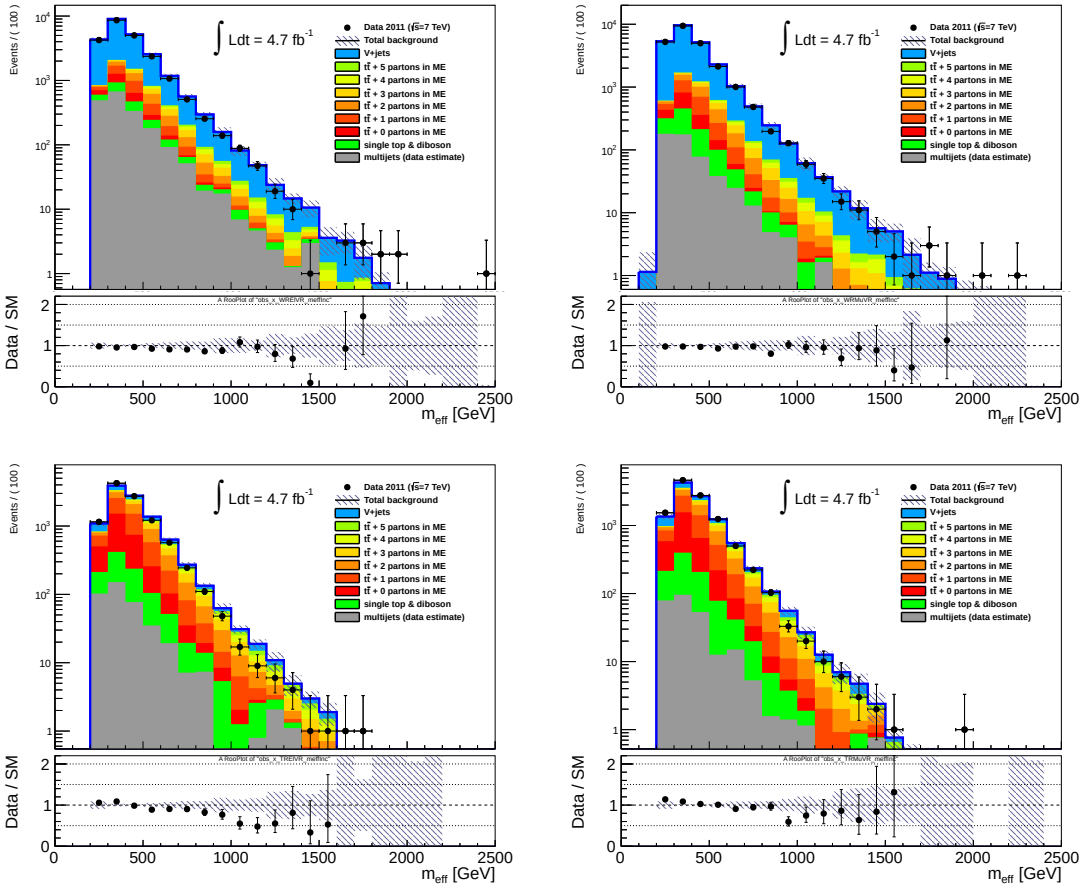

Figure 55: Inclusive effective mass in the control region for W boson production (top) and top quark pair production (bottom), separated for events with exactly one hard electron (left) and one hard muon (right). The error bands cover all systematic uncertainties as discussed in chapter 6.5.

signal regions as shown in table 21, a good description of $m_{\text{eff}}^{\text{incl}}$ is essential in order to obtain a reliable background prediction in the signal regions and a correction is necessary, which will be discussed and validated in chapter 7. As already announced in chapter 5.2, one of the key components of the combined fit is to fit the individual cross sections of the subsamples with a fixed number of additional final state partons for vector boson + jets und top quark pair production in particular. As these different samples populate different parts of the $m_{\text{eff}}^{\text{incl}}$ distribution and jet momenta distributions - as presented in figures 55, 56 and 57 - the observed discrepancy is compatible with a variation of the renormalization scale.

For the final states with one soft electron or muon - as listed in table 22 - and final states with two leptons defined in table 23, dedicated control regions for the major backgrounds are defined as well as shown in table 25. For the regions including a requirement on the number of b-tagged jets, only the two selected jets are examined for the b-tag for the soft lepton final state, while also a potential third jet is checked for the b-tag for the dileptonic final state.

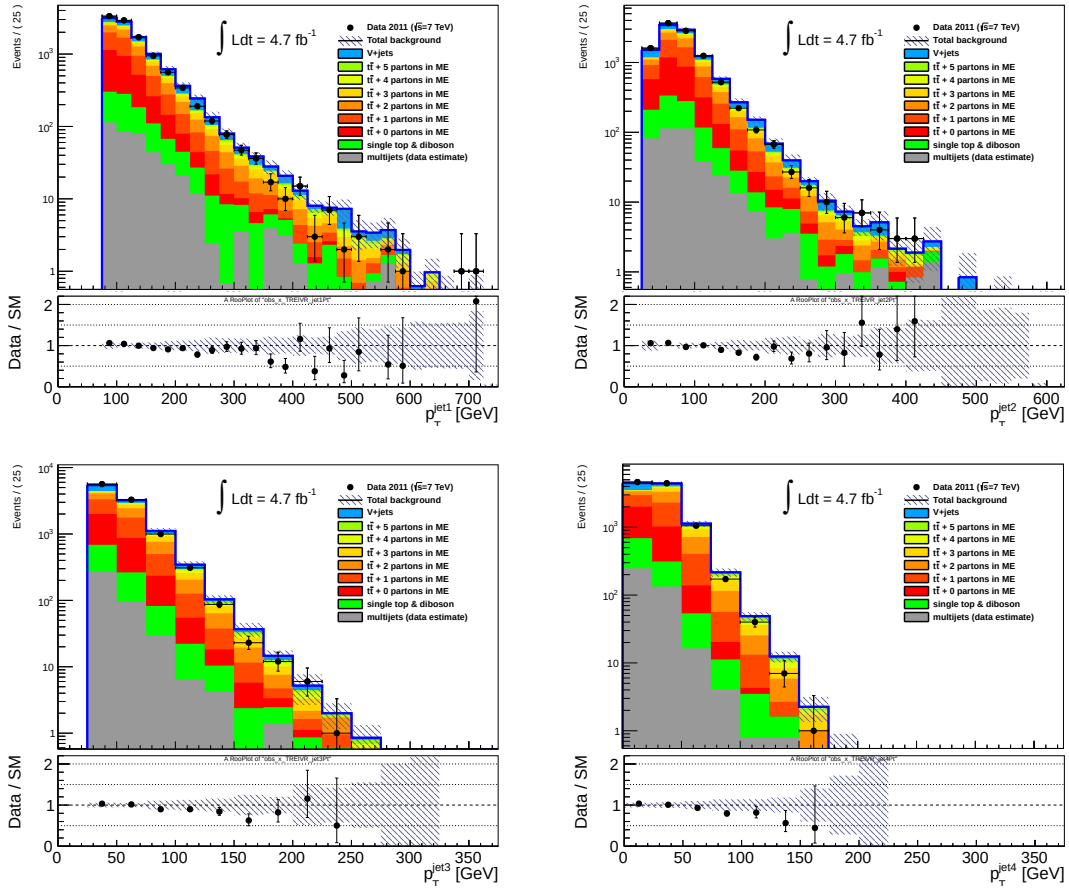

Figure 56: Jet transverse momenta in the top control region without an explicit cut on $m_{\text{eff}}^{\text{incl}}$ for the single electron channel. The error bands cover all systematic uncertainties as discussed in chapter 6.5.

6.4.2 Minor backgrounds

Minor backgrounds are composed of single top production and diboson events. The corresponding generators and cross sections are listed in table 10. These backgrounds are not estimated using data, but purely taken from Monte Carlo simulation.

6.4.3 QCD

The QCD multijet background is estimated using a data driven matrix method described in detail in [105]. The data driven approach is necessary because of the small Monte Carlo samples for QCD dijet production (compared to the huge cross section) and the difficult modelling of fake lepton efficiencies.

The method sketched in this chapter is based on a tight and loose sample in terms of lepton identification quality. The tight sample is supposed to contain true charged leptons, whereas the loose sample contains mostly lepton fakes arising from misidentified jets. The number of events for the loose sample, which also pass the tight selection cuts can be written as

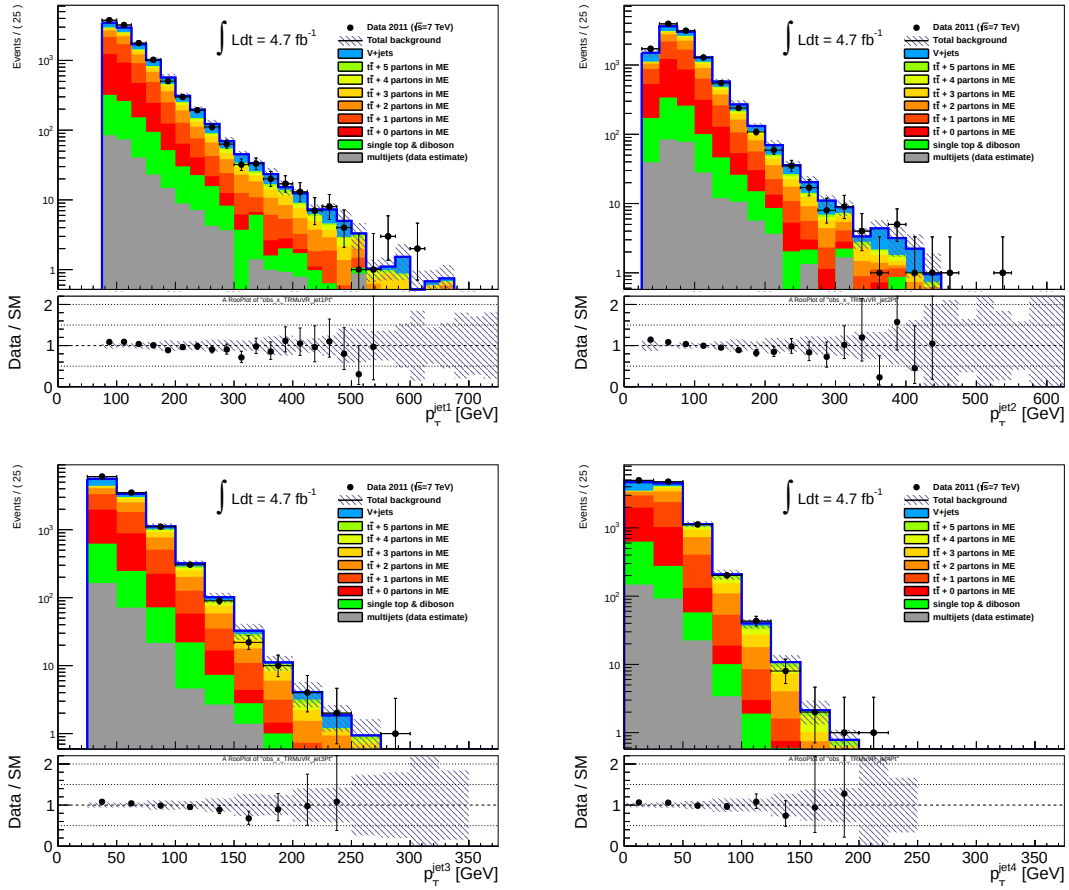

Figure 57: Jet transverse momenta in the top control region without an explicit cut on $m_{\text{eff}}^{\text{incl}}$ for the single muon channel. The error bands cover all systematic uncertainties as discussed in chapter 6.5.

$$N_{\text{pass}} = \epsilon_{\text{fake}} N_{\text{fake}} + \epsilon_{\text{real}} N_{\text{real}} \tag{56}$$

while the number of QCD events for the loose sample, which do not pass the tight selection cuts is expressed like

$$N_{\text{fail}} = (1 - \epsilon_{\text{fake}}) N_{\text{fake}} + (1 - \epsilon_{\text{real}}) N_{\text{real}} \tag{57}$$

where N_{fake} (N_{real}) describes the number of events with a fake (real) lepton in the loose sample. ϵ_{fake} and ϵ_{real} denote the efficiencies for a fake lepton and a real lepton to survive the tight selection. They are defined as

$$\epsilon_{\text{fake}} = \frac{N_{fake}^{tight}}{N_{fake}^{loose}} \tag{58}$$

$$\epsilon_{\text{real}} = \frac{N_{real}^{tight}}{N_{real}^{loose}} \tag{59}$$

and depend on the lepton transverse momentum and pseudorapidity. N_{fake}^{tight} (N_{fake}^{loose}) denotes the number of fake leptons passing the tight (loose) selection, and N_{real}^{tight}

	Control Regions			
	Soft lepton		Dilepton	
Variable	W Boson	Top Quark	Z Boson	Top Quark
$n_{\text{lepton}} : p_T$	≥ 1 : 7-25(6-20) GeV		≥ 2	
$n_{\text{jet}} : p_T$	≥ 2 : 130, 25 GeV		≥ 2 : 80, 50 GeV or ≥ 4 : 50, 50, 50, 50 GeV	
n_{bTags}	0	≥ 1	-	≥ 1
E_T^{miss}	$\in$[180,250] GeV		< 50 GeV	$\in$[30,80] GeV
m_T	$\in$[40,80] GeV		-	
$m_{\ell\ell}$	-		$\in$[81,101] GeV	< 81 GeV or > 101 GeV

Table 25: Control regions for W boson production, Z boson production and top quark pair production for final states with exactly one soft lepton or two leptons.

(N_{real}^{loose}) the number of real leptons passing the tight (loose) selection. These efficiencies are measured in specific control regions:

1. $\epsilon_{\textbf{real}}$
   This efficiency is measured using a tag and probe method on $Z \rightarrow \ell^+\ell^-$ events. The leptons arising from Z boson decays cover most of the momentum regime of interest.

2. $\epsilon_{\textbf{fake}}$ **for electrons above 25 GeV**
   A control sample is defined using a single electron trigger and asking for at least one loose electron. In addition, one jet above 30 GeV must be present in the event and the missing transverse energy is restricted to values lower than 30 GeV, in order to suppress real leptons arising from W boson decays. This sample has a high fraction of QCD dijet events, where one jet fakes a loose electron and the other jet is reconstructed properly as a hadronic jet. The exact values of $\epsilon_{\textbf{fake}}$ are measured as a function of the electrons pseudorapidity and transverse momentum and range from roughly 32% for very low p_T electrons to roughly 12% for electrons with a high transverse momentum.

3. $\epsilon_{\textbf{fake}}$ **for muons above 20 GeV**
   A control sample is defined using a single muon trigger and requiring at least one muon to satisfy the loose selection criteria. Furthermore, exactly one muon is asked to fulfill $|d_0/\sigma_{d_0}| > 5$, where d_0 denotes the transverse impact parameter and σ_{d_0} its total uncertainty. In addition, one jet with at least 60 GeV of transverse momentum must be present in the event. Again, the control sample is enriched with QCD dijet events, where one jet is associated to the muon and the other one reconstructed as a proper jet. The fake efficiency ranges from roughly 35% for very low p_T muons to roughly 22% for muons above 50 GeV.

More information can be found in [105]. Given these efficiencies, the number of fake leptons surviving the tight selection can be estimated using:

$$\begin{pmatrix} N_{loose} \\ N_{tight} \end{pmatrix} = \begin{pmatrix} 1/\epsilon_{fake} & 1/\epsilon_{real} \\ 1 & 1 \end{pmatrix} \begin{pmatrix} N_{fake}^{tight} \\ N_{real}^{tight} \end{pmatrix} \tag{60}$$

where N_{tight} (N_{loose}) denotes the number of observed leptons passing the tight (loose) selection. Solving for N_{fake}^{tight} finally yields

$$N_{fake}^{tight} = \epsilon_{fake} \frac{\epsilon_{real} N_{fail} - (1 - \epsilon_{real} N_{tight})}{\epsilon_{real} - \epsilon_{fake}} \tag{61}$$

which allows to calculate the number of fake leptons passing the tight lepton selection in various regions of phase space. This matrix method is implemented in the `FakeLeptBkg` package [117] and version 00-00-06 was used to estimate the QCD contribution in all control and signal regions.

6.5 Systematic uncertainties

In this section, all relevant systematic uncertainties will be briefly discussed qualitatively. Technical details about how they are incorporated in the combined fit will be discussed in chapter 7.3.

6.5.1 Luminosity uncertainty

A variation of the total integrated luminosity displays itself in a variation of the event yields for all physics processes, as described in equation 42. The total uncertainty on the integrated luminosity for the whole 2011-dataset is 3.8% [33] and measured via vdM-scans, as discussed in chapter 3.2.1.

6.5.2 Jet related uncertainties

1. **jet energy scale and resolution**
   The jet energy scale (JES) systematic uncertainty denotes the uncertainty on how the parton energy translates into the jet energy measured in the ATLAS calorimeter. It includes several uncertainties like the choice of the hadronization model, the underlying event modelling, the impact of calorimeter noise thresholds and uncertainties on the exact knowledge of the ATLAS material budget. It was measured using testbeam studies and dedicated Monte Carlo simulation samples [123] and validated via in situ techniques with collision data as described in [124] and [125] for example. The JES uncertainty is extracted as a function of the jet transverse momentum and pseudorapidity. The left plot in figure 58 shows the total systematic uncertainty and its breakdown into components for central jets as a function of the jet transverse momentum for the `AntiKt` algorithm with a distance parameter of 0.6. For the low momentum region below approximately 45 GeV, the total uncertainty on the jet energy scale is of the order of 4% and has sizeable contributions from all uncertainties that are taken into account. Between roughly 60 and 200 GeV, the uncertainty is at 2%, while it grows again up to almost 4% for the very high momentum region. For these momenta, the total uncertainty is by far dominated by the single particle response of the calorimeters. In order to estimate the impact of the jet energy scale uncertainty on the event yields, each jet is varied within its JES uncertainties up and downwards.

   For a given jet energy scale, the measured energies fluctuate around the central value, which is called the jet energy resolution. It was measured via different in situ techniques on data as described in [35]. As the jet energy resolution slightly differs in the Monte Carlo simulation and data, a small correction is applied to the jet energies in order to match the resolution measured in data. For the analysis presented in this thesis, the most recent recommendations from the dedicated ATLAS jet group were used [126] [127] [128].

2. **heavy flavour tagging uncertainties**
   As already mentioned in section 6.2.5, a heavy flavour tagger is used to obtain control samples for top quark pair production and W boson events. The

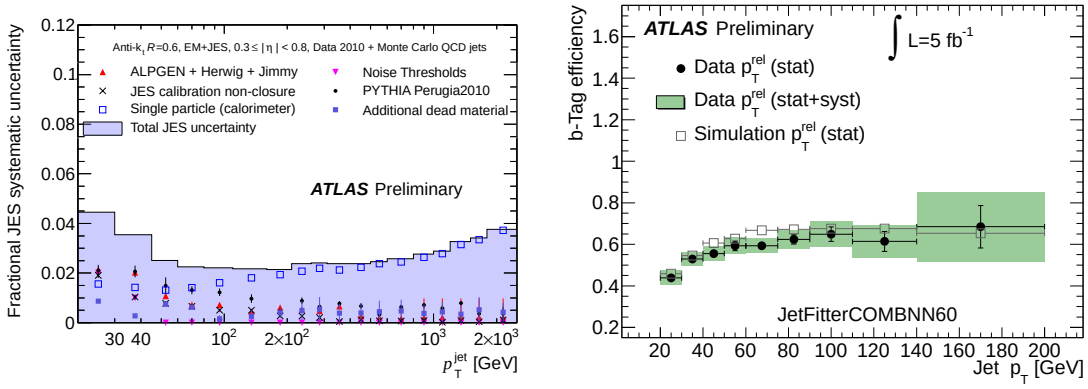

Figure 58: Major jet related systematic uncertainties. Left: total JES uncertainty for jets with R=0.6 as a function of the jet transverse momentum [123]. Right: B-tagging efficiencies for true b jets and their total absolute uncertainties as a function of the jet transverse momentum [102].

efficiency of the tagger used and the uncertainties on the measured efficiencies and light jet rejections are extracted on data as a function of the jet transverse momentum as described in [101] and [102]. As for the jet energy scale and resolution, the latest recommendation given by the dedicated combined performance group was used [129]. The right plot of figure 58 shows the measured b-tagging efficiencies and their total uncertainties as a function of the jet transverse momentum. Slight discrepancies in the tagging efficiency between Monte Carlo simulation and data are corrected by rescaling the Monte Carlo events using the tagging efficiency measured in data. The impact of the b-tagging efficiency uncertainty is estimated by varying the tagging efficiency and light jet rejections up and downwards within its uncertainties.

6.5.3 Lepton related uncertainties

1. **lepton energy scale and resolution**
   As for the jets, the energy scales, resolutions and corresponding uncertainties for electrons and muons were estimated by dedicated performance groups [135] [88] and these recommendations were used in the analysis [130] [131]. Figure 59 shows the invariant dielectron mass and dimuon mass obtained on $Z \rightarrow \ell^+\ell^-$ events. While the electron energy resolution is roughly at 1.6 GeV (2 GeV) for central (endcap) electrons, the muon momentum resolution is at approximately 2.5 GeV over the whole range in pseudorapidity. As for the jet energy resolution, a slight discrepancy between the measured resolution and Monte Carlo simulation is corrected.

2. **lepton identification efficiencies**
   As discussed in sections 6.2.1 and 6.2.2, several identification criteria are imposed on the preselected leptons in order to suppress jets which are misidentified as leptons. The identification efficiencies and associated errors for the

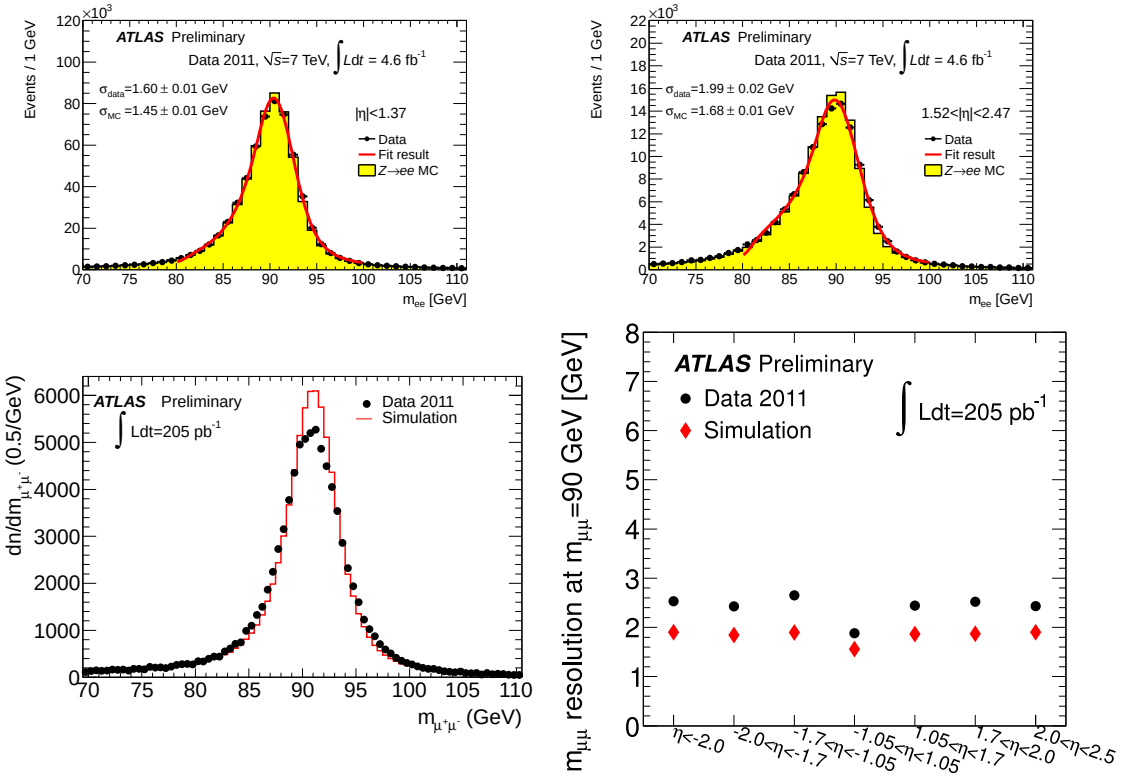

Figure 59: Electron and muon energy resolutions. Top: Reconstructed dielectron mass in $Z \rightarrow e^+e^-$ events for events, where both electrons are reconstructed in the barrel region (left) and in the endcap region (right) [135]. Bottom left: Reconstucted dimuon mass for $Z \rightarrow \mu^+\mu^-$ events, where both muons fulfill $|\eta| < 2.5$. Bottom right: Absolute dimuon invariant mass resolution in GeV for different pseudorapidities [88].

electron and muon identification requirements, as listed in tables 16 and 17, were also provided by the corresponding performance groups [131] [134].

Given figure 59, the impact of the lepton related uncertainties on the final result is expected to be rather small, as will be quantified in chapter 7.5.

6.5.4 Trigger related uncertainties

The trigger efficiencies are measured on data as shown in chapter 6.1 and the errors on these efficiencies, which are below 1% are used as a systematic uncertainty [79] [80].

6.5.5 Missing transverse energy related uncertainties

As the missing transverse energy is based on physics objects, all object related uncertainties listed above are propagated into the total uncertainty on the missing energy. In addition, the contribution of energy deposits not assigned to any of the analysis objects is varied within systematic uncertainties [99]. Furthermore, effects of pileup uncertainties are propagated to E_T^{miss} [132].

6.5.6 Theory uncertainties

All theoretical uncertainties discussed in chapter 5 are taken into account as systematic uncertainties. Details about how they are incorporated in the combined fit are given in the next chapter.

In addition, a dedicated systematic uncertainty related to the choice of the hadronization model was derived, comparing simulations for W boson production and top quark pair production with the *same* generator but *different* hadronization models [83] for phasespace regions relevant for supersymmetry searches [133]. The uncertainties in the single lepton signal regions are estimated to be of the order of 10-15%.

7 The combined fit

In this chapter, the combined fit, which is used to predict the background expectations in the signal regions and to quantify the agreement between data and simulation for various supersymmetric models will be discussed, starting with the statistical methods used. The technical implementation is done using the `HistFactory` [118] framework, which is based on `RooFit` [119] and `RooStats` [120].

7.1 Statistical methods

The combined fit is based on a maximum likelihood method described in [121] in detail. The main aspects of this test are sketched in this section, following the nomenclature and presentation as in [121]. The LLR test is based on the likelihood function, written as the product of several poisson probabilities

$$\begin{aligned} L(n, \theta^0 | \mu, b, \theta) &= P_{SR} \times P_{CR} \times P_{syst} \\ &= P(n_s | \lambda_s(\mu, b, \theta)) \times \prod_{i \in CRs} P(n_i | \lambda_i(\mu, b, \theta)) \times P_{syst}(\theta^0, \theta) \end{aligned} \tag{62}$$

where n_s (n_i) denotes the number of observed events in the signal (control) regions as defined in chapter 6.3. λ_s (λ_i) denotes the poisson expectations for the considered signal and various backgrounds. As the fit uses information from various control region, the total likelihood function is built of products of individual poisson probabilities, where 'i' sums over all control regions. The poisson expectations depend on the following parameters:

1. The background normalization factors b
2. Nuisance parameters parametrizing the systematic uncertainties θ
3. The signal strength μ, which equals zero for the background-only hypothesis and equals one for the nominal signal expectation for the model under consideration

The dependency of the poisson expectations as a function of these parameters can be expressed as

$$\lambda_s = \mu \cdot c_{s,SR}(\theta) \cdot s + \sum_j c_{j,CR}(\theta) \cdot b_j \tag{63}$$

$$\lambda_i = \mu \cdot c_{s,i}(\theta) \cdot s + \sum_j c_{i,j}(\theta) \cdot b_j \tag{64}$$

introducing the simulation based transfer factors $c_{i,j}$, which are responsible to extrapolate between different phase space regions defined as

$$c_{\text{process j,region i}} = \frac{n^{mc}_{\text{process j,region i}}}{n^{mc}_{\text{process j,region j}}} \times [1 + \sum_k \Delta_{ijk} \theta_k] \tag{65}$$

Here, region j for process j denotes the dedicated control region for the process j, if available. The effect of systematic uncertainties on the transfer factors is described in the last term, where Δ_{ijk} denote the kth systematic uncertainty for the process j

in region i.

The last term in equation 62 denotes the probability density function including systematic uncertainties. Here θ^0 denotes the nominal value of the systematic uncertainty considered.

Several fit configurations are performed for different purposes:

1. **Background-only fit**
   In this setup, no signal contamination in the control regions is assumed. Furthermore, the signal regions are excluded from the fit. In addition, all nuisance parameters related to the signal strength are also removed from the fit and no extrapolation of the background expectation into the signal regions is done. Therefore, only the agreement between data and a standard model hypothesis in the control regions is maximized.

2. **Discovery fit**
   In this configuration, still no signal contamination in the control regions is assumed, but the signal regions are taken into account in the fit. Therefore, the fit tests the standard model hypothesis in the signal regions and fits the absolute number of additional non standard model events in these regions. As no specific model is tested, the nuisance parameters for the signal cross section uncertainty and Monte Carlo statistical uncertainty for the signal is set to zero. Since no signal is considered in the control regions, the background estimate in the signal regions is conservative, because potential signal contamination in the control regions would lower the background prediction.

3. **Exclusion fit**
   This configuration tests the agreement between data and standard model expectation plus a *specific* model of new physics. The signal contamination in the control regions for this specific model is taken into account and the signal strength is set to one accordingly. In addition, all nuisance parameters related to the specific signal model are turned on in the fit.

   In order to exploit shape differences in the effective mass between standard model background and the tested supersymmetric signals, the signal regions listed in tables 21 - 23 are binned in variables, which grant additional separation power between signal and background, as shown in table 26. For this purpose, the explicit cut on the effective mass (the ratio of E_T^{miss} and m_{eff}^{incl}) for the hard lepton (soft lepton) final states is omitted.

7.2 The combined fit setup

In this section, the general fit configuration is discussed. As already presented in chapter 5, scale variations significantly influence the number of radiated partons

Signal Region	**Variable**	**Binning / Range**
Soft Lepton	E_T^{miss} / m_{eff}	6 Bins / [0.1, 0.7]
Hard Lepton + 3 Jets	m_{eff}^{incl}	6 Bins / [400 GeV, 1400+ GeV]
Hard Lepton + 4 Jets	m_{eff}^{incl}	4 Bins / [800 GeV, 1400+ GeV]
Dilepton + 2 Jets	m_{eff}^{incl}	5 Bins / [700 GeV, 1500+ GeV]
Dilepton + 4 Jets	m_{eff}^{incl}	5 Bins / [600 GeV, 1400+ GeV]

Table 26: Binning of variables used as inputs in the exclusion fit setup within the signal regions without the cut on m_{eff}^{incl} (E_T^{miss} / m_{eff}) for the hard lepton (soft lepton) final states. The last bin includes the overflow.

above a certain transverse momentum, which translates into a sizeable uncertainty on the effective mass and the missing transverse energy. As the transfer from control regions into the signal regions is dominantly done by extrapolating in the effective mass, the background predictions for vector boson production and top quark pair production strongly depend on the choice of the renormalization and factorization scale. It was argued in chapter 5.2 that scale uncertainties can be measured on data by extracting the cross sections for subsamples with a fixed number of additional partons calculated in the matrix element by fitting a distribution, which is sensitive to the number of additional partons like the jet multiplicity. In addition, as already mentioned in chapter 6, several channels with different lepton multiplicities and transverse momenta are combined, yielding a simultaneous estimation of shared backgrounds. Therefore, the following input information is used by the fit:

1. **Choice of input distributions**
   Given the control regions defined in chapter 6.4.1, the following channels are used to constrain the backgrounds arising from top quark pair production and vector boson production. In all cases, the number of reconstructed jets defined like in table 18 with a minimum transverse momentum of 25 GeV is used as the input distribution.

   (a) Hard Lepton control regions
   For both lepton flavors, a dedicated control region for top quark pair production and W boson production exists as listed in table 24, yielding four channels in total. In each control region, seven multiplicity bins ranging from three to nine jets are taken as the input distribution, where the minimal number of jets is motivated by the explicit three jet requirement used in the control region definition.

   (b) Soft Lepton control region
   Similar to the hard lepton final state, four channels are used in total with a slightly modified number of jet multiplicity bins, taking into account the explicit two jet requirement in the control region definition shown in table 25. Six bins ranging from two to seven jets are used as the input distribution.

(c) Dilepton control regions
For the same flavor channels (ee and $\mu\mu$), one control region for Z boson production and one control region for top quark pair production per channel is used as listed in table 25. For the mixed flavor final state, only a top control region is chosen[56]. Eight jet multiplicity bins ranging from two to nine jets are taken as input bins.

For all of these channels, the number of observed events, the nominal background expectations given by the Monte Carlo simulation as listed in table 10, and the nominal values of systematic uncertainties as will be discussed in chapter 7.3 are used as inputs.

2. **Choice of fit parameters**
The parameters are split into parameters, which are completely unconstrained and floated in the fit, and nuisance parameters, which describe systematic uncertainties and are constrained within the total input uncertainty.

(a) Floating Parameters
The normalizations for vector boson production samples and top quark pair production samples for a *fixed* number of additional partons calculated in the matrix element are fitted[57]. Given the explicit dijet requirement for the soft lepton and dilepton control regions, as listed in table 25, the normalizations for the subsamples for zero and one additional parton in the matrix element are fixed to the nominal value for W boson and Z boson production[58]. For top quark pair production, the normalizations for zero to exactly two partons in the matrix element are fitted. The samples with three to five partons in the matrix element are added up and fit with a single normalization factor[59]. In addition, the normalizations for the signal samples are fitted as well.

All floating parameters are *completely* unconstrained and the combined fit can vary them as much as necessary to fit data. Unconstrained pa-

[56] In principle, eμ final states can also occur in Z boson events via Z$\rightarrow\tau\tau$. However, given the low branching ratio and relevance for the eμ signal region, no dedicated control region for this process is defined.

[57] For the vector boson samples, dedicated Monte Carlo samples with additional one or two heavy flavor quarks exist. As for the light flavor samples, these processes are generated with an additional number of final state partons calculated in the matrix element. The heavy flavor samples with one (two) heavy flavor quarks and N additional final state partons calculated in the matrix element are combined with the light flavor samples with N+1 (N+2) additional final state legs. In order to avoid double counting of events, which are present in both types of samples, a heavy flavor overlap removal between the two classes of samples is performed [122].

[58] Fits with floating normalizations for these samples were performed for testing purposes. However, it turned out that after the dijet requirement not enough events were left for the fit to be sensitive to these normalization factors.

[59] Test configurations using separate normalization factors for top quark pair production with three, four and five partons in the matrix element were performed. It turned out that the number of events in the high jet multiplicity bins is not large enough to obtain sufficient sensitivity on the individual normalization factors.

rameters are denoted with a prefix of `mu_`.

(b) Nuisance Parameters
Beside these normalization factors, several systematic uncertainties are included in the fit configuration in form of nuisance parameters, as will be discussed in detail in chapter 7.3. In contrast to the normalization factors for the different parton subsamples, which are unconstrained, the nuisance parameters are constrained by a gaussian with a width that corresponds to the size of the uncertainty.

The estimate for QCD multijet production is taken from the matrix method described in chapter 6.4.3. Within each channel, the number of QCD events is constrained by the fit within the uncertainties given by the matrix method. In addition, for the background samples that are not fit like described above (vector boson with 0 and 1 additional partons calculated in the matrix element and all minor backgrounds) a nuisance parameter is assigned, which describes the total uncertainty on the normalizations. How these uncertainties are derived will be explained in detail in section 7.3

All gaussian constrained parameters are denoted with a prefix of `alpha_`. A value of zero for `alpha_` corresponds to the nominal value of the input systematic uncertainty, while the error on `alpha_` corresponds to the width of the gaussian, and a value of one corresponds to the 1σ uncertainty before fit. In addition to the gaussian constrained nuisance parameters, poissonian constrained nuisance parameters - describing the statistical uncertainty arising from the limited number of Monte Carlo events - are denoted with `gamma_`.

7.3 Treatment of systematic uncertainties

In this chapter, it will be explained how the systematic uncertainties - introduced in chapter 6.5 - are implemented in the combined fit. Depending on the source and physical meaning of the systematic uncertainty, several different implementations are used. If data does not allow for a full variation of some input uncertainties, the fit is allowed to constrain the corresponding nuisance parameters, which is called 'profiling' in the following.

1. **Overall Normalizations**
For this type of implementation, the systematic uncertainty under consideration is described by a global scale factor, fully correlated among all bins of the input distribution, while not affecting the shape of the distribution. The amount of allowed change in normalization is constrained by a gaussian with a mean of $1\pm\ \alpha$ and a width of $\sigma \cdot$ E, where E denotes the total input uncertainty and α and σ are fit parameters. The following systematic uncertainties are described by a global scale factor:

(a) Cross section uncertainties for the considered supersymmetric models.
This uncertainty is fully correlated between all input channels

(b) Uncertainties on lepton energy scales, resolutions and identification efficiencies.
For each type of lepton related uncertainties, lepton flavor and lepton multiplicity, an individual nuisance parameter is introduced.

(c) Uncertainties on trigger efficiencies.
For each type of lepton flavor and multiplicity, an individual nuisance parameter is introduced.

(d) MLM matching uncertainties for W boson + jets and top quark pair production in the signal regions.
The uncertainties are derived on generator level, using the samples introduced in chapter 5, by comparing the event yields between the nominal value of $p_T^{\text{min}} = 15$ GeV and the extreme case of $p_T^{\text{min}} = 30$ GeV. Due to the limited Monte Carlo statistics in the signal regions, these uncertainties are not calculated for each bin of the effective mass distribution as shown in table 26. For both types of processes (top quark pair production and W boson production), the uncertainties on the MLM matching cutoffs are correlated between all signal regions. The total change in the event yield, which is taken as the systematic uncertainty arising from variations of the MLM matching cutoff, is 12% (16%) for the top quark background in the three jet (four jet) signal region. For W boson production, the uncertainty is 19% (8%) in the three jet (four jet) signal region.

(e) Uncertainties on the normalizations of the W boson + jets and Z boson + jets samples binned as a function of the true Z boson or W boson transverse momentum as listed in table 20.
For a given vector boson true momentum sample, the nuisance parameters describing the uncertainty on the normalization for this sample are correlated between all control regions.

(f) Normalization uncertainties on the W boson and Z boson samples with zero or one additional parton calculated in the matrix element.
As already mentioned in section 7.2, the choice of control regions does not allow the fit to be sensitive on these parton multiplicity and the total scale uncertainty as calculated in chapter 5.1.1 is used as a systematic uncertainty. Each of the two resulting uncertainties is correlated among all regions.

(g) Normalization uncertainties of the minor backgrounds.
A conservative normalization uncertainty of 20% is assigned to all minor backgrounds taken from the Monte Carlo simulation, which are not floated in the fit. This uncertainty is correlated among all regions and contains for example the unertainty on the cross sections.

(h) Heavy flavor tagging efficiency uncertainties.
This uncertainty is only assigned to regions with a b-tagging requirement

or veto. All phase space regions are treated as correlated[60].

2. **Shape systematics including changes in normalization**
This type of implementation is used for systematic uncertainties that change the shape *and* normalization of the fit input distribution. Technically, two additional histograms are created, which correspond to the input distribution under consideration with an upward and downward variation of the specific systematic uncertainty. As also changes in the normalization are allowed, these additional histograms do not need to have the same integral as the nominal distribution. In the fitting procedure, a linear interpolation between the upward and downward varied histogram is performed, treating all bins as fully correlated. The fit parameters obey $\alpha \pm \sigma \cdot E_i$, where E_i denotes the total uncertainty in the ith bin, α absorbs the change in normalization and σ potentially constrains the input uncertainty in the ith bin. The following systematic uncertainties are implemented as this type of shape systematic:

   (a) Jet energy scale uncertainty.
   The JES uncertainty is separated into three components as a function of the jet transverse momentum, each described by a single nuisance parameter. For the 'low' component, only jets below 40 GeV are varied within their JES uncertainties. For the 'medium' ('high') components, jets between 40 GeV and 100 GeV (above 100 GeV) are varied. This approach was chosen, as the control regions and signal regions are populated by jets of different average transverse momentum. Separating the JES uncertainty as a function of the jet transverse momenta avoids overprofiling of the JES uncertainty in the signal regions. Each of the three resulting uncertainties are correlated between all regions and backgrounds. An additional, independent JES nuisance parameter is assigned for the signal samples.

   (b) Uncertainties on the missing transverse energy caused by pileup uncertainties, which are correlated between all regions and backgrounds.

   (c) Uncertainties on the missing transverse energy caused by topological clusters not assigned to any physics object, which are correlated between all regions and backgrounds.

   (d) Cross section uncertainties for vector boson + heavy flavour samples.
   The cross sections for all W boson + heavy flavor samples listed in table 10 are rescaled by correction factors measured on ATLAS data, and a corresponding normalization uncertainty is imposed. The cross sections for the $Wb\bar{b}$ and $Wc\bar{c}$ are scaled by 1.63 ± 0.76, while the Wc sample is rescaled by 1.11 ± 0.35 [136]. The uncertainty on the cross sections for the $Zb\bar{b}$ samples is conservatively taken to be 100%[61]. Each of these uncertainties is treated as correlated among all regions. As these samples are

[60] This effectively means a full anticorrelation between the top control regions and W boson control regions for the hard lepton final states, as these regions are orthogonally separated by the b-tagging requirement.

[61] It should be stressed that this process only plays a very minor role for the analysis. Only in the dileptonic control regions some minor contributions exist.

combined with the corresponding light flavor samples with one additional (Wc) and two additional ($Wb\bar{b}$, $Wc\bar{c}$ and $Zb\bar{b}$) partons calculated in the matrix element - as discussed in section 7.2 - their cross section uncertainties cannot be handled as a pure normalization uncertainty, because only the heavy flavor components of the combined samples are affected.

(e) QCD normalization in each control region.
The amount of QCD events in each phase space region is computed via the matrix method described in 6.4.3. The uncertainty on this number is given by the uncertainties on the efficiencies for real leptons, fake leptons and the background subtraction in the regions, where these efficiencies have been measured. Within these uncertainties, the fit constrains the amount of QCD in each region, treating all regions as uncorrelated.

3. **Shape systematics excluding changes in normalization**
This implementation is similar to the previous case, but no variation of the total normalization is allowed. Therefore the additional histograms, describing the variation in shape, are normalized to the nominal histogram and the linear interpolation is done afterwards. Following systematic uncertainties are treated like this:

(a) MLM matching uncertainties for W boson + jets and top quark pair production in the control regions.
The deviations in the event yield between the nominal choice of p_T^{min} = 15 GeV and the extreme case of p_T^{min} = 30 GeV are calculated for *each bin* of the input distributions on generator level. Table 27 shows the corresponding numbers. For each process (W boson and top pair production), a nuisance parameter is introduced, which is shared among all control regions.

(b) Hadronization uncertainties for W boson + jets and top quark pair production in the signal regions.
For each process (top quark pair production or W boson production), the uncertainties are correlated between all signal regions.

4. **Monte Carlo statistical uncertainties**
A poissonian error with mean γ_i for the sum of all samples in each bin of the input distributions is assigned. No correlations among the histogram bins are assumed as well as no correlations between the different channels.

7.4 Self consistency studies

Before applying the combined fit to the measured data sample, a set of pseudo experiments - testing the reliability of the fit configuration - is performed. For this purpose, the background probability density function is sampled with randomly generated events for each pseudo experiment. Given this toy data, the background-only fit is performed on the hypothetical data sample. The failure rate (i.e. the fraction of pseudo experiments, which do not yield a convergent fit) is below 1‰.

Background	**3J**	**4J**	**5J**	**6J**	**7J**	**8J**	**9J+**
Top quark pair production	8%	5%	0.3%	2%	5%	4%	10%
W boson production	0.1%	2%	0.6%	6%	20%	2%	6%

Table 27: Relative uncertainties arising from variations of the MLM matching cutoff in each bin of the jet multiplicity fit input distribution, comparing the nominal choice of $p_T^{\min} = 15$ GeV with the alternative choice of $p_T^{\min} = 30$ GeV. The uncertainties were calculated on generator level, applying the control region cuts as listed in table 24 (without the b-tagging requirement).

As a first important test, the fitted values of the normalization factors for all top quark samples and vector boson samples with a fixed number of final state legs are compared with the nominal values, in order to spot any bias in their computation. As the pseudo data set was constructed by sampling the probability density function of the pure standard model expectation, all normalization factors should be distributed like a gaussian with a mean of one and a width, which reflects the total uncertainty on these factors. Figure 60 shows all normalization factors obtained on 1000 pseudo experiments. Furthermore, a gaussian fit to the pseudo data sample is performed. All distributions follow a gaussian with a mean of one within statistical uncertainties, which validates that the fit configuration - despite its complexity - frequently manages to find the minimum that corresponds to the 'real' values.

In addition, the pull distributions for the fitted normalization parameters are examined to spot a potential underestimation or overestimation of uncertainties. For each parameter of interest, the pull distribution is defined as the deviation of the fitted value from the nominal value (i.e. one for all normalization parameters), divided by the uncertainty on the fitted value. For a perfectly unbiased fit, the pull should be distributed like a gaussian around zero, with a RMS of one, if the uncertainties reflect the spread of fitted parameters around the nominal value. Figure 61 shows the pull distributions for all normalization parameters. In addition, a gaussian fit to the pseudo data sample is performed and shown. While all pull distributions approximately follow a gaussian, some biases are observed for some of the normalization parameters. In addition, the RMS values are systematically above 1, which must be interpreted as a slight underestimation of errors. The bias in the distributions does not arise from a bias in the normalization factors - as was shown in figure 60 - but is caused by a wrong calculation of uncertainties.

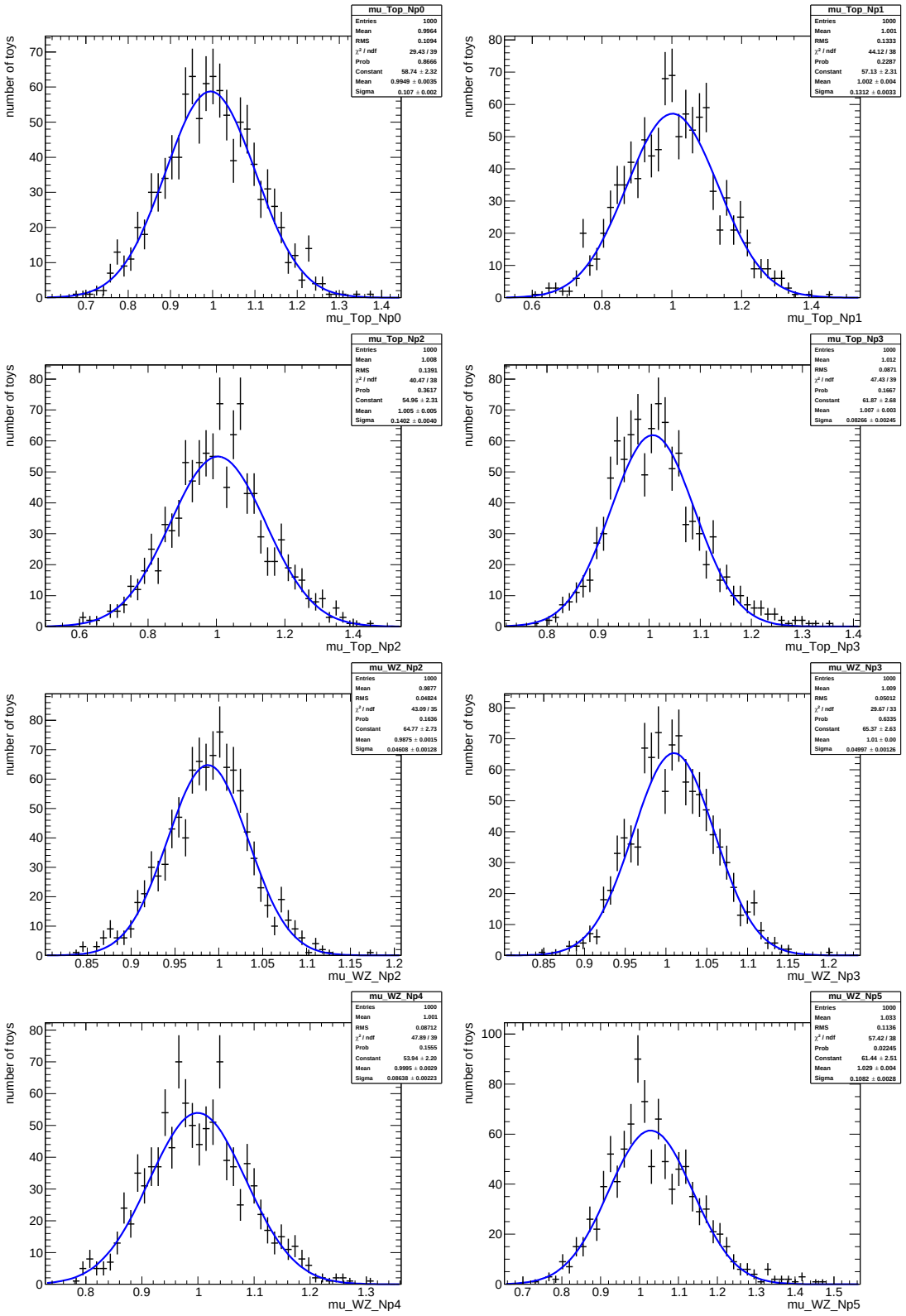

Figure 60: Distributions of the fitted normalization factors, derived with 1000 pseudo experiments on toy data, using the background-only fit configuration. A gaussian fit to the data is shown as well. Top: Normalization parameters for top quark pair production with zero to three additional partons calculated in the matrix element. Bottom: Normalization parameters for vector boson production with two to five additional partons calculated in the matrix element.

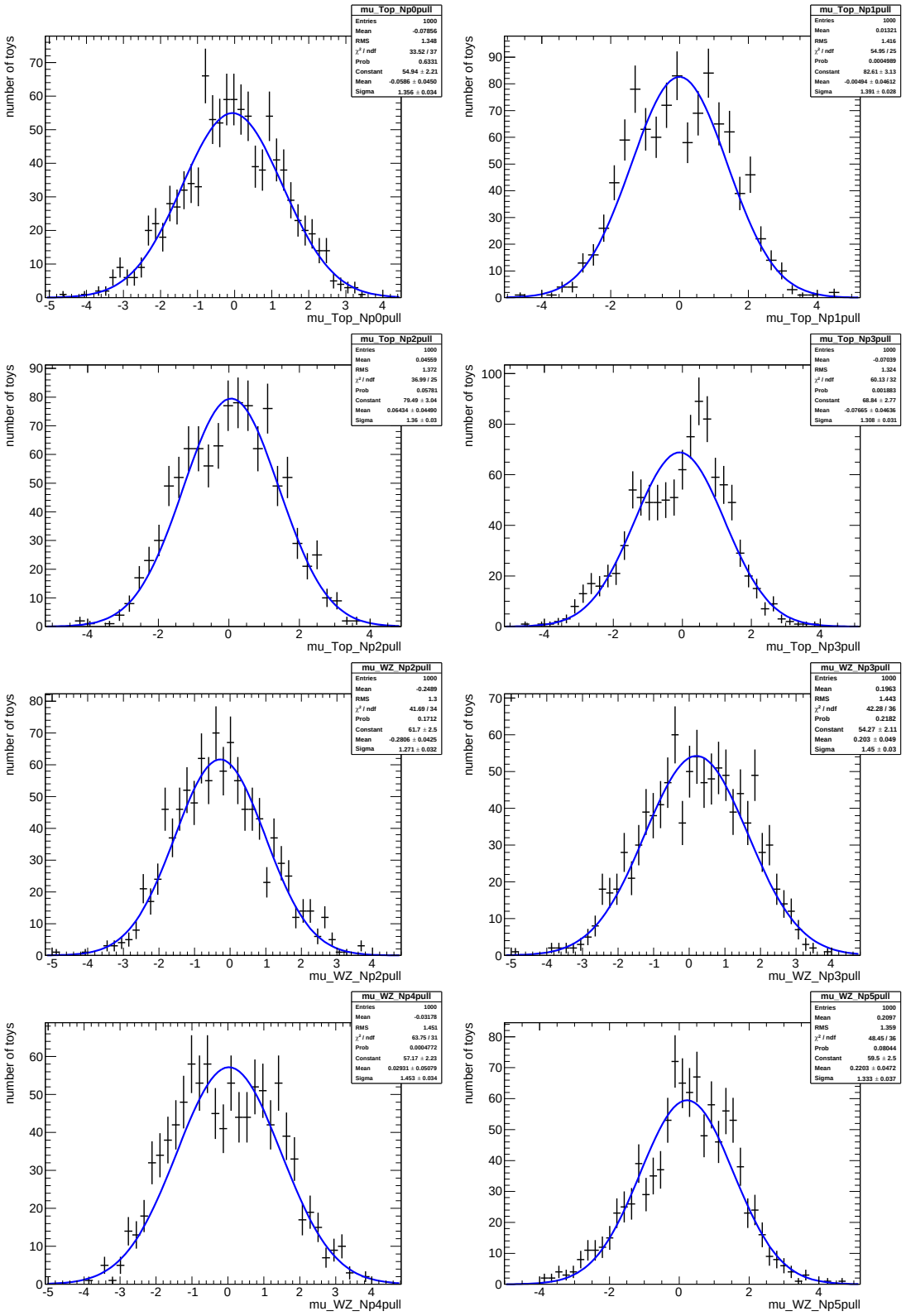

Figure 61: Pull distributions, derived with 1000 pseudo experiments on toy data, using the background-only fit configuration. A gaussian fit to the data is shown as well. Top: Normalization parameters for top quark pair production with zero to three additional partons calculated in the matrix element. Bottom: Normalization parameters for vector boson production with two to five additional partons calculated in the matrix element.

7.5 Fit results

In this section, the fit results and resulting event yields in all relevant phase space regions after the fit will be discussed. Based on this result, the exclusion limits in various signal models and model independent upper limits on the number of non standard model events in all signal regions will be derived and presented in the next chapter.

7.5.1 Background-only fit

The fit parameters, relevant for the hard one lepton analysis, are listed in table 28 for the background-only fit configuration. All nuisance parameters, *only* affecting the soft lepton and dilepton analysis and Monte Carlo statistical uncertainties are removed from this list to improve clarity. A complete set of fit parameters for the background-only fit is shown in Appendix C.
A slight adjustment of the normalizations for the vector boson and top quark pair production samples with a fixed number of additional partons calculated in the matrix element is done. The normalization for top quark pair production plus no additional partons in the matrix element is significantly increased by 27%, while the normalizations for the other parton bins are consistent with one within uncertainties. For the vector boson simulation, especially the normalizations for samples with two and five additional partons calculated in the matrix element are significantly changed.

In addition, some of the input uncertainties, which have a drastic impact on the input distributions like JES or heavy flavor tagging efficiencies can be constrained, reducing the total systematic uncertainty on the background prediction. For most of the minor uncertainties like lepton resolutions and scales, the input distributions are not sensitive on the resulting small variations.

A subset of the full correlation matrix is shown in figure 64, focussing on all normalization parameters and nuisance parameters related to some of the dominant systematic uncertainties. Given this correlation matrix and the partially ocurring large (anti)correlations, the fit configuration does not fully disentangle all different parameters, as different parameters can have similar impacts on the jet multiplicity distribution. For example, subsamples with a different number of final state partons can lead to the same amount of reconstructed jets in the final state. Furthermore, variations in the jet energy scale can mimic variations in the renormalisation scale[62]. For a simplified fit configuration without any nuisance parameters - as shown in [67] - large anticorrelations of the normalization parameters between neighbouring par-

[62] Although even large correlations between the fit parameters are not a severe problem - as long as these correlations a propagated properly into the final uncertainties - they hint towards potential improvements of the method. Using more input information than just the number of reconstructed jets might help to further decorrelate the individual parameters and to obtain a smaller total uncertainty on the background prediction in the signal regions.

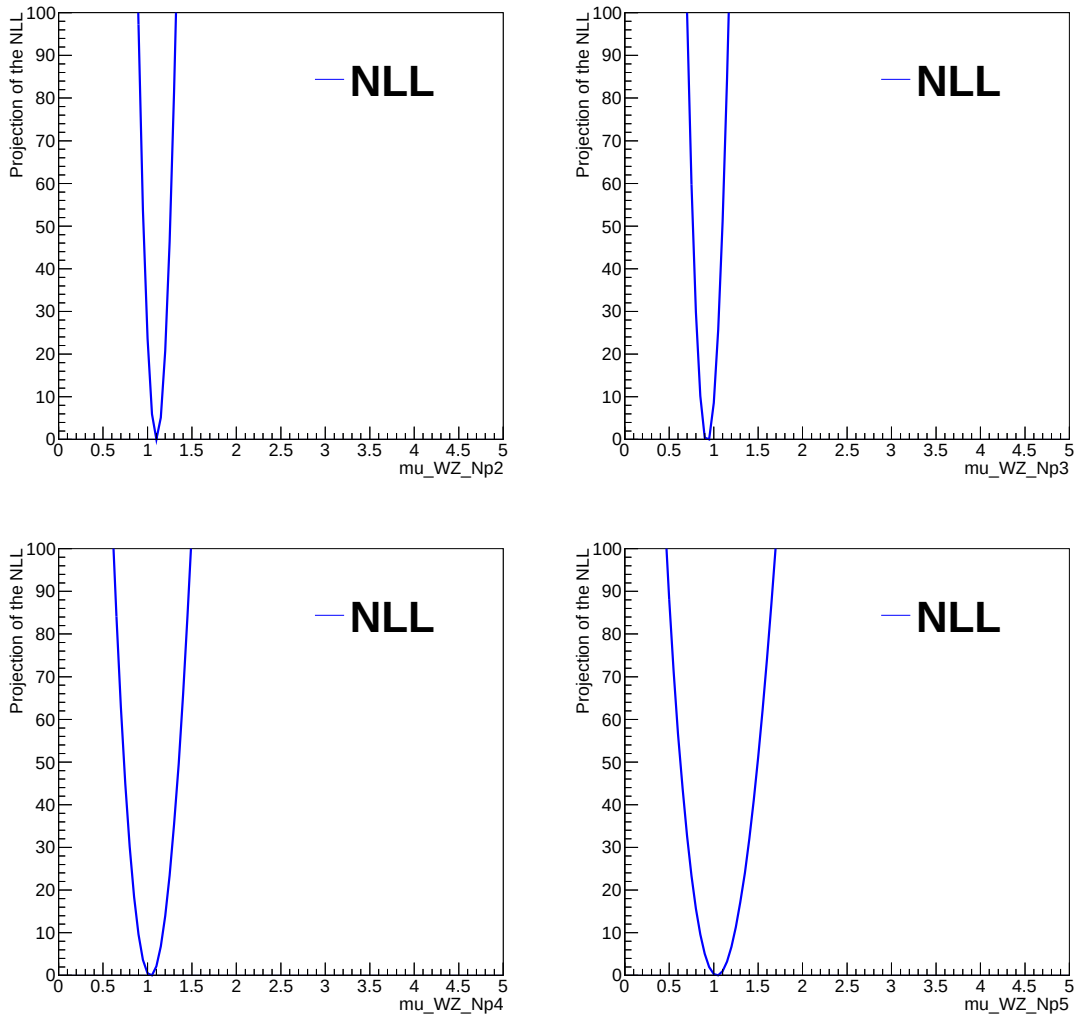

Figure 62: Projections of the Likelihood function, evaluated at the global minimum, onto the normalization factors for W boson production.

ton multiplicities are observed, caused by sizable contributions of both samples in the same jet multiplicity bin. However, after including more channels and all nuisance parameters, this intuitive behaviour of the correlation matrix is spoiled, as each normalization parameter can now correlate with the nuisance parameters as well[63].

In addition to the correlations between the different parameters, the projection of the Likelihood function - evaluated at the global minimum - onto the normalization factors for top quark and W boson production are shown in figures 62 and 63. All figures show the expected parabola shape, and the width of the parabola reflects the uncertainty on the fitted parameter.

[63]In chapter 7.4, the fit setup was validated on toy Monte Carlo, showing that the jet multiplicity distribution provides enough information to determine all parameters with reasonable uncertainties. Given this, the loss of transparency due to the quite sophisticated fit configuration is just an esthetic problem.

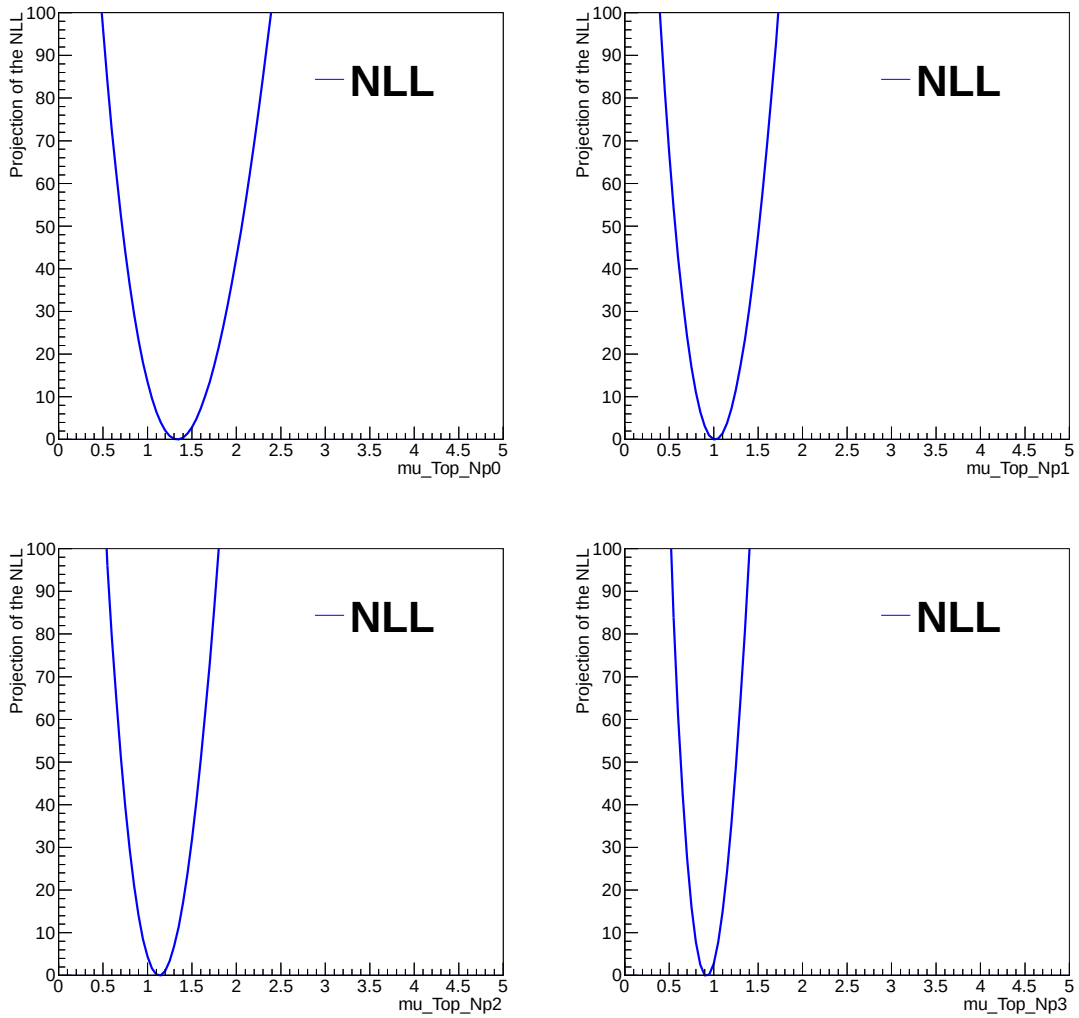

Figure 63: Projections of the Likelihood function, evaluated at the global minimum, onto the normalization factors for top quark pair production.

Figures 65 and 66 show the input distributions for the hard single lepton regions before and after the background-only fit. The input distributions for the other channels are shown in Appendix D. All channels show slight discrepancies between data and Monte Carlo simulation before the fit. By trend, the simulation overestimates the high jet multiplicities for vector boson production and top quark pair production events in all input channels. After the combined fit, an almost perfect agreement within uncertainties between data and Monte Carlo simulation is observed. Furthermore, the total uncertainty on the number of events in each bin of the input distributions is reduced. Table 29 shows the number of measured data events, the number of Monte Carlo events before fit and the number of predicted background events after fit for all hard single lepton control regions. The results for all other channels is given in Appendix E. In all control regions, an improvement of the agreement between observed data and simulation after fit is observed.

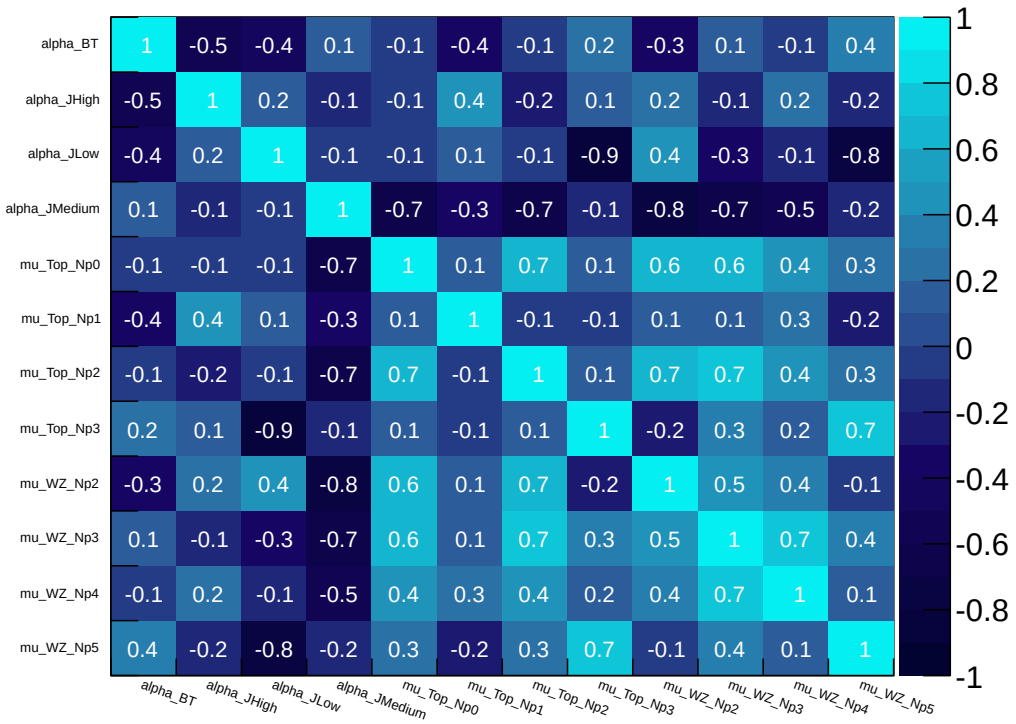

Figure 64: Correlations between all normalization parameters for top quark pair production, vector boson production and a subset of nuisance parameters related to jet energy scale and b-tagging uncertainties. If the absolute value of the correlation is smaller than 0.1, the value is rounded to 0.1 (-0.1) for correlated (anticorrelated) parameters.

7.5.2 Exclusion fit

As explained in section 7.1, a slighty different fit configuration is used in order to obtain the exclusion limits in various supersymmetric models as shown in chapter 8, taking into account the signal contamination in each control region. An example for fitted parameters for the mSUGRA model point with m_0 = 3060 GeV and $m_{1/2}$ = 300 GeV - which is within the sensitivity reach of this analysis - is shown in Appendix F. As the signal contamination in the control regions for this model point is relatively small, almost no change in the background normalization factors is obtained and all normalizations agree with the ones obtained by the background-only fit configuration within uncertainties. Figure 67 shows the corresponding effective mass distributions in the different one hard lepton signal regions before fit. As the number of predicted background events after fit depends on the signal contamination of the specific model, the distributions after fit and corresponding numbers differ between all models and therefore are not shown. The corresponding distributions for the dilepton and soft lepton signal regions are shown in Appendix G.

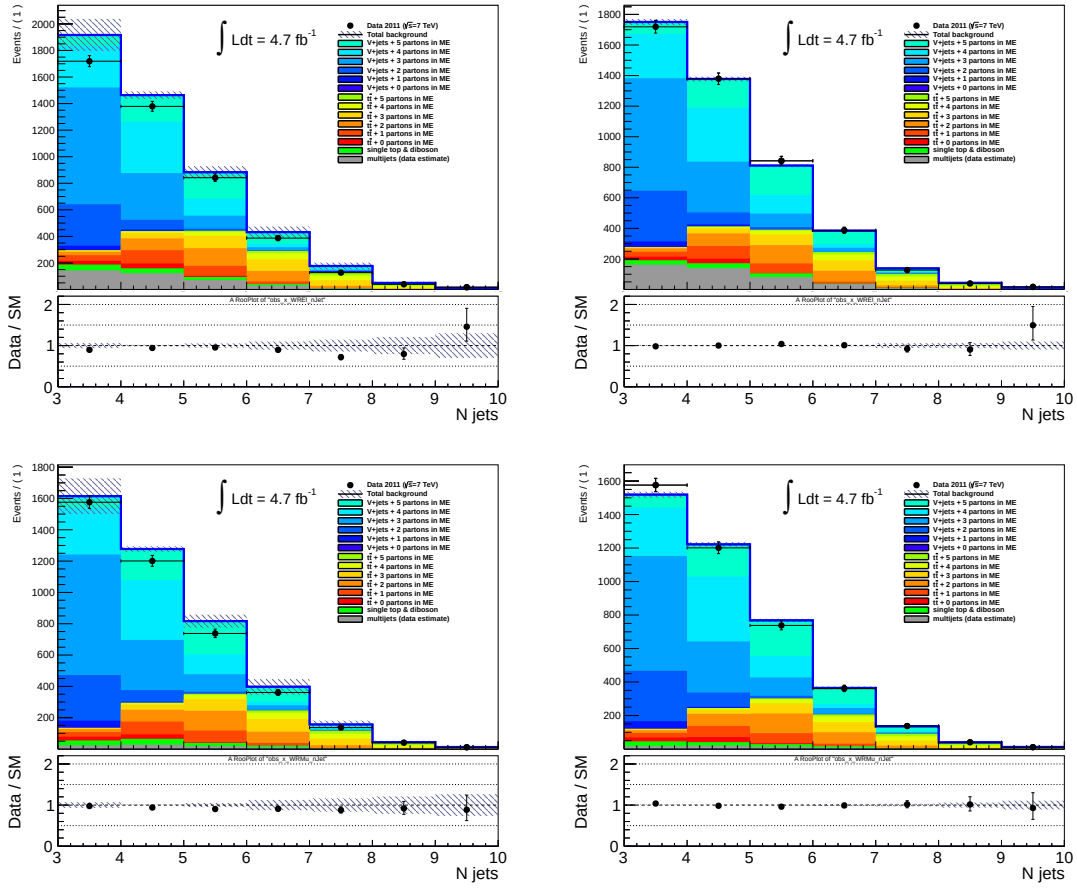

Figure 65: Jet multiplicity input distribution in the W boson control region for the final state with one hard electron (top) and one hard muon (bottom) before fit (left) and after fit (right). The uncertainty bands cover all systematic uncertainties introduced in chapter 6.5.

7.5.3 Discovery fit

Model independent limits on the number of non standard model events in the signal regions are calculated in chapter 8.2, quantifying the agreement between data and background prediction after fit in the signal regions - including an explicit cut on m_{eff}^{incl} - as listed in table 21. Table 30 shows the oberserved data events, Monte Carlo prediction and background expectation after fit for all single hard lepton signal regions, which is used as an input for this type of limit calculation. The numbers for the soft lepton and dilepton signal regions are given in Appendix H. In all hard single lepton signal regions, a reasonable agreement between fitted standard model background and observed data is found. For the electron channel, two (four) events are observed in the three jet (four jet) signal region with a fitted background prediction of 2.3 $\pm$ 0.9 (3.5 $\pm$ 0.9) events. For the muon channel, the observed events are slightly outside the 1σ error of the background prediction. For the three jet signal region, one event is measured with a background expectation of 2.6 $\pm$ 0.8, while two events are observed in the four jet signal region with a background prediction of 1.5 $\pm$ 0.3 events.

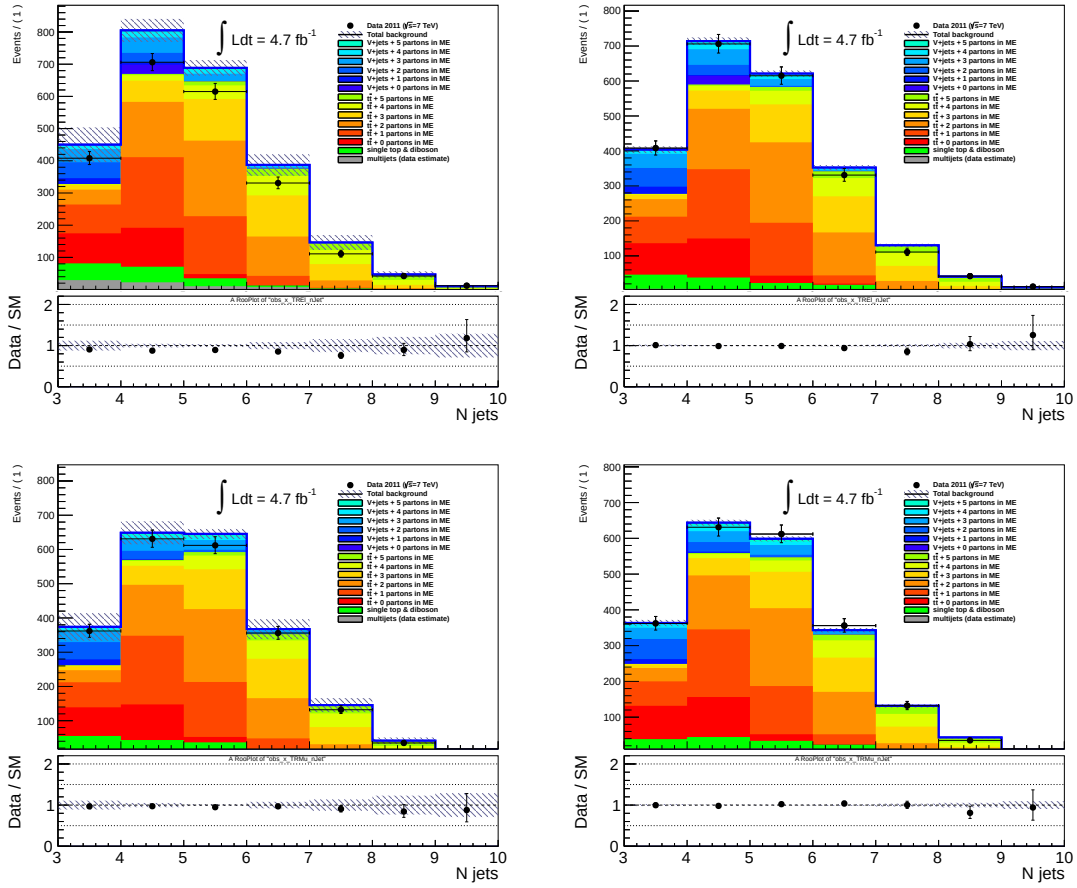

Figure 66: Jet multiplicity input distribution in the top control region for the final state with one hard electron (top) and one hard muon (bottom) before fit (left) and after fit (right). The uncertainty bands cover all systematic uncertainties introduced in chapter 6.5.

7.5.4 Dominant systematic uncertainties

The breakdown of all systematic uncertainties, which are taken into account for the computation of the total uncertainty on the background predictions is shown in table 31. In all signal regions, the dominant source of uncertainty is given by the limited sample size of the background simulations. In addition, sizeable contributions arise from the jet energy scale uncertainties, hadronization uncertainties and errors on the normalization factors.

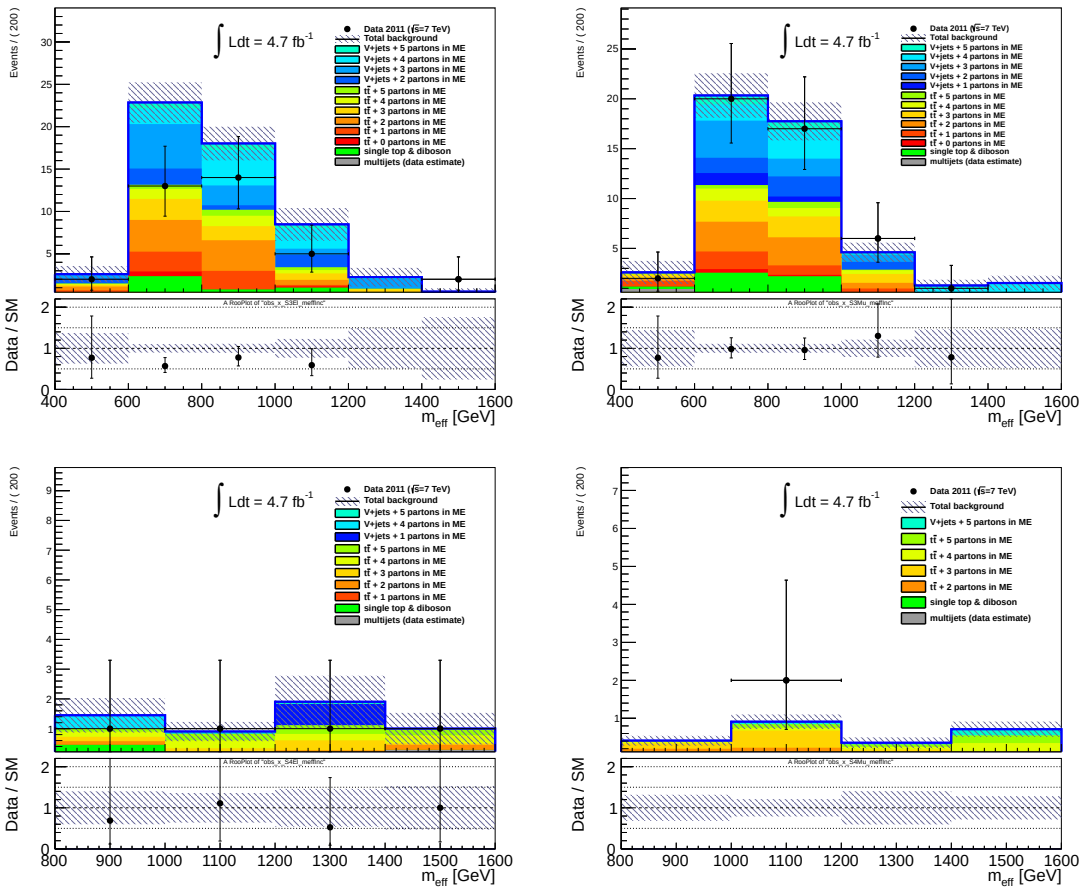

Figure 67: Effective mass distributions in the three jet signal regions (top) and four jet signal regions (bottom) for the hard single electron final state (left) and the hard single muon final state (right) used as inputs for the exclusion fit configuration. The error band covers all systematics introduced in chapter 6.5.

Variable	Value	Uncertainty
Normalization Parameters		
μ(Top Np0)	1.27	± 0.10
μ(Top Np1)	0.99	± 0.06
μ(Top Np2)	1.07	± 0.09
μ(Top Np3-Np5)	0.92	± 0.08
μ(Vector boson Np2)	1.14	± 0.08
μ(Vector boson Np3)	1.07	± 0.06
μ(Vector boson Np4)	1.02	± 0.06
μ(Vector boson Np5)	1.24	± 0.13
Nuisance Parameters		
α(b-tagging)	0.82	± 0.28
α(JES high p_T)	-0.9	± 0.27
α(JES medium p_T)	-0.56	± 0.36
α(JES low p_T)	-0.29	± 0.29
α(Electron energy scale)	0.16	± 0.49
α(Muon energy scale)	0.01	± 1.14
α(Electron ID efficiency)	-0.66	± 0.88
α(Muon ID efficiency)	0.01	± 0.99
α(Muon resolution / tracker)	-0.04	± 1.01
α(Muon resolution / muon system)	0.06	± 1.01
α(Electron trigger efficiency)	-0.27	± 0.94
α(Muon trigger efficiency)	0.43	± 0.48
$\alpha(E_T^{\text{miss}}$ / cluster)	-0.86	± 0.47
$\alpha(E_T^{\text{miss}}$ / pileup)	0.28	± 0.48
$\alpha(p_T^{\text{min}}$ / Top)	-0.86	± 0.47
$\alpha(p_T^{\text{min}}$ / Vector boson)	1.14	± 0.68
α(Minor background normalization)	-0.05	± 0.97
α(Heavy flavor cross section)	0.12	± 0.46
α(Vector boson Np0 normalization)	0.01	± 0.96
α(Vector boson Np1 normalization)	0.29	± 0.18
α(Vector boson p_T reweighting / 150 GeV)	0.08	±0.74
α(Vector boson p_T reweighting / 200 GeV)	-0.27	±0.72
α(Vector boson p_T reweighting / 50 GeV)	0.12	±0.70

Table 28: Fit parameters obtained using the background-only fit configuration on data, ommiting all nuisance parameters related to Monte Carlo statistical uncertainties. All parameters, which solely influence the dilepton or soft lepton regions are taken out to improve readability.

	Top Quark CR		**W boson CR**	
	Electron	Muon	Electron	Muon
Observed events	2225	2137	4510	4064
		Fit Results		
Fitted bkg events	2270.9 ± 40.1	2130.8 ± 39.0	4515.3 ± 62.9	4060.4 ± 60.3
Fitted top events	1842.2 ± 53.0	1724.0 ± 50.5	882.5 ± 63.7	806.8 ± 57.2
Fitted W and Z events	292.6 ± 40.7	255.0 ± 36.3	3103.0 ± 89.3	3116.3 ± 72.1
Fitted other BGs events	119.6 ± 23.6	101.2 ± 21.0	90.9 ± 19.0	73.7 ± 15.8
Fitted QCD	16.6 ± 33.4	50.6 ± 26.6	438.9 ± 107.6	63.6 ± 68.2
		Monte Carlo Expectation		
MC exp. SM events	2533.4	2232.4	4932.1	4317.3
MC exp. top events	2012.4	1816.7	1154.0	1006.6
MC exp. W and Z events	315.5	261.4	3281.5	3119.8
MC exp. other BGs events	132.2	116.4	115.7	104.1
Data-driven QCD	73.3	37.9	380.8	86.8

Table 29: Background-only fit results for the single lepton control regions, for an integrated luminosity of 4.7 fb^{-1}. The errors shown are the Monte Carlo statistical plus systematic uncertainties. The pure Monte Carlo expecation is given for comparison.

	3 Jet SRs		**4 Jet SRs**	
	Electron	Muon	Electron	Muon
Observed events	2	1	4	2
		Fit Results		
Fitted bkg events	2.3 ± 0.9	2.6 ± 0.8	3.5 ± 0.9	1.5 ± 0.3
Fitted top events	0.4 ± 0.2	0.5 ± 0.2	2.3 ± 0.6	1.3 ± 0.3
Fitted W and Z events	1.5 ± 0.6	2.0 ± 0.6	0.9 ± 0.2	0.2 ± 0.1
Fitted other BGs events	0.0 ± 0.0	0.1 ± 0.1	$0.0^{+0.3}_{-0.0}$	< 0.05
Fitted QCD	0.3 ± 0.4	< 0.05	0.3 ± 0.4	< 0.05
		Monte Carlo Expectation		
MC exp. SM events	2.7	2.8	5.3	2.4
MC exp. top events	0.9	0.6	3.1	2.0
MC exp. W and Z events	1.5	2.0	1.3	0.3
MC exp. other BGs events	0.0	0.2	0.5	0.1
Data-driven QCD	0.3	0.0	0.3	0.0

Table 30: Background-only fit results for the single hard lepton signal regions, for an integrated luminosity of 4.7 fb^{-1}. The errors shown are the Monte Carlo statistical plus systematic uncertainties. The pure Monte Carlo expecation is given for comparison.

	3 Jet SRs		**4 Jet SRs**	
	Electron	Muon	Electron	Muon
Total statistical ($\sqrt{N_{\text{obs}}}$)	±1.41	±1.00	±2.00	±1.41
Total background systematic	±0.92	±0.82	±0.93	±0.33
	Normalization Parameters			
μ(Top Np1)	±0.00	±0.00	±0.01	±0.00
μ(Top Np2)	±0.01	±0.02	±0.04	±0.02
μ(Top Np3)	±0.03	±0.03	±0.16	±0.10
μ(Vector boson Np3)	±0.07	±0.02	±0.00	±0.00
μ(Vector boson Np4)	±0.00	±0.08	±0.00	±0.00
μ(Vector boson Np5)	±0.03	±0.04	±0.02	±0.02
	Nuisance Parameters			
α(JES high p_T)	±0.12	±0.11	±0.26	±0.15
α(JES low p_T)	±0.06	±0.03	±0.02	±0.06
α(JES medium p_T)	±0.00	±0.05	±0.26	±0.20
α(Electron energy scale)	±0.01	±0.00	±0.01	±0.00
α(Electron ID efficiency)	±0.04	±0.00	±0.05	±0.00
α(Electron trigger efficiency)	±0.02	±0.00	±0.02	±0.00
α(Muon trigger efficiency)	±0.00	±0.06	±0.00	±0.03
α(E_T^{miss} / cluster)	±0.04	±0.03	±0.04	±0.01
α(E_T^{miss} / pileup)	±0.00	±0.04	±0.14	±0.06
α(Minor background normalization)	±0.00	±0.03	±0.00	±0.00
α(Heavy flavor cross section)	±0.16	±0.00	±0.14	±0.00
α(Vector boson Np1 normalization)	±0.00	±0.00	±0.01	±0.00
α(Vector boson p_T reweighting / 150 GeV)	±0.01	±0.00	±0.00	±0.00
α(Vector boson p_T reweighting / 200 GeV)	±0.10	±0.11	±0.06	±0.01
α(Vector boson p_T reweighting / 50 GeV)	±0.00	±0.01	±0.00	±0.00
α(Hadronization $t\bar{t}$)	±0.07	±0.07	±0.15	±0.09
α(Hadronization vector boson)	±0.19	±0.25	±0.05	±0.01
α(QCD normalization)	±0.38	±0.00	±0.38	±0.00
γ(Monte Carlo statistics)	±0.80	±0.75	±0.72	±0.20

Table 31: Breakdown of the dominant systematic uncertainties on background estimates in the hard single lepton signal regions. As systematic uncertainties can be (anti)correlated, they do not quadratically add up to the total uncertainty within each region. Systematic uncertainties listed as zero correspond to values below 0.005. If a systematic uncertainty is below 0.005 events for all four signal regions, it is removed from the list.

7.6 Fit validation

In this section, the agreement between data and simulation after fit is studied in phase space regions *between* the control and signal regions, in order to study the impact of the fit on variables, in which the extrapolation between control regions and signal regions is performed. This is very important for variables like $m_{\text{eff}}^{\text{incl}}$, which significantly differ between the control regions and signal regions.

As already described, the combined fit method extracts a background estimation in dedicated control regions, which cover a different phase space than the signal regions. In order to improve the background prediction in the signal regions, an extrapolation of the background, measured in the control regions, into the signal regions is performed. For this purpose, it is necessary to study the agreement between data and simulation for the variables in which this extrapolation is done.

Comparing tables 21, 22 and 23, which summarize the phase space requirements for the signal regions, with tables 24 and 25, which list the phase space cuts for the background measurements, shows that the extrapolation takes place in the missing transverse energy, transverse mass and effective mass. In order to check the reliability of the fit results, the impact of the fit results on these distributions, in regions enriched by either W boson events or top quark pair events, is studied.

The distributions, relevant for the extrapolation into the signal regions have already been shown before the fit in chapter 6 for a loose preselection in the context of the Z_{P_T} fit. A reasonable agreement between data and Monte Carlo simulation was observed for W boson events after correcting the W boson Monte Carlo simulation as a function of the true W boson transverse momentum. In addition, a severe shape discrepancy of the effective mass between data and simulation for top quark pair production events was shown in chapter 6.4.1, which is caused by a mismodelling of the jet transverse momenta as shown in figures 56 and 57. Figure 68 shows the inclusive effective mass after the combined fit for the W boson control region and top control region without the explicit $m_{\text{eff}}^{\text{incl}}$ requirement. After fit, the description of the top quark pair production background is much better, while the fit results do not spoil the good agreement for the W boson events, which was already shown in figure 55. It has already been argued that the discrepancy in the effective mass for top quark pair production events is dominantly caused by a mismodelling of the jet transverse momenta. Figures 69 and 70 show the transverse momenta of the leading four jets in the top quark pair production control region without the explicit cut on $m_{\text{eff}}^{\text{incl}}$ after the combined background-only fit. A significant improvement in the agreement between data and Monte Carlo simulation is observed for all jet transverse momenta for both lepton flavors, yielding a much more reliable extrapolation of the top quark background into the signal regions.

Furthermore, the fit results are extrapolated into dedicated validation regions (**VRs**), which cover phase space regions between the control regions and signal regions, granting orthogonality to both. The validation regions for the hard single lepton

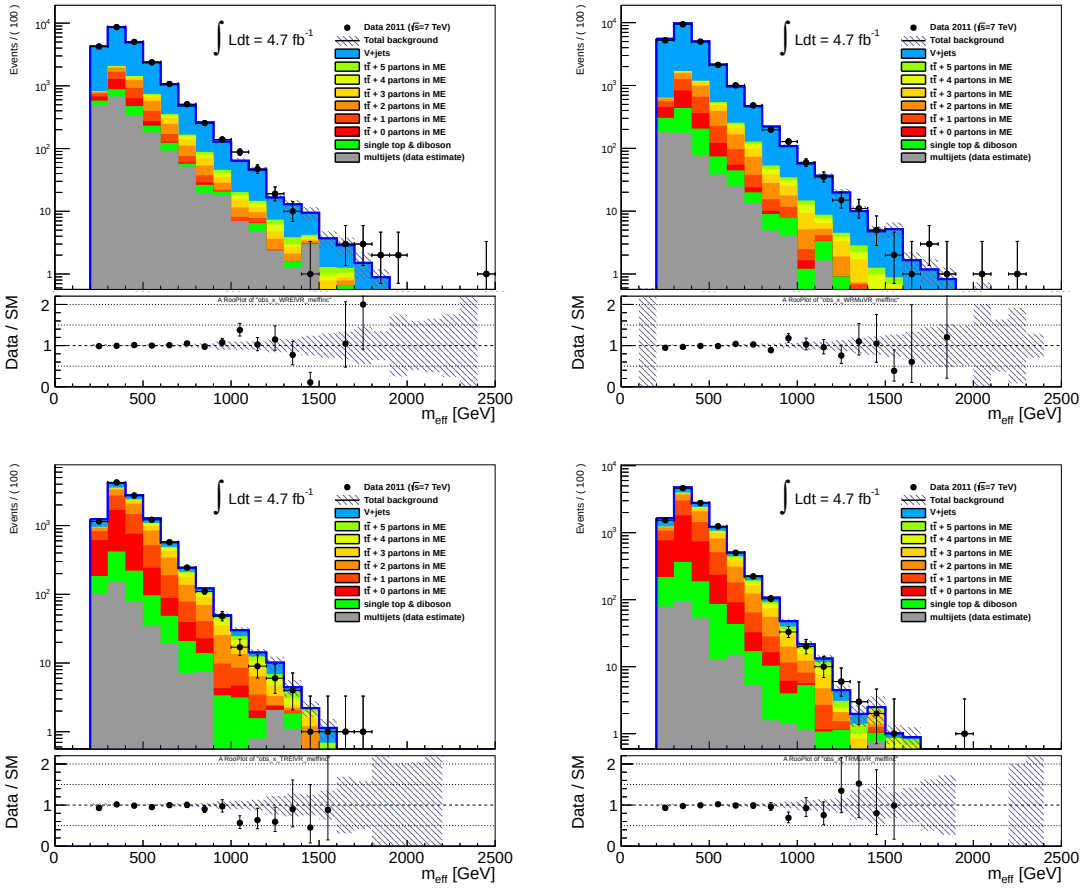

Figure 68: Inclusive effective mass in the control region for W boson production (top) and top quark pair production (bottom), separated for events with exactly one hard electron (left) and one hard muon (right) after applying the results obtained with the background-only fit configuration. The error bands cover all systematic uncertainties as discussed in chapter 6.5.

analysis are listed in table 32. The requirements, which define the validation regions for the soft lepton and dilepton channel can be found in [83]. One set of validation regions is designed to investigate the extrapolation in the missing transverse energy within the intermediate transverse mass window, which is imposed to define the control regions. As discussed in chapter 4.5.1, dileptonic top quark pair production events dominate the total number of top quark pair events after cutting harsh on the transverse mass. The high m_T region is defined to study the agreement between Monte Carlo simulation and data for dileptonic top events, where one lepton is either a hadronic tau lepton or not reconstructed in the ATLAS detector.

Table 33 list the number of data events, the Monte Carlo expectation and the number of predicted background events after fit for the single hard electron validation regions. The corresponding numbers for the muon channel are given in table 34. All regions - except top validation region for the muon channel - show reasonable agreements between data and the fitted background prediction.

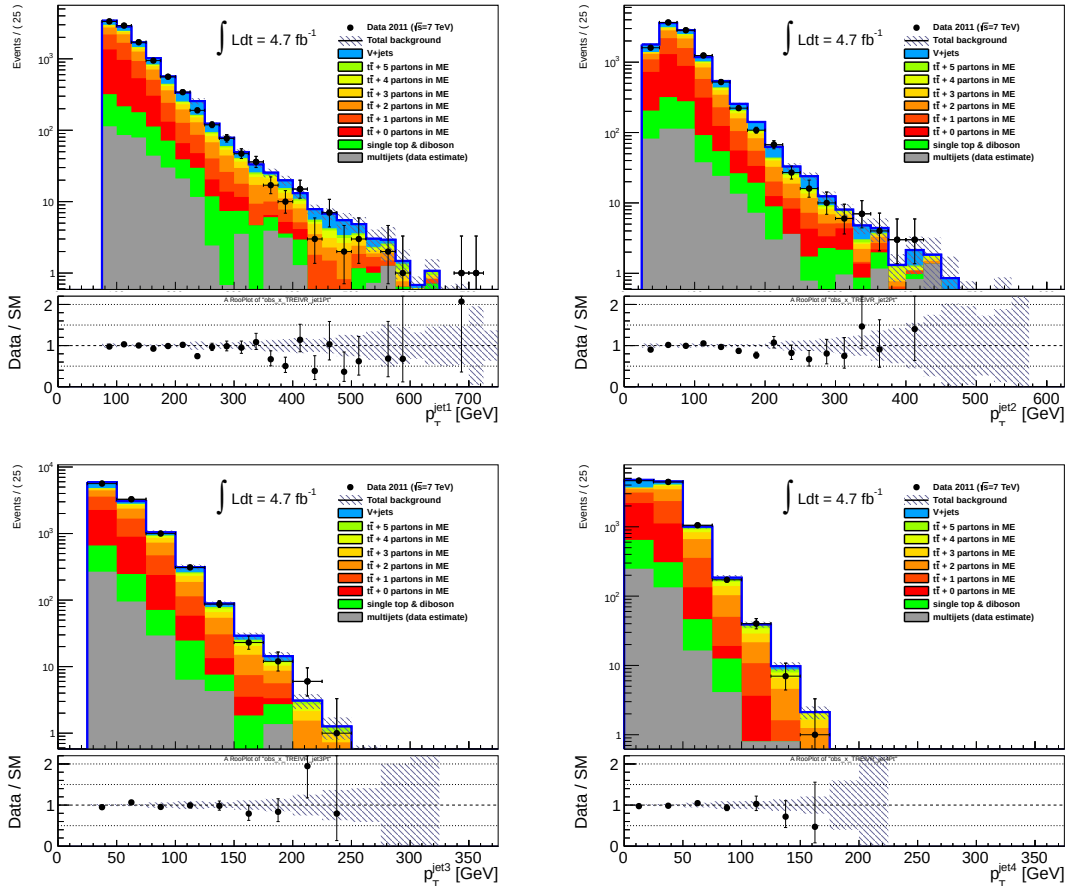

Figure 69: Jet transverse momenta in the top control region without an explicit cut on m_{incl}^{eff} for the single electron channel after fit. The error bands cover all systematic uncertainties as discussed in chapter 6.5.

The results for all control- and validation regions are summarized in figure 71, which shows the deviations between observed data and predicted total background, divided by the quadratic sum of the systematic and statistical uncertainty of the background prediction after fit. The left panel shows the results in the control regions, while the right panel shows the results in the validation regions. Focussing on the hard single lepton control regions, the largest deviation is present in the top control regions for the electron channel. As shown in the top right panel of figure 66, this excess of Monte Carlo simulation is located in the 6 and 7 jet bins and mainly caused by the top quark pair production sample with 3-5 additional partons calculated in the matrix element. Given the much larger discrepancy before fit - as shown in the left top panel - the normalization for this sample is already scaled down by a factor of 0.92 - as listed in table 28 - in order to improve the agreement between data and Monte Carlo simulation. However, a further lowering of the normalization parameter is not possible due to the muon channel, which already shows a slight overshoot of data above Monte Carlo prediction after fit for the sample under consideration, as one can see in the bottem right panel of figure 66[64].

[64]This discussion is a bit simplified as all impacts of the dileptonic control regions, soft lepton

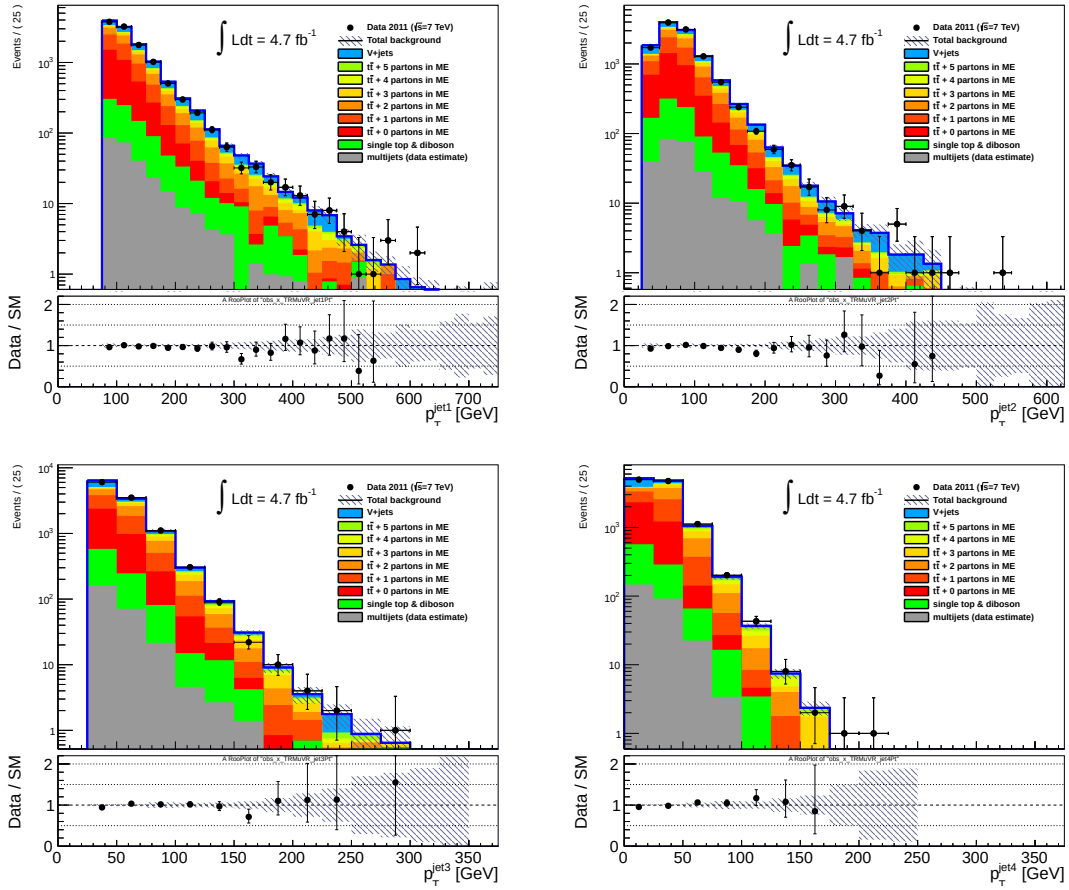

Figure 70: Jet transverse momenta in the top control region without an explicit cut on m_{incl}^{eff} for the single muon channel after fit. The error bands cover all systematic uncertainties as discussed in chapter 6.5.

The results for all single lepton signal channels are summarized in figure 72, which again shows the deviations between observed data and predicted total background, divided by the quadratic sum of the systematic and statistical uncertainty of the background prediction after fit. In all signal regions, data is compatible with the standard model prediction within one standard deviation.

control regions and hard single lepton W boson control regions on the fitted parameters were neglected. Nevertheless, given that the single hard lepton channel provides the smallest statistical uncertainty on the data - for the bins where the relevant sample dominates - the argumentation is valid in the first order.

	E_T^{miss} **VR**		**High** m_T **VR**
Variable	W Boson	Top Quark	Top Quark
n_{lepton}	$== 1 : 25(20)$ GeV		
n_{jet}	$\geq 3 : 80, 25, 25$ GeV		
n_{bTags}	0	≥ 1	-
E_T^{miss}	$\in$[120, 250] GeV		$\in$[40, 250]GeV
m_T	$\in$[40, 80] GeV		> 80 GeV
m_{eff}^{incl}	> 500 GeV		

Table 32: Validation regions to study the agreement between data and Monte Carlo simulation in phase space regions between the control regions and signal regions. All validation regions are othogonal to the control regions and signal regions and designed to either study specific variables (E_T^{miss} VR) or background components (High m_T VR).

Single Electron	**High** m_T **VR**	E_T^{miss} **VR**	
	Top Quark	W Boson	Top Quark
Observed events	7698	1068	499
		Fit Results	
Fitted bkg events	7618.1 ± 553.9	1017.8 ± 42.9	501.6 ± 16.7
Fitted top events	3014.6 ± 113.3	213.5 ± 16.9	410.6 ± 17.5
Fitted W and Z events	3936.4 ± 162.7	778.1 ± 39.5	58.2 ± 9.7
Fitted other BGs events	231.2 ± 46.3	26.2 ± 5.7	32.8 ± 6.6
Fitted QCD	435.9 ± 525.6	0.0 ± 0.0	0.0 ± 0.0
		Monte Carlo Expectation	
MC exp. SM events	8054.7	1160.3	561.7
MC exp. top events	3382.1	281.0	447.7
MC exp. W and Z events	3987.6	842.3	72.7
MC exp. other BGs events	249.1	37.0	41.3
Data-driven QCD	435.9	0.0	0.0

Table 33: Background-only fit results for the hard single electron validation regions, for an integrated luminosity of 4.7 fb^{-1}. The errors shown are the Monte Carlo statistical plus systematic uncertainties. The pure Monte Carlo expecation is given for comparison.

Single Muon	**High m_T VR**	**E_T^{miss} VR**	
	Top Quark	W Boson	Top Quark
Observed events	7088	1020	428
		Fit Results	
Fitted bkg events	7298.0 ± 152.8	1038.0 ± 37.7	474.9 ± 11.6
Fitted top events	2884.0 ± 111.9	192.1 ± 14.5	371.1 ± 14.8
Fitted W and Z events	4148.8 ± 143.5	816.9 ± 34.0	74.6 ± 9.5
Fitted other BGs events	229.6 ± 45.8	24.1 ± 5.1	26.1 ± 5.3
Fitted QCD	35.7 ± 85.0	5.0 ± 11.5	3.2 ± 5.2
		Monte Carlo Expectation	
MC exp. SM events	7503.2	1120.9	493.5
MC exp. top events	3213.3	243.2	386.8
MC exp. W and Z events	3998.6	840.7	74.7
MC exp. other BGs events	255.7	32.0	28.8
Data-driven QCD	35.7	5.0	3.2

Table 34: Background fit results for the hard single muon validation regions, for an integrated luminosity of 4.7 fb^{-1}. The errors shown are the Monte Carlo statistical plus systematic uncertainties. The pure Monte Carlo expecation is given for comparison.

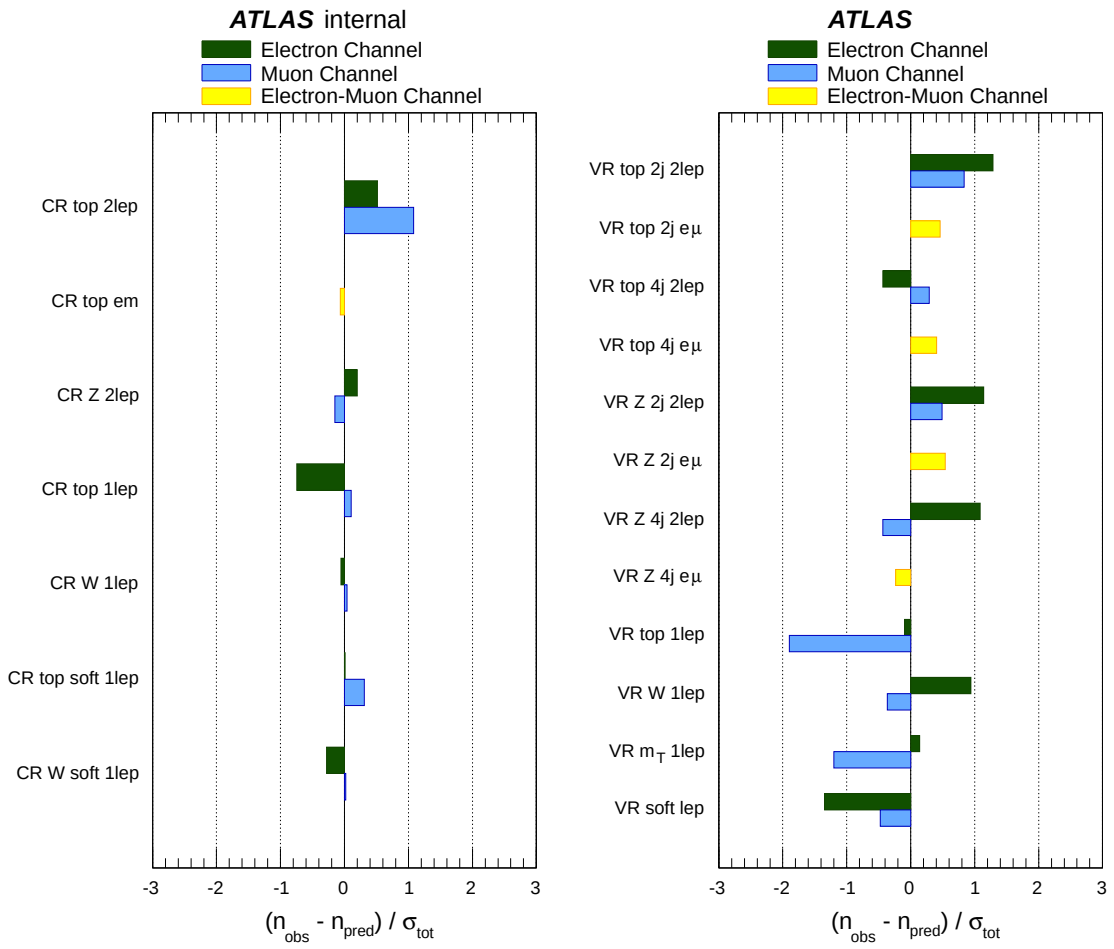

Figure 71: Difference between observed and predicted events after fit, divided by the total uncertainty (statistical + systematic) on the prediction for each control region (left) and validation region (right).

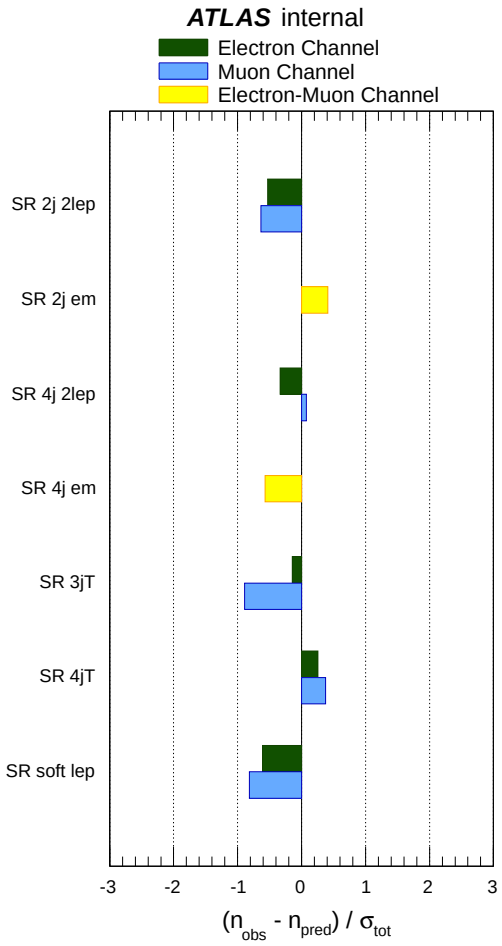

Figure 72: Difference between observed and predicted events after fit, divided by the total uncertainty (statistical + systematic) on the prediction for signal region

8 Interpretation

In this chapter, the fit results shown in the previous chapter are interpreted in various supersymmetric models, presented in chapters 4.3 and 4.4. In addition, model independent limits on the number of non standard model events using the discovery fit configuration are calculated and presented in section 8.2.
Not all final states included in the combined fit yield sensitivity for each supersymmetric model studied. Therefore, only signal regions, which contribute significantly to the sensitivity of the model under consideration are combined for the limit setting. The question which of the signal regions should be included in the combination can be answered by kinematic arguments and will be discussed in the corresponding sections.

8.1 Statistical methods

In this section, a brief introduction on how exclusion limits are derived using the fit results is given, which follows the presentation in [121], [137] and [138].
The exclusion limits derived in this chapter are based on the CL_s method [139] [140], using the profile likelihood function, which was already introduced in equation 62. Given the total likelihood function $L(n, \theta^0|\mu, b, \theta)$, a test statistic quantifying the agreement of data and simulation, is defined based on the log likelihood ratio:

$$\Lambda(\mu, n, \theta^0) \equiv -2\ln\frac{L(n, \theta^0|\mu, \hat{\hat{b}}, \hat{\hat{\theta}})}{L(n, \theta^0|\hat{\mu}, \hat{b}, \hat{\theta})} \tag{66}$$

Here, $\hat{\mu}$, $\hat{b}$, $\hat{\theta}$ globally maximize the likelihood function, while $\hat{\hat{b}}$,$\hat{\hat{\theta}}$ maximize the likelihood function for a specific value of μ. The optimal value of the signal strength in the global maximum is constrained via

$$0 < \hat{\mu} < \mu \tag{67}$$

The lower bound naturally ensures that the number of fitted signal events does not turn negative, while the upper bound is imposed by hand. For the case of an upward fluctuation in data - leading to $\hat{\mu} > \mu$ - not constraining $\hat{\mu}$ would worsen the test statistics with respect to the signal+background hypothesis (i.e. the tested signal model with signal strength μ). As an upward fluctuation of such kind should *not* be considered as evidence against the tested model, constraining $\hat{\mu}$ like shown in relation 67 is reasonable.

In order to quantify the compatibility between data and prediction for the case, where the likelihood is maximized for a *specific* value of the signal strength, the corresponding p-value for the signal+background hypothesis is calculated via

$$p_{s(\mu)} = \int_{\Lambda(\mu),n}^{\infty} f(\Lambda|\mu)d\Lambda \tag{68}$$

where $\Lambda(\mu), n$ denotes the value of the test statistics given the number of observed events n and $f(\Lambda|\mu)$ the corresponding probability density function for a specific

value of μ, which can be obtained via Monte Carlo methods or using approximate analytical functions [141]. Therefore, integrating the probability density function from $\Lambda(\mu), n$ until infinity represents the probability that the given value of μ yields a value of the test statistics, which is larger than the one that corresponds to the observed value n (evaluated using the same signal strength μ). For the special case of the background-only hypothesis ($\mu = 0$), the corresponding p-value evaluates as

$$1 - p_b = \int_{\Lambda(0),n}^{\infty} f(\Lambda|\mu) d\Lambda \tag{69}$$

which represents the probability that the pure standard model expectation yields a larger value of the test statistics compared to the observed value with signal strenth zero. The left panel of figure 73 exemplarily shows the probability density functions of the test statistics Λ for the background-only hypothesis (f(Λ|b)) and the signal+background hypothesis (f(Λ|s+b))[65]. In addition, the observed value of the test statistics and the probabilities defined in equation 68 and 69 are shown in yellow (green) for the background-only (signal+background) hypothesis.

For the exclusion limits, the CL_s values - using equation 68 and 69 - are calculated like

$$CL_s = \frac{p_{s(\mu=1)}}{1 - p_b} = \frac{CL_{s+b}}{1 - CL_b} \tag{70}$$

For the tested value of μ, the corresponding model is excluded at a confidence level of (1-α), if $CL_s < \alpha$. The common convention for exclusion limits is to consider a model as excluded if the CL_s value is smaller than 0.05, which translates into a confidence level of 95%. In order to set exclusion limits in areas of parameter spaces, the CL_s values are calculated for each grid point - which sample the corresponding parameter space - in the various signal models.

In addition to computing exclusion limits using the nominal cross section for the signal model under consideration, upper limits on the cross section are calculated by deriving the CL_s value for *different* values of the signal strength. The particular value of the μ, that yields a 95% CL limit is translated into a cross section limit, by multiplying the signal strength with the nominal cross section. This procedure is exemplarily shown in the right panel of figure 73, where the tested signal strength is plotted on the x-axis, and the corresponding CL_b, CL_{s+b} and CL_s values are shown on the y-axis. To guide the eye, the p-value of 0.05, which corresponds to a 95% CL limit, is shown as a horizontal, red line.

[65]It should be mentioned that this sketch does not exactly represent what is done within the ATLAS collaboration and in this thesis. Given the definition of the test statistics in equation 66, it can never turn negative, because the denominator always contains the *global* maximum of the likelihood function and the logarithm is therefore always negative. In other collaborations and working groups, the denominator contains the likelihood function maximized under the condition of a vanishing signal strength. Therefore, if data looks signal-like, the numerator can become larger than the denominator and the test statistics turns negative. The shown sketch corresponds to this procedure and was chosen for illustrative reasons.

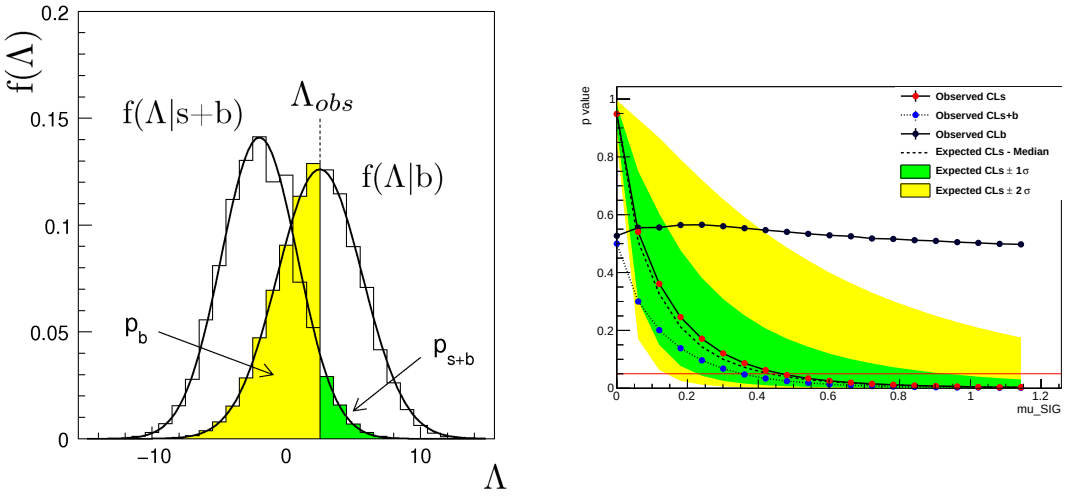

Figure 73: Left: Schematic picture explaining the CL_s method [137]. Right: Example of an upper limit calculation for a specific simplified model using the CL_s method.

In addition to equations 68 and 69, where the number of observed events is used to evaluate the test statistics for the lower integration bound, *expected* limits are calculated using the *expected* number of events for the signal+background and background-only hypotheses. In order to obtain smooth exclusion curves, an interpolation of the CL_s values for all signal grid points of each model using the delaunay triangulation [142] is performed.

8.2 Model independent limits

Model independent limits on the number of non standard model events in the signal regions are calculated using the discovery fit configuration. The number of observed events and background predictions as shown in tables 30, 39, 40 and 41 are used as inputs for the limit calculation. For this purpose, an additional parameter, quantifying the number of possible non standard model events in a given signal region is introduced. Limits at 95% CL on the number of non standard model events are calculated for each signal region. The number of non standard model events is divided by the integrated luminosity in order to obtain a limit on $\sigma_{tot} \times \epsilon$, where ϵ denotes the probability for a hypothetical non standard model physics process to end up in the given signal region[66].

Table 35 shows the 95% CL limits on the visible cross section obtained in each single hard lepton signal region. The corresponding limits for all other signal regions are listed in Appendix J. For all signal regions, the number of excluded non standard model events agrees with the expected limit on the number of non standard model events within uncertainties. For the three jet signal region, 4.4 (3.6)

[66]The term $\sigma_{tot} \times \epsilon$ is an abbreviatory notation for the product of the cross section, the branching ratio into the corresponding lepton multiplicity, the detector acceptance and the selection efficiency.

Signal channel	$\langle\epsilon\sigma\rangle^{95}_{\text{obs}}$[fb]	S^{95}_{obs}	S^{95}_{exp}	CL_B
hard electron, 3-jet	0.94	4.4	$4.3^{+2.0}_{-0.8}$	0.54
hard muon, 3-jet	0.75	3.6	$4.2^{+2.0}_{-0.7}$	0.27
hard electron, 4-jet	1.22	5.8	$5.3^{+2.6}_{-1.3}$	0.63
hard muon, 4-jet	0.95	4.5	$3.8^{+1.3}_{-0.7}$	0.75

Table 35: 95% CL limits on the visible cross section (first column), the number of signal events (second column) and the expected limit on number of signal events, taking into account the background prediction and its uncertainties (third column). The last column shows the confidence level for the background-only hypothesis. The results are shown for the hard single lepton signal regions.

events are excluded for the electron (muon) channel, while 5.8 (4.5) events in the electron (muon) channel are excluded for the four jet signal region. Due to the slight undershoot of data compared to the standard model expectation for the three jet muon signal region - as shown in table 30 - the limit on the number of signal events is slightly lower than expected. Furthermore, the slight excess of data over the background expectation in the four jet signal region yields a slightly more stringent limit on the number of non standard model backgrounds in comparison with the expectation.

For all signal regions, the CL_b values, which quantify the compatibility of measured data with the background-only hypothesis according to equation 69, show no evidence for a need of physics beyond the standard model to describe the observed data. In the single muon and 3 jets signal region, the agreement between data and standard model prediction is worst, which leads to a CL_b value of only 27%, while all other signal regions yield a CL_b value of at least 50%[67].

8.3 Exclusion limits in mSUGRA

For the mSUGRA scenario, the gaugino mass relation 47 ensures a sufficiently large lepton transverse momentum arising from weak gaugino decays, as discussed in chapter 4.2. Therefore, only the hard single lepton and dilepton signal regions are combined for the exclusion limit. The product of signal efficiencies and detector acceptances for the mSUGRA parameter space and all hard electron signal regions are shown in figure 74. The corresponding plots for the muon channels can be found in Appendix I for the single muon final state, and in the auxiliary material of [73] for the soft muon and dimuon analysis[68]. As already explained in chapter 6.3.4, the

[67] As the 3 jet single muon signal regions shows an undershoot of data compared to the standard model prediction, the relatively low CL_b value of 0.27 should not be interpreted as a slight hint for non standard model physics in this phase space region.

[68] It should be mentioned that the dilepton signal regions were not optimized for mSUGRA but for the GMSB scenario.

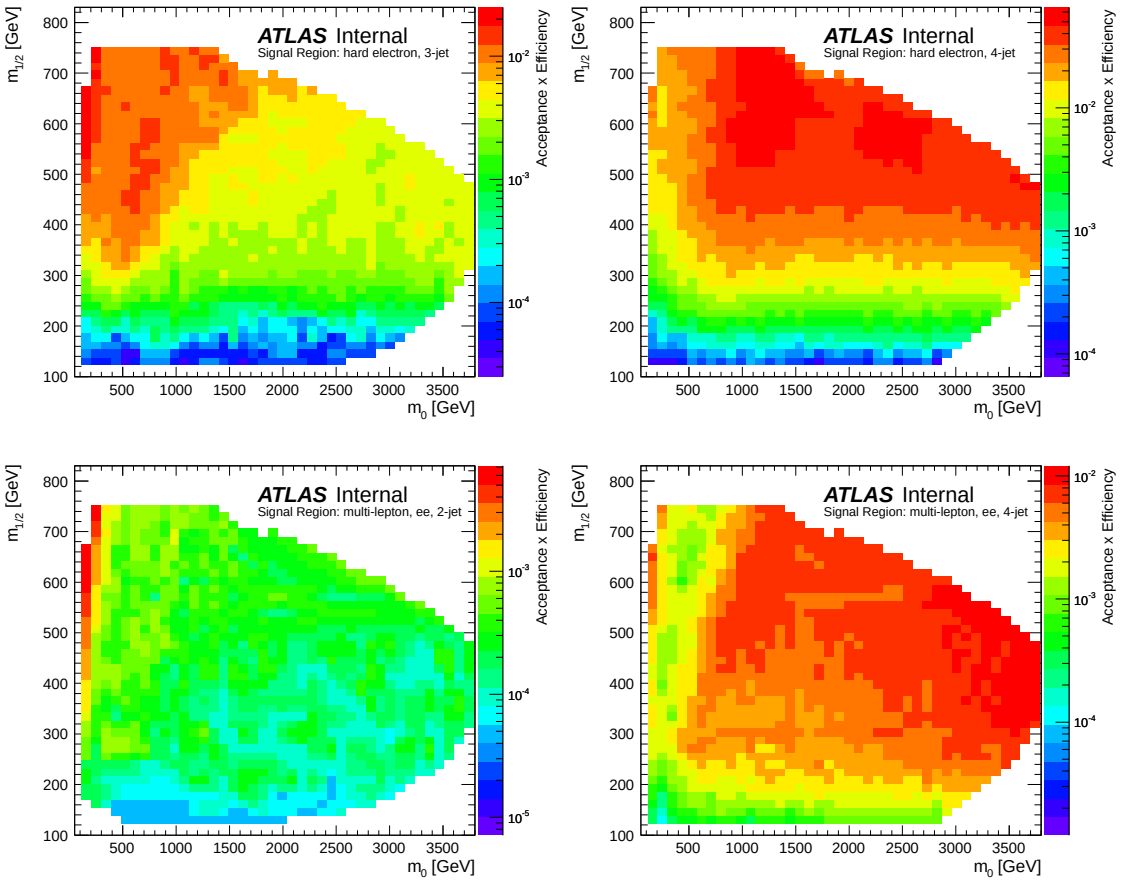

Figure 74: Detector acceptance times selection efficiency for the mSUGRA model with $\tan(\beta) = 10$, $A_0 = 0$ and $\mu > 0$ in the hard electron channels. Top left: Three jet single electron signal region. Top right: Four jet single electron signal region. Bottom left: Two jet dielectron signal region. Bottom right: Four jet dielectron signal region. [73]

different jet multiplicity requirements for the hard lepton signal regions reflect the decay kinematics in different areas of the m_0 - $m_{1/2}$ plane. The three jet region was optimized for a high discovery potential in the region with $m_0 << m_{1/2}$, while the four jet region yields a high sensitivity in the area with $m_0 >> m_{1/2}$. Comparing the top panels of figure 74, this is qualitatively illustrated by an decrease (increase) of A$\times\epsilon$ around the diagonal of $m_0 \approx m_{1/2}$ towards (away from) large m_0 values for the three jet (four jet) selection. The same statement holds for the dileptonic signal regions[69].

Figure 75 shows the expected and observed exclusion curve at 95% CL. For the given

[69]One should be cautious drawing conclusions about the expected sensitivity for the different signal regions from these distributions. What determines the sensitivity is not only the expected amount of signal, but also the expected standard model background. In addition, as the shape of the effective mass distribution is used for the exclusion fit, it is also important how the effective mass is distributed for the backgrounds and various signal points as shown in figure 67 for the hard one lepton signal regions and in Appendix J for the dilepton and soft lepton signal regions.

set of $\tan(\beta)$, A_0 and $\text{sign}(\mu)$ and $m_{1/2}$ values smaller than roughly 320 GeV, the whole range in m_0 can be excluded. The limit is independent of m_0 for m_0-values larger than roughly 2 TeV. This behaviour of the limit is somewhat expected, as the gluino is significantly lighter than the squarks for large values of m_0 and small values of $m_{1/2}$. Therefore, gluino pair production dominates the total cross section as previously shown in figure 32, which is almost independent of m_0. For m_0 values smaller than approximately 2 TeV, the limit extends to higher values of $m_{1/2}$, as gluino-squark and squark pair production start to contribute to the total cross section.

Comparing this limit with the most stringent limits before the LHC era - as shown in figure 6 - a drastic improvement regarding the excluded mSUGRA parameter space is obtained. For parameter regions fulfilling $m_{\tilde{q}} \approx m_{\tilde{g}}$, gluino and squark masses up to roughly 1.2 TeV are excluded as can be deduced from the dashed mass contours. For the squarks, this statement is true in general, as the whole parameter region, which yields squark masses below 1.2 TeV, is excluded. As the complete m_0 range can be excluded for $m_{1/2}$ values smaller than roughly 320 GeV, gluinos with masses smaller than approximately 800 GeV are excluded for the whole mSUGRA model with the given values of $\tan(\beta) = 10$, $A_0 = 0$ and $\mu > 0$.

To show the contributions of the individual signal regions to the final exclusion curve, expected limits were computed only using a subset of signal regions, which allows to quantify the benefit from the combining several signal regions. The subsets are defined as:

1. **One lepton 3J SRs**
   A combination of the three jet signal region for hard single electron and muon final states is performed

2. **One lepton 4J SRs**
   A combination of the four jet signal region for hard single electron and muon final states is performed

3. **Dilepton 2J SRs**
   A combination of the two jet signal region for electron-electron, muon-muon and electron-muon final states is performed

4. **Dilepton 4J SRs**
   A combination of the four jet signal region for electron-electron, muon-muon and electron-muon final states is performed

Within each subset, the definition of signal regions matches the ones given in tables 21 and 23. Furthermore, the binnings in $m_{\text{eff}}^{\text{incl}}$ are again as listed in table 26. The left panel of figure 76 shows the exlusion curves obtained by combining only the signal regions within each subset. The four jet single lepton signal region by far contributes most to the sensitivity over a large area of the m_0 and $m_{1/2}$ plane. The three jet single lepton region also significantly contributes at low m_0 values, due to the signal region cuts and decay-kinematics in that region, as explained in

chapter 4.3. As also explained in 4.3, dileptonic final states are comparably rare in the mSUGRA model. For decay chains where the leptons result from electroweak gaugino decays, dileptonic final states are less likely compared to the single lepton final states due to the small branching ratio of W and Z bosons into leptons. However, given the small standard model background, the sensitivity combining the dilepton four jet signal regions is comparable to the one obtained by combining the one lepton four jet regions at very high m_0 values.

In addition to the question which signal regions contribute to the expected limit, the benefit of using the $m_{\text{eff}}^{\text{incl}}$ shape as shown in table 26 is quantified by comparing this configuration to a simple cut-and-count approach. Obviously, for signal models, which yield an effective mass distribution that differs from the standard model background, this approach gives a better separation power with respect to a one-bin cut-and-count experiment within each channel. The right panel of figure 76 shows a comparison of the expected exclusion in the m_0 - $m_{1/2}$ plane, comparing the default setup with a simplified setup, where all bins listed in table 26 are unified in one bin over the corresponding range in $m_{\text{eff}}^{\text{incl}}$ for each signal region. All of these one-bin single lepton and dilepton signal regions are again combined, in order to compute the final expected limit. A flat detoriation of the expected limit of roughly 20-40 GeV in $m_{1/2}$ is observed, indicating that shape differences in the effective mass are present within the relevant areas of the mSUGRA parameter space.

Figure 77 shows the ATLAS mSUGRA limit obtained with the 0 lepton + 2-6 jet analysis [143] in the right panel, and the CMS results obtained with the hard single lepton analysis [144] in the left panel. Both limits are obtained on the same dataset as analyzed in this thesis. At low m_0 values, the ATLAS 0 lepton analysis performs slighty better, while the exclusion power is comparable the combined leptonic ATLAS analysis shown in figure 75. The CMS 1 lepton analysis shows a comparable performance at low m_0 values, while the ATLAS combined leptonic analysis excludes a significantly larger area of the m_0-$m_{1/2}$ plane at high m_0 values.

8.4 Exclusion limits in simplified models

For all simplified models, a combination of all signal regions is performed. For large mass splittings of the supersymmetric particles involved in the cascade decays, the hard single lepton signal regions yield the highest sensitivity for the one step models, while the soft lepton final state is important for compressed spectra. The hard dilepton channel is less important for the one step models, because dileptonic final states only occur, if both W bosons decay leptonically, which is suppressed due to the low branching ratio. However, for the two step models - in particular with sleptons in the decay chain - the dilepton analysis is most important due to the high probability of having two prompt leptons in the final state.

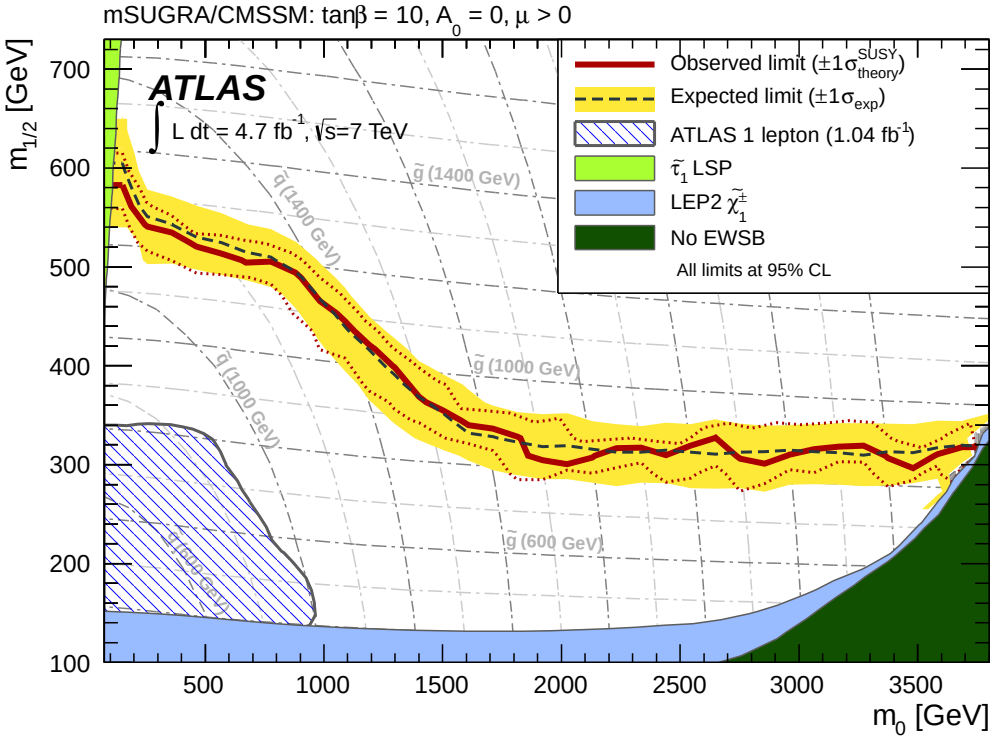

Figure 75: Expected and observed 95% CL limits in the mSUGRA model with $\tan(\beta) = 10$, $A_0 = 0$ and $\mu > 0$ as a function of the unified mass parameters m_0 and $m_{1/2}$. The dashed red lines correspond to a $\pm 1\sigma$ variation of the signal cross sections, while the yellow area indicates the $\pm 1\sigma$ variation of the fitted parameters. In addition, theoretically excluded regions and older limits by ATLAS and LEP2 are shown.

8.4.1 One step decays

Figure 78 exemplarily shows the product of detector acceptance times the selection efficiency for the one step simplified model with fixed compression factor and gluino pair production for various signal regions in the electron channel. As the charged leptons in this model arise from leptonic W boson decays, A×ϵ looks comparable for the muon channels - apart from slightly different lepton selection efficiencies - due to lepton universality. The corresponding figures for the muon channel are given in Appendix I. Figures for the other one step grids, the soft muon and dimuon analysis can be found in the auxiliary material of [73]. The four jet single hard electron signal regions has the highest A×ϵ over a large area of the shown parameter space, reaching approximately 5% for the points with a very large mass splitting. For the dilepton four jet signal region A×ϵ is roughly one to two orders of magnitude smaller. For all hard lepton final states, the efficiency drops rapidly for compressed spectra towards the diagonal of $m_{\tilde{\chi}_1^0} \approx m_{\tilde{g}}$. For the model points with the smallest mass splitting, only the soft lepton analysis contributes with an A×ϵ of order 0.1‰.
Figure 80 shows the expected and observed 95% CL exclusion limits for one step simplified models with gluino pair production and squark pair production as discussed in chapter 4.4. Furthermore, the upper limits on the cross section, calculated

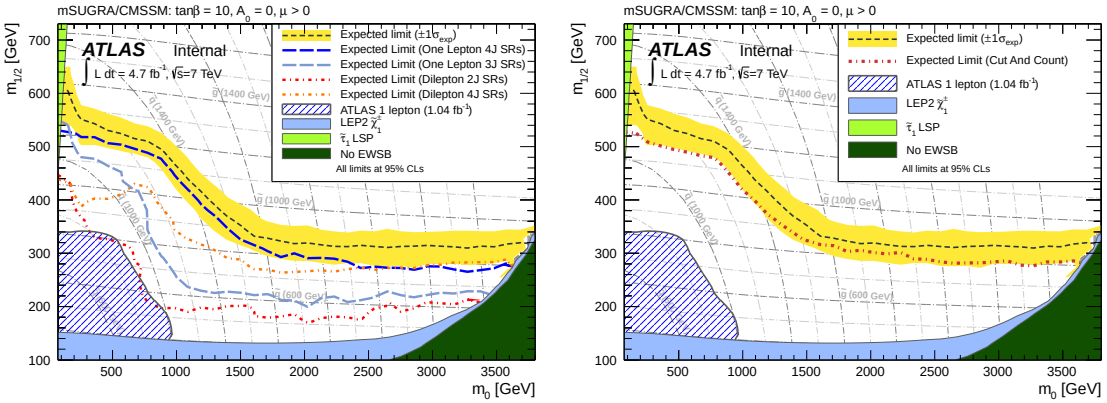

Figure 76: Left: Comparison of expected 95% CL limits in the mSUGRA model with $\tan(\beta) = 10$, $A_0 = 0$ and $\mu > 0$ as a function of the unified mass parameters m_0 and $m_{1/2}$ for four different fit configurations. The dashed black line shows the expected limit obtained with the nominal setup as already shown in figure 75, while the other dashed lines correspond to expected limits obtained only combining a subset of signal regions. Right: Comparison of expected 95% CL limits in the mSUGRA model with $\tan(\beta) = 10$, $A_0 = 0$ and $\mu > 0$ as a function of the unified mass parameters m_0 and $m_{1/2}$ for two different fit configurations. The dashed black line shows the limit obtained with the nominal setup as already shown in figure 75, while the red dashed line corresponds to the limit obtained using only one bin in $m_{\text{eff}}^{\text{incl}}$. In both plots, the yellow area indicates the $\pm$ 1σ variation of the fit results for the nominal setup. In addition, theoretically excluded regions and older exclusion limits by ATLAS and LEP2 are shown.

as explained in 8.1, are shown. In general, for both choices of the compression factor, the limits extend further for the gluino pair production, explained by the significantly larger cross sections as shown in figure 35. For the grids with a fixed compression factor, two components in the limit are visible, which result from the soft lepton signal regions close to the diagonal, and hard lepton signal regions at large mass splittings, as already indicated by the different A$\times\epsilon$ shown in figure 78. For the grids with fixed LSP mass and variable compression factors, the soft lepton channels contribute at low values of x_1, where the small mass difference between the $\tilde{\chi}_1^{\pm}$ and the $\tilde{\chi}_1^0$ leads to low lepton transverse momenta. For the grids with gluino pair production - assuming a light LSP of 60 GeV - gluinos with a mass of up to 950 GeV are ruled out for an equidistant mass splitting of $x_1 \approx 1/2$. For models with a small mass difference between the lightest chargino and the LSP, the limit on the gluino mass is worsened to roughly 700 GeV. For squark pair production, the most stringent limit on the squark mass is $m_{\tilde{q}} > 500$ GeV, again obtained for a light LSP and a compression factor of approximately 1/2.

8.4.2 Two step decays

All two step simplified models either contain sleptons or two W bosons and two Z bosons, which leads to a a large branching ratio into final states with at least two

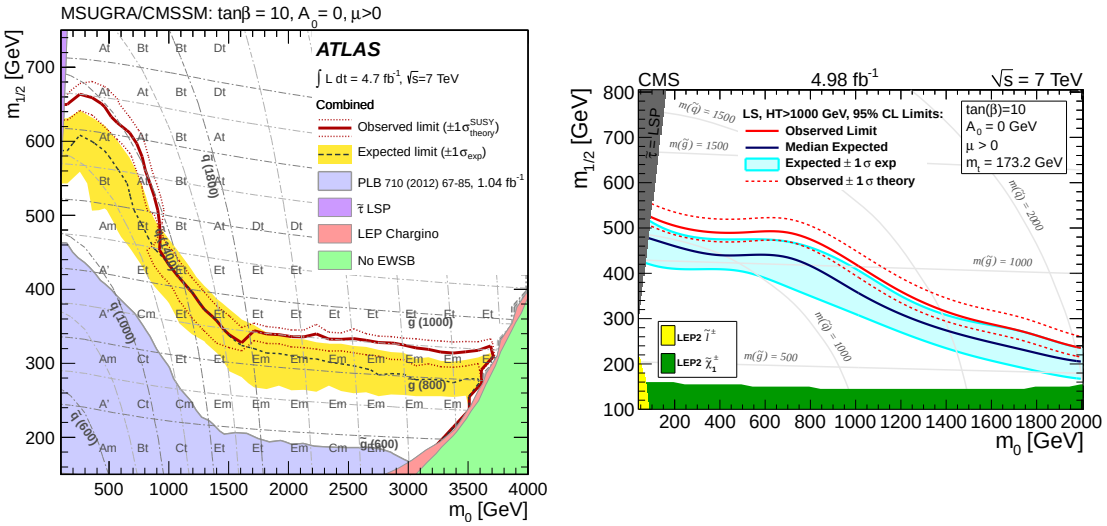

Figure 77: Left: Expected and observed 95% CL limits in the mSUGRA model with $\tan(\beta) = 10$, $A_0 = 0$ and $\mu > 0$ as a function of the unified mass parameters m_0 and $m_{1/2}$, obtained with the 0 lepton + 2-6 jets analysis at the ATLAS experiment[143]. Right: Expected and observed 95% CL limits in the mSUGRA model with $\tan(\beta) = 10$, $A_0 = 0$ and $\mu > 0$ as a function of the unified mass parameters m_0 and $m_{1/2}$, obtained with the 1 lepton + jets analysis at the CMS experiment[144].

leptons as already discussed in chapter 4.4. Therefore, the dilepton signal regions are much more important, while the soft single lepton signal regions again significantly contribute for strongly compressed mass spectra. Figure 79 again shows a comparison of A×ϵ for the different hard electron signal regions.

Figure 81 shows the expected and observed 95% CL exclusion limits for two step simplified models with gluino pair production. For the model including sleptons in the cascade, the limit extends very close to the diagonal and gluino masses up to roughly 1 TeV can be excluded for very low LSP masses. For the model including electroweak gauge bosons in the cascade, slightly lower gluino masses of roughly 900 GeV can be excluded for sufficiently large mass splittings. As no constraints on the decay of the standard model gauge bosons is imposed, the slightly lower limit on the gluino mass can be explained by the loss of events, where all W bosons and Z bosons decay hadronically, while the model including sleptons *always* yields two leptons.

Figure 81 shows the expected and observed 95% CL exclusion limits for two step simplified models with squark pair production. As for the one step models, the limits are significantly worse compared to the two step models with gluino pairs in the initial state, due to the much smaller cross section. Squark masses up to roughly 550 GeV (for the model with decays via $\tilde{\chi}_2^0$) and 700 GeV (for models with decays purely via charginos) are excluded for low LSP masses.

Interpretations of searches for supersymmetry in phenomenological models were also performed with the CMS experiment [146]. Given that the choice of simplified models is slightly different to the models analyzed by ATLAS, a direct comparison of

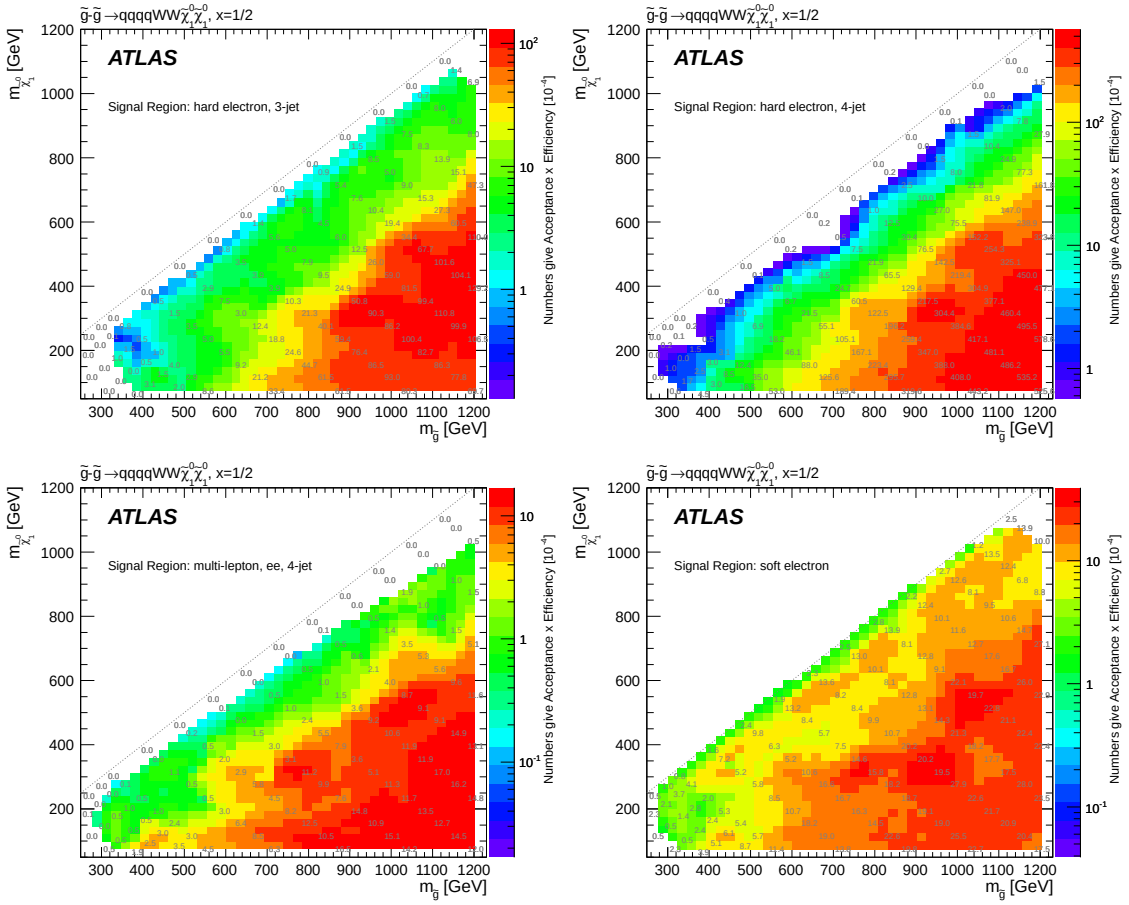

Figure 78: Detector acceptance times the selection efficiency for the one step simplified model with gluino pair production and a fixed compression factor for various signal regions in the electron channels. Top left: Three jet single electron signal region. Top right: Four jet single electron signal region. Bottom left: Four jet dielectron signal region. Bottom right: Soft electron signal region. [73]

the limits is not possible. However, comparing models that almost target the same cascade decays, the excluded masses are in the same range as derived for the ATLAS analysis.

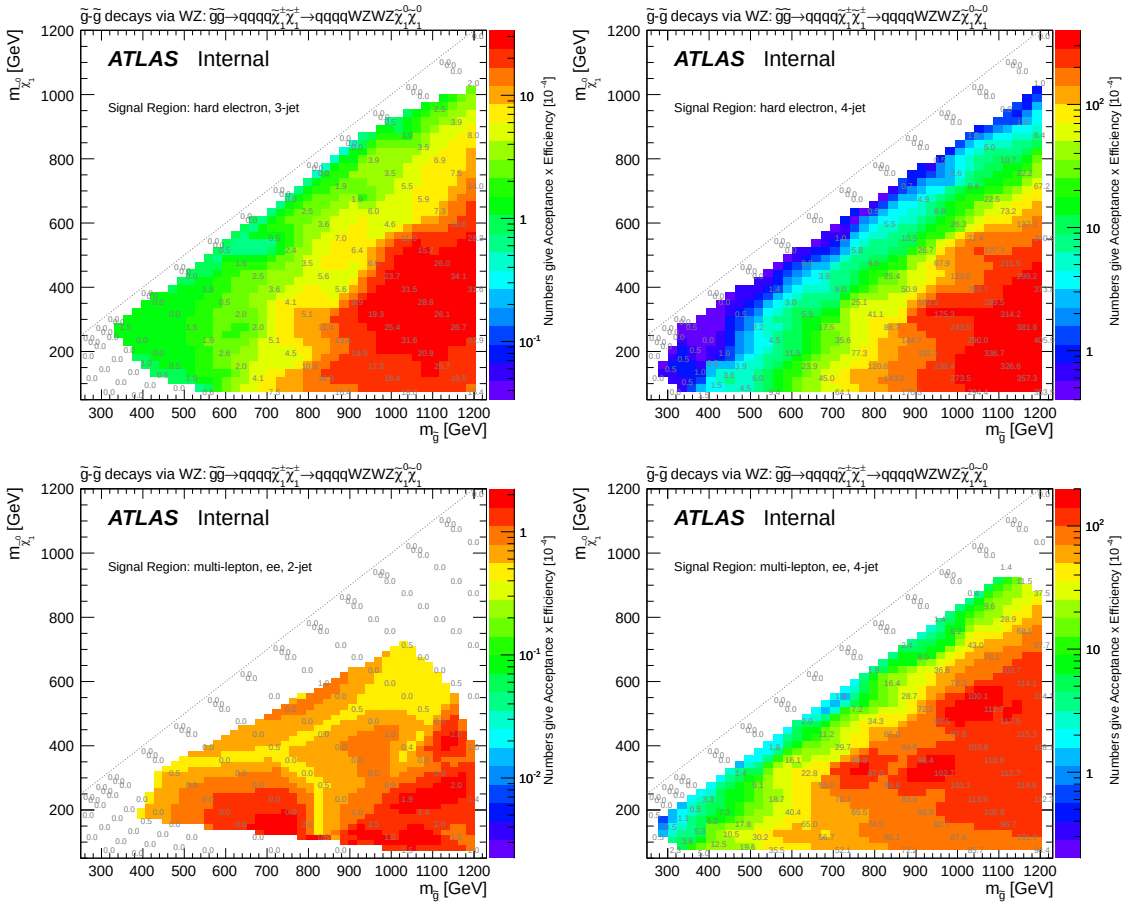

Figure 79: Detector acceptance times the selection efficiency for the two step simplified model with gluino pair production, a fixed compression factor and W and Z bosons in the cascade for various signal regions in the electron channels. Top left: Three jet single electron signal region. Top right: Four jet single electron signal region. Bottom left: Two jet dielectron signal region. Bottom right: Four jet dielectron signal region. [73]

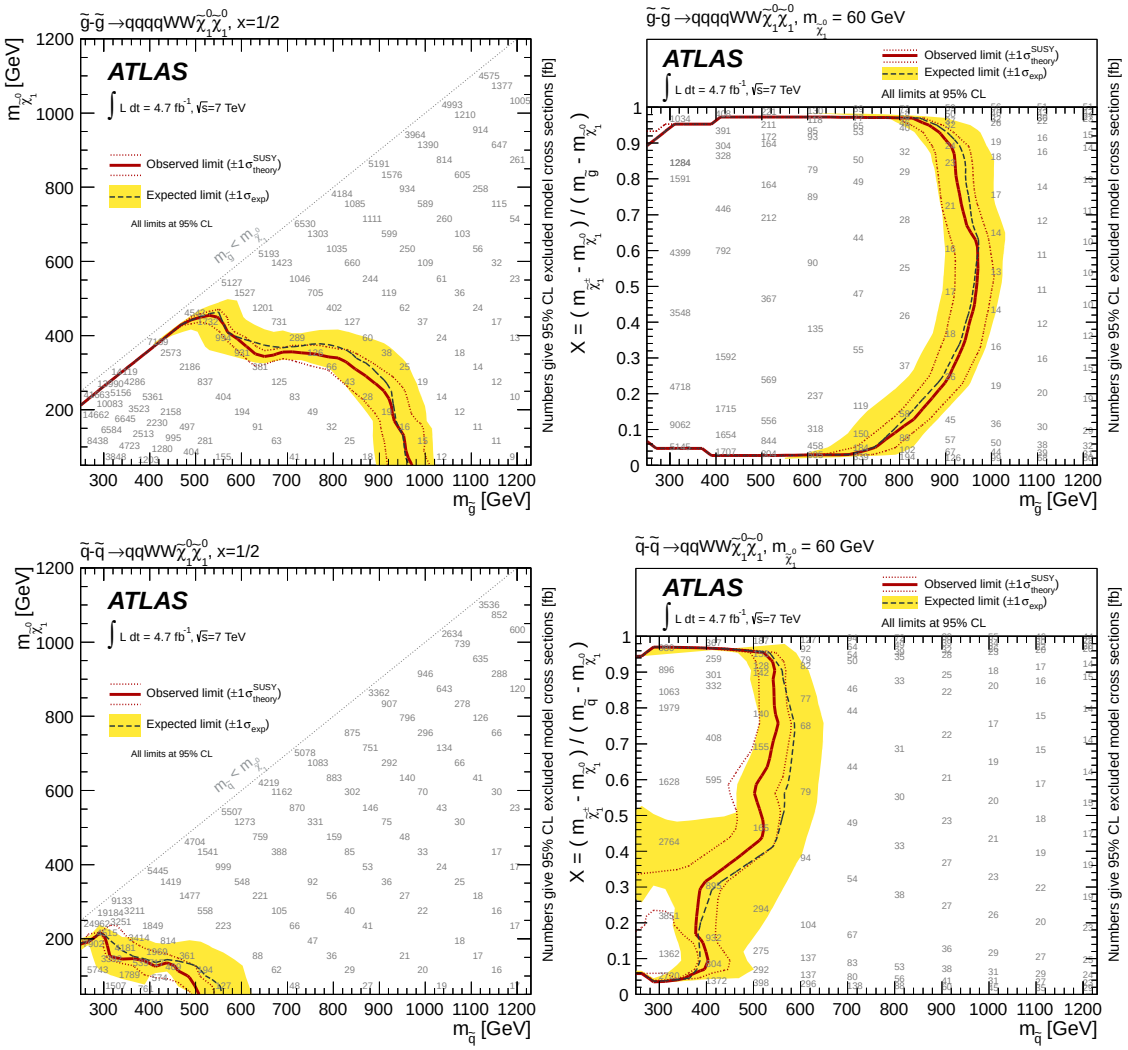

Figure 80: Expected and observed 95 % CL limits in the one step simplified models with gluino pair production (top) and squark pair production (bottom). The models with a fixed compression factor and variable LSP mass are shown on the left side, while the models with a LSP mass of 60 GeV and a variable compression factor are shown on the right side. The dashed red lines correspond to a $\pm$ 1σ variation of the cross sections, while the yellow area indicates the $\pm$ 1σ variation of the fit results.

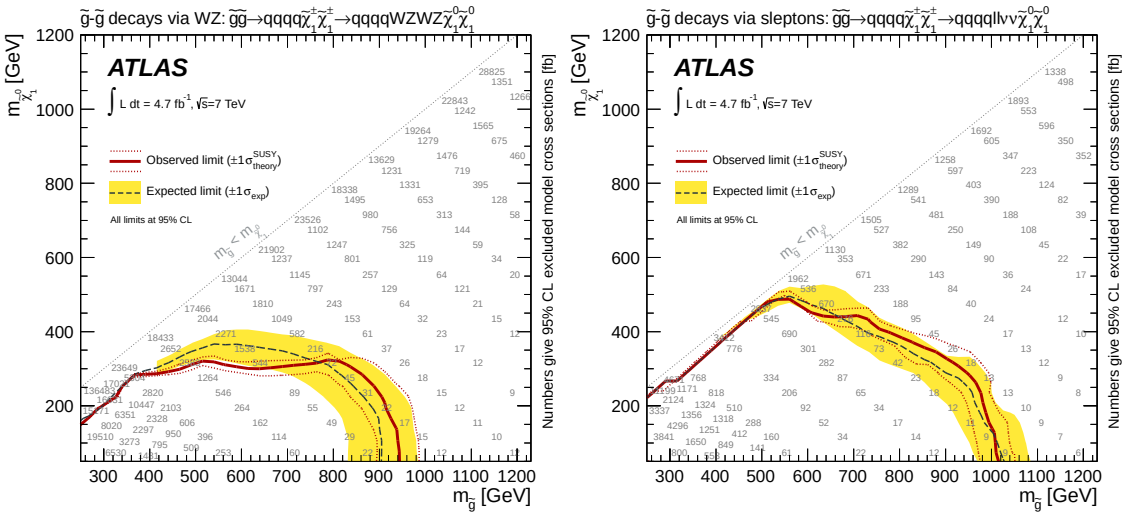

Figure 81: Expected and observed 95 % CL limits in the two step simplified models with gluino pair production, decaying via standard model vectorbosons (left) and sleptons (right). The dashed red lines correspond to a $\pm$ 1σ variation of the cross sections, while the yellow area indicates the $\pm$ 1σ variation of the fit results.

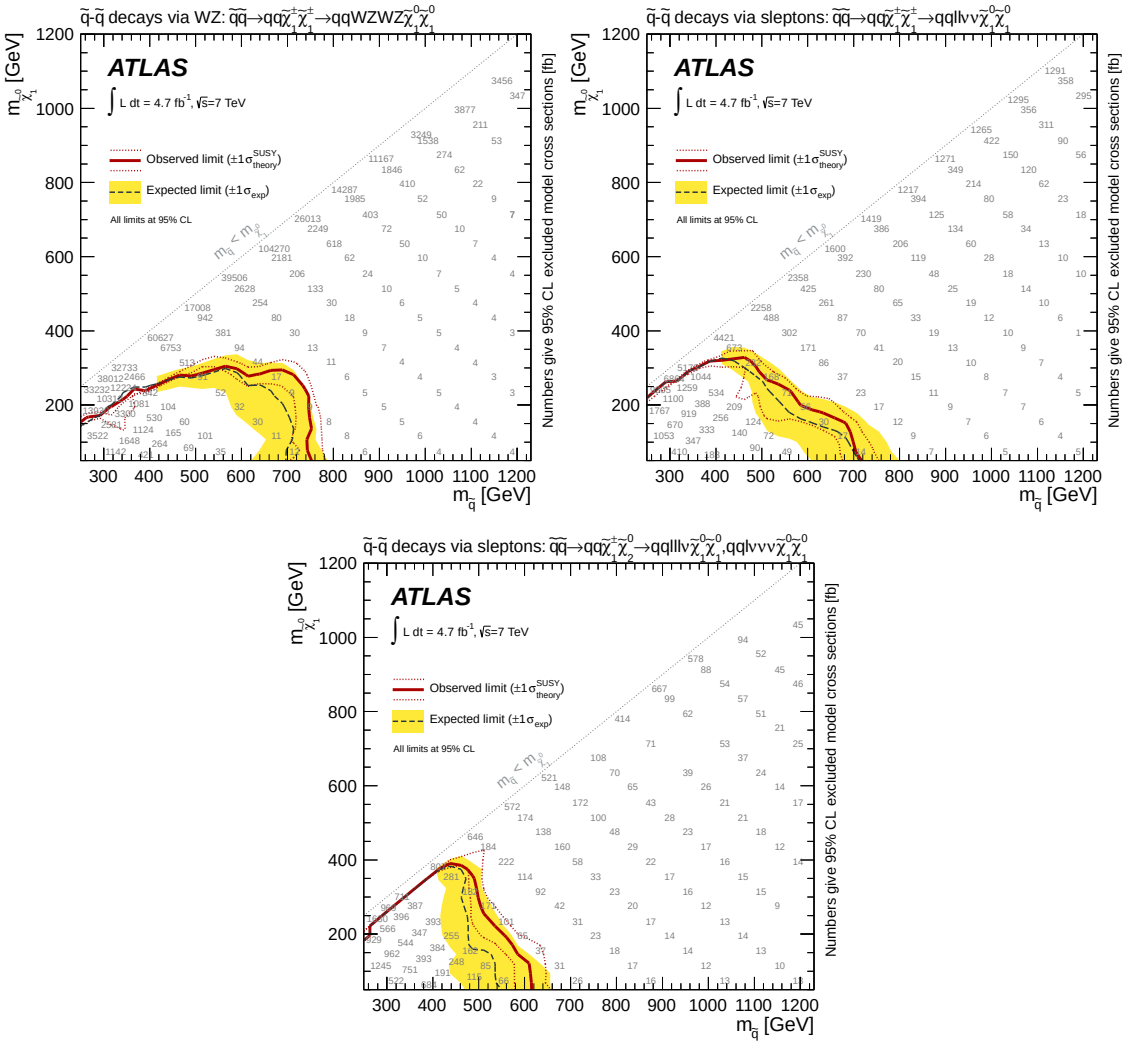

Figure 82: Expected and observed 95% CL limits in the two step simplified models with squark pair production, decaying via standard model vectorbosons (top left), sleptons and two charginos (top right) and sleptons and a chargino and a neutralino (bottom). The dashed red lines correspond to a $\pm$ 1σ variation of the cross sections, while the yellow area indicates the $\pm$ 1σ variation of the fit results.

9 Summary and Outlook

In this thesis, a search for supersymmetry in final states with exactly one isolated electron or muon, jets and missing transverse energy, based on 4.7 fb^{-1} of ATLAS data was presented. A fitting technique was developed, improving the background modelling by combining results from various different search channels with isolated leptons in the final state. As one of the major aspects of this fit, theoretical uncertainties arising from the ignorance of the renormalization scale and factorization scale were constrained by fitting the jet multiplicities in top pair events and vector boson events.

Limits were set in various supersymmetric models, either significantly improving current exclusion bounds, or constraining parameter spaces, where no limits existed so far. For the mSUGRA scenario with $\tan(\beta) = 10$, $A_0 = 0$ and $\mu > 0$, gluinos (squarks) up to 800 GeV (1.2 TeV) are excluded. For the assumption of $m_{\tilde{q}} \approx m_{\tilde{g}}$, the mass limit for the gluino is improved to 1.2 TeV as well. In addition, limits on the masses of squarks, gluinos and the lightest neutralino were derived for specific production and decay modes. For the one step simplified models, where squarks and gluinos decay via the lightest chargino, the most stringent limits on the mass of the gluino (squarks) were at approximately 950 GeV (500 GeV) for the extreme case of a light LSP and a compression factor of 1/2.

Furthermore, model independent limits were set on the number of non standard model events for all signal regions, which can be translated into limits on the visible cross section. As in all signal regions a reasonable agreement between measured data and the standard model expectation is observed, the probability that the observed number of data events arises from standard model processes is quite high, ranging between 27% - for the region with the worst agreement - and 75% for the region with the best agreement. The limits on the visible cross sections range between 0.75 fb (single muon three jet signal region) and 1.22 fb (single electron four jet region).

In the year 2012, a data amount of over 20 fb^{-1} was collected with the ATLAS experiment at a center of mass energy of $\sqrt{s} = 8$ TeV. A subset of 5.8 fb^{-1} was already analyzed in the context of a single lepton analysis and made public [145]. At the time this thesis is written, the analysis of the full dataset is still ongoing, and preliminary results show significant improvements of the sensitivity on various supersymmetric models, given the much larger amount of data and the higher center of mass energy. However, at the time this thesis was written, this analysis followed a simplified approach regarding the background extraction. Instead of using the jet multiplicity distribution in order to control the top quark and W boson background, only the total number of events for both types of backgrounds is used to extract the backgrounds in dedicated control regions. Furthermore, both backgrounds are described by a single normalization factor, not adjusting the individual normalizations of the samples with a fixed number of final state legs. This approach does - for example - not allow for constraining theoretical scale or jet energy scale uncertainties, due to the lack of variables sensitive to changes in these systematic uncertainties.

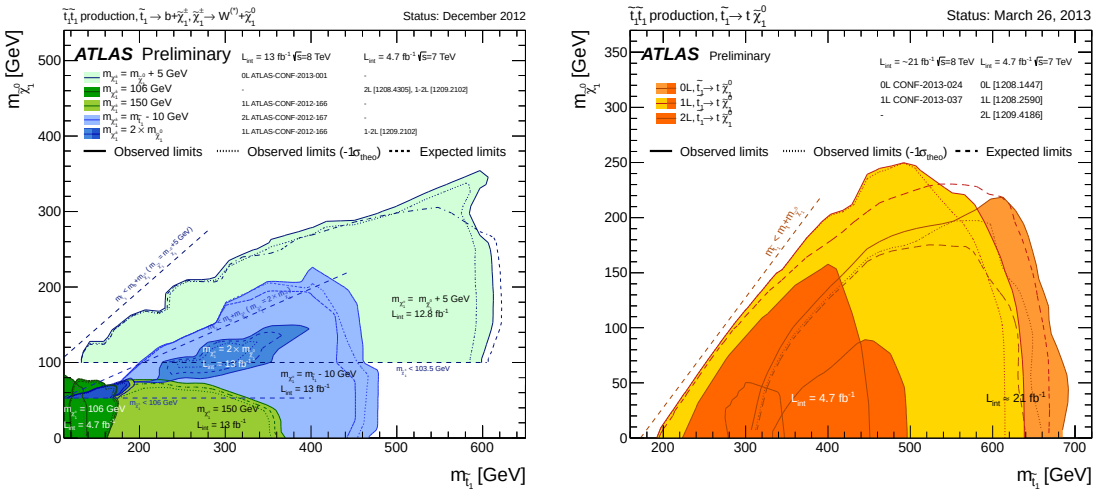

Figure 83: 95% exclusion limits in the $m_{\tilde{t}_1}$ - $m_{\tilde{\chi}_1^0}$ - plane, obtained with the ATLAS experiment in various search channels. The left figure shows the limits obtained on models where the stop decays into a b quark and chargino, with a subsequent decay of the chargino into the LSP and a W boson. Several assumptions on the mass of the lightest chargino are studied. The right figure shows the limits obtained on models where the stop quark directly decays into the LSP and a top quark [147].

Given the long shutdown phase of the LHC in 2013/2014, a further analysis of the 2012 dataset, incorporating more sophisticated methods to improve the background prediction and sensitivity, seems desirable.

Given the discovery of the Higgs like resonance with a mass of roughly 125 GeV one the one hand, and the fact that no evidence for physics beyond the standard model was observed so far on the other hand, the focus of searches for supersymmetry is shifting away from the generic inclusive searches towards more specific final states. Especially the scalar top quark is of major interest, given that the loop contributions to the Higgs mass are dominated by the top quark. Therefore, a comparably light stop quark, which compensates for these large corrections seems natural. Furthermore, cosmology favours a dark matter candidate with a mass around the electroweak scale. As the most common dark matter candidate within supersymmetry is the lightest neutralino, it should not be too heavy in order to be compatible with the cosmologically favoured mass range. Several searches for a comparably light scalar top quark and a light neutralino were performed with the ATLAS experiment in various search channels. Figure 83 shows the excluded regions in the $m_{\tilde{t}_1}$ - $m_{\tilde{\chi}_1^0}$ plane, obtained with various analyses targeting the production of two stop quarks.

Given the upgrades of the ATLAS detector and the LHC[37][38], expected sensitivities were calculated for some benchmark values of the integrated luminosity and a center of mass energy of 14 TeV [148]. Concerning supersymmetry, it was already argued that searches for scalar top quarks and light neutralinos are of major importance. For the Higgs sector, the next goal is to measure the properties of the Higgs

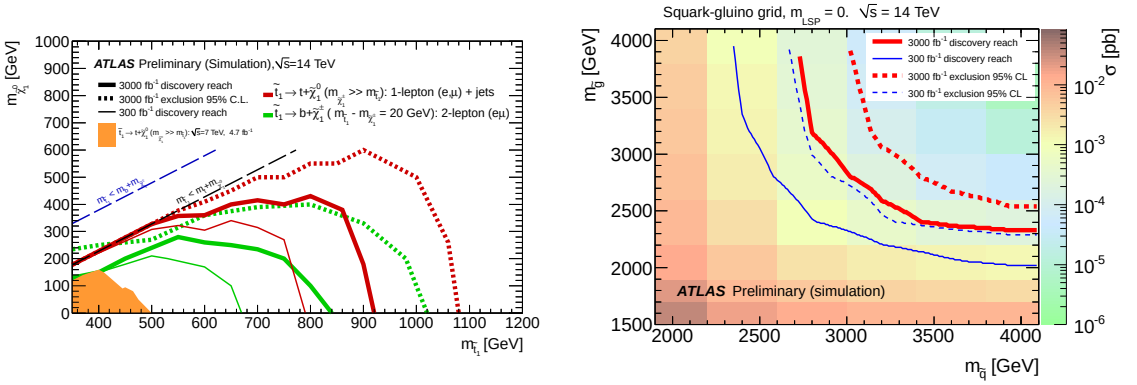

Figure 84: Expected 5σ discovery and 95% exclusion reaches in the $m_{\tilde{t}_1}$ - $m_{\tilde{\chi}_1^0}$ - plane (left) and $m_{\tilde{q}}$ - $m_{\tilde{g}}$ - plane (right) for a center of mass energy of 14 TeV and integrated luminosities of 3000 fb^{-1} and 300 fb^{-1} [148].

like resonance in order to test the compatibility with the standard model Higgs boson.

The left panel of figure 84 shows the 5σ discovery and 95% exclusion reaches in the $m_{\tilde{t}_1}$ - $m_{\tilde{\chi}_1^0}$ - plane obtained with hypothetical 3000 fb^{-1} of collected data, obtained with the 1 lepton + jets (dileptonic) analysis , targeting the decay of the stop quark into a top quark and the LSP (the decay of the stop quark into the lightest chargino and a bottom quark). For both channels, stop quarks with masses around 1 TeV can be excluded for a sufficiently large mass splitting. The right panel of 84 shows the 5σ discovery and 95% exclusion reaches in the $m_{\tilde{q}}$ - $m_{\tilde{g}}$ - plane for a massless LSP, obtained with the 0 lepton analysis. For the larger dataset, squarks and gluinos with masses of multiple TeV can be excluded.

The left panel of 85 shows the expected relative uncertainties on $\sigma \times$ BR for various Higgs production and decay modes, given a center of mass energy of 14 TeV and an integrated luminosity of 3000 fb^{-1} and 300 fb^{-1}. Given a dataset of 3000 fb^{-1}, a measurement of $\sigma \times$ BR with a relative uncertainty of maximal 20% can be achieved. For the $\gamma\gamma$ and ZZ channels, the signal strength can even be measured at the level of 5%. The left panel of figure 85 shows the expected measurement precision on the partial widths for several Higgs production and decay modes, not making any assumptions on the particle content of the H$\rightarrow\gamma\gamma$ and $g\rightarrow tt$ loops. Furthermore, potential BSM contributions to the total width of the Higgs are not taken into account as well.

In summary - given figure 84 and 85 - the prospects for both main aspects of the LHC physics programm (The Higgs discovery/measurements and searches of physics beyond the standard model) look very promising, justifying the time and money intense upgrade plans for the upcoming decade.

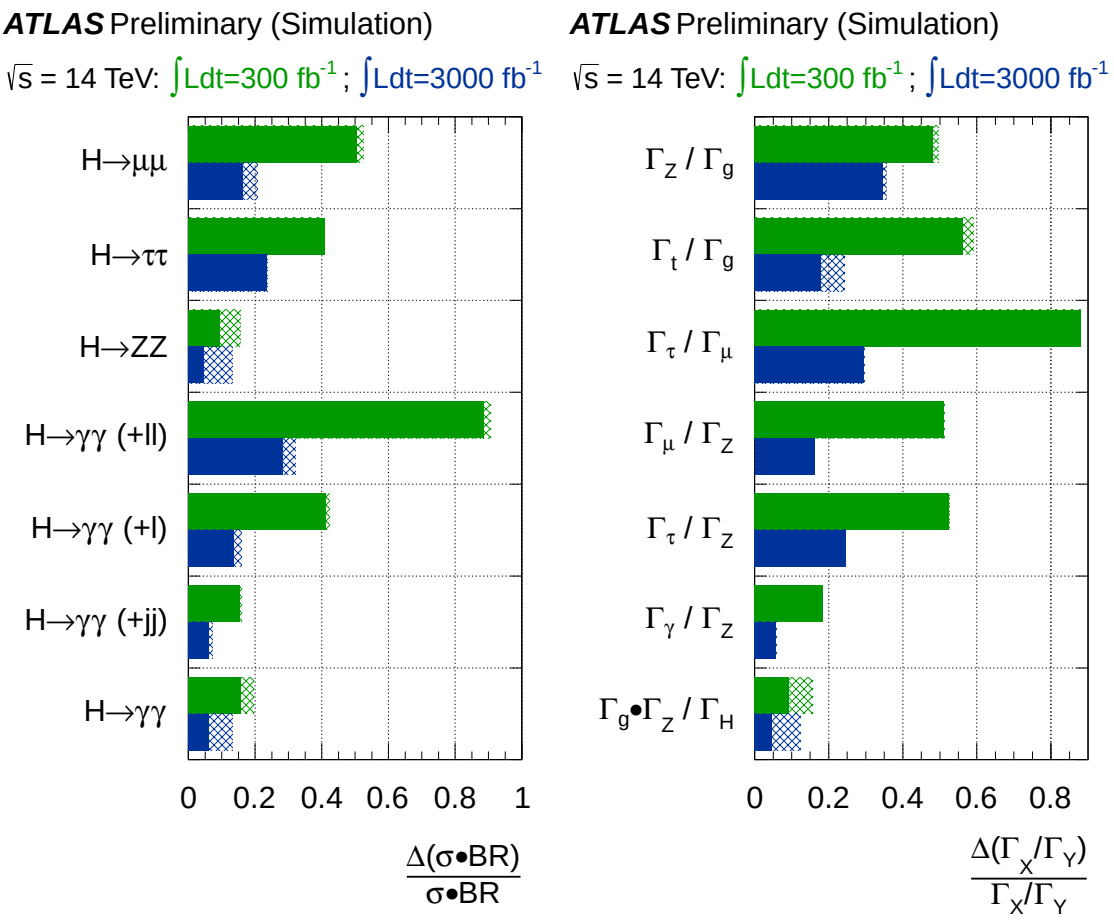

Figure 85: Expected relative uncertainties on $\sigma \times$ BR (left) and the partial widths (right) of the Higgs boson for various production and decay modes for a center of mass energy of 14 TeV and integrated luminosities of 3000 fb^{-1} and 300 fb^{-1} [148].

References

[1] "Particle Data Group", http://pdg.lbl.gov

[2] **The ATLAS Collaboration** "Observation of a New Particle in the Search for the Standard Model Higgs Boson with the ATLAS Detector at the LHC",Phys. Lett. B716 (2012) 1–29, arXiv:1207.7214v2 [hep-ex]

[3] **The CMS Collaboration**, "Observation of a new boson at a mass of 125 GeV with the CMS experiment at the LHC", Phys. Lett. B 716 (2012) 30-61

[4] S.L. Glashow: Nucl. Phys. 22 (1961) 279.
A. Salam: Phys. Rev. 127 (1962) 331.
S. Weinberg: Phys. Rev. Lett. 19 (1967) 1264.

[5] J. W. F. Valle, "Neutrino physics overview", arXiv:0608101 [hep-ph]

[6] **The ALEPH Collaboration, the DELPHI Collaboration, the L3 Collaboration, the OPAL Collaboration, the SLD Collaboration, the LEP Electroweak Working Group, the SLD electroweak, heavy flavour groups**, "Precision Electroweak Measurements on the Z Resonance", Phys. Rept. 427 (2006) 257–454, arXiv:0509008 [hep-ex]

[7] J. Wess and B. Zumino, "A Lagrangian Model Invariant Under Supergauge Transformations", Phys. Lett. B49 (1974) 52

[8] J. Wess and B. Zumino, "Supergauge Transformations in Four-Dimensions", Nucl. Phys. B70 (1974) 39-50

[9] Stephen P. Martin, "A Supersymmetry Primer", arXiv:9709356v6 [hep-ph]

[10] U. Ellwanger, C. Hugonie, A. M. Teixeira, "The Next-to-Minimal Supersymmetric Standard Model", Phys. Rept. 496 (2010) 1–77, arXiv:0910.1785 [hep-ph]

[11] J. E. Kim and H. P. Nilles, "The mu Problem and the Strong CP Problem", Phys. Lett. B138 (1984) 150.

[12] J. Ellis, J.R. Espinosa, G.F. Giudice, A. Hoecker and A. Riotto, "The Probable Fate of the Standard Model", Phys. Lett. B679 (2009) 369–375, arXiv:0906.0954 [hep-ph]

[13] Pijushpani Bhattacharjee et al., "Sizing-up the WIMPs of Milky Way : Deriving the velocity distribution of Galactic Dark Matter particles from the rotation curve data", arXiv:1210.2328v1 [astro-ph]

[14] Douglas Clowe et al., "A direct empirical proof of the existence of dark matter ", arXiv:0608407 [astro-ph]

[15] http://www.mpa-garching.mpg.de/galform/presse/

[16] **The WMAP Collaboration**, "Seven-Year Wilkinson Microwave Anisotropy Probe (WMAP) Observations: Cosmological Interpretation ", Astrophys. J. Suppl. 192 (2011) 18, arXiv:1001.4538 [astro-ph.CO].

[17] R. D. Peccei, "The Strong CP Problem and Axions", arXiv:0607268 [hep-ph]

[18] G. Bertone, D. Hooper and J. Silk, "Particle Dark Matter: Evidence, Candidates and Constraints", Phys. Rept. 405 (2005) 279–390, arXiv:0404175 [hep-ph]

[19] M. Milgrom, "The MOND Paradigm", arXiv:0801.3133 [astro-ph]

[20] **The ATLAS Collaboration**, "Search for a heavy neutral particle decaying into an electron and a muon using 1 fb^{-1} of ATLAS data", EPJC 71 (2011) 1809

[21] **The ATLAS Collaboration**, "Constraining R-parity violating Minimal Supergravity with stau_1 LSP in a four lepton final state with missing transverse momentum", ATLAS-CONF-2012-035 https://cdsweb.cern.ch/record/1432202

[22] A. Yu. Smirnov, F. Vissani, "Upper bound on all products of R-parity violating couplings λ' and λ" from proton decay", arXiv:9601387[hep-ph]

[23] **The D0 Collaboration**, V.Abazov, et al. "Search for squarks and gluinos in events with jets and missing transverse energy using 2.1 fb^{-1} of ppbar collision data at $\sqrt{(s)} = 1.96$ TeV", Phys. Lett. B660 (2008) 449–457 , arXiv:0712.3805v2 [hep-ex]

[24] http://lepsusy.web.cern.ch/lepsusy/

[25] **The D0 Collaboration**, V.Abazov, et al. "Search for associated production of charginos and neutralinos in the trilepton final state using 2.3 fb^{-1} of data ", Phys. Lett. B680 (2009) 34–43, arXiv:0901.0646 [hep-ex]

[26] L. Evans, P. Bryant: "LHC Machine". In: Journal of Instrumentation. 3, Nr. 8, 2008, S. S08001

[27] https://twiki.cern.ch/twiki/bin/view/AtlasPublic/LuminosityPublicResults

[28] John C. Collins, Davison E. Soper and George F. Sterman, "Factorization for Short Distance Hadron - Hadron Scattering", Nucl.Phys. B261 (1985) 104

[29] http://aliweb.cern.ch/

[30] J.L. Caron, "CERN Accelerator Complex (operating and approved projets). Chaine des accelerateurs du CERN (en fonctionnement et avec les projets aprouves).", http://cds.cern.ch/record/841493

[31] http://cms.web.cern.ch/

[32] **The ATLAS Collaboration**, 2008 "The ATLAS Experiment at the CERN Large Hadron Collider", JINST 3 S08003

[33] **The ATLAS Collaboration**, "Luminosity Determination in pp Collisions at sqrt(s) = 7 TeV using the ATLAS Detector in 2011", ATLAS-CONF-2011-116

[34] **The ATLAS Collaboration** , " Performance of the ATLAS inner Detector Track and Vertex Reconstruction in the High Pile-Up LHC Environment", ATLAS-CONF-2012-042

[35] **The ATLAS Collaboration**, "Jet energy resolution in proton-proton collisions at $\sqrt{s}$ = 7 TeV recorded in 2010 with the ATLAS detector", arXiv:1210.6210 [hep-ex]

[36] R. Achenbach et al., "The ATLAS Level-1 Calorimeter Trigger", 2008 JINST 3 P03001

[37] **The ATLAS Collaboration** , "Letter of Intent for the Phase-I Upgrade of the ATLAS Experiment", CERN-LHCC-2011-012 ; LHCC-I-020

[38] C. Buttar and D. della Volpe, "Letter of Intent for the Phase-II Upgrade of the ATLAS Experiment", ATL-COM-UPGRADE-2012-040

[39] https://indico.cern.ch/conferenceDisplay.py?confId=223756

[40] T. Sjoestrand, S. Mrenna and P. Skands , "PYTHIA 6.4 Physics and Manual", arXiv:0603175 [hep-ph]

[41] http://geant4.cern.ch/

[42] **The ATLAS Collaboration**, "The ATLAS Simulation Infrastructure", arXiv:1005.4568v1 [hep-ex]

[43] **The ATLAS Collaboration**, "Search for Supersymmetry in Events with Three Leptons and Missing Transverse Momentum in $\sqrt{s}$=7 TeV pp Collisions with the ATLAS Detector", Phys. Rev. Lett. 108, 261804 (2012)

[44] http://madgraph.hep.uiuc.edu/

[45] C. Guetschow and Z. Marshall, "Setting limits on supersymmetry using simplified models", arXiv:1202.2662 [hep-ex]

[46] http://web.physik.rwth-aachen.de/service/wiki/bin/view/Kraemer/SquarksandGluinos

[47] W. Beenakker, R. Hopker, M. Spira and P.M. Zerwas, "Squark and Gluino Production at Hadron Colliders", Nucl. Phys. B492 (1997) 51–103, arXiv:9610490 [hep-ph]

[48] A. Kulesza and L. Motyka, "Threshold resummation for squark-antisquark and gluino-pair production at the LHC", Phys. Rev. Lett. 102 (2009) 111802, arXiv:0807.2405 [hep-ph]

[49] A. Kulesza and L. Motyka, "Soft gluon resummation for the production of gluino-gluino and squark-antisquark pairs at the LHC", Phys. Rev. D80 (2009) 095004, arXiv:0905.4749 [hep-ph]

[50] Wim Beenakker, Silja Brensing, Michael Krämer, Anna Kulesza, Eric Laenen and Irene Niessen, "Soft-gluon resummation for squark and gluino hadroproduction", JHEP 0912 (2009) 041, arXiv:0909.4418 [hep-ph]

[51] P. Bechtle, K. Desch, M. Uhlenbrock and P. Wienemann, "Constraining SUSY models with Fittino using measurements before, with and beyond the LHC", Eur. Phys. J. C66 (2010)

[52] O. Buchmueller, R. Cavanaugh, A. De Roeck, J.R. Ellis, H. Flaecher, S. Heinemeyer, G. Isidori, K.A. Olive, P. Paradisi, F.J. Ronga and G. Weiglein , "Predictions for Supersymmetric Particle Masses in the CMSSM using Indirect Experimental and Cosmological Constraints", JHEP 0809 (2008) 117

[53] C. Quigg, "LHC Potential vs. Energy", arXiv:0908.3660 [hep-ex]

[54] Werner Porod, "SPheno, a program for calculating supersymmetric spectra, SUSY particle decays and SUSY particle production at e+ e- colliders", arXiv:0301101v4 [hep-ph]

[55] Irene Niessen, "Supersymmetric Phenomenology in the mSUGRA Parameter Space", arXiv:0809.1748 [hep-ph]

[56] K. Choi, H. P. Nilles, "The Gaugino Code", arXiv:0702146 [hep-ph]

[57] M. Aliev et al., "– HATHOR – HAdronic Top and Heavy quarks crOss section calculatoR", Comput.Phys.Commun.182:1034-1046, 2011

[58] C. Meyer, "Suche nach Supersymmetrie mit Gaugino-Massenspektren in und jenseits von mSUGRA im 1-Lepton-Kanal am ATLAS-Detektor", Diplomarbeit an der Rheinischen Friedrich Wilhelms Universitaet 2009

[59] http://www-d0.fnal.gov/Run2Physics/top/top_public_web_pages/top_feynman_diagrams.html

[60] K. Melnikov and F. Petriello, "Electroweak gauge boson production at hadron colliders through $O(\alpha_{s^2})$", Phys. Rev. D74 (2006) 114017, arXiv:0609070 [hep-ph]

[61] S. Pratt and S. D. Gupta, "Statistical models of nuclear fragmentation", Phys. Rev. C62 (2000) 044603

[62] T. Sjoestrand, S. Mrenna and P. Skands, "A Brief Introduction to PYTHIA 8.1", Comput.Phys.Commun. 178 (2008) 852-867

[63] G. Corcella et al., "HERWIG 6: An event generator for hadron emission reactions with interfering gluons (including supersymmetric processes)", JHEP 01 (2001) 010, arXiv:0011363 [hep-ph]

[64] M.L. Mangano, M. Moretti, F. Piccinini, R. Pittau, and A. Polosa, "ALPGEN, a generator for hard multiparton processes in hadronic collisions", JHEP 07 (2003) 001, arXiv:0206293 [hep-ph]

[65] S. Frixione and B. R. Webber, "Matching NLO QCD computations and parton shower simulations", JHEP06(2002)029

[66] P. Nason, "Recent developments in POWHEG", arXiv:1001.2747 [hep-ph]

[67] M. Hohlfeld, M. Lungwitz, C. Meyer and T. Mueller, "Estimating theory uncertainties in W/Z+jets and ttbar+jets events using the Alpgen generator", ATL-COM-PHYS-2012-070

[68] C. Berger et al., "Next-to-Leading Order QCD Predictions for W+3-Jet Distributions at Hadron Colliders", Phys. Rev. D80 (2009) 074036, arXiv:0907.1984 [hep-ph]

[69] A. Schalicke and F. Krauss, "Implementing the ME+PS merging algorithm", JHEP 07 (2005) 018, arXiv:0503281 [hep-ph]

[70] A.D. Martin, W.J. Stirling, R.S. Thorne and G. Watt, "Update of Parton Distributions at NNLO", Phys. Lett. B652 (2007) 292

[71] **The ATLAS Collaboration**, "Search for supersymmetry in final states with jets, missing transverse momentum and one isolated lepton in $\sqrt{s}$=7 TeV pp collisions using 1 fb^{-1} of ATLAS data", PRD 85 (2012) 012006

[72] W. Beenakker, R. Hopker, M. Spira, P.M. Zerwas, "Squark and gluino production at hadron colliders", Nucl. Phys. B492 (1997), 51.

[73] **The ATLAS Collaboration**, "Further search for supersymmetry at $\sqrt{s}$=7 TeV in final states with jets, missing transverse momentum, and isolated leptons with the ATLAS detector", PRD 86 (2012) 092002

[74] **The ATLAS Collaboration**, "Search for squarks and gluinos with the ATLAS detector in final states with jets and missing transverse momentum using 4.7 fb^{-1} of $\sqrt{s}$ = 7 TeV proton-proton collision data", Phys.Rev. D87 (2013) 012008, arXiv:1208.0949 [hep-ex]

[75] **The ATLAS Collaboration**, "Hunt for new phenomena using large jet multiplicities and missing transverse momentum with ATLAS in 4.7 fb^{-1} of $\sqrt{s}$ = 7 TeV proton-proton collisions", JHEP 1207 (2012) 167

[76] **The ATLAS Collaboration**, "Search for direct production of charginos and neutralinos in events with three leptons and missing transverse momentum in $\sqrt{s}$ = 7 TeV pp collisions with the ATLAS detector", arXiv:1208.3144 [hep-ex]

[77] **The ATLAS Collaboration**, "Search for a heavy top-quark partner in final states with two leptons with the ATLAS detector at the LHC", JHEP 11 (2012) 094

[78] **The ATLAS Collaboration**, "Search for scalar bottom pair production with the ATLAS detector in pp collisions at $\sqrt{s} = 7$ TeV", PRL 108 (2012) 181802

[79] **The ATLAS Collaboration**, "Performance of the Electron and Photon Trigger in p-p Collisions at $\sqrt{s} = 7$ TeV with the ATLAS Detector at the LHC in 2011", ATLAS-CONF-2012-048

[80] **The ATLAS Collaboration**, "Performance of the ATLAS muon trigger in 2011", ATLAS-CONF-2012-099

[81] http://atlasdqm.web.cern.ch/atlasdqm/grlgen

[82] **The ATLAS Collaboration**, "Electron performance measurements with the ATLAS detector using the 2010 LHC proton-proton collision data", Eur. Phys. J. C72 (2012) 1909, arXiv:1110.3174 [hep-ex]

[83] **The ATLAS Collaboration**, "Search for supersymmetry with jets and missing transverse momentum and one or more leptons at $\sqrt{s}$=7 TeV with the ATLAS detector", ATL-PHYS-INT-2012-082

[84] **The ATLAS Collaboration**, "Identification efficiency measurement for electrons with transverse energy between 7 and 50 GeV", ATL-COM-PHYS-2011-1669

[85] **The ATLAS Collaboration**, "Electron identification efficiency dependence on pileup", ATL-COM-PHYS-2011-1636

[86] R Nicolaidou et al., "Muon identification procedure for the ATLAS detector at the LHC using Muonboy reconstruction package and tests of its performance using cosmic rays and single beam data", 2010 J. Phys.: Conf. Ser. 219 032052

[87] S. Hassani et al., "A Muon identification and combined reconstruction procedure for the ATLAS detector at the LHC using (Muonboy, STACO, MuTag) reconstruction packages" , Nuclear Instr. and Methods A572, 2007, 77-79.

[88] **The ATLAS Collaboration**, "Pile-up Depedence of the ATLAS Muon Performance", ATL-COM-PHYS-2011-1640

[89] M. Cacciari, G. P. Salam, and G. Soyez, "The anti-kt jet clustering algorithm" , JHEP 04 (2008) 063, arXiv:0802.1189 [hep-ph].

[90] **The ATLAS Collaboration**, "Properties of Jets and Inputs to Jet Reconstruction and Calibration with the ATLAS Detector Using Proton-Proton Collisions at $\sqrt{s} = 7$ TeV", ATLAS-CONF-2010-053

[91] **The ATLAS Collaboration**, "Jet energy measurement with the ATLAS detector in proton-proton collisions at $\sqrt{s} = 7$ TeV", submitted to Eur. Phys. J , arXiv:1112.6426 [hep-ex].

[92] D.W. Miller, A. Schwartzman and D. Su, "Jet-Vertex Association Algorithm", ATL-COM-PHYS-2008-008

[93] D.W. Miller, A. Schwartzman and D. Su, "Pile-up jet energy scale corrections using the jet-vertex fraction method", ATL-PHYS-INT-2009-090

[94] T. Mueller, "Suche nach Supersymmetrie im 2-Lepton-Endzustand mit dem ATLAS-Experiment" Diplomarbeit, Johannes-Gutenberg-Universitaet Mainz, 2010

[95] **The ATLAS Collaboration**, "Performance of primary vertex reconstruction in proton-proton collisions at $\sqrt{s} = 7$ TeV in the ATLAS experiment", ATLAS-CONF-2010-069

[96] **The ATLAS Collaboration**, "Search for Supersymmetry with jets and missing transverse momentum and one lepton at $\sqrt{(s)} = 7$ TeV", ATL-PHYS-INT-2011-082, 2011

[97] **The ATLAS Collaboration** ,"Search for supersymmetry with jets and missing transverse momentum and one lepton $\sqrt{s}$=7 TeV", ATL-PHYS-INT-2011-056

[98] **The ATLAS Collaboration**, "Performance of Missing Transverse Momentum Reconstruction in Proton-Proton Collisions at 7 TeV with ATLAS" Eur. Phys. J. C72 (2012)

[99] **The ATLAS Collaboration**, "Reconstruction and Calibration of Missing Transverse Energy and Performance in Z and W events in ATLAS Proton-Proton Collisions at $\sqrt{s}$=7 TeV", ATLAS-CONF-2012-101

[100] **The ATLAS Collaboration**, "Commissioning of high-performance b-tagging algorithms in pp collisions at $\sqrt{s}$=7 TeV with the ATLAS experiment", ATLAS-CONF-2011-102

[101] **The ATLAS Collaboration**, "Measuring the b-tag efficiency in a top-pair sample with 4.7 fb^{-1} of data from the ATLAS detector", ATLAS-CONF-2012-097

[102] **The ATLAS Collaboration**, "Measurement of the b-tag Efficiency in a Sample of Jets Containing Muons with 5 fb^{-1} of Data from the ATLAS Detector", ATLAS-CONF-2012-043

[103] B. P. Kersevan, E. Richter-Was, "AcerMC Monte-Carlo Generator", http://borut.web.cern.ch/borut/

[104] M. Lungwitz, "Supersymmetry searches in Dilepton Final States with the ATLAS Experiment", PhD Thesis Johannes Gutenberg-Universität Mainz 2013

[105] **The ATLAS Collaboration**, "Search for Supersymmetry with jets and missing transverse momentum and one or more leptons at $\sqrt{(s)} = 7$ TeV", ATLAS-COM-PHYS-2011-1743

[106] SUSYTools package https://svnweb.cern.ch/trac/atlasoff/browser/PhysicsAnalysis/SUSYPhys/SUSYTools/tags/SUSYTools-00-00-61

[107] J. Campbell , R.K. Ellis and D. Rainwater, "Next-to-leading order QCD predictions for W+2j and Z+2j production at the CERN LHC", Phys. Rev. D68 (2003) 094021

[108] J. M. Campbell and R. Keith Ellis, "$t\bar{t}$ W production and decay at NLO", JHEP 1207 (2012) 052

[109] A. Lazopoulos, T. McElmurry, K. Melnikov and F. Petriello, "Next-to-leading order QCD corrections to t-tbar-Z production at the LHC", Phys. Lett B666 (2008) 62

[110] J.M.Butterworth, J.R.Forshaw and M.H.Seymour, "Multiparton Interactions in Photoproduction at HERA", Z. Phys. C72 (1996) 637, arXiv:9601371 [hep-ph]

[111] J. Pumplin, D.R. Stump, J. Huston, H.L. Lai, P. Nadolsky and W.K. Tung, "New Generation of Parton Distributions with Uncertainties from Global QCD Analysis", arXiv:0201195 [hep-ph]

[112] Hung-Liang Lai, Marco Guzzi, Joey Huston, Zhao Li, Pavel M. Nadolsky, Jon Pumplin and C.-P. Yuan, "New parton distributions for collider physics", Phys. Rev. D82 (2010) 074024, arXiv:1007.2241 [hep-ph]

[113] A. Sherstnev and R.S. Thorne "Different PDF approximations useful for LO Monte Carlo generators", arXiv:0807.2132 [hep-ph]

[114] M. Bahr, S. Gieseke, M. A. Gigg, D. Grellscheid, K. Hamilton, O. Latunde-Dada, S. Platzer, P. Richardson, M. H. Seymour, A. Sherstnev, J. Tully and B. R. Webber, "Herwig++ Physics and Manual", arXiv:0803.0883

[115] A. Sherstnev and R.S. Thorne "Parton Distributions for LO Generators", Eur. Phys. J. C55 (2008) 553, arXiv:0711.2473 [hep-ph]

[116] Howard Baer, Frank E. Paige, Serban D. Protopescu and Xerxes Tata, "ISAJET 7.69: A Monte Carlo Event Generator for pp, $\bar{p}p$, and e^+e^- Reactions", arXiv:0312045 [hep-ph]

[117] FakeLeptBkg package, https://svnweb.cern.ch/trac/atlasoff/browser/PhysicsAnalysis/SUSYPhys/FakeLeptBkg

[118] K. Canmer et al., "HistFactory: A tool for creating statistical models for use with RooFit and RooStats", CERN-OPEN-2012-016

[119] W. Verkerke, D. Kirkby, "RooFit Users Manual v2.07", http://roofit.sourceforge.net/

[120] https://twiki.cern.ch/twiki/bin/view/RooStats/WebHome

[121] R. Bruneliere, M. Baak, J. Lundberg, M.C. Rammensee and T.J Khoo, "Setting exclusion limits in ATLAS supersymmetry searches with a likelihood ratio based method", ATL-PHYS-INT-2011-032

[122] https://twiki.cern.ch/twiki/bin/viewauth/AtlasProtected/HforTool

[123] **The ATLAS Collaboration**, "Jet energy measurement with the ATLAS detector in proton-proton collisions at $\sqrt{s} = 7$ TeV", arXiv:1112.6426 [hep-ex]

[124] **The ATLAS Collaboration**, "Probing the measurement of jet energies with the ATLAS detector using photon+jet events in proton-proton collisions at $\sqrt{s} = 7$ TeV", ATLAS-CONF-2012-063

[125] **The ATLAS Collaboration**, "Probing the measurement of jet energies with the ATLAS detector using Z+jet events from proton-proton collisions at $\sqrt{s} = 7$ TeV", ATLAS-CONF-2012-053

[126] JetEtmiss Group, JESUncertaintyProvider, https://twiki.cern.ch/twiki/bin/viewauth/AtlasProtected/JESUncertaintyProvider

[127] JetEtmiss Group, MultijetJESUncertaintyProvider, https://twiki.cern.ch/twiki/bin/viewauth/AtlasProtected/MultijetJESUncertaintyProvider

[128] JetEtmiss Group, JetEnergyResolutionProvider, https://twiki.cern.ch/twiki/bin/viewauth/AtlasProtected/JetEnergyResolutionProvider

[129] Flavour tagging working group, https://twiki.cern.ch/twiki/bin/viewauth/AtlasProtected/Analysis17MC11b_intermediate_release

[130] Egamma Group, https://twiki.cern.ch/twiki/bin/viewauth/AtlasProtected/EnergyRescaler

[131] Muon Combined Performance Group, https://twiki.cern.ch/twiki/bin/viewauth/AtlasProtected/MCPAnalysisGuidelinesRel17MC11a

[132] JetEtmiss Group, "MissingEt Utility package", https://svnweb.cern.ch/trac/atlasoff/browser/Reconstruction/MissingETUtility

[133] T. Eifert, "Parton-Shower uncertainty in SUSY 1-lep TFs ", ATLAS SUSY 1 lepton channel sharepoint, 19.03.12. https://espace.cern.ch/atlas-susy-etmiss/1leptonchannel/Shared%20Documents/susy_1lep_PSunc.pdf.

[134] Egamma Group, https://twiki.cern.ch/twiki/bin/viewauth/AtlasProtected/EfficiencyMeasurementsElectron_efficiencies_2011_Morio

[135] **The ATLAS Collaboration**, "Calibrated Z->e+e- mass with 2011 data", ATL-COM-PHYS-2011-1637

[136] **The ATLAS Collaboration**, "Measurement of the charge asymmetry in top quark pair production in pp collisions at $\sqrt{s} = 7$ TeV using the ATLAS detector" , Eur. Phys.J. C72 (2012) 2039 arXiv:1203.4211 [hep-ex]

[137] G. Cowan, K. Cranmer, E. Gross and O. Vitells, "Asymptotic formulae for likelihood-based tests of new physics", Eur.Phys.J.C71 (2011) 1554, arXiv:1007.1727 [physics.data-an]

[138] **The ATLAS Collaboration**, "Procedure for the LHC Higgs boson search combination in summer 2011", ATL-PHYS-PUB-2011-011

[139] T. Junk "Confidence level computation for combining searches with small statistics", Nucl. Instrum. Methods Phys. Res., Sec A 434 (1999) 435

[140] A. L. Read, "Presentation of search results: the CLs technique", Journal of Physics G: Nuclear and Particle Physics 28 (2002) n0. 10, 2693.

[141] S. Wilks, "The large-sample distribution of the likelihood ratio for testing composite hypotheses", Ann. Math. Statist. 9 (1938) 60-62

[142] B. Delaunay, "Sur la sphÃ¨re vide, Izvestia Akademii Nauk SSSR, Otdelenie Matematicheskikh i Estestvennykh Nauk", 7:793-800, 1934

[143] **The ATLAS Collaboration**, "Search for squarks and gluinos with the ATLAS detector in final states with jets and missing transverse momentum using 4.7 fb-1 of $sqrts = 7$ TeV proton-proton collision data", Phys. Rev. D 87, 012008 (2013)

[144] **The CMS Collaboration**, "Search for supersymmetry in pp collisions at $\sqrt{s} = 7$ TeV in events with a single lepton, jets, and missing transverse momentum", EPJC (2013) 73:2402

[145] **The ATLAS Collaboration**, "Search for supersymmetry at $\sqrt{s} =$ TeV in final states with jets, missing transverse momentum and one isolated lepton", ATLAS-CONF-2012-104

[146] **The CMS Collaboration**, "Interpretation of searches for supersymmetry with simplified models", arXiv:1301.2175 [hep-ex]

[147] T. Eifert, M. D'Onofrio, A. Hoecker, T. Lari, Y. Nakahama, S. Pataraia and I. Vivarelli, "SUSY mass reach and direct stop search summaries for March 26, 2013 (CERN ATLAS-SUSY seminar)", ATL-COM-PHYS-2013-339

[148] **The ATLAS Collaboration**, "Physics at a High-Luminosity LHC with ATLAS", https://cds.cern.ch/record/1472518

A Comparison of jet related variables for different choices of renormalization and factorization scale

Jet related variables on generator level for two examplary parton multiplicities, comparing samples with nominal and varied scale.

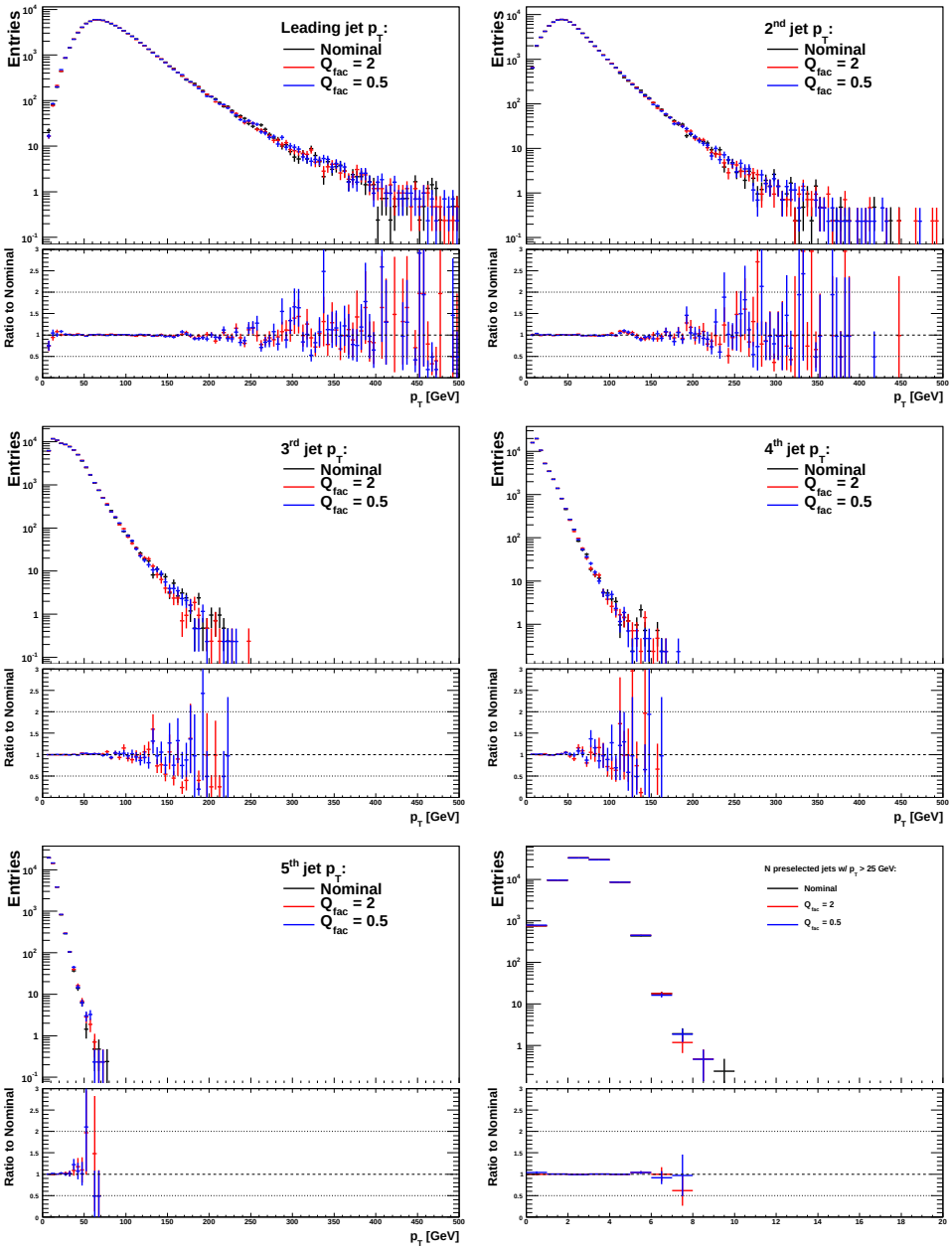

Figure 86: jet transverse momenta and multiplicity on generator level for the process $t\bar{t} \rightarrow bbll\nu\nu$ + no additional parton and different choices for the factorization scale Q_{fac}.

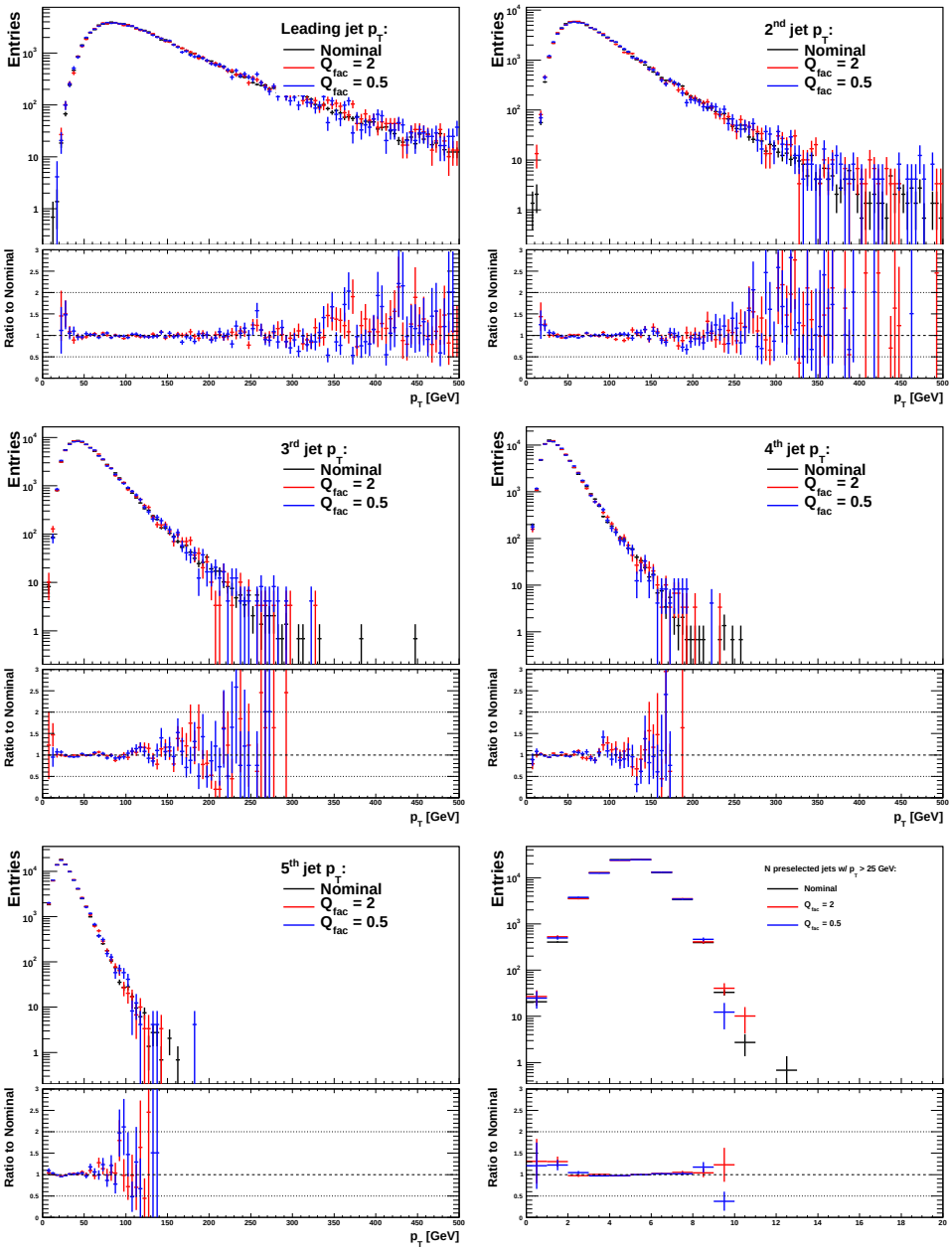

Figure 87: jet transverse momenta and multiplicity on generator level for the process $t\bar{t} \rightarrow bbll\nu\nu + 3$ additional partons and different choices for the factorization scale Q_{fac}.

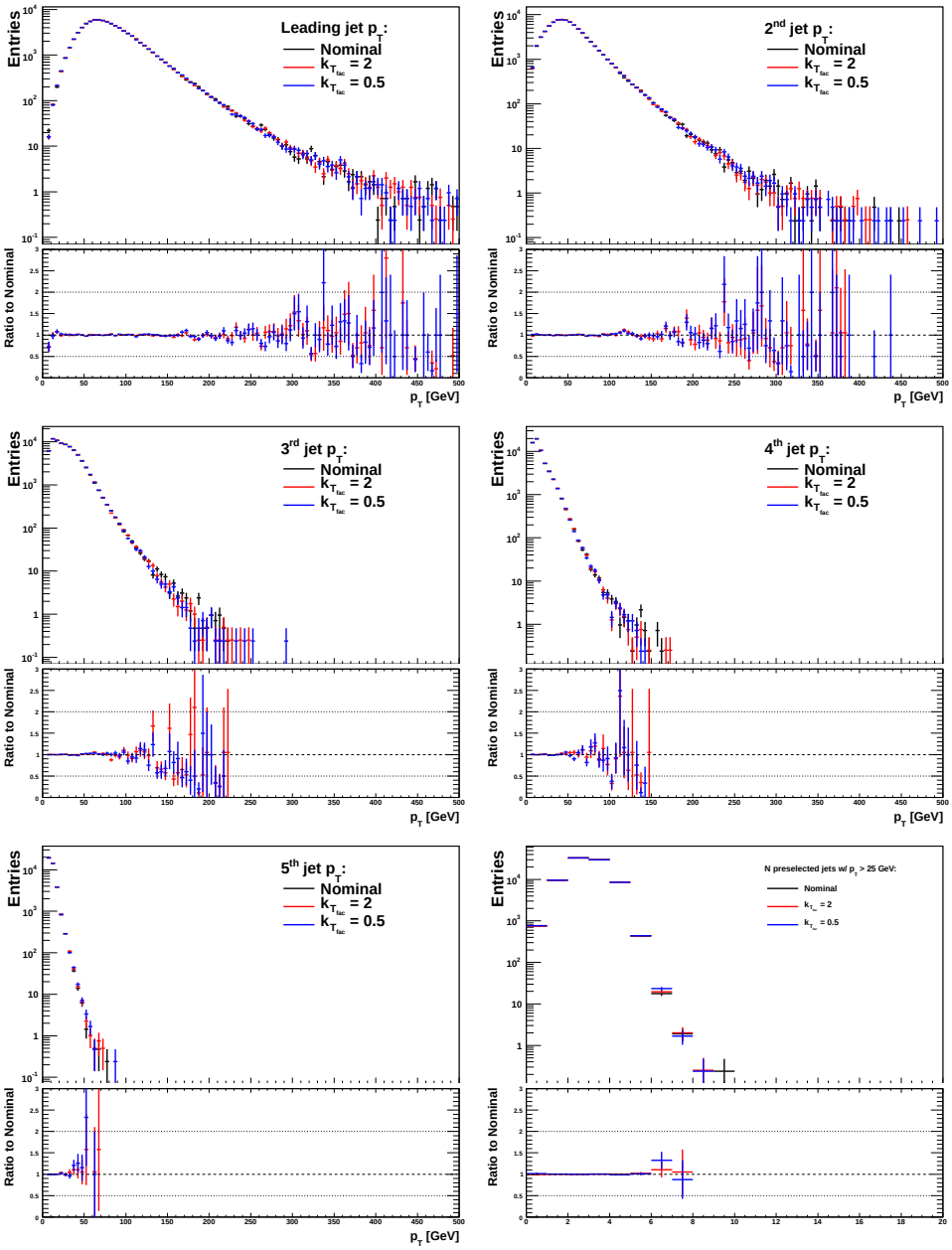

Figure 88: jet transverse momenta and multiplicity on generator level for the process $t\bar{t} \rightarrow bbll\nu\nu$ + no additional parton and different choices for the renormalization scale $k_{T_{fac}}$.

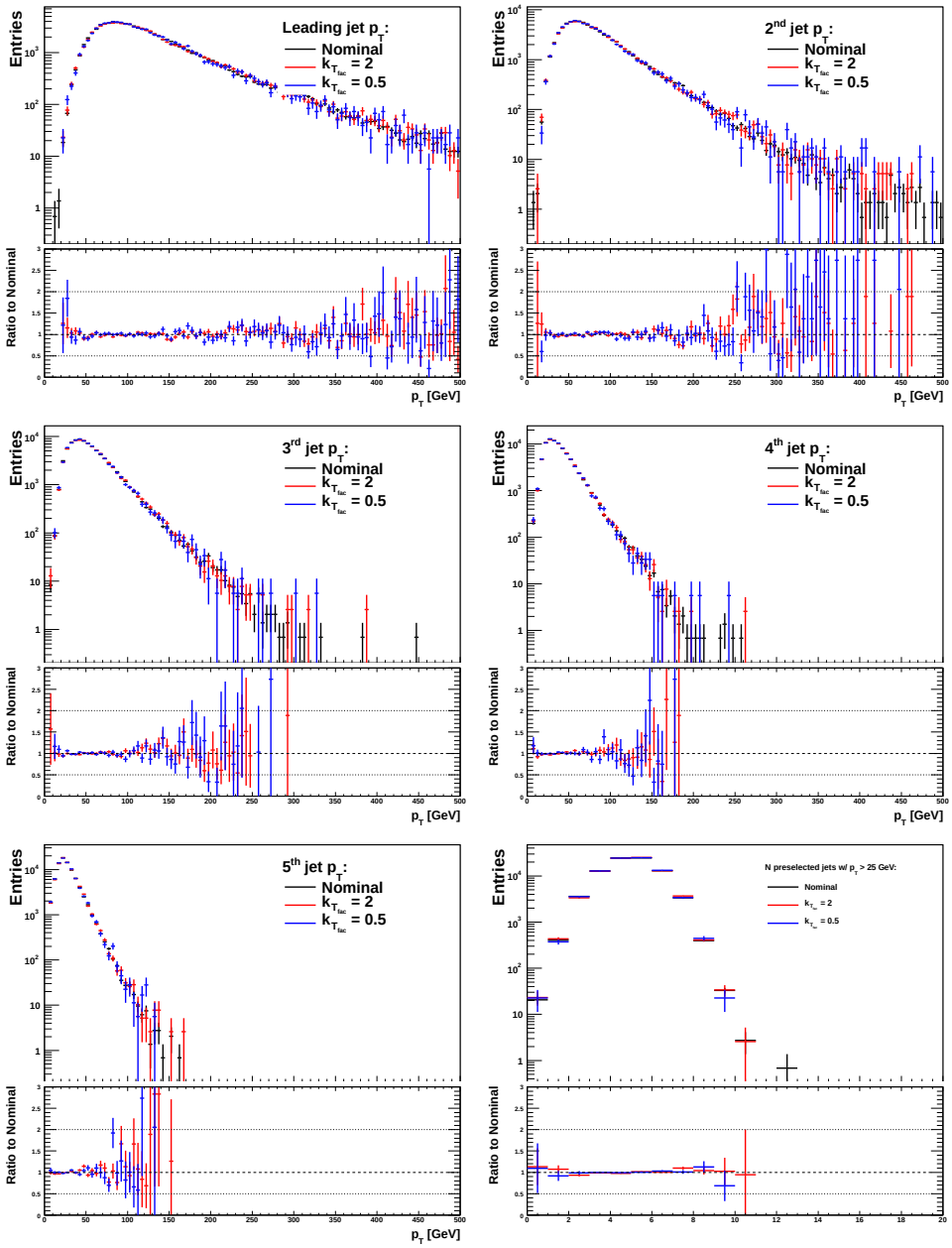

Figure 89: jet transverse momenta and multiplicity on generator level for the process $t\bar{t} \rightarrow bbll\nu\nu + 3$ additional partons and different choices for the renormalization scale $k_{T_{fac}}$.

B Packages used to define objects and corrections for the Monte Carlo simulation

Packages included in SUSYTools-00-00-61:

atlasoff/PhysicsAnalysis/D3PDTools/RootCore/tags/RootCore-00-00-31
atlasoff/PhysicsAnalysis/AnalysisCommon/ObjectSelectorCore/
tags/ObjectSelectorCore-00-00-09
atlasoff/PhysicsAnalysis/JetMissingEtID/JetSelectorTools/
tags/JetSelectorTools-00-00-11
atlasoff/PhysicsAnalysis/MuonID/MuonIDAnalysis/MuonEfficiencyCorrections/
tags/MuonEfficiencyCorrections-01-00-10
atlasoff/PhysicsAnalysis/MuonID/MuonIDAnalysis/MuonMomentumCorrections/
tags/MuonMomentumCorrections-00-05-03
atlasoff/Reconstruction/egamma/egammaEvent/tags/egammaEvent-03-06-20
atlasoff/Reconstruction/egamma/egammaAnalysis/egammaAnalysisUtils/
tags/egammaAnalysisUtils-00-02-76
atlasoff/PhysicsAnalysis/JetTagging/JetTagPerformanceCalibration/
CalibrationDataInterface/
tags/CalibrationDataInterface-00-01-02
atlasoff/DataQuality/GoodRunsLists/tags/GoodRunsLists-00-00-96
atlasoff/PhysicsAnalysis/AnalysisCommon/PileupReweighting/
tags/PileupReweighting-00-02-02
atlasoff/Reconstruction/Jet/JetUncertainties/tags/JetUncertainties-00-03-05-01
atlasgrp/CombPerf/JetETMiss/JetCalibrationTools/ApplyJetCalibration/
tags/ApplyJetCalibration-00-00-09
atlasoff/Reconstruction/Jet/JetResolution/tags/JetResolution-01-00-00
atlasoff/Reconstruction/MissingETUtility/tags/MissingETUtility-00-02-13
atlasoff/PhysicsAnalysis/AnalysisCommon/ReweightUtils/tags/ReweightUtils-00-02-06
atlasoff/Trigger/TrigAnalysis/TrigRootAnalysis/tags/TrigRootAnalysis-00-00-07

C Background-only fit results

Fit results for the background-only configuration:

```
RooFitResult: minimized FCN value: -134963,
              estimated distance to minimum: 0.000431228
              covariance matrix quality: Full, accurate covariance matrix
              Status : MINIMIZE=0

  Floating Parameter    FinalValue +/-  Error
--------------------  --------------------------
            alpha_BT    8.2123e-01 +/-  2.77e-01
            alpha_HF    1.1700e-01 +/-  4.59e-01
         alpha_JHigh   -9.0297e-01 +/-  2.71e-01
          alpha_JLow   -2.9170e-01 +/-  2.89e-01
       alpha_JMedium   -5.6379e-01 +/-  3.60e-01
         alpha_LESee    1.3750e-01 +/-  2.04e-01
         alpha_LESel    1.6230e-01 +/-  4.88e-01
         alpha_LESem    1.0827e-02 +/-  9.63e-01
         alpha_LESmm   -1.0714e-02 +/-  9.79e-01
         alpha_LESmu    9.2659e-03 +/-  1.14e+00
         alpha_LESse    1.7247e-02 +/-  5.78e-01
         alpha_LESsm   -1.2051e-02 +/-  9.93e-01
          alpha_LEee    1.2590e+00 +/-  6.20e-01
          alpha_LEel   -6.6297e-01 +/-  8.82e-01
          alpha_LEem   -5.9210e-02 +/-  8.38e-01
          alpha_LEmm    1.8984e-02 +/-  8.56e-01
          alpha_LEmu    8.9295e-03 +/-  9.91e-01
          alpha_LEse   -3.7047e-01 +/-  5.88e-01
          alpha_LEsm    4.6735e-03 +/-  9.93e-01
         alpha_LRIem   -1.1518e-02 +/-  9.47e-01
         alpha_LRImm   -1.1050e-02 +/-  8.57e-01
         alpha_LRImu   -4.2262e-02 +/-  1.01e+00
         alpha_LRIsm   -2.7316e-02 +/-  9.15e-01
         alpha_LRMem   -2.6651e-02 +/-  9.49e-01
         alpha_LRMmm    3.9411e-02 +/-  9.21e-01
         alpha_LRMmu    6.4819e-02 +/-  1.01e+00
         alpha_LRMsm   -3.0665e-02 +/-  9.66e-01
            alpha_MC   -8.6103e-01 +/-  4.68e-01
            alpha_MP    2.8320e-01 +/-  4.81e-01
      alpha_PtMinTop    5.6652e-03 +/-  1.76e-01
       alpha_PtMinWZ    1.1400e+00 +/-  6.77e-01
alpha_QCDNorm_SVTEl_nJet    4.0307e-01 +/-  4.15e-01
alpha_QCDNorm_SVTMu_nJet    3.7979e-01 +/-  6.05e-01
alpha_QCDNorm_SVWEl_nJet   -1.3298e+00 +/-  8.10e-02
alpha_QCDNorm_SVWMu_nJet   -3.9108e-01 +/-  6.09e-01
alpha_QCDNorm_TREl_nJet   -7.6837e-01 +/-  6.47e-01
```

```
alpha_QCDNorm_TRMu_nJet    2.6128e-01 +/-  6.53e-01
alpha_QCDNorm_TRee_nJet    5.2791e-01 +/-  7.48e-01
alpha_QCDNorm_TRem_nJet    5.1741e-02 +/-  1.11e+00
alpha_QCDNorm_TRmm_nJet    1.1228e-01 +/-  1.25e+00
alpha_QCDNorm_WREl_nJet    1.3172e-01 +/-  2.41e-01
alpha_QCDNorm_WRMu_nJet   -2.8610e-01 +/-  8.92e-01
alpha_QCDNorm_ZRee_nJet    1.4336e-02 +/-  9.55e-01
alpha_QCDNorm_ZRmm_nJet    3.2123e-02 +/-  1.02e+00
          alpha_TEee    3.6007e-01 +/-  9.16e-01
          alpha_TEel   -2.7167e-01 +/-  9.41e-01
          alpha_TEem   -1.5103e-01 +/-  6.49e-01
          alpha_TEmm    4.5870e-01 +/-  5.36e-01
          alpha_TEmu    4.3290e-01 +/-  4.76e-01
     alpha_Zpt100GeV    2.1610e-01 +/-  6.07e-01
     alpha_Zpt150GeV    8.0396e-02 +/-  7.36e-01
     alpha_Zpt200GeV   -2.6990e-01 +/-  7.20e-01
      alpha_Zpt50GeV    1.2496e-01 +/-  6.99e-01
        alpha_err_BG   -4.7096e-02 +/-  9.72e-01
    alpha_err_WZ_Np0    1.1261e-02 +/-  9.56e-01
    alpha_err_WZ_Np1    2.8783e-01 +/-  1.81e-01
gamma_stat_SVTEl_nJet_bin_0    1.1592e+00 +/-  1.48e-01
gamma_stat_SVTEl_nJet_bin_1    9.3785e-01 +/-  9.28e-02
gamma_stat_SVTEl_nJet_bin_2    1.0599e+00 +/-  9.69e-02
gamma_stat_SVTEl_nJet_bin_3    1.0202e+00 +/-  1.33e-01
gamma_stat_SVTEl_nJet_bin_4    9.2554e-01 +/-  1.39e-01
gamma_stat_SVTEl_nJet_bin_5    1.0715e+00 +/-  3.21e-01
gamma_stat_SVTMu_nJet_bin_0    1.0117e+00 +/-  9.76e-02
gamma_stat_SVTMu_nJet_bin_1    9.5312e-01 +/-  8.09e-02
gamma_stat_SVTMu_nJet_bin_2    1.0146e+00 +/-  7.87e-02
gamma_stat_SVTMu_nJet_bin_3    1.0510e+00 +/-  7.29e-02
gamma_stat_SVTMu_nJet_bin_4    1.0045e+00 +/-  1.52e-01
gamma_stat_SVTMu_nJet_bin_5    1.0546e+00 +/-  2.74e-01
gamma_stat_SVWEl_nJet_bin_1    9.6839e-01 +/-  4.70e-02
gamma_stat_SVWEl_nJet_bin_2    9.3503e-01 +/-  7.01e-02
gamma_stat_SVWEl_nJet_bin_3    9.8481e-01 +/-  1.04e-01
gamma_stat_SVWEl_nJet_bin_4    1.0877e+00 +/-  1.64e-01
gamma_stat_SVWEl_nJet_bin_5    9.9079e-01 +/-  2.12e-01
gamma_stat_SVWMu_nJet_bin_2    9.7136e-01 +/-  6.05e-02
gamma_stat_SVWMu_nJet_bin_3    9.4722e-01 +/-  9.02e-02
gamma_stat_SVWMu_nJet_bin_4    1.0650e+00 +/-  1.52e-01
gamma_stat_SVWMu_nJet_bin_5    1.0805e+00 +/-  2.25e-01
gamma_stat_TREl_nJet_bin_5    1.0076e+00 +/-  5.31e-02
gamma_stat_TREl_nJet_bin_6    1.0293e+00 +/-  9.92e-02
gamma_stat_TRMu_nJet_bin_6    9.9807e-01 +/-  7.13e-02
gamma_stat_TRee_nJet_bin_4    1.0334e+00 +/-  7.43e-02
gamma_stat_TRee_nJet_bin_5    9.5275e-01 +/-  1.64e-01
```

```
gamma_stat_TRee_nJet_bin_6    9.7862e-01 +/-  2.58e-01
gamma_stat_TRee_nJet_bin_7    9.4746e-01 +/-  6.74e-01
gamma_stat_TRem_nJet_bin_4    1.0219e+00 +/-  4.81e-02
gamma_stat_TRem_nJet_bin_5    9.6577e-01 +/-  1.10e-01
gamma_stat_TRem_nJet_bin_6    1.0326e+00 +/-  2.46e-01
gamma_stat_TRem_nJet_bin_7    9.6471e-01 +/-  4.86e-01
gamma_stat_TRmm_nJet_bin_4    1.0506e+00 +/-  6.34e-02
gamma_stat_TRmm_nJet_bin_5    9.8600e-01 +/-  1.49e-01
gamma_stat_TRmm_nJet_bin_6    1.0560e+00 +/-  3.05e-01
gamma_stat_TRmm_nJet_bin_7    1.6062e+00 +/-  6.20e-01
gamma_stat_WREl_nJet_bin_4    9.3416e-01 +/-  5.87e-02
gamma_stat_WREl_nJet_bin_5    9.9502e-01 +/-  4.92e-02
gamma_stat_WREl_nJet_bin_6    1.0515e+00 +/-  8.42e-02
gamma_stat_WRMu_nJet_bin_5    1.0042e+00 +/-  4.84e-02
gamma_stat_WRMu_nJet_bin_6    9.9940e-01 +/-  8.26e-02
gamma_stat_ZRee_nJet_bin_5    1.0373e+00 +/-  9.60e-02
gamma_stat_ZRee_nJet_bin_6    9.6586e-01 +/-  1.77e-01
gamma_stat_ZRee_nJet_bin_7    8.8978e-01 +/-  3.96e-01
gamma_stat_ZRmm_nJet_bin_5    1.0445e+00 +/-  7.52e-02
gamma_stat_ZRmm_nJet_bin_6    1.0280e+00 +/-  1.76e-01
gamma_stat_ZRmm_nJet_bin_7    1.2097e+00 +/-  3.04e-01
          mu_Top_Np0    1.2677e+00 +/-  9.95e-02
          mu_Top_Np1    9.8943e-01 +/-  5.91e-02
          mu_Top_Np2    1.0716e+00 +/-  8.62e-02
          mu_Top_Np3    9.2026e-01 +/-  7.59e-02
           mu_WZ_Np2    1.1416e+00 +/-  7.90e-02
           mu_WZ_Np3    1.0677e+00 +/-  5.99e-02
           mu_WZ_Np4    1.0195e+00 +/-  6.25e-02
           mu_WZ_Np5    1.2441e+00 +/-  1.28e-01
```

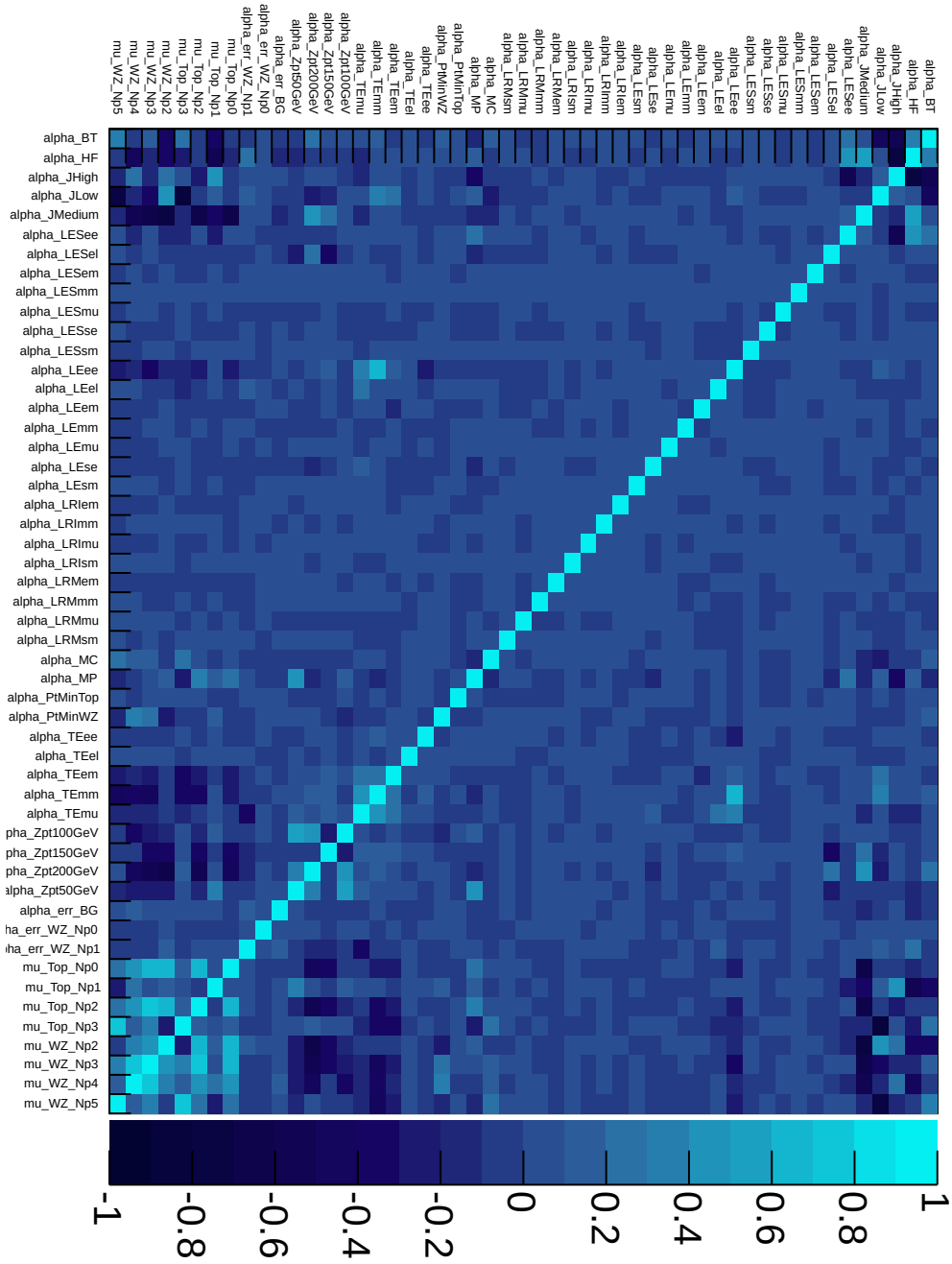

Figure 90: Correlation matrix for the background-only fit.

D Jet multiplicity input distributions for the soft lepton and dilepton control regions

Jet multiplicities for the soft lepton and dilepton control regions before and after fit.

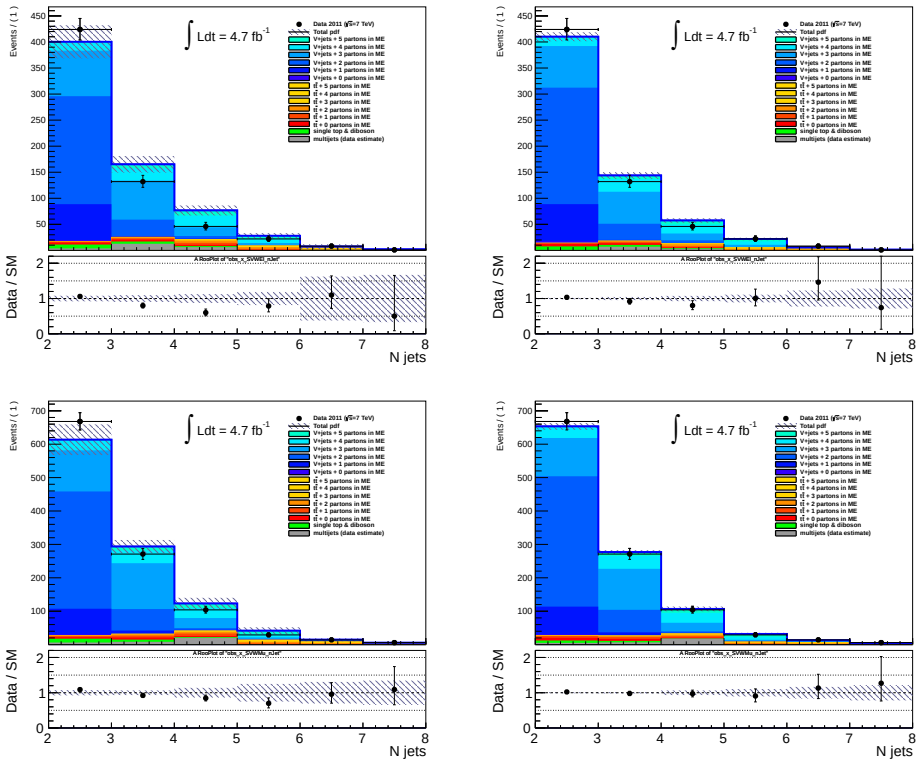

Figure 91: Jet multiplicity input distribution in the W boson control region for the final state with one soft electron (top) and one soft muon (bottom) before fit (right) and after fit (left). The shown uncertainty bands cover all systematic uncertainties introduced in chapter 6.5.

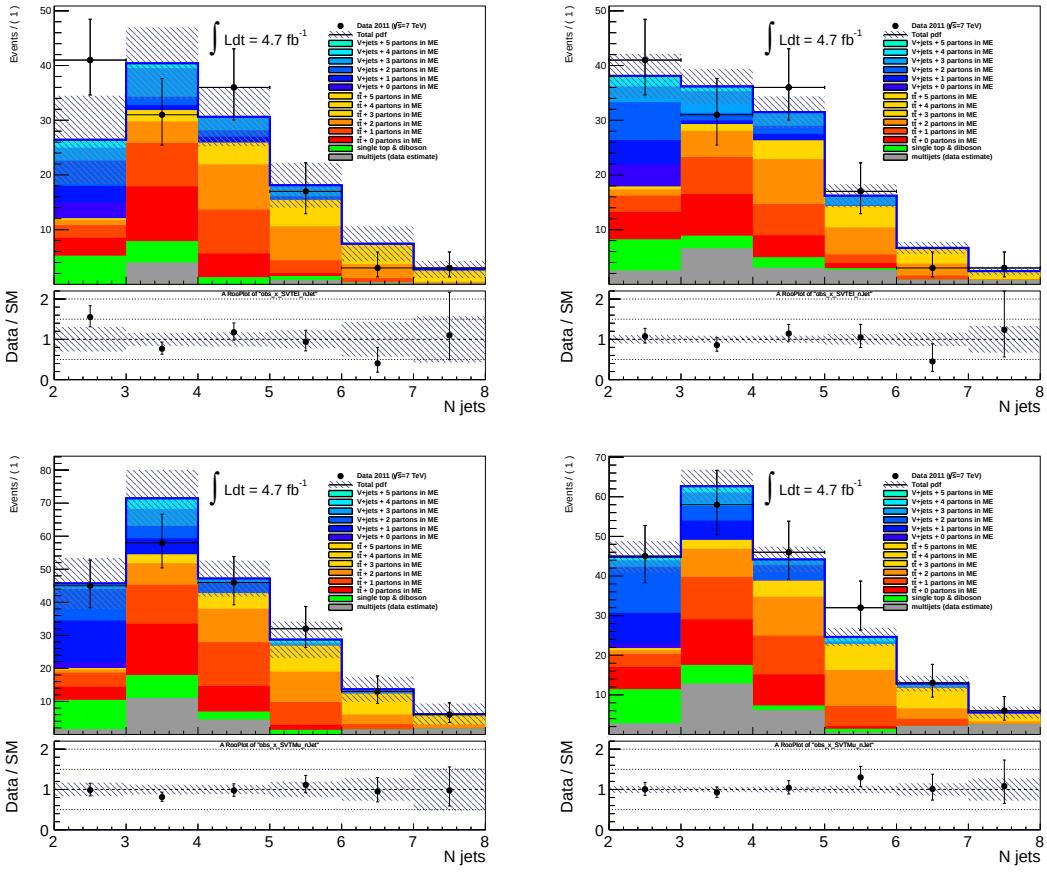

Figure 92: Jet multiplicity input distribution in the top control region for the final state with one soft electron (top) and one soft muon (bottom) before fit (right) and after fit (left). The shown uncertainty bands cover all systematic uncertainties introduced in chapter 6.5.

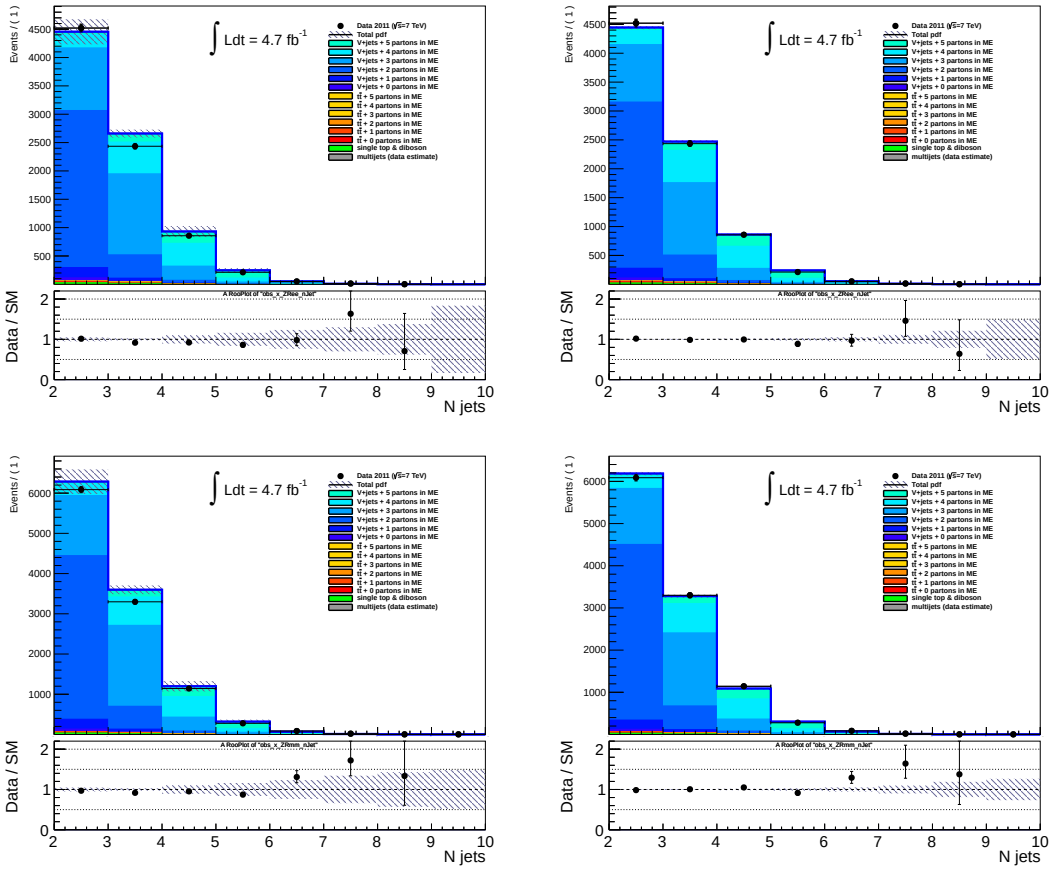

Figure 93: Jet multiplicity input distribution in the Z boson control region for the final state with two hard electrons (top) and two hard muons (bottom) before fit (right) and after fit (left). The shown uncertainty bands cover all systematic uncertainties introduced in chapter 6.5.

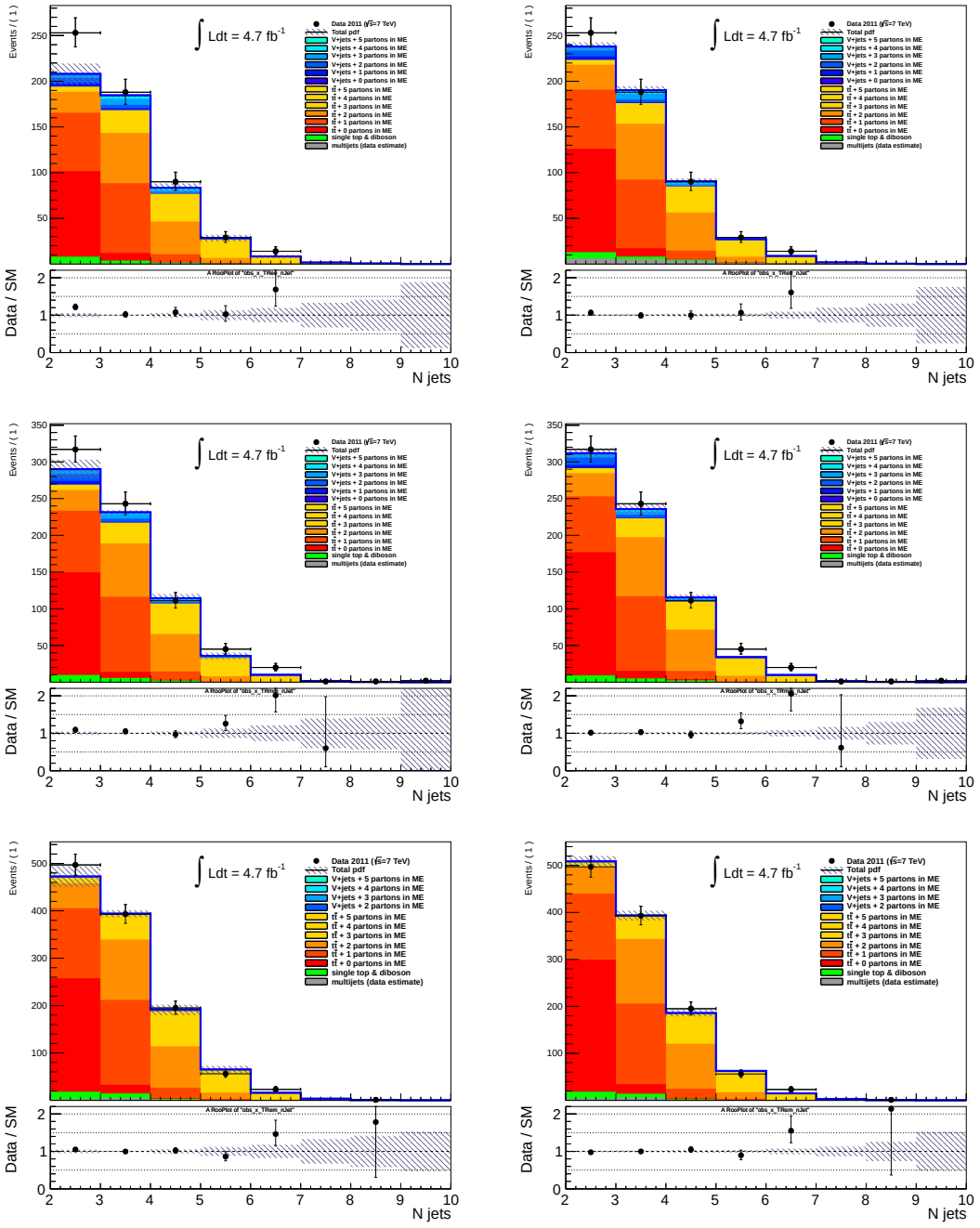

Figure 94: Jet multiplicity input distribution in the top control region for the final state with two hard electrons (top), two hard muons (middle) and one hard electron-muon pair (bottom) before fit (right) and after fit (left). The shown uncertainty bands cover all systematic uncertainties introduced in chapter 6.5.

E Fit results for the soft lepton and dilepton control regions

Fit results for the soft lepton and dilepton channels in the control regions:

channel	Top ee	Top $\mu\mu$	Top eμ
Observed events	574	740	1165
Fitted bkg events	559.3 ± 16.1	706.9 ± 15.6	1168.0 ± 29.4
Fitted top events	495.8 ± 13.2	648.3 ± 15.9	1129.5 ± 31.2
Fitted WZ events	36.5 ± 0.9	40.5 ± 1.0	3.2 ± 0.3
Fitted other BGs events	11.8 ± 2.3	16.6 ± 3.3	26.4 ± 5.3
Fitted QCD	15.1 ± 14.9	1.6 ± 2.7	8.9 ± 13.7
MC exp. SM events	510.1	678.6	1141.5
MC exp. top events	461.3	619.4	1101.5
MC exp. WZ events	34.1	40.9	3.4
MC exp. other BGs events	11.5	17.0	28.5
Data-driven QCD	3.2	1.2	8.1

Table 36: Background fit results for the dileptonic top control regions, for an integrated luminosity of 4.7fb^{-1}. Nominal MC expectations (normalised to MC cross-sections) are given for comparison. The errors shown are the statistical plus systematic uncertainties.

channel	Z ee	Z $\mu\mu$
Observed events	8090	10915
Fitted bkg events	8065.1 ± 91.8	10937.5 ± 102.5
Fitted top events	67.8 ± 1.9	82.2 ± 2.2
Fitted WZ events	7924.2 ± 104.2	10763.6 ± 102.8
Fitted other BGs events	69.8 ± 14.0	91.2 ± 18.3
Fitted QCD	3.2 ± 37.4	0.5 ± 4.0
MC exp. SM events	7393.4	10273.0
MC exp. top events	65.1	80.9
MC exp. WZ events	7253.2	10093.8
MC exp. other BGs events	73.0	98.0
Data-driven QCD	2.2	0.3

Table 37: Background fit results for the dileptonic Z control regions, for an integrated luminosity of 4.7fb^{-1}. Nominal MC expectations (normalised to MC cross-sections) are given for comparison. The errors shown are the statistical plus systematic uncertainties.

channel	Top e	W e	Top μ	W μ
Observed events	131	633	200	1092
Fitted bkg events	131.0 ± 10.2	640.1 ± 20.9	194.4 ± 11.7	1093.5 ± 28.0
Fitted top events	69.4 ± 5.8	31.8 ± 3.2	107.4 ± 6.4	57.7 ± 5.0
Fitted WZ events	34.4 ± 4.4	593.9 ± 19.9	43.1 ± 6.2	998.7 ± 28.8
Fitted other BGs events	10.6 ± 2.2	11.2 ± 2.3	16.2 ± 3.3	12.0 ± 3.2
Fitted QCD	16.5 ± 11.4	3.1 ± 0.5	27.7 ± 11.4	25.1 ± 21.1
MC exp. SM events	125.7	679.3	212.8	1091.5
MC exp. top events	78.8	44.3	122.6	72.5
MC exp. WZ events	30.3	597.0	50.0	961.5
MC exp. other BGs events	11.2	14.2	19.5	21.0
Data-driven QCD	5.4	23.9	20.7	36.4

Table 38: Background fit results for the soft lepton control regions, for an integrated luminosity of 4.7fb^{-1}. Nominal MC expectations (normalised to MC cross-sections) are given for comparison. The errors shown are the statistical plus systematic uncertainties.

F Exclusion-fit result for an example mSUGRA model point

Fit results for the exclusion fit configuration for an example mSUGRA model point with $m_0 = 3060$ GeV and $m_{\frac{1}{2}} = 300$ GeV.

```
RooFitResult: minimized FCN value: -113216,
              estimated distance to minimum: 0.00388989
              covariance matrix quality: Full, accurate covariance matrix
              Status : MINIMIZE=0

  Floating Parameter    FinalValue +/-  Error
--------------------  --------------------------
                Lumi    1.0000e+00 +/-  3.68e-02
            alpha_BT    6.1716e-01 +/-  2.01e-01
            alpha_HF   -1.8372e-01 +/-  4.06e-01
         alpha_JHigh   -5.8397e-01 +/-  1.68e-01
          alpha_JLow    1.7754e-02 +/-  1.06e-01
       alpha_JMedium   -4.1112e-01 +/-  2.75e-01
          alpha_JSig   -1.4920e-03 +/-  1.01e+00
         alpha_LESee    1.4343e-01 +/-  1.89e-01
         alpha_LESel    4.2309e-02 +/-  1.32e-01
         alpha_LESem    2.3759e-03 +/-  9.44e-01
         alpha_LESmm   -1.2616e-02 +/-  9.77e-01
         alpha_LESmu    9.6822e-03 +/-  9.78e-01
         alpha_LESse    1.4730e-02 +/-  9.53e-01
         alpha_LESsm   -1.2249e-02 +/-  9.92e-01
          alpha_LEee    1.3428e+00 +/-  5.69e-01
          alpha_LEel   -8.2052e-01 +/-  8.70e-01
          alpha_LEem    1.5764e-02 +/-  9.52e-01
          alpha_LEmm    2.2169e-02 +/-  7.98e-01
          alpha_LEmu    9.6580e-03 +/-  9.34e-01
          alpha_LEse   -3.7166e-01 +/-  5.85e-01
          alpha_LEsm    5.0370e-03 +/-  9.93e-01
         alpha_LRIem   -1.1064e-02 +/-  9.41e-01
         alpha_LRImm   -1.2561e-02 +/-  8.13e-01
         alpha_LRImu   -4.6099e-02 +/-  8.97e-01
         alpha_LRIsm   -2.8187e-02 +/-  9.78e-01
         alpha_LRMem   -3.1488e-02 +/-  9.49e-01
         alpha_LRMmm    3.9314e-02 +/-  9.03e-01
         alpha_LRMmu    7.9642e-02 +/-  1.05e+00
         alpha_LRMsm   -3.9153e-02 +/-  9.59e-01
            alpha_MC   -9.5757e-01 +/-  4.38e-01
            alpha_MP    4.4960e-02 +/-  1.78e-01
      alpha_PtMinTop    1.6802e-02 +/-  2.10e-01
    alpha_PtMinTopSR    6.9747e-02 +/-  8.56e-01
```

```
       alpha_PtMinWZ    1.0601e+00 +/-  6.76e-01
     alpha_PtMinWZSR   -2.2760e-01 +/-  6.63e-01
alpha_QCDNorm_S2em_meffInc    1.0325e-02 +/-  9.88e-01
alpha_QCDNorm_S3El_meffInc   -3.0757e-01 +/-  9.15e-01
alpha_QCDNorm_S3Mu_meffInc    2.3426e-01 +/-  9.87e-01
alpha_QCDNorm_S4El_meffInc    6.9537e-02 +/-  9.05e-01
alpha_QCDNorm_S4ee_meffInc   -8.9678e-02 +/-  8.53e-01
alpha_QCDNorm_S4em_meffInc   -1.2372e-02 +/-  9.38e-01
alpha_QCDNorm_S4mm_meffInc    3.7986e-03 +/-  1.01e+00
alpha_QCDNorm_SVTEl_nJet    4.0287e-01 +/-  4.12e-01
alpha_QCDNorm_SVTMu_nJet    2.6420e-01 +/-  5.64e-01
alpha_QCDNorm_SVWEl_nJet   -1.3652e+00 +/-  1.68e-02
alpha_QCDNorm_SVWMu_nJet   -4.6585e-01 +/-  6.07e-01
alpha_QCDNorm_TREl_nJet   -7.5689e-01 +/-  6.43e-01
alpha_QCDNorm_TRMu_nJet    9.9552e-02 +/-  5.87e-01
alpha_QCDNorm_TRee_nJet    6.9443e-01 +/-  7.20e-01
alpha_QCDNorm_TRem_nJet    2.6732e-01 +/-  9.87e-01
alpha_QCDNorm_TRmm_nJet    1.5028e-01 +/-  1.27e+00
alpha_QCDNorm_WREl_nJet    1.3121e-01 +/-  1.70e-01
alpha_QCDNorm_WRMu_nJet   -1.8093e-01 +/-  6.90e-01
alpha_QCDNorm_ZRee_nJet    2.2489e-02 +/-  9.16e-01
alpha_QCDNorm_ZRmm_nJet    2.8327e-02 +/-  9.93e-01
       alpha_SigXSec    1.4828e-03 +/-  9.00e-01
          alpha_TEee    3.7415e-01 +/-  8.03e-01
          alpha_TEel   -3.3679e-01 +/-  9.02e-01
          alpha_TEem    4.5806e-02 +/-  6.14e-01
          alpha_TEmm    5.9874e-01 +/-  4.85e-01
          alpha_TEmu    4.6970e-01 +/-  4.38e-01
     alpha_Zpt100GeV    1.9573e-01 +/-  5.94e-01
     alpha_Zpt150GeV    1.8136e-01 +/-  6.65e-01
     alpha_Zpt200GeV   -2.1015e-01 +/-  5.89e-01
      alpha_Zpt50GeV    9.7869e-02 +/-  6.59e-01
        alpha_err_BG   -6.1572e-02 +/-  8.16e-01
    alpha_err_WZ_Np0    9.9890e-03 +/-  1.19e+00
    alpha_err_WZ_Np1    4.7006e-01 +/-  2.69e-01
        alpha_hadTop   -6.1200e-02 +/-  1.22e-01
         alpha_hadWZ    2.2785e-03 +/-  1.35e-01
gamma_stat_S2ee_meffInc_bin_2    9.6831e-01 +/-  9.47e-01
gamma_stat_S2ee_meffInc_bin_3    8.8757e-01 +/-  9.06e-01
gamma_stat_S2ee_meffInc_bin_4    9.0378e-01 +/-  6.52e-01
gamma_stat_S2em_meffInc_bin_1    9.5753e-01 +/-  6.79e-01
gamma_stat_S2em_meffInc_bin_2    9.2854e-01 +/-  4.91e-01
gamma_stat_S2em_meffInc_bin_3    9.2806e-01 +/-  5.45e-01
gamma_stat_S2em_meffInc_bin_4    1.1330e+00 +/-  4.02e-01
gamma_stat_S2mm_meffInc_bin_1    9.5485e-01 +/-  6.76e-01
gamma_stat_S2mm_meffInc_bin_2    9.7035e-01 +/-  5.41e-01
```

```
gamma_stat_S2mm_meffInc_bin_3    8.9966e-01 +/-  7.87e-01
gamma_stat_S2mm_meffInc_bin_4    9.6351e-01 +/-  5.04e-01
gamma_stat_S3El_meffInc_bin_0    8.6374e-01 +/-  2.67e-01
gamma_stat_S3El_meffInc_bin_1    9.6756e-01 +/-  1.03e-01
gamma_stat_S3El_meffInc_bin_2    9.7715e-01 +/-  1.10e-01
gamma_stat_S3El_meffInc_bin_3    9.5866e-01 +/-  1.82e-01
gamma_stat_S3El_meffInc_bin_4    7.5094e-01 +/-  3.30e-01
gamma_stat_S3El_meffInc_bin_5    1.1025e+00 +/-  2.59e-01
gamma_stat_S3Mu_meffInc_bin_0    9.7263e-01 +/-  3.00e-01
gamma_stat_S3Mu_meffInc_bin_1    1.0184e+00 +/-  9.39e-02
gamma_stat_S3Mu_meffInc_bin_2    1.0434e+00 +/-  9.65e-02
gamma_stat_S3Mu_meffInc_bin_3    1.0508e+00 +/-  1.64e-01
gamma_stat_S3Mu_meffInc_bin_4    9.6592e-01 +/-  2.69e-01
gamma_stat_S3Mu_meffInc_bin_5    7.6082e-01 +/-  3.83e-01
gamma_stat_S4El_meffInc_bin_0    1.0780e+00 +/-  3.98e-01
gamma_stat_S4El_meffInc_bin_1    1.0017e+00 +/-  1.61e-01
gamma_stat_S4El_meffInc_bin_2    9.5191e-01 +/-  2.77e-01
gamma_stat_S4El_meffInc_bin_3    1.0035e+00 +/-  1.81e-01
gamma_stat_S4Mu_meffInc_bin_0    9.8031e-01 +/-  2.79e-01
gamma_stat_S4Mu_meffInc_bin_1    1.0450e+00 +/-  1.70e-01
gamma_stat_S4Mu_meffInc_bin_2    9.9514e-01 +/-  1.48e-01
gamma_stat_S4Mu_meffInc_bin_3    9.9213e-01 +/-  1.14e-01
gamma_stat_S4ee_meffInc_bin_0    1.0288e+00 +/-  9.45e-02
gamma_stat_S4ee_meffInc_bin_1    9.7751e-01 +/-  1.05e-01
gamma_stat_S4ee_meffInc_bin_2    9.7659e-01 +/-  1.40e-01
gamma_stat_S4ee_meffInc_bin_3    9.8620e-01 +/-  1.82e-01
gamma_stat_S4ee_meffInc_bin_4    9.9022e-01 +/-  2.23e-01
gamma_stat_S4em_meffInc_bin_0    9.9908e-01 +/-  6.17e-02
gamma_stat_S4em_meffInc_bin_1    9.9320e-01 +/-  7.24e-02
gamma_stat_S4em_meffInc_bin_2    9.8899e-01 +/-  1.03e-01
gamma_stat_S4em_meffInc_bin_3    1.0005e+00 +/-  1.53e-01
gamma_stat_S4em_meffInc_bin_4    1.0141e+00 +/-  1.60e-01
gamma_stat_S4mm_meffInc_bin_0    1.0062e+00 +/-  7.37e-02
gamma_stat_S4mm_meffInc_bin_1    1.0104e+00 +/-  1.03e-01
gamma_stat_S4mm_meffInc_bin_2    9.7853e-01 +/-  1.29e-01
gamma_stat_S4mm_meffInc_bin_3    1.0115e+00 +/-  1.66e-01
gamma_stat_S4mm_meffInc_bin_4    9.8487e-01 +/-  2.32e-01
gamma_stat_SVTEl_nJet_bin_0    1.2096e+00 +/-  1.45e-01
gamma_stat_SVTEl_nJet_bin_1    9.3453e-01 +/-  9.13e-02
gamma_stat_SVTEl_nJet_bin_2    1.0608e+00 +/-  9.45e-02
gamma_stat_SVTEl_nJet_bin_3    1.0080e+00 +/-  1.32e-01
gamma_stat_SVTEl_nJet_bin_4    9.2429e-01 +/-  1.39e-01
gamma_stat_SVTEl_nJet_bin_5    1.0614e+00 +/-  3.18e-01
gamma_stat_SVTMu_nJet_bin_0    1.0177e+00 +/-  9.56e-02
gamma_stat_SVTMu_nJet_bin_1    9.4906e-01 +/-  7.84e-02
gamma_stat_SVTMu_nJet_bin_2    1.0136e+00 +/-  7.76e-02
```

```
gamma_stat_SVTMu_nJet_bin_3    1.0453e+00 +/-  7.32e-02
gamma_stat_SVTMu_nJet_bin_4    1.0062e+00 +/-  1.50e-01
gamma_stat_SVTMu_nJet_bin_5    1.0435e+00 +/-  2.69e-01
gamma_stat_SVWEl_nJet_bin_1    9.6470e-01 +/-  4.71e-02
gamma_stat_SVWEl_nJet_bin_2    9.2632e-01 +/-  7.12e-02
gamma_stat_SVWEl_nJet_bin_3    9.7688e-01 +/-  1.04e-01
gamma_stat_SVWEl_nJet_bin_4    1.0836e+00 +/-  1.66e-01
gamma_stat_SVWEl_nJet_bin_5    9.8652e-01 +/-  2.12e-01
gamma_stat_SVWMu_nJet_bin_2    9.6849e-01 +/-  5.93e-02
gamma_stat_SVWMu_nJet_bin_3    9.3858e-01 +/-  8.98e-02
gamma_stat_SVWMu_nJet_bin_4    1.0515e+00 +/-  1.51e-01
gamma_stat_SVWMu_nJet_bin_5    1.0872e+00 +/-  2.25e-01
gamma_stat_TREl_nJet_bin_5    1.0060e+00 +/-  5.31e-02
gamma_stat_TREl_nJet_bin_6    1.0286e+00 +/-  9.72e-02
gamma_stat_TRMu_nJet_bin_6    9.9850e-01 +/-  7.06e-02
gamma_stat_TRee_nJet_bin_4    1.0334e+00 +/-  7.38e-02
gamma_stat_TRee_nJet_bin_5    9.5317e-01 +/-  1.63e-01
gamma_stat_TRee_nJet_bin_6    9.7189e-01 +/-  2.57e-01
gamma_stat_TRee_nJet_bin_7    9.6393e-01 +/-  5.82e-01
gamma_stat_TRem_nJet_bin_4    1.0223e+00 +/-  4.80e-02
gamma_stat_TRem_nJet_bin_5    9.6581e-01 +/-  1.09e-01
gamma_stat_TRem_nJet_bin_6    1.0256e+00 +/-  2.20e-01
gamma_stat_TRem_nJet_bin_7    9.7829e-01 +/-  3.90e-01
gamma_stat_TRmm_nJet_bin_4    1.0513e+00 +/-  6.34e-02
gamma_stat_TRmm_nJet_bin_5    9.8643e-01 +/-  1.46e-01
gamma_stat_TRmm_nJet_bin_6    1.0426e+00 +/-  2.60e-01
gamma_stat_TRmm_nJet_bin_7    1.6056e+00 +/-  6.22e-01
gamma_stat_WREl_nJet_bin_4    9.3146e-01 +/-  5.80e-02
gamma_stat_WREl_nJet_bin_5    9.9431e-01 +/-  4.91e-02
gamma_stat_WREl_nJet_bin_6    1.0496e+00 +/-  8.33e-02
gamma_stat_WRMu_nJet_bin_5    1.0057e+00 +/-  4.82e-02
gamma_stat_WRMu_nJet_bin_6    9.9955e-01 +/-  8.14e-02
gamma_stat_ZRee_nJet_bin_5    1.0393e+00 +/-  9.57e-02
gamma_stat_ZRee_nJet_bin_6    9.6808e-01 +/-  1.77e-01
gamma_stat_ZRee_nJet_bin_7    9.0632e-01 +/-  3.72e-01
gamma_stat_ZRmm_nJet_bin_5    1.0443e+00 +/-  7.51e-02
gamma_stat_ZRmm_nJet_bin_6    1.0232e+00 +/-  1.73e-01
gamma_stat_ZRmm_nJet_bin_7    1.2075e+00 +/-  3.04e-01
              mu_SIG    3.7596e-08 +/-  1.58e-01
          mu_Top_Np0    1.2305e+00 +/-  9.07e-02
          mu_Top_Np1    9.7231e-01 +/-  5.63e-02
          mu_Top_Np2    1.0398e+00 +/-  6.81e-02
          mu_Top_Np3    8.4885e-01 +/-  4.02e-02
           mu_WZ_Np2    1.1532e+00 +/-  6.08e-02
           mu_WZ_Np3    1.0308e+00 +/-  4.14e-02
           mu_WZ_Np4    9.8793e-01 +/-  6.61e-02
```

```
mu_WZ_Np5     1.1458e+00 +/-  7.46e-02
```

G Kinematic distributions used for the exclusion-fit for the soft lepton and dilepton analysis

Kinematic distributions used for the exclusion-fit for the soft lepton and dilepton analysis:

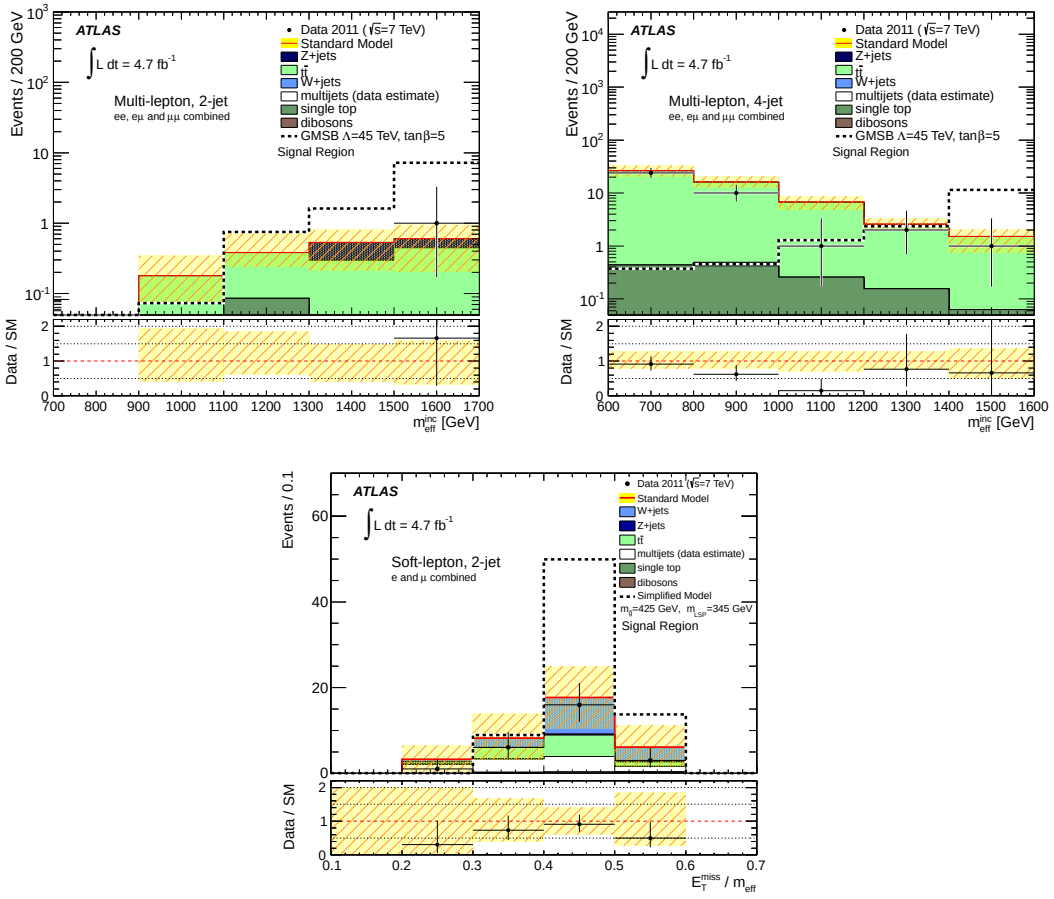

Figure 95: Distributions used for the exclusion fit configuration for the dilepton and soft lepton signal regions. Top left: Inclusive effective mass in the dileptonic two jet signal region. Top right: Inclusive effective mass in the dileptonic four jet signal region. Bottom: Ratio of missing transverse energy and inclusive effective mass in the soft lepton signal region. The error band includes all systematic uncertainties on the background prediction.

H Fit results in the soft lepton and dilepton signal regions

Fitted background events in the soft lepton and dilepton signal region:

channel	2 Jet ee	2 Jet $\mu\mu$	2 Jet eμ
Observed events	0	0	1
Fitted bkg events	0.3 ± 0.2	0.4 ± 0.2	0.7 ± 0.2
Fitted top events	0.1 ± 0.1	0.2 ± 0.1	0.6 ± 0.2
Fitted WZ events	0.1 ± 0.1	0.1 ± 0.0	0.0 ± 0.0
Fitted other BGs events	0.1 ± 0.1	0.1 ± 0.0	0.1 ± 0.0
Fitted QCD & fake lepton events	0.0 ± 0.0	0.0 ± 0.0	0.0 ± 0.0
MC exp. SM events	0.3	0.5	0.9
MC exp. top events	0.2	0.3	0.7
MC exp. WZ events	0.1	0.1	0.1
MC exp. other BGs events	0.1	0.1	0.1
Data-driven QCD	0.0	0.0	0.0

Table 39: Background fit results for the dileptonic signal regions with two jets, for an integrated luminosity of 4.7fb^{-1}. Nominal MC expectations (normalised to MC cross-sections) are given for comparison. The errors shown are the statistical plus systematic uncertainties.

channel	4 Jet ee	4 Jet $\mu\mu$	4 Jet eμ
Observed events	8	12	18
Fitted bkg events	9.1 ± 1.5	11.7 ± 1.7	$21.1 \pm 3.$
Fitted top events	9.1 ± 1.4	11.1 ± 1.7	$20.1 \pm 3.$
Fitted WZ events	0.0 ± 0.0	0.2 ± 0.1	0.4 ± 0.1
Fitted other BGs events	0.0 ± 0.0	0.4 ± 0.1	0.6 ± 0.1
Fitted QCD & fake lepton events	0.0 ± 0.2	0.0 ± 0.0	0.0 ± 0.0
MC exp. SM events	11.4	14.7	27.1
MC exp. top events	11.1	13.9	26.0
MC exp. WZ events	0.1	0.3	0.4
MC exp. other BGs events	0.2	0.5	0.7
Data-driven QCD	0.0	0.0	0.0

Table 40: Background fit results for the dileptonic signal regions with four jets, for an integrated luminosity of 4.7fb^{-1}. Nominal MC expectations (normalised to MC cross-sections) are given for comparison. The errors shown are the statistical plus systematic uncertainties.

channel	Electron	Muon
Observed events	11	14
Fitted bkg events	14.0 ± 3.3	19 ± 5
Fitted top events	3.8 ± 0.6	3.8 ± 0.8
Fitted WZ events	5.8 ± 1.0	11.4 ± 2.3
Fitted other BGs events	0.6 ± 0.1	0.2 ± 0.1
Fitted QCD & fake lepton events	3.8 ± 2.5	3.6 ± 2.5
MC exp. SM events	14.2	18.0
MC exp. top events	4.3	3.8
MC exp. WZ events	5.5	10.5
MC exp. other BGs events	0.5	0.1
Data-driven QCD	3.8	3.6

Table 41: Background fit results for the soft lepton signal regions, for an integrated luminosity of 4.7fb^{-1}. Nominal MC expectations (normalised to MC cross-sections) are given for comparison. The errors shown are the statistical plus systematic uncertainties.

I Detector acceptance times selection efficiency for the mSUGRA scenario for the one muon signal regions

Detector acceptance times selection efficiency for the mSUGRA scenario for the one muon signal regions:

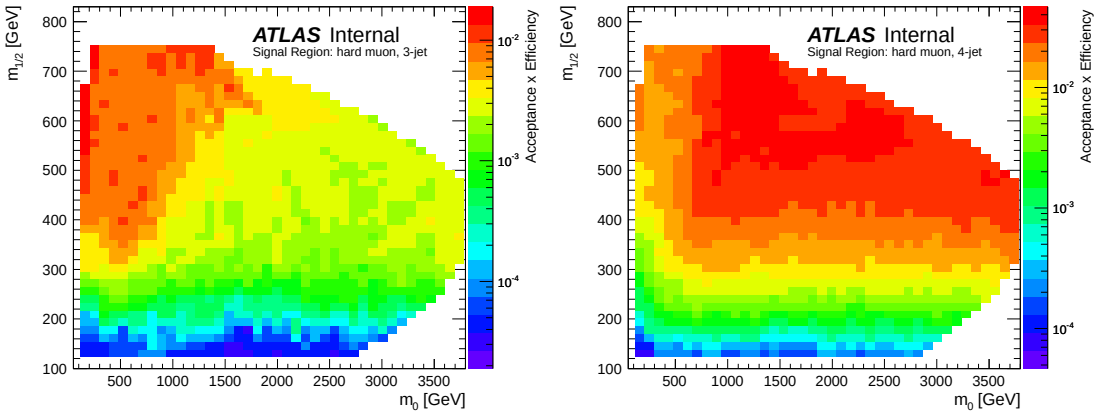

Figure 96: Detector acceptance times selection efficiency for the mSUGRA model with $\tan(\beta) = 10$, $A_0 = 0$ and $\mu > 0$ in the hard muon channels. Left: Three jet single muon signal region. Right: Four jet single muon signal region.

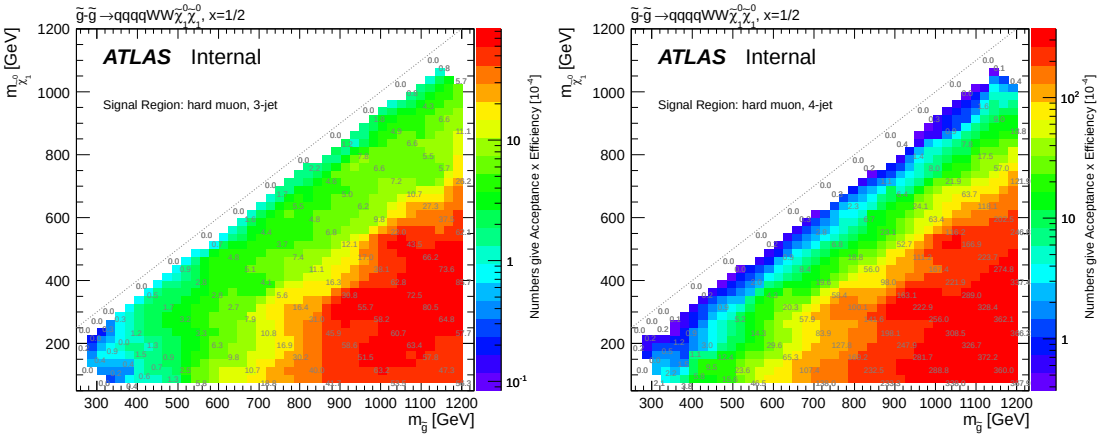

Figure 97: Detector acceptance times the selection efficiency for the one step simplified model with gluino pair production and a fixed compression factor for various signal regions in the muon channels. Left: Three jet single muon signal region. Right: Four jet single muon signal region.

J Model independent limits on the visible cross section for the soft lepton and dilepton final state

95% CL limits on the visible cross section for the soft lepton and dilepton final state:

Signal channel	$\langle\epsilon\sigma\rangle^{95}_{\text{obs}}$[fb]	S^{95}_{obs}	S^{95}_{exp}	CL_B
soft electron	1.82	8.6	$10.4^{+4.2}_{-3.1}$	0.28
soft muon	1.92	9.0	$12.5^{+5.4}_{-3.8}$	0.21
multi-lepton, ee, 2-jet	0.71	3.3	3.5 ± 0.1	0.48
multi-lepton, $\mu\mu$, 2-jet	0.76	3.6	3.5 ± 0.1	0.46
multi-lepton, $e\mu$, 2-jet	0.83	3.9	$3.6^{+0.6}_{-0.2}$	0.85
multi-lepton, ee, 4-jet	1.53	7.2	$7.7^{+3.2}_{-2.1}$	0.39
multi-lepton, $\mu\mu$, 4-jet	1.93	9.1	$8.8^{+3.3}_{-3.0}$	0.55
multi-lepton, $e\mu$, 4-jet	2.14	10.1	$11.5^{+4.8}_{-3.5}$	0.28

Table 42: 95% CL limits on the visible cross section (first column), the number of signal events (second column) and the number of signal events, taking into account the background prediction and its uncertainties (third column). The last column shows the confidence level for the background-only hypothesis. The results are shown for the dileptonic and soft lepton signal regions.